INL/EXT-15-37307

Geothermal Risk Reduction via Geothermal/Solar Hybrid Power Plants: Final Report

Daniel Wendt and Greg Mines
Idaho National Laboratory

Craig Turchi and Guangdong Zhu
National Renewable Energy Laboratory

November 2015

The INL is a U.S. Department of Energy National Laboratory
operated by Battelle Energy Alliance

INL/EXT-15-37307

Geothermal Risk Reduction via Geothermal/Solar Hybrid Power Plants: Final Report

Daniel Wendt and Greg Mines
Idaho National Laboratory

Craig Turchi and Guangdong Zhu
National Renewable Energy Laboratory

November 2015

Idaho National Laboratory
Idaho Falls, Idaho 83415

http://www.inl.gov

Prepared for the
U.S. Department of Energy
Geothermal Technologies Office
Under DOE Idaho Operations Office
Contract DE-AC07-05ID14517

FOREWORD

This report documents a series of analyses undertaken by Idaho National Laboratory and the National Renewable Energy Laboratory related to the design and optimization of geothermal-solar hybrid power plants. The work was performed under funding from the U.S. Department of Energy's Geothermal Technologies Office under the task "Geothermal Risk Reduction via Geothermal/Solar Hybrid Power Plants."

The report also includes data and analyses developed in a Cooperative Research and Development Agreement (CRADA) between the two national laboratories and Enel Green Power North America. Complementary work documented in this report was performed by NREL with funding from the United States Agency for International Development (USAID).

EXECUTIVE SUMMARY

Geothermal and solar-thermal power technologies rely on Rankine power cycles to convert renewable thermal energy into electricity. Both technologies implement heat transfer fluids to move and sometimes store thermal energy. In addition to these shared features, the technologies have important differences. Geothermal resources tend to be difficult to find and develop, but provide long-term, low-cost heat on a near-continuous basis. In contrast, solar resources are well documented and follow predictable daily and seasonal patterns, but are subject short-term variability due to weather. The commonalities and differences have led many to examine the advantages and technical feasibility of combining geothermal and solar-thermal energy in hybrid systems.

The technical merits associated with renewable geothermal-solar hybrid plant concepts often take advantage of the concurrence of solar energy with elevated daily temperatures that decrease the efficiency of geothermal power plants. This is particularly relevant to air-cooled binary plants where high ambient temperatures increase working fluid condensing temperature and turbine exhaust pressure, leading to lower thermal-electric efficiency. In most of the western United States, electrical power demand is generally at peak levels during periods of elevated ambient temperature and it is therefore especially important to utilities to be able to provide electrical power during these periods. Use of solar heat to increase air-cooled geothermal power plant performance during these periods can improve the correlation between power plant output and utility load curves.

This report documents several different potential geothermal-solar hybrid designs. The “brine preheating” configuration evaluates a method of introducing solar heat into a geothermal power system by heating the production fluid with solar energy prior to the power block. Such a design makes no changes to the geothermal power system and is most advantageous as a retrofit to plants whose geothermal reservoir has cooled over time. Adding solar energy achieves a double benefit of providing additional generation and increasing conversion efficiency by returning the power block to its original design-point operating conditions. Although solar thermal energy storage could be applied, in most cases the greatest benefit occurs during time periods coinciding with solar availability, and the additional cost of thermal energy storage is not warranted.

System models of these and other hybrid configurations are developed by combining NREL’s System Advisor Model (SAM) for solar-thermal hardware with models of Rankine power systems developed in Aspen, IPSEpro, and MATLAB simulation software. Simulation results illustrate the ability of the hybrid designs to offset the lower generation that is associated with degraded power output during periods of high ambient temperature (Figure ES-1).

While retrofit hybrid plants are likely to use the solar-thermal energy to increase the temperature or flowrate of the brine upstream of the power block, greenfield hybrids have greater flexibility to utilize the solar heat in more efficient configurations. The “ORC working fluid heating” configuration models a design in which heat from the solar field is input directly to the ORC working fluid to boost temperature or mass flow to the power turbine. Such a design requires greater integration of the two technologies versus the brine preheating configuration, but also offers higher overall efficiency by allowing the system to tap into the higher temperature and exergy available with solar-thermal heat. For example, the temperature range of geothermal power sources is generally no higher than about 200°C, while concentrating solar-thermal collectors can readily achieve temperatures of 400°C or above.

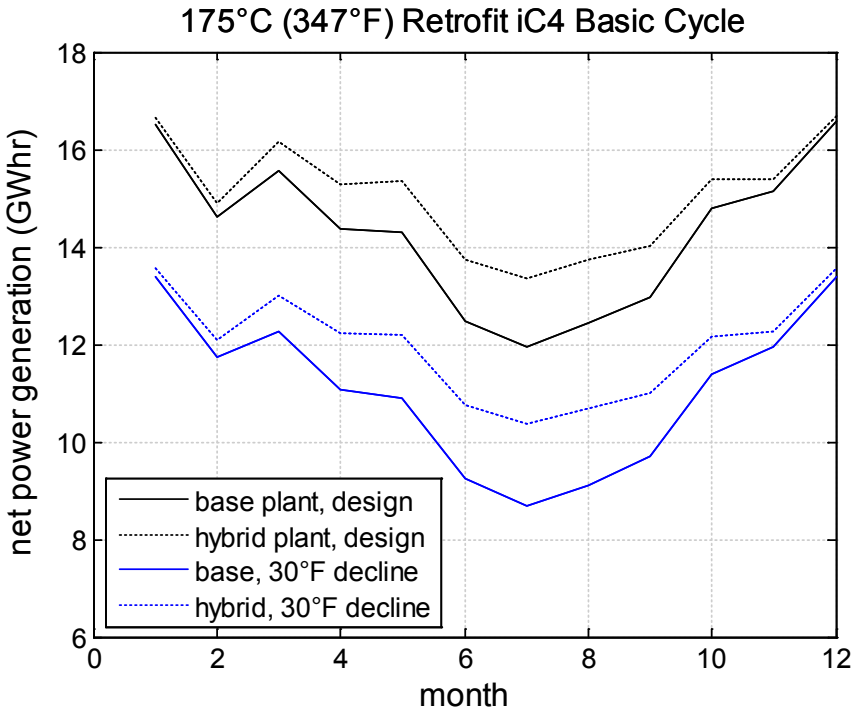

Figure ES-1. Addition generation from a brine-preheating hybrid design is most apparent during periods of high-ambient temperature, such as summer afternoons. Geothermal plants that have experienced reservoir temperature declines are good candidates for hybridization.

The economics of geothermal-solar hybridization depends strongly on the cost of solar thermal collectors and the efficiency of the power block system. Development and deployment of solar thermal hardware in concentrating solar power (CSP) plants has led to significant decreases in collector costs over the past decade. The study found that solar-thermal collectors can supply heat at a lower levelized cost than natural gas boilers based on 2014 industrial gas cost in California and the typical solar resource in the state.

While deploying solar-thermal collectors in hybrid plants avoids the need for a dedicated CSP power island, if the hybrid power conversion efficiency is too low, this cost benefit can be overwhelmed by the efficiency penalty (versus a stand-alone CSP power cycle running at ca. 390 °C). Thus, economic viability depends on the solar-thermal system capital cost and the marginal conversion efficiency of the integrated solar-thermal energy. It is estimated that installed solar field costs of less than about $\$100/m^2$ to $\$150/m^2$ (corresponding to about $\$210/m^2$ to $\$280/m^2$ for complete project costs) are necessary for economic viability in most cases, although project economics are highly influenced by site-specific resource and financial conditions. Figure ES-2 highlights the estimated hybrid plant levelized cost of energy (LCOE) as a function of installed solar field cost for a greenfield scenario without time-of-delivery energy pricing.

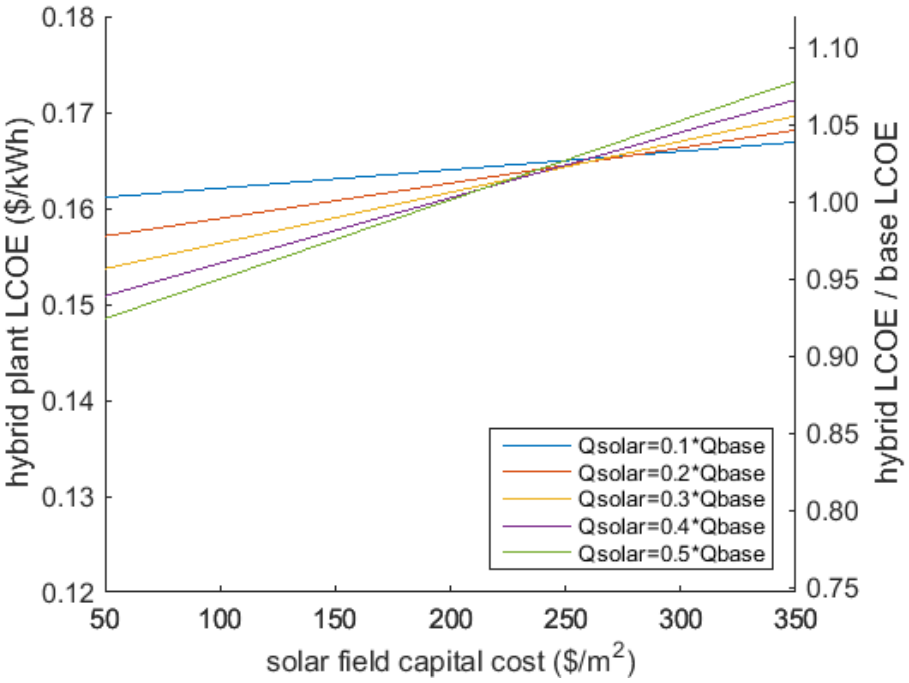

Figure ES-2. Greenfield hybrid plant minimum electricity sales price (left y-axis) and ratio of hybrid-to-base LCOE (right y axis) plotted as function of solar field capital costs for level pricing scheme (basic cycle with 175°C production fluid design temperature).

Additional analysis examined the potential for retrofitting flash steam plants with solar-thermal collectors. Many of the considerations are the same as for binary-cycle ORC plants. However, the greater power cycle conversion efficiency and the ability to integrate solar-generated steam directly provide greater potential for steam plant designs. Lastly, a greenfield design that incorporates geothermal energy for feedwater heating in a CSP plant illustrated that such a design provides superior exergy efficiency for the two heat sources. Conversion efficiency of geothermal energy was approximately twice that available in a stand-alone binary-cycle plant on the same resource, while overall power output of the hybrid plant increased by 8% versus a stand-alone CSP plant of the same solar-field size. The greatest challenge for such a configuration is making effective use of the geothermal energy during the absence of sunlight.

The tools developed in the current work have been used to simulate operating conditions of Enel Green Power's Stillwater Geothermal-Solar Hybrid plant. The analysis has proven valuable to the plant operators by identifying operating conditions that maximize power generation and efficiency of the solar retrofit. Various modifications to plant operating strategy were predicted to increase hybrid plant annual net power generation by up to 3.8% (relative to non-optimized hybrid plant operations), and the possibility of additional increases in power generation through use of an alternate ORC working fluid was identified for further investigation. The methodology used in these analyses could be used to assess the attractiveness of hybrid designs for other locations.

CONTENTS

FIGURES

TABLES

ACRONYMS

ACC	air-cooled condenser
CRADA	cooperative research and development agreement
CSP/CST	concentrating solar power/thermal
DNI	direct normal insolation
DO	distant observer
EGP	Enel Green Power
GTO	Geothermal Technologies Office
HTF	heat transfer fluid
IAM	incident angle modifier
IGV	inlet guide vanes
INL	Idaho National Laboratory
MACRS	Modified Accelerated Cost Recovery System
NPV	Net Present Value
NREL	National Renewable Energy Laboratory
ORC	organic Rankine cycle
PPA	Power Purchse Agreement
PV	photovoltaic
SAM	System Advisor Model
SCA	solar collector assembly
TMY	typical meteorological year
TOD	time-of-delivery
VFD	variable frequency drive
WF	working fluid

Geothermal Risk Reduction via Geothermal/Solar Hybrid Power Plants: Final Report

1. Introduction

There are numerous technical merits associated with a renewable geothermal-solar hybrid plant concept. The performance of air-cooled binary plants is lowest when ambient temperatures are high due to the decrease in air-cooled binary plant performance that occurs when the working fluid condensing temperature, and consequently the turbine exhaust pressure, increases. Electrical power demand is generally at peak levels during periods of elevated ambient temperature and it is therefore especially important to utilities to be able to provide electrical power during these periods. The time periods in which air-cooled binary geothermal power plant performance is lowest generally correspond to periods of high solar insolation. Use of solar heat to increase air-cooled geothermal power plant performance during these periods can improve the correlation between power plant output and utility load curves.

While solar energy is a renewable energy source with long term performance that can be accurately characterized, on shorter time scales of hours or days it can be highly intermittent. Concentrating solar power (CSP), aka solar-thermal, plants often incorporate thermal energy storage to ensure continued operation during cloud events or after sunset. Hybridization with a geothermal power plant can eliminate the need for thermal storage due to the constant availability of geothermal heat. In addition to the elimination of the requirement for solar thermal storage, the ability of a geothermal/solar-thermal hybrid plant to share a common power block can reduce capital costs relative to separate, stand-alone geothermal and solar-thermal power plant installations. These attributes have been discussed in previous analyses [1-5] and demonstrated in field testing [6-10].

The common occurrence of long-term geothermal resource productivity decline provides additional motivation to consider the use of hybrid power plants in geothermal power production. Geothermal resource productivity decline is a source of significant risk in geothermal power generation. Many, if not all, geothermal resources are subject to decreasing productivity manifested in the form of decreasing production fluid temperature, flow rate, or both during the life span of the associated power generation project. The impacts of geothermal production fluid temperature decline on power plant performance can be significant; a reduction in heat input to a power plant not only decreases the thermal energy available for conversion to electrical power, but also adversely impacts the power plant efficiency. As indicated by simulated results for an isobutane basic organic Rankine cycle (ORC) with a 175°C resource design temperature presented in Figure 1, over time a steady unmitigated annual production fluid temperature decline could decrease the power generation of an aging air-cooled binary geothermal power plant to a fraction of its design point performance.

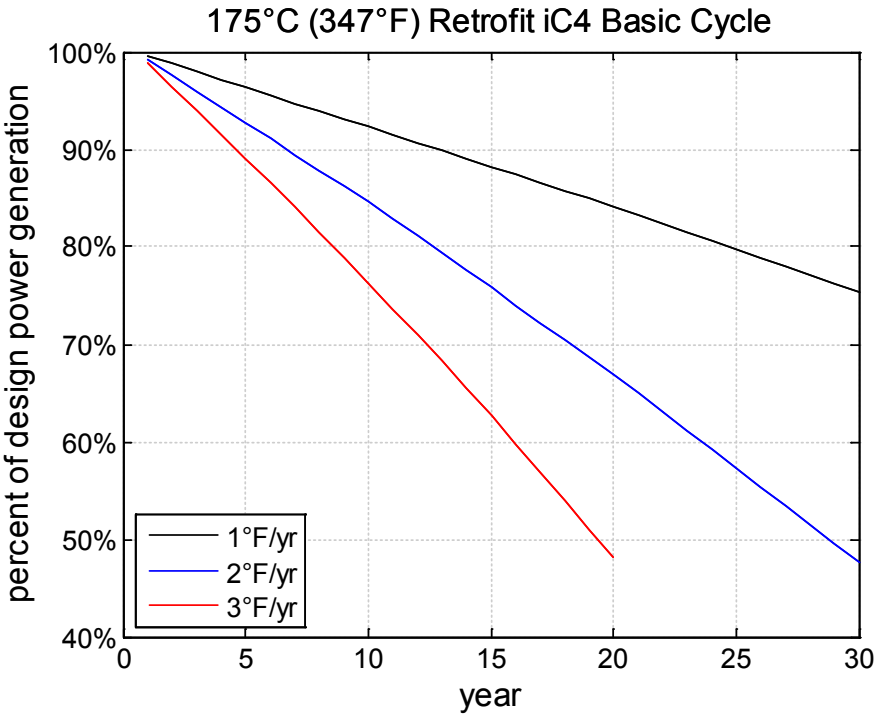

Figure 1. Decrease in annual power generation of an isobutane basic cycle with 175°C (347°F) resource design temperature plotted for various rates of resource temperature decline

The impact of resource productivity decline on power generation project economics can be equally detrimental. The reduction in power generation is directly correlated to a reduction in revenues from power sales. Further, projects with Power Purchase Agreement (PPA) contracts in place may be subject to significant economic penalties if power generation falls below a specified default level. While the magnitude of PPA penalties varies on a case-by-case basis, it is not unrealistic for these penalties to be on the order of the value of the deficit power sales such that the utility may purchase the power elsewhere.

This report evaluates the use of geothermal/solar-thermal hybrid plant technology for mitigation of resource productivity decline, which has not been a primary topic of investigation in previous analyses in the open literature. Solar heat can be used to augment the heat input to a geothermal power plant operating from a resource with declining productivity to increase the thermal input to the power plant to conditions closer to those for which it was designed, restoring power output, returning the power block to its most efficient operating condition, and potentially preventing default on PPA contract terms and the associated penalties.

Although geothermal wellfield expansion is the most common approach utilized to offset decreases in geothermal resource productivity, there are several potential advantages associated with use of solar heat to restore heat input to the power plant. First, the risk associated with characterizing and developing the solar resource at a given power plant location is less than that associated with expansion of an existing geothermal well field, which may or may not produce geofluid having the desired temperature and flow properties; an additional risk associated with wellfield expansion is the possibility that additional production capacity may accelerate the rate of resource productivity decline [11]. Second, the thermal capacity of the solar field could be dynamically matched with long-term declines in geothermal resource productivity through modular expansion of the solar field, which would allow existing geothermal power plant installations to operate closer to their capacity while simultaneously extending their operational life.

Augmentation of geothermal power plants by solar-thermal energy is furthered by the collocation of the two resources. Figure 2 shows U.S. direct normal irradiance (DNI) overlayed with geothermal plants

and geothermal development activities, which is used as a surrogate for areas with good geothermal resource. DNI is a measure of solar resource for concentrating solar technologies, such as used for geothermal/solar-thermal hybrid designs. Clearly, geothermal development activities in the United States generally lie in regions with very good solar resource, here defined as an annual average resource of about 5.5 kWh/m^2-day or greater.

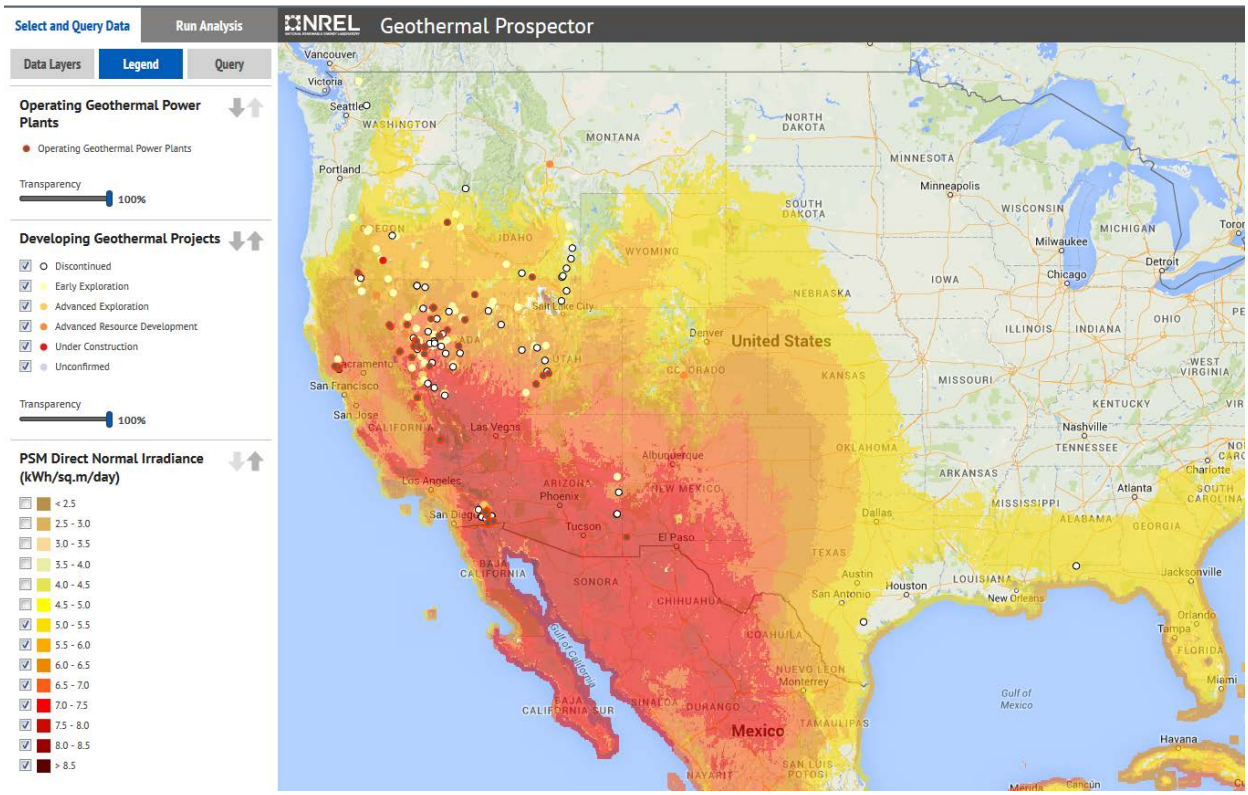

Figure 2. Most geothermal power projects and exploration in the United States fall within regions that also have good-to-excellent solar thermal resources.

2. Concentrating Solar Thermal Collectors

Solar-thermal collector technologies cover a wide range of temperature capabilities spanning from non-tracking, flat-plate collectors to two-axis-tracking concentrators that can reach over 1000°C. High-temperature collectors designed for use in electricity generation are commonly referred to as concentrating solar power (CSP) systems. We will use the more generic "solar-thermal collector" in this report. The temperature of interest for augmenting geothermal power plants is about 150° to 250°C, depending on the design operating temperature of the geothermal power block. This target exceeds the capabilities of flat-panel and compound-parabolic collectors and resides in the domain of single-axis-tracking linear collectors such as parabolic troughs and linear Fresnel systems.

2.1 Parabolic Troughs

Parabolic trough collectors are the most mature of the solar-thermal collector technologies and have been used for several decades in industrial and power generation applications. The solar field is modular in nature and comprises many parallel rows of solar collectors, normally aligned on a north-south horizontal axis. Each solar collector has a linear parabolic-shaped reflector that focuses the sun's direct-beam radiation on a linear receiver located at the focus of the parabola, see Figure 3. The collectors track the sun from east to west during the day to ensure that the sunlight is continuously focused on the linear receiver. A heat-transfer fluid (HTF) circulates through the receiver and returns to one or more heat exchangers where the HTF transfers its heat to the process or power generation system. State-of-the-art parabolic trough CSP plants regularly generate high-pressure, superheated steam to about 100 bar and 371°C to drive a conventional steam turbine/generator to produce electricity [12].

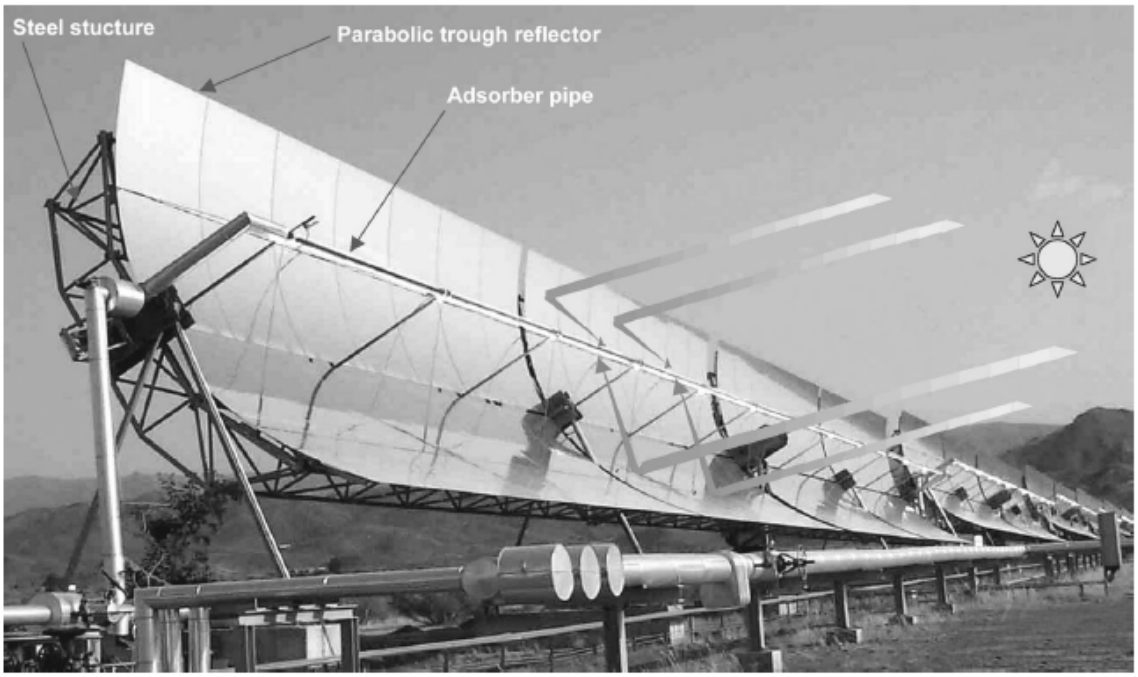

Figure 3. Parabolic trough collectors rotate the reflector and absorber as one unit to maintain focus [12].

Although commercial CSP stations have moved toward larger trough designs, smaller troughs have been developed and optimized for lower-temperature industrial-heat applications, for example, Figure 4. Thus, one can group parabolic troughs into small-trough (aperture ~ 2 m) and large-trough (aperture ≥ 5 m) designs. The small size of a geothermal/solar thermal hybrid plant would favor small-trough designs; however, at least one large-trough supplier, SkyFuel, is pursuing smaller plant sizes typical of the process-heat market. Table 1 lists properties for two small-trough and three large-trough designs. The

temperature limitations result more from the selection of the HTF than any inherent optical limitation. Parabolic trough collectors have been designed to operate at temperatures exceeding 500°C for high-pressure steam and molten-salt fluids.

Figure 4. Small-aperture troughs have been developed for low- to medium-temperature process-heat applications. PT1 collectors available from Abengoa Solar are shown. (Photo credit: NREL PIX 03954)

Table 1. Representative small and large parabolic trough specifications.

Developer	Abengoa Solar	NEP Solar	Inventive Power	LUZ	SkyFuel	Flabeg GmbH
Model	PT1	PolyTrough 1200*	Power Trough 110	LS-3	SkyTrough	Ultimate Trough
County	USA	Switz, Aus	Mexico	USA	USA	Germany
Aperture width (m)	2.3	1.2	1.1	5.76	6	7.51
Element length (m)	6.1	24	3.0	12	14.4	24
Receiver diameter (m)	0.0445	0.025	0.0334	0.070	0.090	0.094
Geometric conc. ratio	51	47	33	82	67	80
HTF	water	water	water	oil	oil	oil
Max. temperature (°C)	260	230	200	390	390	390
Reference	[13, 14]	[14, 15]	[16]	[12]	[15]	[17]

* NEP Solar is also marketing a larger PolyTrough 1800 [18]

2.2 Linear Fresnel

Linear Fresnel collectors are another line-focus, solar thermal collector technology. As shown in Figure 5, linear Fresnel collectors use an array of low-profile, flat or nearly flat primary reflectors and a fixed receiver assembly that includes one or more linear receiver tubes and may include an optional secondary reflector. The primary reflectors track the sun in the daytime while the receiver assembly remains fixed. The low-profile reflector architecture allows increasing concentration ratio without increasing wind loads, which is otherwise the case for parabolic troughs. The low-profile design is beneficial because the wind-torque load is roughly proportional to the square of the mirror height.

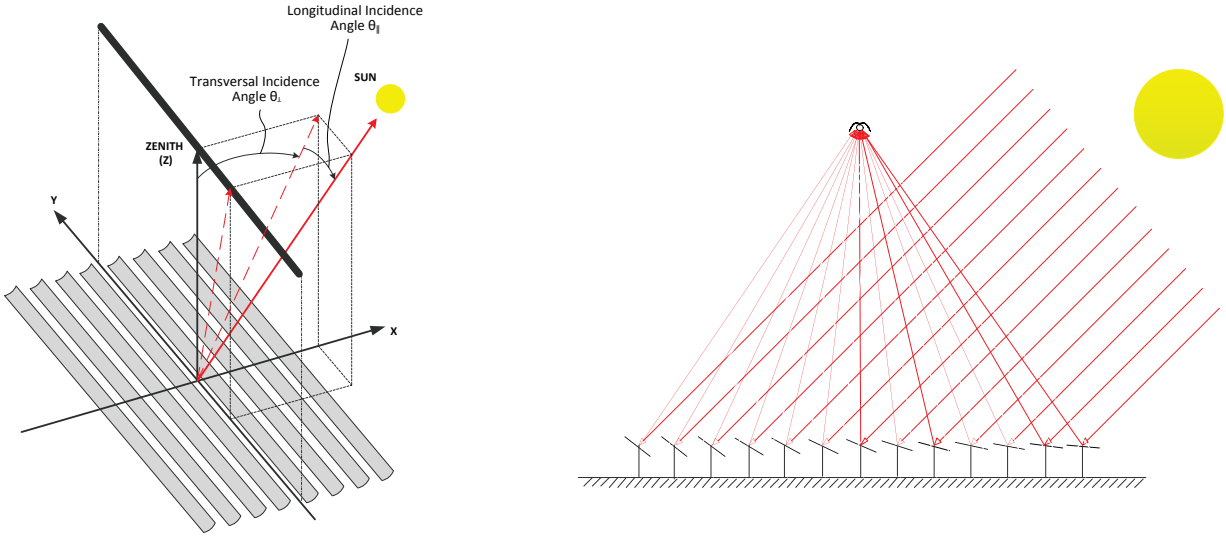

Figure 5. Linear Fresnel systems use rows of flat or nearly flat mirrors mounted near the ground to reflect incoming sunlight onto a fixed receiver mounted overhead [19].

Because the low-profile architecture provides for great flexibility in selecting a concentration ratio, linear Fresnel collectors can be readily tailored for different target temperatures to meet varying application needs. Accordingly, linear Fresnel collectors are a good option for integration with geothermal heat sources, which typically operate at temperatures of 150° to 250°C. Linear Fresnel also has applications in building cooling and heating, industrial process-heat supply, and water treatment [19]. State-of-the-art linear Fresnel collectors can be designed to produce high-temperature heat for large-scale industrial-heat processes or utility-scale electricity generation.

A linear Fresnel collector typically includes an array of mirror panels, so its design may differ in terms of the individual mirror dimensions and the overall arrangement. In addition, the fixed nature of the receiver assembly provides considerable design freedom. On the other hand, linear Fresnel collectors have lower optical/thermal efficiency than parabolic troughs because the combination of a fixed receiver and the one-axis tracking mirror panels in a horizontal plane results into greater shading/blocking and cosine losses than experienced by troughs.

The collector efficiency for troughs and linear Fresnel systems is quantified using an incidence-angle modifier (IAM). IAM is used with linear collectors to correlate their optical performance with the angle of the sun relative to the orientation of the collector field. Cosine-angle adjustments are made for the longitudinal and transverse angle, see Figure 5. Both troughs and linear Fresnel systems suffer a similar longitudinal IAM loss. Because parabolic troughs track the sun from east to west, the transversal IAM for a trough is generally equal to 1, whereas the flat linear Fresnel system must accept a cosine penalty, as well as shading and blocking losses. IAM values as a function of transverse and longitudinal incidence angle are shown in Figure 6. The sharp falloff in IAM shown for troughs at approximately 70 degree transversal angle is due to shading effects between trough rows, rather than sun angle. Linear Fresnel design relies on lower-cost collector components to offset this inherent optical penalty [20].

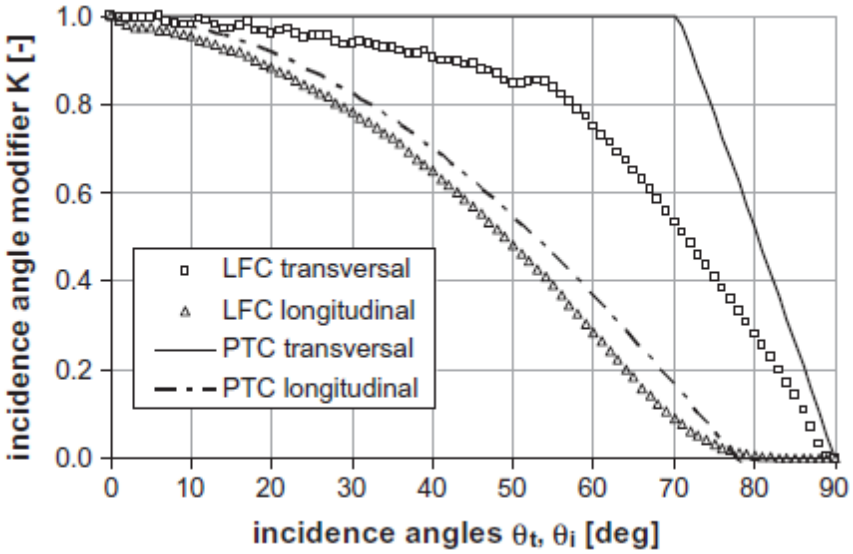

Figure 6. Simulated incidence-angle modifiers (relative to DNI) for the linear Fresnel collector (LFC) for transversal and longitudinal directions, compared to the parabolic trough collector (PTC) [20].

Another advantage of the linear Fresnel system is better utilization of land area, because reflector panels can be closely spaced, see Figure 7. Trough rows must be spaced far enough apart to avoid row-to-row shading. Trough rows are generally spaced at 3x the collector aperture width, although this can be reduced if one is willing to sacrifice some morning and evening sunlight collection. Hence, the maximum collector area for a trough field is about one-third the land area. In contrast, linear Fresnel systems can be packed to occupy almost two-thirds of the available land area. That is, roughly twice as much collector area can be used in a given site, albeit with lower optical efficiency, as discussed above. An analysis of shading and energy collection can be performed to select the optimum trough spacing if it is desired to minimize solar field land area.

Figure 7. Linear Fresnel system showing ground-mounted flat mirrors and a fixed overhead receiver (Areva Solar, NREL PIX 19883).

2.3 Modeling Solar-Thermal System Performance

The performance of solar-thermal systems is simulated in NREL's System Advisor Model (SAM) [https://sam.nrel.gov/]. SAM includes models of parabolic trough and linear Fresnel systems, along with other solar thermal and photovoltaic design options. Solar resource data for locations throughout the United States and several countries can be accessed within SAM's *Location and Resource* page. Solar data for more specific locations throughout much of North and Central America can be found via the National Solar Radiation Database at https://maps.nrel.gov/nsrdb-viewer.

While SAM is a state-of-the-art simulation package for CSP systems, the use of SAM for modeling geothermal/solar-thermal hybrid systems is complicated by the fact that SAM's solar-thermal models are provided within systems that include a steam-Rankine power block. The user must understand the complexities added by the included steam power cycle in order to extract model results that are relevant for the case where the solar field is only providing thermal energy. Accordingly, NREL developed guidelines to help users understand what aspects of the SAM models were most important for modeling thermal-only applications.

As an example case, NREL modeled the solar field at Enel Green Power's Stillwater Geothermal Plant. A simple representation of the hybrid integration at Stillwater is provided in Figure 8. The design employs 24,778 m^2 of parabolic troughs arranged in 11 loops. Because of the land area at Stillwater, each loop consists of two 115-m solar collector assemblies (SCAs) plus two shorter, 86-m SCAs. An SCA is a string of troughs that is controlled by a single drive and moves as one unit. The troughs are 6-m aperture SkyTroughs supplied by SkyFuel of Arvada, Colorado. The specific hardware dimensions and operating conditions were set up in a SAM case file. Three different cases were made in SAM version 2015-06-30:

1) SAM's default Physical Trough model with solar field, collector, and receiver inputs adjusted to represent the Stillwater field,
2) The inputs as in Case (1) plus modified inputs on SAM's *Power Cycle* page to minimize the influence of the power cycle code on simulation of the solar field, and

3) The inputs as in Case (1) exported to TCS Console, an NREL software tool that allows manipulation of the core performance code for the Physical Trough model, so that the solar field components could be modeled in the absence of any power cycle.

These cases proceed in increasing order of sophistication with respect to the understanding of SAM and represent what might be undertaken by a novice SAM user, a frequent SAM user, and an advanced SAM user, respectively. The goal was to provide the best simulation from SAM with the least required knowledge on the part of the user in order to make SAM more accessible for geothermal/solar-thermal hybrid analysis.

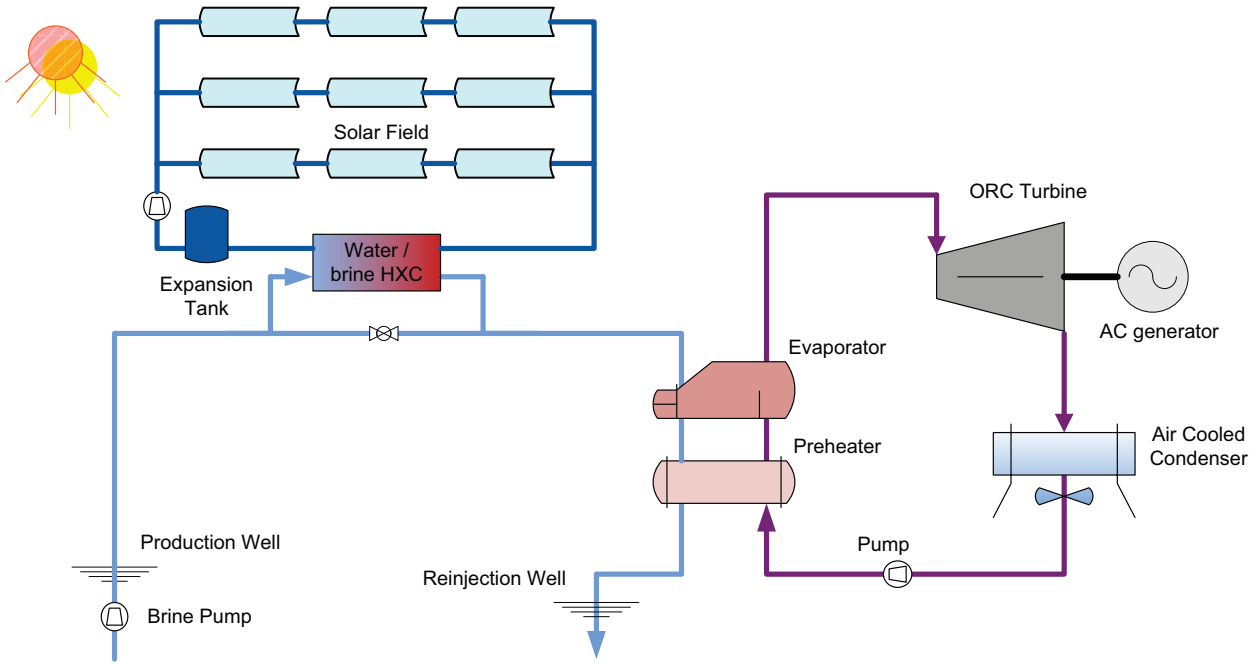

Figure 8. Geothermal/Solar-thermal hybrid configuration similar to that employed at Stillwater.

A comparison of SAM's annual *Field Thermal Power Produced* for the three cases is provided in Table 2. This is one of SAM's output variables for solar field performance and represents the predicted thermal energy from the solar field HTF after accounting for incoming DNI and optical and thermal losses in the solar field. Table 2 also shows the total thermal energy incident on the solar field aperture area, the total thermal energy absorbed by the solar field, and energy dumped due to forced defocusing of the solar field.

Table 2. Relevant annual solar field performance estimates from different cases. Running the solar collector code without any power cycle interference (Case 3) is required to obtain the best estimate of thermal energy potential.

Annual thermal energy estimates (MWh_{th})	**Case (1)** **Solar Field with SAM's default power cycle**	**Case (2)** **Solar Field with power cycle input changes in SAM**	**Case (3)** **Stand-alone trough modeled via TCS Console**
Field thermal power incident	76,120	76,120	76,120
Field thermal power dumped	31	518	0
Field thermal power produced	35,506	38,988	41,465
Estimated generation (relative)	85.6%	94.0%	100%

2.3.1 Recommendations for Modeling Solar Fields for Geothermal/Solar Hybrid Plants

The simplest way to use SAM to simulate the thermal output from a parabolic trough field is to open a default case of the Physical Trough Model and adjust the *Location and Resource* and solar field settings via the *Solar Field, Collectors (SCAs)*, and *Receivers (HCEs)* pages to model the size and hardware details of the field in question (see Figure 9). However, as is apparent from Table 2, if the SAM user simply runs the default Physical Trough Model in this fashion without addressing the default *Power Cycle* page inputs, SAM will underestimate energy production. It is also possible the model will not even run due to a mismatch in power cycle and solar field properties. These errant results are due to SAM trying to "force fit" the specified solar field and power cycle parameters.

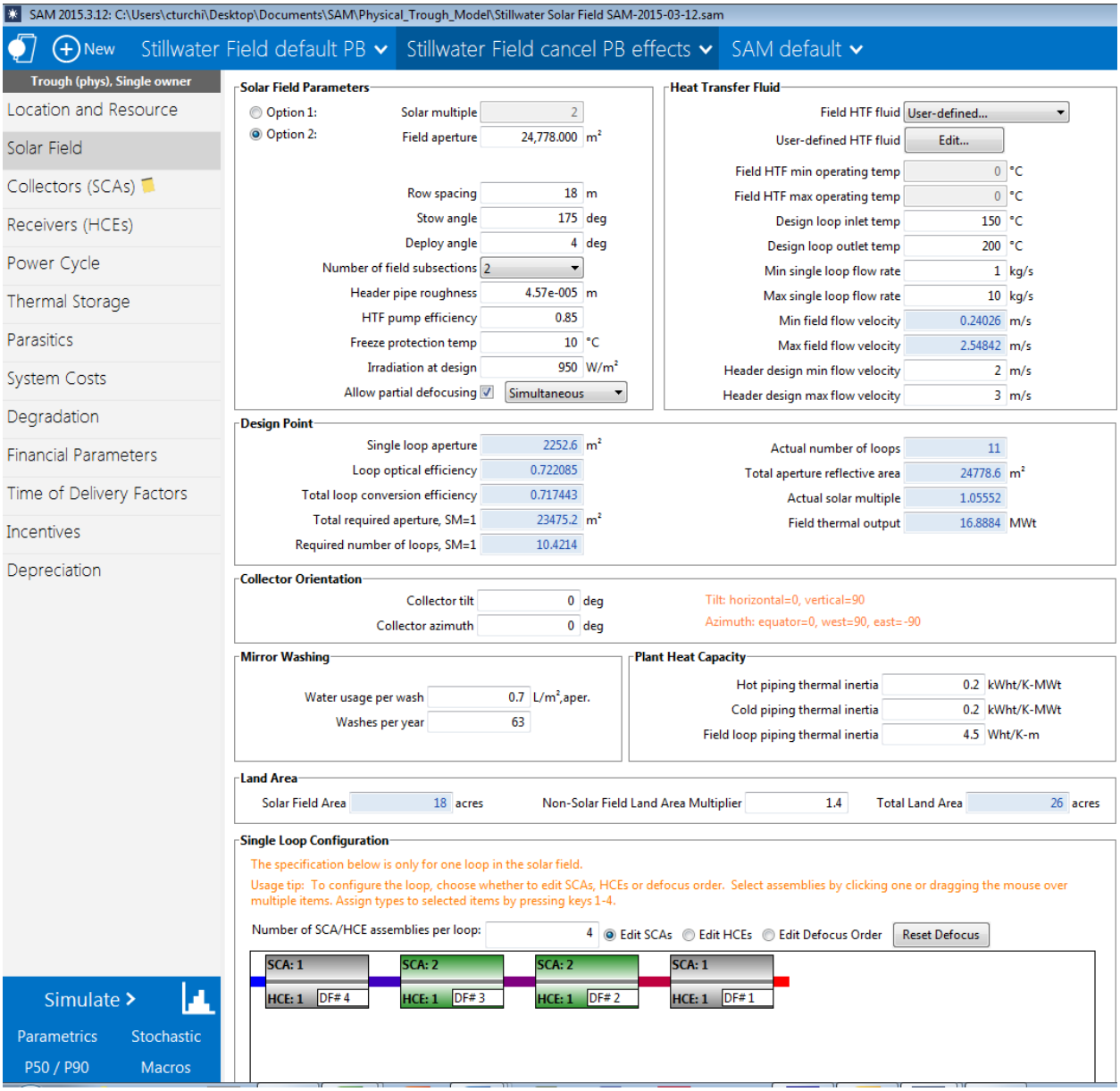

Figure 9. Solar Field inputs page in the Physical Trough Model in SAM 2015-03-12.

Case (2) addresses many of these concerns by adjusting *Power Cycle* inputs to minimize the influence of the power cycle code on the solar field performance. This results in a case with less potential for

convergence errors and a better estimate of the potential output from the solar field. The specific recommended changes for this case are outlined in Table 3.

Table 3. Changes to SAM's Power Cycle inputs page to minimize power cycle influence over the solar field performance. If thermal storage is used, additional adjustments need to be made on the Thermal Storage page.

Power Cycle page Input	SAM default	Recommended change
Design gross output	111	Set equal to thermal power rating of solar field
Estimated gross to net conversion factor	0.9	no change
Availability and Curtailment inputs	various	no change
Rated cycle conversion efficiency	0.3774	1.0
Boiler operating pressure	100	set equal to saturated steam pressure at solar field outlet temp
Steam cycle blowdown fraction	0.02	no change
Fossil backup boiler LHV efficiency	0.9	no change
Aux heater outlet set temp	391	set equal to solar field outlet temp
Fossil dispatch mode	Min backup level	no change
Low resource standby period	2	no change
Fraction of thermal power needed for startup	0.2	0
Power block startup time	0.5	0
Minimum required startup temp	300	set equal to solar field inlet temp
Max turbine over design operation	1.05	2
Min turbine operation	0.25	0.02
Turbine inlet pressure control	Fixed Pressure	no change
Cooling System inputs	various	no change

Finally, Case (3) removes the Physical Trough code completely from the SAM interface and runs the code within NREL's TCS Console environment. TCS Console was developed by NREL to allow manipulation of the model systems originally developed the TRNSYS FORTRAN format. For this work, NREL developed a script within TCS Console that separates the power block controller functions from the solar field performance model and allows for recirculation of the solar field HTF as necessary.

Running the Physical Trough model in this fashion avoids any conflict with the power cycle code and provides a clean estimate of parabolic trough performance. However, the process is more complex than simply adjusting inputs within SAM's Graphical User Interface, and requires access to NREL's TCS Console tool. While this report documents a procedure to access accurate predictions from the Physical Trough model in the absence of a steam power cycle (see Appendix B), the use of TCS Console is cumbersome and not a recommended solution for the typical SAM user. TCS Console was an interim fix for NREL programmers and is not intended as a public-use tool. Recognizing the need for access to SAM's collector/receiver models and the limitations of the procedure described here, NREL plans to develop a more intuitive SAM-based interface for accessing these tools in FY16.

In summary, SAM's normal interface can be used to estimate parabolic trough performance for solar-thermal applications if one takes a number of steps to minimize the influence of the power cycle simulation requirements on the solar field. Similar adjustments can be used with SAM's Linear Fresnel model. For the example shown here, skipping these steps results in solar field thermal-energy generation estimates that are 85% of the value estimated without interference from the power cycle component

model. Making a series of adjustments to SAM's default power cycle inputs improved the estimate to be within 94% of the estimated stand-alone solar field value.

For initial performance estimates, creating a case with SAM and minimizing the influence of the power cycle by the methods outlined above (i.e., following Case 2) is probably sufficient. For more detailed analysis, stand-alone-trough model estimates can be developed via NREL's TCS Console environment. However, performing this analysis requires requesting access to TCS Console from NREL. Recognition of this limitation has led NREL to undertake a task to modify SAM to allow for easier access to the solar field performance codes within SAM's user-friendly interface. Such a change will promote greater use of SAM of thermal-energy production in geothermal hybrids and for other thermal-energy applications. Look for these features to appear in later versions of SAM.

2.4 Solar Collector Cost Information

Multiple CSP technology vendors are actively pursuing process-heat applications for their collector technologies. A sampling of such developers is depicted in Table 4. In 2015, NREL approached a number of vendors with a request for freight-on-board (FOB) factory price information for a solar field that would occupy a square, 20-hectare (50 acre) project site. NREL converted the reported information into hardware cost per square meter and added estimates for shipping costs and installation. Shipping costs were estimated from the city of origin to southern California via worldfreightrates.com, assuming truck transportation to the nearest port of departure, ocean transit to San Diego, CA (if applicable), and final truck transportation to a hypothetical plant site.

Table 4. Potential suppliers of CSP collector technology for process heat applications.

Collector Type	Suppliers	Website
Linear Fresnel	Novatec Solar GmbH Karlsruhe, Germany	http://www.novatecsolar.com/
	Industrial Solar GmbH Freiberg, Germany	http://www.industrial-solar.de/
	Soltigua Gambettola, Italy	http://www.soltigua.com/
	Areva Solar France	http://www.areva.com/EN/solar-220/areva-solar.html
	Solar Power Group GmbH Ratingen, Germany	http://www.solarpowergroup.com/
	Fera Milan, Italy	http://www.ferasolar.it/
	CNIM France	http://www.cnim.com/en/cnim-and-solar-energy.aspx
Parabolic Trough (small aperture)	Abengoa Solar Lakewood, CO, USA	http://www.abengoasolar.com/web/en/nuestros_productos/aplicaciones_industriales/
	Soltigua Gambettola, Italy	http://www.soltigua.com/
	Inventive Power Mexico	http://www.inventivepower.com.mx/
	NEP Solar Zurich, Switzerland	http://www.nep-solar.com/
	Solarlite Duckwitz, Germany	http://solarlite-csp.com/
	Trivelli Energia Bressana, Italy	http://www.trivellienergia.com/
Parabolic Trough (large aperture)	Abengoa Solar Spain	http://www.abengoasolar.com/web/en/nuestros_productos/plantas_solares/
	SkyFuel Arvada, CO, USA	www.skyfuel.com
	Gossamer Innovations Huntington Beach, CA, USA	http://www.gossamersf.com/solar-power-products.htm
	Torresol Energy (Sener), Spain	http://www.torresolenergy.com/TORRESOL/cylindrical-parabolic-collector-technology/en
	Flagsol GmbH Germany	http://www.heliotrough.com/index.html http://www.flagsol.com/

Solar field installation costs (foundation and pylons, field wiring, and assembly labor) were estimated from Turchi [21], using merit-shop labor rates for Arizona. This source is for large troughs and several vendors report low installation costs due to their design [22], so a high and a low range were applied to installation costs. The high range was set from [21] adjusting from 2009 to 2013 using Chemical Engineering Plant Cost Indices (CEPCI). The low range was taken to be 50% lower. Actual installation costs are expected to vary with system design and fall between these limits. A summary of the results is shown in Figure 10 (vendors names are removed as the survey request guaranteed anonymity). There was no clear pattern between the different technologies so all data are represented together.

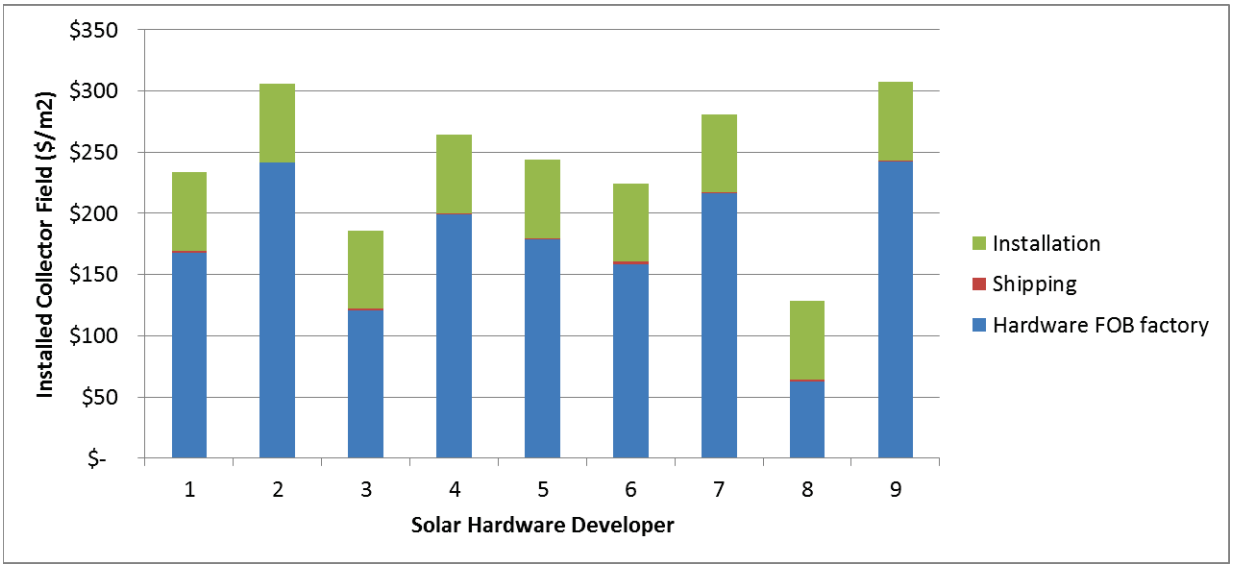

Figure 10. Estimated installed solar-field cost based on hardware price from different vendors along with estimated shipping and installation costs.

The installed solar-field values range from \$130/m^2 to just over \$300/m^2. The average cost from the survey data is \$242/m^2. These values suggest that \$200/m^2 to \$250/m^2 is a reasonable current cost for solar thermal collectors, with \$100/m^2 to \$150/m^2 as a low-end target. As further evidence, NREL recently completed a detailed cost assessment of a modern parabolic trough design and concluded that the installed cost for a large solar field deploying this trough would cost approximately \$170/m^2 [23]. The lower cost compared to values in Figure 10 is at least partially due to a larger project size and resulting economies of scale. At an April, 2014 DOE-sponsored CSP industry workshop, a major CSP developer indicated that their trough collectors could soon hit a target cost of less than \$125/m^2 (not including receiver tubes), and DOE's own "COLLECTS" FOA target is \$50/m^2. Adding the cost for the receiver tubes to these numbers suggests that \$100 to \$150/m^2 is a suitable future goal for the installed solar field cost. Note that these costs are for the installed solar field only. A full project cost would also include HTF system piping, expansion tank, fluid, heat exchanger, and project contingency and indirect costs. Some accommodation must also be made for the project scale – CSP developer costs normally assume a very large project (~1,000,000 m^2); whereas, geothermal hybrids will utilize much smaller solar fields (< 100,000 m^2). Ultimately, technology selection will depend on formal price quotes from vendors for the specific site. No subsidies or incentives are included in the numbers shown here.

2.5 Estimated Cost of Solar-Thermal Energy

The levelized cost of heat (LCOH) is defined as a convenient metric for estimating lifetime cost of a solar collector system for process heat applications. LCOH is defined analogously to LCOE, which conventionally refers to electric energy. In a simple form, where annual costs and generation is unchanged every year, LCOH can be defined as:

$$LCOH = \frac{(Total\ Installed\ Project\ Cost) * (FCR) + (Annual\ O\&M)}{Annual\ thermal\ generation} \quad (1)$$

where the FCR is the fixed charge rate. The FCR depends on a range of financial parameters that can have a significant influence on LCOH. The latest release of SAM (version 2015-06-30) includes a procedure for estimating and using the FCR method, which is used in this study. More information on the approach is summarized in Appendix A.

An example analysis of the LCOH is calculated assuming Enel Green Power's Stillwater Hybrid Plant as a baseline size for solar hybridization hardware. The LCOH for that design was estimated based on the estimated cost and performance of the system. The total hybridization cost includes the solar collector/receiver hardware; solar field HTF, piping, pump(s), and expansion vessel; HTF-to-brine heat exchanger; site preparation; installation costs; project contingency; and project indirect costs. A summary of the cost categories and values is given in Table 5.

Table 5. Cost assumptions used for the assessment of economic potential.

Baseline Hybridization Case	**Value**	**Reference or Comment**
Solar field aperture area (m^2)	24,780	[24]
Design point thermal capacity (MW_{th})	16.4	Based on resource data for the site
HTF-to-brine heat exchanger area	560 m^2 (6000 ft^2)	[25]
Cost Components		
Installed solar field cost ($/$m^2$)	Parametric variable	Includes parabolic trough collector and vacuum-insulated receiver
Site preparation ($/$m^2$)	10	[21], assuming an existing plant site
HTF system ($/$m^2$)	40	[26], based on water-HTF solar field as in SAM's linear Fresnel model
HTF-to-brine heat exchanger	$238,000	Installed cost from [27]; adjusted to 2013$
Contingency	7%	[26]
Hybridization project indirect costs	25%	[28, 29], representative value accounting for EPC and owner project costs
O&M cost ($/$kW_{th}$-year)	7.4	[21]
Fixed Charge Rate (FCR)	0.090	See Appendix

The LCOH can be used to estimate if solar collectors for process heat are competitive with alternative sources of thermal energy. Figure 11 illustrates the LCOH estimated for a range of solar resource, solar/project cost, and natural gas price. The financial parameters used are shown in Table 5. The alternative heat source shown in Figure 11 is a natural gas burner. In addition to the fuel cost, the natural gas LCOH assumes an 80% efficiency burner, 50% capacity factor, and $200/kW-th capital cost for the burner/heat exchanger. For comparison, the average industrial-use natural gas price in California in 2014 was $7.7/MMBtu and the U.S. national average price for industrial-use natural gas in 2014 was $5.5/MMBtu [30].

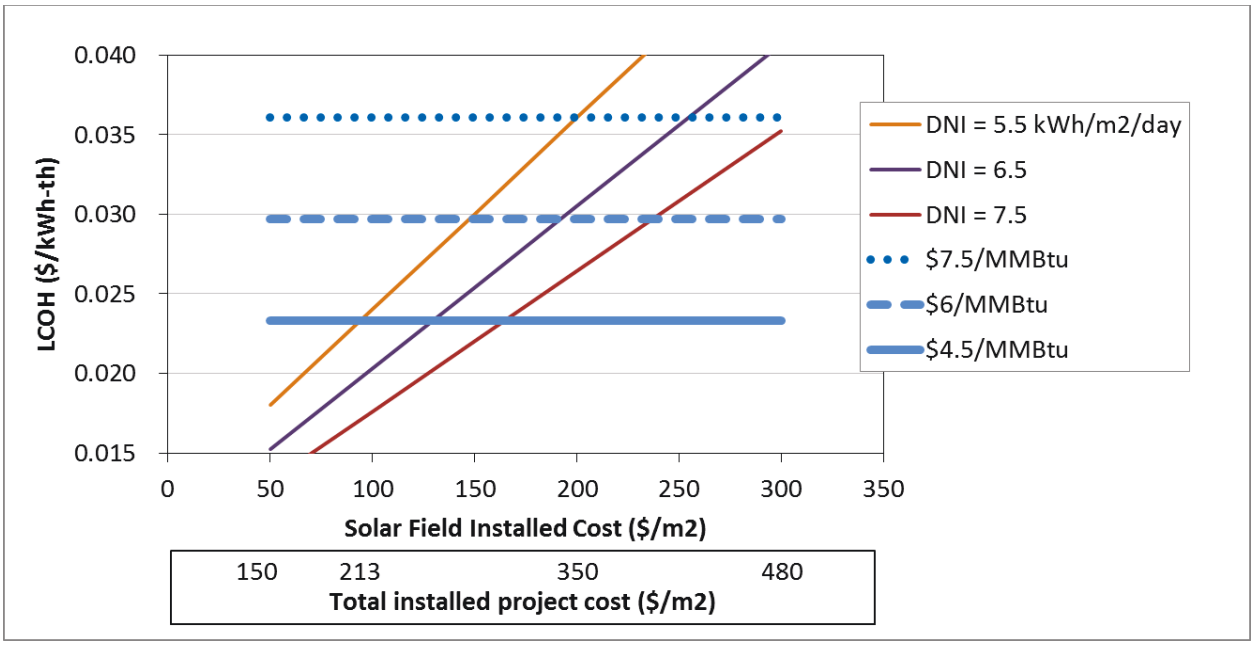

Figure 11. Estimated LCOH from solar-thermal collectors for a process heat application for three different levels of direct normal insolation (DNI). See Appendix A for more details on the financial assumptions.

The results presented in Figure 11 indicate that an installed solar field at $200/m^2 (project cost = $350/m^2) provides heat at a cost that is competitive with natural gas throughout most of California, where the average industrial-use gas price was $7.7/MMBtu in 2014 and solar DNI exceeds 5.5 kWh/(m^2 day) throughout most of the state.

3. ORC Analyses

While numerous heat integration configurations are possible for a retrofit geo-solar hybrid plant, a "brine preheating" configuration, in which the solar thermal energy is used to increase the temperature of the geothermal production fluid en route to a geothermal power plant, minimizes disruptions to existing geothermal power plant infrastructure and operations. Since the solar heat is used to restore the brine temperature to conditions closer to the original design point, no significant modifications to power block operating or control strategy are necessary, which is beneficial from the perspective of minimizing the cost of a retrofit project. The largest disturbance to existing geothermal power plant operations are associated with installation of the solar field HTF-to-brine heat exchanger, which requires the brine flow to be stopped or rerouted during heat exchanger installation. Use of solar heat to increase the brine temperature directly addresses the issue of geothermal resource productivity decline and allows the power plant to operate with heat input and, consequently, performance closer to design values. The brine preheating hybrid plant configuration is illustrated in Figure 12.

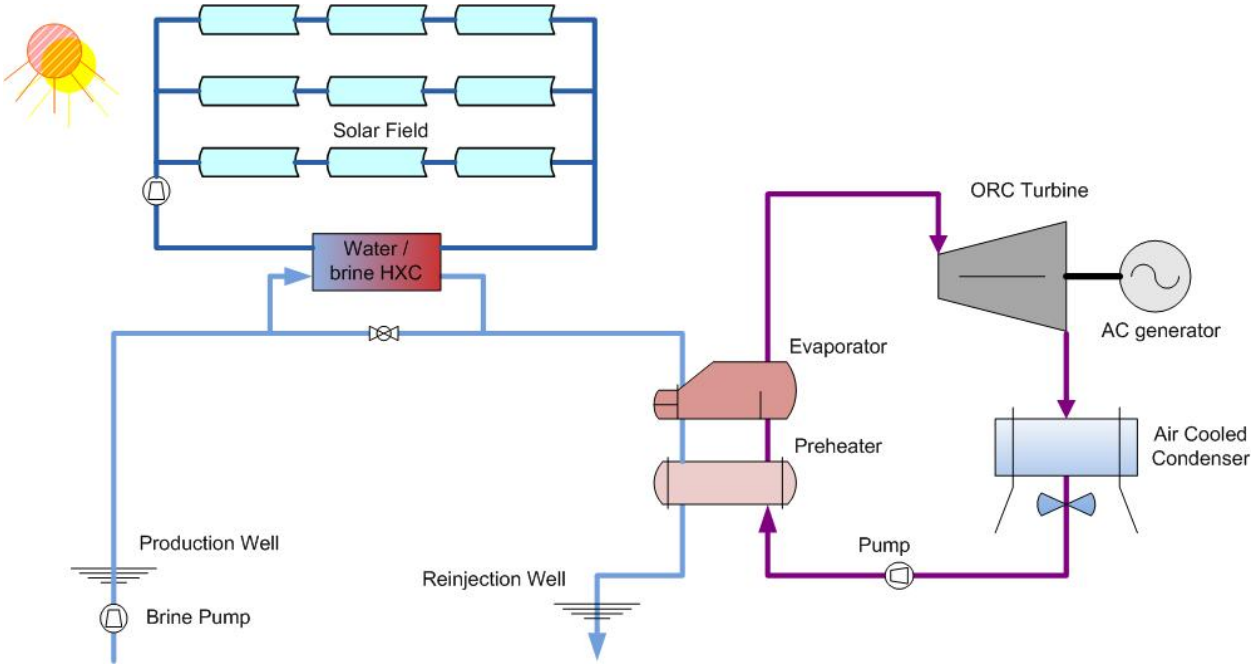

Figure 12. Brine preheating hybrid plant configuration

Although there are distinct advantages associated with the brine preheating retrofit strategy from the perspective of minimizing disruptions to the existing geothermal plant, there are also disadvantages associated with this approach. Typical geofluid production temperatures are low relative to the temperatures typical of the HTF exiting a concentrating solar trough collector (where temperatures of 500°C are possible). The brine preheating configuration utilizes the solar heat at temperatures that are more closely aligned with the geothermal power block design point, which reduces the efficiency with which the solar heat can be converted to electrical power. This relatively low power block thermal efficiency may prevent a brine preheating retrofit hybrid plant from being economically viable unless there are additional factors that provide economic incentive to perform the retrofit. These factors could include offsetting PPA penalties associated with the stand-alone geothermal plant failing to meet contractual levels of power generation, or tax credits and/or renewable energy incentives that could offset the solar field capital costs.

While retrofit hybrid plants would be likely to use the solar thermal energy to increase the temperature of the brine upstream of the power block, greenfield hybrid power plant projects would have greater flexibility to utilize the solar heat in more efficient configurations. This report evaluates the use of

the “ORC working fluid heating” configuration, in which heat from the solar field is input directly to the ORC working fluid, for its ability to overcome some of the limitations associated with the brine preheating configuration. The ORC working fluid heating configuration, which is illustrated in Figure 13, is more likely to be implemented in greenfield projects due to the increased integration of solar and geothermal heat input to the hybrid plant power block. As with the brine preheating configuration, the ORC working fluid heating configuration can use solar heat to offset declines in geothermal resource productivity. However, the ORC working fluid heating configuration does increase the power block capital costs as well as modify power block operating conditions.

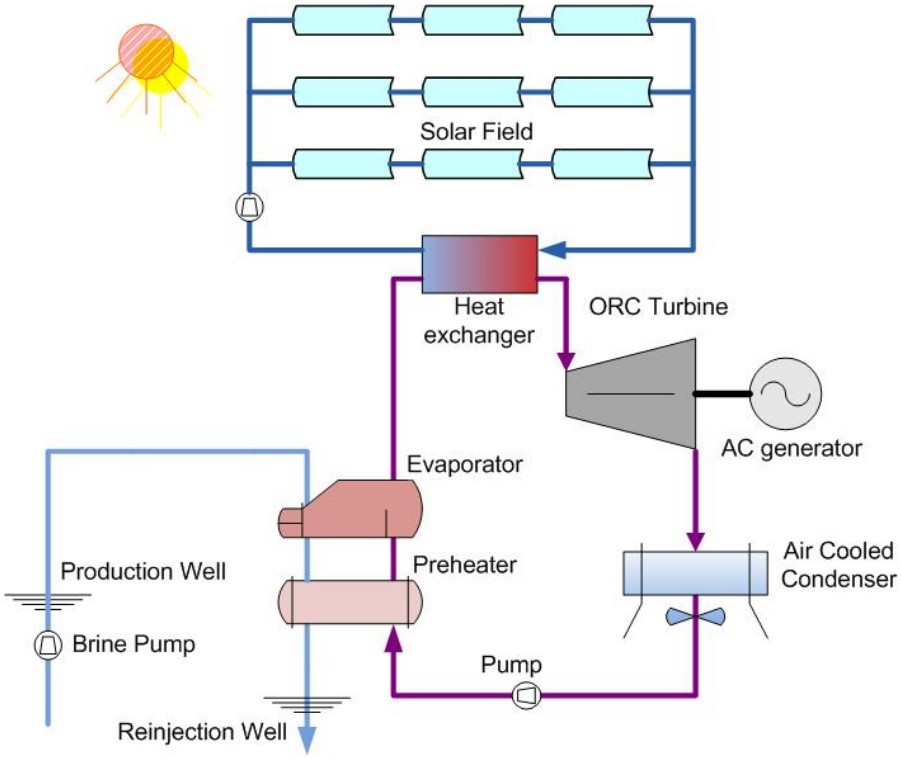

Figure 13. ORC working fluid hybrid plant configuration

The cost of solar heat is relatively expensive when compared to geothermal due to the large capital costs associated with the solar field. However, it is likely that the capital costs of the solar field hardware may decrease with time. Solar field cost reductions may be possible through improved collector manufacturing techniques, optimization of collectors in the temperature range of interest, and/or use of less costly heat transfer fluids. Economic analyses of retrofit and greenfield hybrid plants presented in subsequent sections identify conditions where geothermal solar hybrid technology could improve project economics relative to a stand-alone geothermal plant. These economic analyses consider a range of possible solar field costs as well as solar field sizes to identify conditions most favorable for hybridization.

3.1 Hybrid Plant Simulation

Geothermal power plant performance is highly dependent on the conditions of the heat source and heat sink. Air-cooled binary plants experience significant hourly fluctuations in net power generation as the ambient temperature changes. Similarly, long-term changes in geothermal resource temperature or flow rate can have significant impacts on power plant performance. Hybrid geothermal/solar-thermal power plants will also experience changes in performance due to the intermittency of the solar resource. In order to evaluate the performance and economics of geothermal/solar-thermal hybrid plants, it is therefore important to be able to accurately simulate the off-design performance.

Aspen Plus models [31] were used to determine equipment design specifications and off-design performance of geo-solar hybrid ORC power plant configurations. The equipment specifications of each power plant were determined using the set of common design parameters specified in Table 6. The power plants were assumed to be equipped with state-of-the art equipment components including turbines with variable geometry inlet guide vanes (IGVs) as well as working fluid pumps and air-cooled condenser fans with variable frequency drive (VFD) motor speed control.

Table 6. Plant equipment design parameters

equipment type	**design specification**	
heat exchanger minimum temperature approach	preheater/vaporizer: air-cooled condenser:	10°F 15°F
rotational equipment efficiencies (isentropic/mechanical)	pump: fan: turbine:	80%/98% 55%/90% 83%/94%
piping and equipment fluid frictional losses	liquid piping: vapor piping: preheater/vaporizer: condenser: control valve: recuperator vapor side recuperator liquid side	10 psi 4 psi 38 psi 1 psi 2 psi 2 psi 5 psi

The net power generation from a hybrid plant is a function of the power plant efficiency, which is in turn dependent on the performance of the individual equipment components included in the plant configuration. The off-design performance of the working fluid pumps and ACC fans was determined through use of representative pump and fan curves, respectively; affinity laws were used to predict performance at different pump and fan shaft speeds. The turbine efficiency was calculated as a function of IGV position as well as fluid inlet and outlet conditions. Preheater, vaporizer, and condenser performance was adjusted for off-design operating conditions using heat transfer correlations for both the hot and cold sides. Solar field performance was obtained from SAM for the SkyFuel SkyTrough in the physical trough model of SAM 2014-01-14; the performance specifications of this trough design are based on stand-alone solar thermal power plant operation (as discussed in Section 2.3) and are not optimized for geo-solar hybrid plant applications.

In addition to predicting the off-design performance of individual equipment components, accurate hybrid plant simulation requires a model that can predict equipment/control system settings for off-design power plant operating conditions and evaluate the performance of the plant as a whole at these operating conditions. The power plant operating point that maximized net power generation while simultaneously meeting operating constraints (e.g., minimum turbine inlet superheat, minimum brine plant exit temperature) was selected through optimization of the working fluid pump speed, ACC fan speed, turbine IGV position, and control valve position.

Since hybrid plant performance is a function of the geothermal resource temperature and flow rate, solar heat input, and ambient temperature, the off-design performance of each geo-solar hybrid power plant must be determined by simulating plant performance over a multidimensional range of each of these variables. The resultant map of power plant performance is used in combination with hourly production fluid temperature, production fluid flow rate, ambient temperature, and solar DNI data to determine base and hybrid plant performance over the designated plant operating period.

The performance of geo-solar hybrid plants with geothermal resource design temperatures of 150, 175, and 200°C were evaluated. A resource productivity decline scenario was defined for each of these geothermal resource design temperatures. The production fluid temperature in each scenario is assumed to

decline at a rate such that the annual power generation decreases by approximately 50% following 30 years of base power plant operation (see Table 7). Each scenario was assumed to have a constant production fluid flow rate of 378 kg/s (3 million lb/hr) for the duration of the power plant operation. Scenarios with and without a brine exit temperature limit for minimization of heat exchanger fouling were evaluated. The brine exit temperature limit was set based upon identification of the temperature at which amorphous silica precipitation would begin [32].

Table 7. Assumed annual production fluid temperature decline rates

design temperature	annual temperature decline
150°C (302°F)	1.0°C (1.8°F)
175°C (347°F)	1.1°C (2.0°F)
200°C (392°F)	1.5°C (2.7°F)

Typical meteorological year (TMY) data for Reno, Nevada were assumed for each year of power plant operation. Reno is a candidate location for hybrid geothermal-solar power plants due to the availability of both geothermal and solar resources. TMY ambient temperature and direct normal irradiation (DNI) data for Reno were obtained from the NREL System Advisor model (SAM) [26]. This data is plotted in Figure 14. Based on the Reno TMY data, an ambient design temperature of 10°C (50°F) was selected for each of the plant designs.

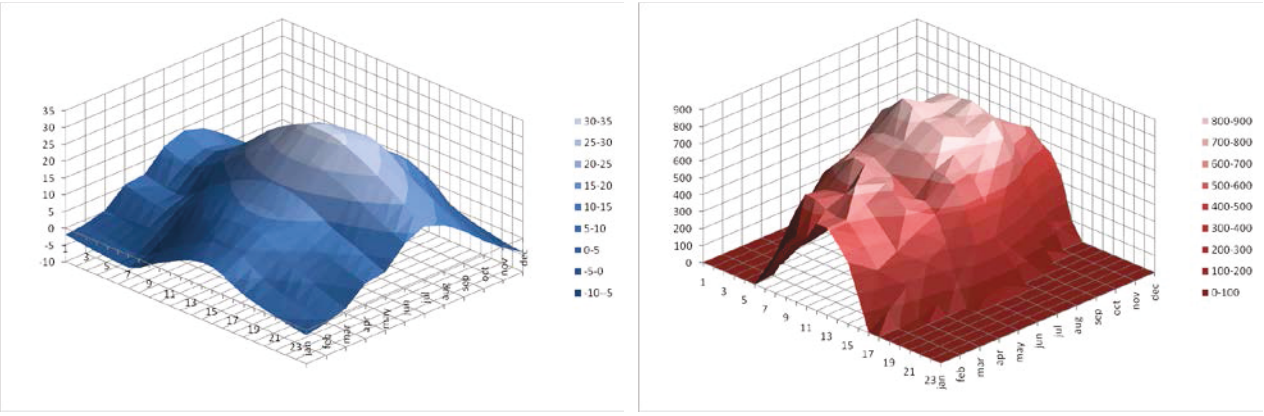

Figure 14. Monthly-averaged hourly TMY ambient temperature (left, units of °C) and DNI (right, units of W/m^2) data for Reno, Nevada.

The retrofit and greenfield hybrid plant analyses in Sections 3.2 and 3.3, respectively, include various plots presenting results of the corresponding technical and economic analyses. Plots for the 175°C basic cycle are presented within the report text, while plots for other geothermal resources and plant configurations are presented in Appendix D.

3.2 Retrofit: Brine Preheating

3.2.1 Hybrid Plant Configuration

Depending on the nature of the geothermal resource productivity decline, there are two possibilities for the location of the heat exchanger used to transfer heat from the solar field HTF to the production fluid in a retrofit brine heating hybrid plant application. If the geothermal resource productivity decline is primarily due to a decrease in production fluid flow rate, a "post-heat" heat exchanger for the addition of solar heat may be configured to heat a portion of the geofluid exiting the power cycle preheater such that this fluid can be recycled to the vaporizer inlet, resulting in vaporizer inlet stream temperature and flow rate closer to design. If the geothermal resource productivity decline has manifested primarily as a decline in production fluid temperature, positioning a "preheat" heat exchanger in the production fluid piping en route to the power cycle vaporizer can result in operating conditions similar to those for which the plant

was designed; the analysis presented in this report is based on the preheat hybrid plant configuration for addressing declines in geothermal resource temperature. The solar collectors were assumed to use a dedicated heat transfer fluid as opposed to circulation of geofluid through the solar field.

Four retrofit hybrid plant scenarios were evaluated. These scenarios included base geothermal power plants with design temperatures of 150°C, 175°C, and 200°C with the geothermal resource temperature decline rates specified in Section 3.2. The 200°C geothermal resource design temperature scenarios were evaluated with and without a brine exit temperature limit operating constraint, while the 150°C and 175°C scenarios did not include the exit temperature constraint. Each of the power plant designs utilizes a basic organic Rankine cycle (no recuperation) configuration with isobutane working fluid. Table 8 summarizes the design point operating performance of the power plants associated with each of the retrofit scenarios.

Table 8. Base power plant design point operation for selected retrofit scenarios

production fluid design temperature	geofluid exit temperature limit constraint	base plant design point heat input (MW_t)	base plant design point power output (MW_e)	base plant design point thermal efficiency	base plant turbine inlet conditions (subcritical or supercritical)
150°C	no	135.7	13.6	10.0%	subcritical
175°C	no	199.2	24.2	12.1%	supercritical
200°C	no	249.6	33.3	13.3%	supercritical
200°C	yes	197.8	28.2	14.3%	supercritical

The quantity of solar heat input was limited to 50% of the base plant design point input. This quantity results in hybrid plant maximum summer generator output values that are approximately equal to base plant maximum winter generator output values (the base plant generation will decrease with time in the event of progressive geothermal resource temperature decline). Due to the similar power generation levels at low ambient temperature and high ambient temperature with the specified levels of solar heat input, simulation results do not include a generator capacity constraint. In practice, the generator capacity of a given power plant must be considered prior to determining the amount of solar heat addition possible (the extent of geothermal production fluid temperature decline will also factor into the quantity of solar heat that can be added without changes to the base plant electrical generation equipment).

Although the primary purpose of solar heat addition in the retrofit scenarios is the restoration of geothermal resource temperature, the analysis investigated various solar array sizes to determine the impact of array size on the cost of the additional power generation. The scenarios evaluated assumed a constant rate of resource temperature decline. During the initial hybrid plant operations when resource productivity decline had not decreased brine temperatures significantly below design conditions, the addition of fixed levels of solar heat (up to 50% of base plant design point heat input) could result in brine temperatures greater than the design values. While the economics of the retrofit hybrid plant configuration generally favor delaying the solar field installation until a significant amount of geothermal resource productivity decline has occurred, additional production fluid pumping capacity was included as needed to prevent vaporization for hybrid plant operating points where the production fluid was heated above the design temperature. In practice, solar heat addition to the production fluid entering a geothermal power plant is limited by the heat exchanger temperature and pressure ratings; this analysis assumes the base power plant heat exchanger ratings are sufficient to allow addition of the solar heat quantities specified in each of the scenarios investigated.

3.2.2 Hybrid Plant Performance

Sample plots of base and hybrid plant performance for the 175°C production fluid design temperature scenario over daily, monthly, and annual time scales are included in Figure 15, Figure 16, and Figure 17, respectively. These plots illustrate the performance characteristics of the hybrid plant relative to the base plant for a case in which the solar collector array is sized such that the maximum solar heat input is equal

to 25% of the base geothermal plant design heat input (solar heat input arbitrarily selected for purposes of illustration).

Figure 15 illustrates the increased mid-day power generation of the hybrid plant for a date in mid-June with various levels of production fluid temperature decline. The additional mid-day power generation of the geo-solar hybrid plant results in a power generation profile that is more closely matched to a typical power demand profile than that from a stand-alone air-cooled binary geothermal power plant. It can additionally be seen from Figure 15 that, provided sufficient solar collector area is installed, it is possible for the hybrid plant mid-day power generation to exceed that of the base power plant even after a significant decrease in production fluid temperature.

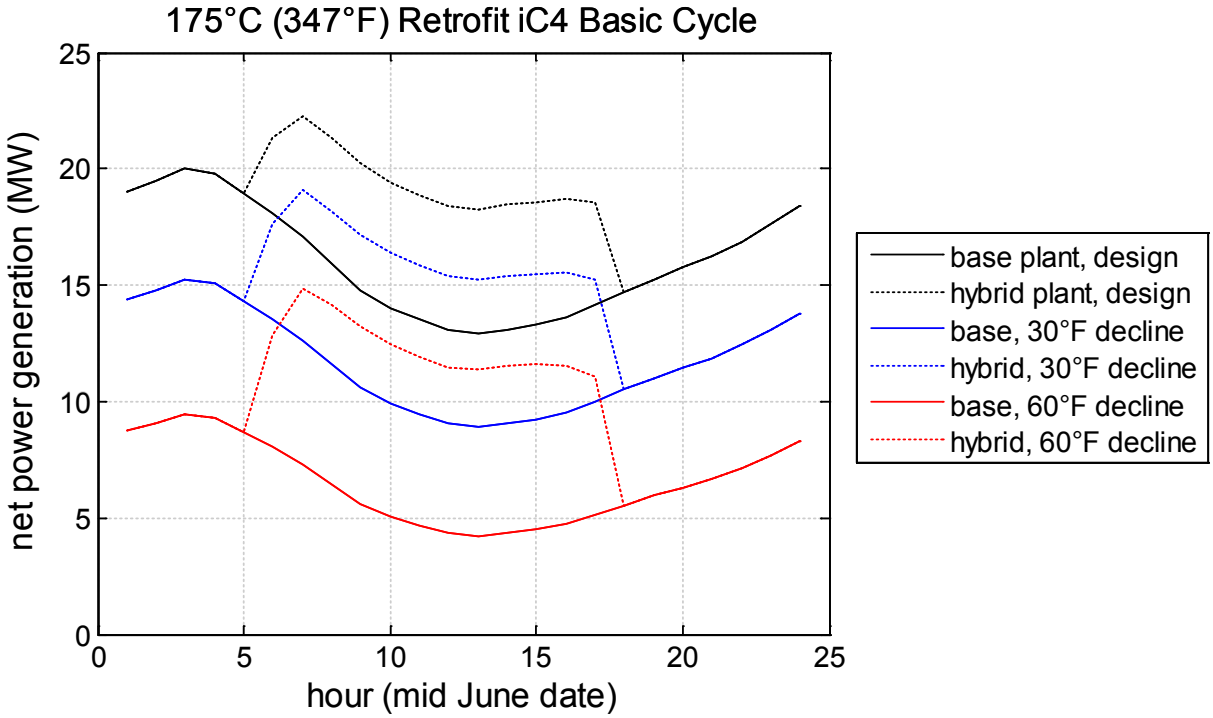

Figure 15. Simulated mid-June iC4 base and hybrid plant (solar heat input equal to 25% of geothermal plant design heat input) for various levels of geothermal resource temperature decline

Monthly power generation for the 175°C production fluid design temperature scenario is plotted in Figure 16. More power generation is realized from each unit area of the solar field during summer months when solar insolation is the greatest (despite the increased dry-bulb ambient temperatures). Base and hybrid plant annual power generation as a function of time for two geothermal resource temperature decline scenarios (a decline rate of 2°F/yr was assumed in the subsequent economic analysis of the 175°C (347°F) resource design temperature scenario) is plotted in Figure 17.

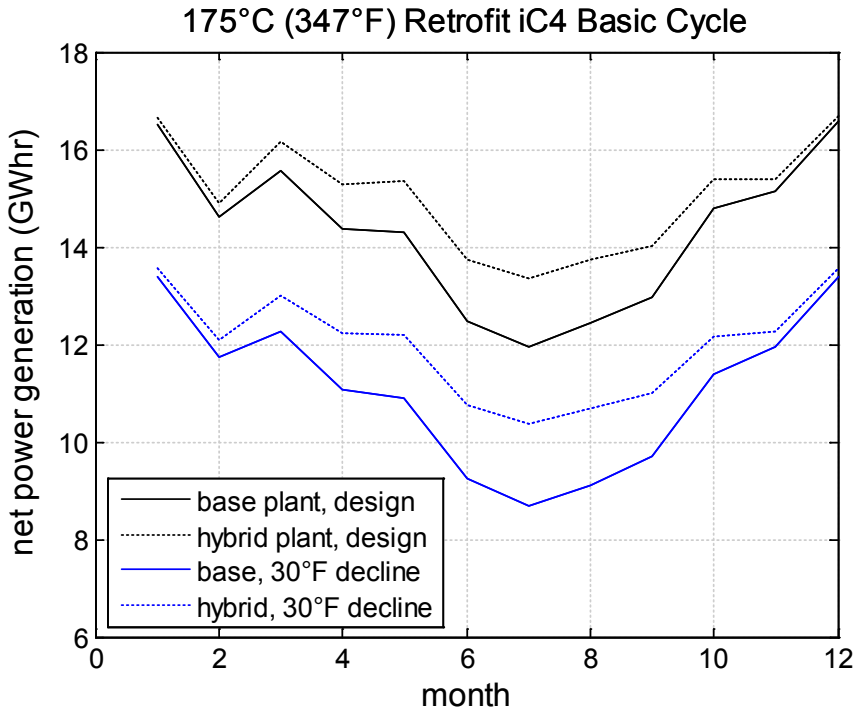

Figure 16. Effect of geothermal resource temperature decline on base and hybrid plant monthly power generation

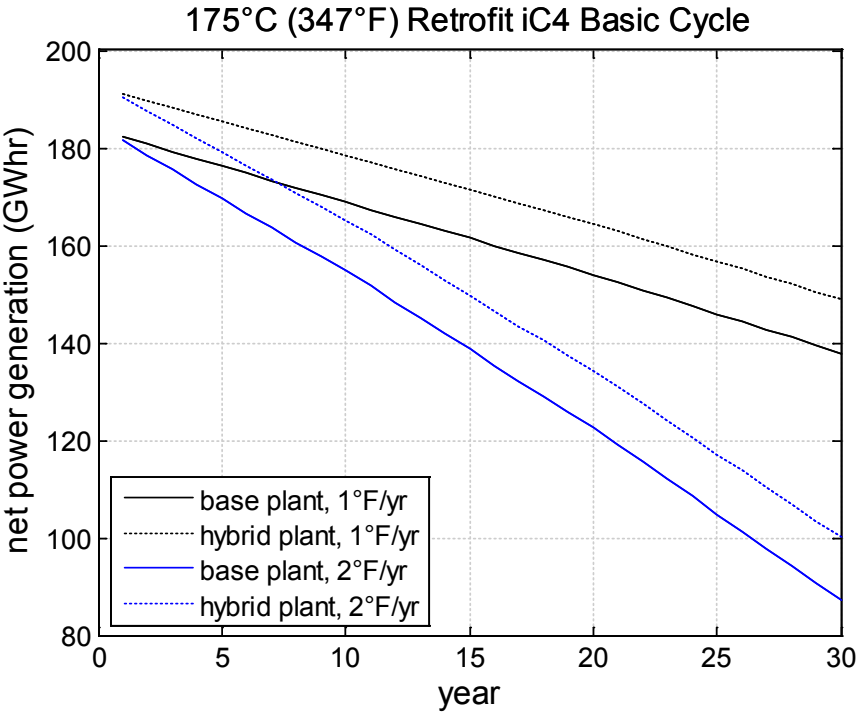

Figure 17. Effect of geothermal resource temperature decline on base and hybrid plant annual power generation

The thermal efficiency of power conversion from solar heat addition equal to 25% of base plant design point heat input as a function of production fluid and ambient temperature is presented in Figure

18. This thermal efficiency value corresponds to the difference between the base and hybrid plant power generation divided by the quantity of solar heat input for each combination of production fluid and ambient temperatures:

$$\eta_{solar} = \frac{\Delta W}{Q_{solar}} = \frac{W_{hybrid} - W_{base}}{Q_{solar}}$$

As discussed in Section 1, geothermal resource productivity decline has a two-fold effect on power plant performance. A reduction in heat input to a power plant not only decreases the thermal energy available for conversion to electrical power, but also adversely impacts the power plant efficiency. A constant decrease in the production fluid temperature will therefore result in an accelerating decrease in the base plant power generation due to the simultaneous decreases in power plant heat input and efficiency as the operating point progressively deviates from the design point.

Figure 18 and Figure 19 indicate that a constant quantity of solar heat addition generally results in increasing solar efficiency as the production fluid temperature decreases. This is due to the solar heat addition offsetting the non-linear decrease in power plant performance associated with geothermal resource temperature decline. Solar heat addition not only increases the energy input to the power block, but allows the power block to operate at conditions closer to design, thereby increasing thermal efficiency. As a result, the power generation from a unit quantity of solar heat input will increase as the geothermal resource temperature decreases.

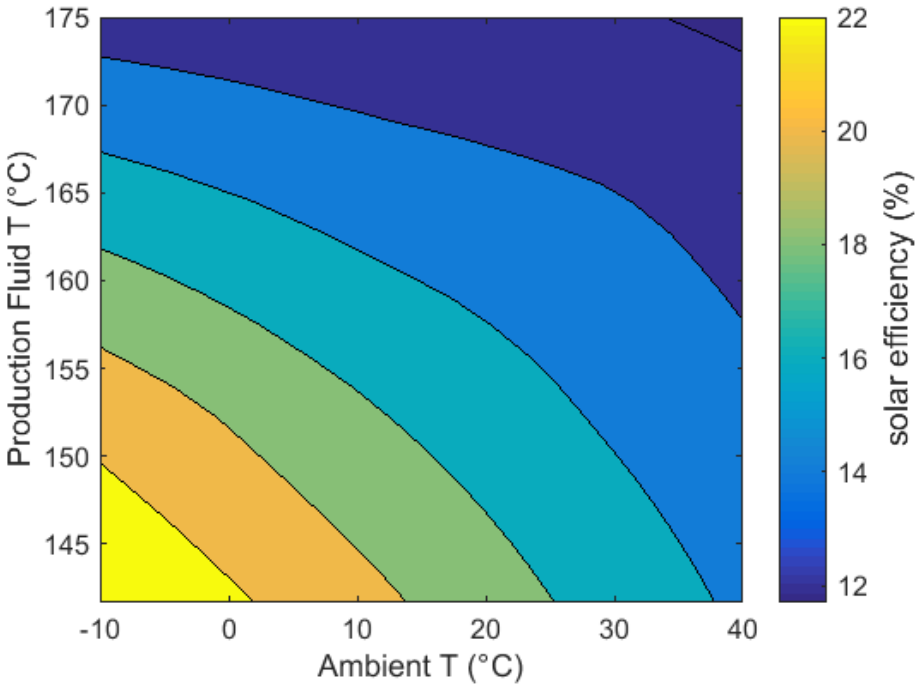

Figure 18. Thermal efficiency of power conversion from solar heat addition equal to 25% of base plant design point heat input plotted as function of production fluid temperature and ambient temperature (175°C production fluid design temperature)

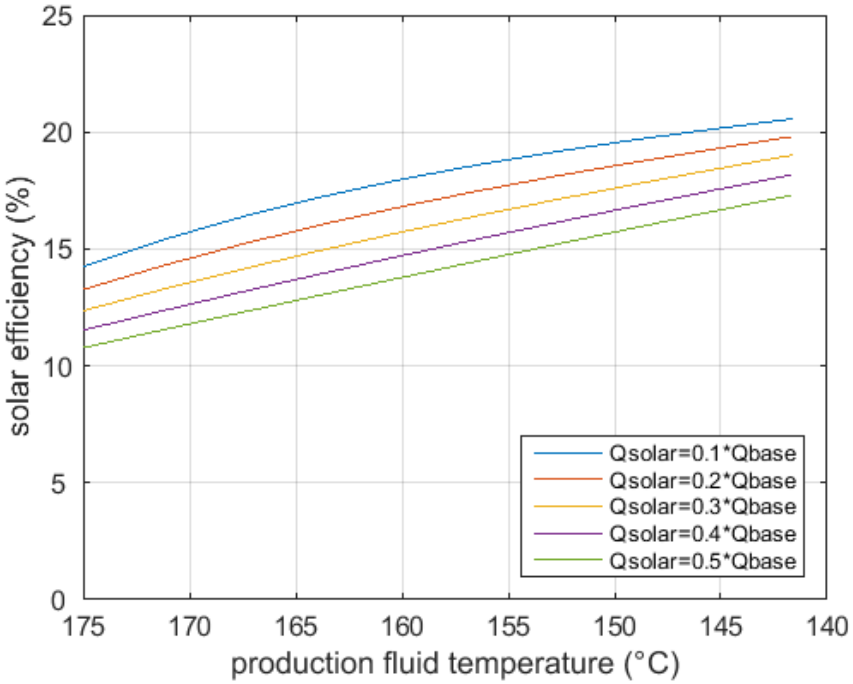

Figure 19. Average annual solar efficiency as a function of production fluid temperature decline (175°C production fluid design temperature).

Additional power generation resulting from various levels of solar heat input is presented in Figure 20 and Figure 21, where solar heat input is presented as a percentage of the base plant design point heat addition (base plant design point heat input values are provided in Table 8). Figure 20 presents the ratio of hybrid to stand-alone geothermal plant annual power generation based on design geothermal resource conditions, while Figure 21 presents the ratio of hybrid to stand-alone geothermal plant annual power generation based on the stand-alone geothermal plant performance at the degraded resource condition. The increase in solar efficiency with decreasing geothermal resource temperature (from a constant quantity of solar heat addition) is clearly visible in the results presented in Figure 21.

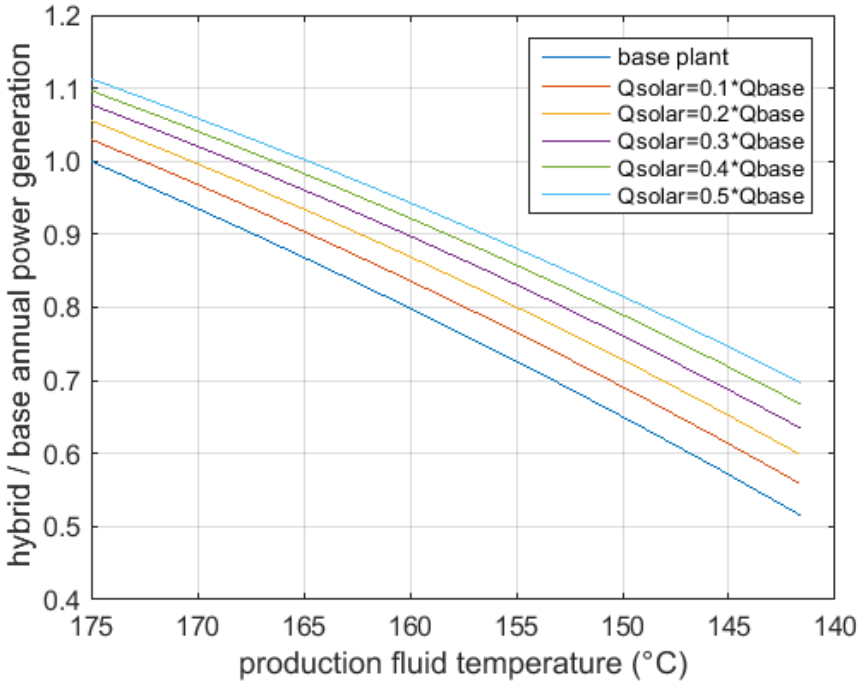

Figure 20. Base and retrofit hybrid plant annual power generation (reported as fraction of base geothermal plant design annual power generation) plotted as function of production fluid temperature decline (175°C production fluid design temperature).

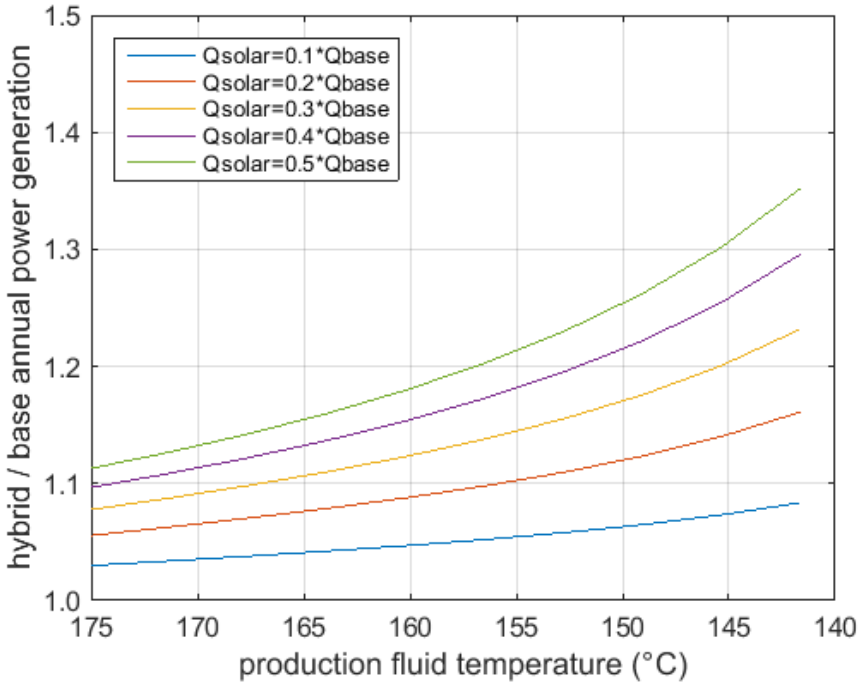

Figure 21. Retrofit hybrid plant annual power generation (reported as fraction of base geothermal plant degraded resource annual power generation) plotted as function of production fluid temperature decline (175°C production fluid design temperature).

The performance of the brine preheating retrofit configuration in geothermal resource flow rate decline scenarios is illustrated in plots included in Appendix E. As previously indicated, a brine post-heat configuration may be best suited to mitigate declines in geothermal resource flow rate.

Enel Green Power North America's Stillwater geothermal/solar thermal retrofit hybrid plant utilizes the brine preheating configuration. A description of hybrid plant power block models used to simulate the performance of this hybrid plant is included in Appendix F, and the full text of a Geothermal Resources Council 2015 Annual Meeting paper discussing optimization of the Stillwater hybrid plant performance is included in Appendix G.

3.2.3 Economics – Marginal LCOE of Additional Power Generation

To evaluate the economic viability of retrofitting the base geothermal plant with concentrating solar heat input, a discounted cash flow analysis was performed to determine the marginal LCOE of the additional power generation associated with the retrofit (revenues and expenses associated with the existing geothermal plant were excluded). The LCOE calculation was based on the methods described in references [33, 34]. The discounted cash flow analysis revenue stream included the additional power sales revenue associated with the hybrid plant configuration, which includes the effects of changes in solar efficiency due to geothermal resource temperature decline as defined for each scenario evaluated. Expenses included the installed capital costs of the solar field and ancillary equipment. These "total hybridization costs" include site preparation, the solar collector hardware, the HTF system, and the HTF-to-brine heat exchanger costs. The HTF-to-brine heat exchanger costs vary depending on the size of the solar field. Additional details on cost components and economic analysis parameters are provided in Table 9. Expenses and/or credits associated with the offset of PPA penalties and/or renewable energy production were deemed project specific and therefore not incorporated into this analysis.

As indicated in Section 2.4, a range of costs are possible for currently available solar field equipment. It is anticipated that advances in collector manufacturing and increased mass production of collectors will lead to further cost decreases, and targets exist for technology cost reductions. Since there is no direct cost for the solar energy used to produce the thermal output from the solar field, the majority of the expenses associated with solar heat are attributed to solar field capital and O&M costs. As a result, the solar field costs are a major factor in the economic viability of a geo-solar hybrid plant. The solar field costs in the retrofit hybrid plant economic analysis were treated as a parametric variable, with solar field costs ranging from $50 to $350 per square meter.

Table 9. Cost assumptions used for the retrofit hybrid plant economic analysis

Cost Components	**Value**	**Reference or Comment**
Installed solar field cost ($/m^2)	Parametric variable ranging from 50-350	Includes parabolic trough collector and vacuum-insulated receiver
Site preparation ($/m^2)	10	[21], assuming an existing plant site
HTF system ($/m^2)	40	[26], based on water-HTF solar field as in SAM's linear Fresnel model
HTF-to-brine heat exchanger	computed based on solar field size	Installed cost from [27]; adjusted to 2013$
Economic Analysis Parameter	**Value**	**Reference or Comment**
Analysis period (years)	30	
Power Plant Availability Factor	0.95	The amount of time that the plant is able to produce electricity over a certain period, divided by the amount of the time in the period.
Discount rate	7%	This is the rate at which future power and costs are discounted in the determination of the LCOE
Depreciation	year 1 20% year 2 32% year 3 19.2% year 4 11.52% year 5 11.52% year 6 5.76%	5 year MACRS cost recovery schedule
Effective Tax Rate	35%	tax rate on profits
Property Tax & Insurance	0.75%	Taxes and Insurance (% of Project Capital Costs)
Contingency	5%	This contingency is applied to all capital costs
O&M cost ($/m^2-year)	4.0	

It was assumed that since the solar heat is used to increase the brine temperature without causing major changes to power block control strategy, existing instrumentation and controls are sufficient for operation of the retrofit hybrid plant power block. The instrumentation and controls costs for the solar field and the solar field HTF-to-brine heat exchanger are included in the total hybridization costs used in the evaluation of the retrofit hybrid plant economics.

The marginal LCOE computed for the hybrid retrofit was independent of the base plant economics, i.e. the expense and revenue streams for the solar retrofit were balanced by determining the marginal LCOE that resulted in a hybrid retrofit NPV equal to zero. The NPV of a base geothermal power plant with a production fluid temperature decline rate that significantly exceeds the design basis is likely to be highly negative if this rate of temperature decline was not factored into the original project assumptions. While the solar retrofit could provide the additional power generation necessary to reduce or eliminate PPA penalties (which could increase the NPV of the base geothermal plant project), sale of the additional power from the solar retrofit at the calculated marginal LCOE would not directly increase the NPV of the base geothermal power plant.

If the marginal LCOE of the additional power generation from the solar retrofit is less than the PPA power sales price, sales of the additional power at the PPA power sales price would result in a positive NPV from the solar retrofit. In this case the addition of the hybrid retrofit could increase the economics of

the overall project, but may not fully restore the economics to those of a design basis that did not account for unplanned production fluid temperature decline.

A sensitivity analysis of marginal LCOE vs. solar field capital costs was performed for each of the power plant design temperatures and the associated geothermal resource temperature decline scenarios. The analysis also evaluated the effect of the solar field size on the marginal LCOE for the retrofit project. Figure 22 is a plot of the marginal LCOE as a function of solar field capital cost (solar field capital costs are a component in the total hybridization costs, which also include site preparation, the HTF system, and the solar field HTF-to-brine heat exchanger) with the solar field size included as a parameter.

The solar field size was varied to provide from 10% to 50% of the base geothermal power plant design point heat input. As illustrated in Figure 18 and Figure 19, solar heat input provides the greatest performance benefit when geothermal resource productivity decline is greatest. The incremental benefits from increased solar heat addition therefore decrease as solar heat input increases, resulting in marginal LCOE values that are lowest when the solar field is smallest. While the marginal LCOE of the retrofit solar heat addition increases with increasing solar field size, there are likely to be cases where use of greater quantities of solar heat input are required to provide the increases power generation needed to offset PPA penalties associated with geothermal resource productivity decline.

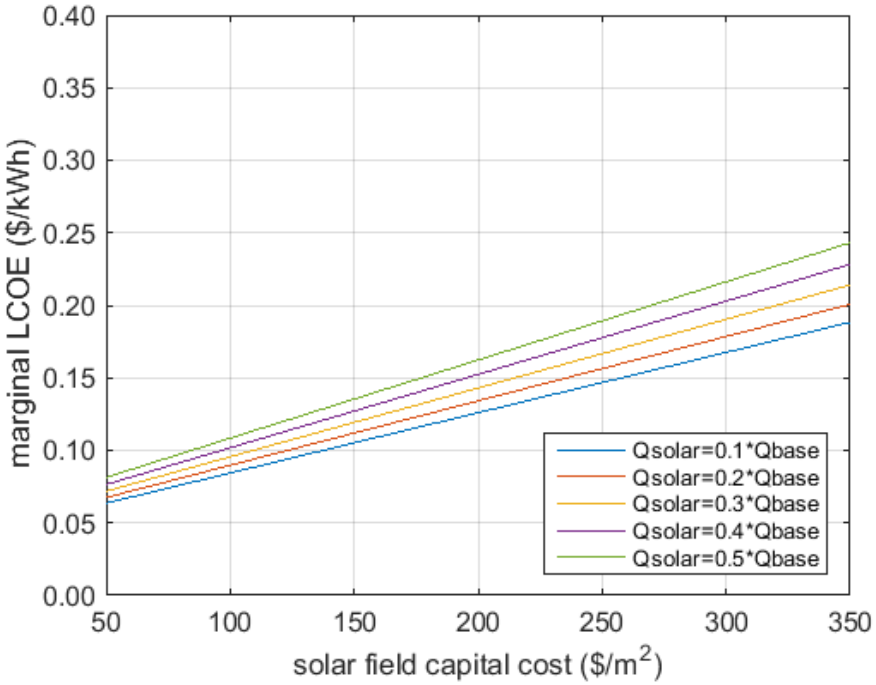

Figure 22. Marginal LCOE of solar retrofit of geothermal power plant plotted as function of solar field capital costs with solar field size as parameter (175°C production fluid design temperature).

In general, power plants designed for higher temperature production fluids result in solar retrofit hybrid plants having lower marginal LCOE for a given set of economic conditions. This is primarily due to the increased efficiency of power plants designed for higher production fluid temperatures. The marginal LCOE for the power plant with the geofluid exit temperature limit is greater than for the case without the temperature limit.

The fact that the marginal LCOE is greater with solar heat input equal to 50% than with solar heat input equal to 10% of the design geothermal heat input indicates that solar heat addition is more expensive than geothermal heat addition. While this indicates that wellfield expansion would likely be a less expensive source of supplemental heat, there may be scenarios in which wellfield expansion is not

possible, introduces more project risk, or may further accelerate the rate of geothermal resource productivity decline. In the greenfield analysis presented in Section 3.3, solar field costs exist at which solar heat becomes less expensive than geothermal.

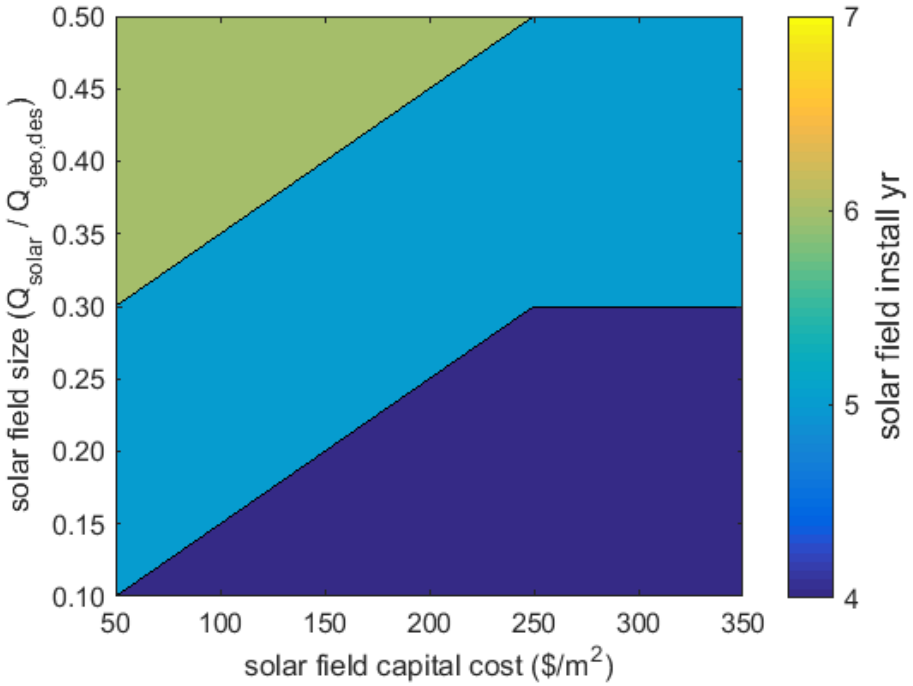

Figure 23. Optimized solar field installation year (175°C production fluid design temperature)

The economic analysis was based on a "single event" installation strategy where all solar collectors are installed at the same time. In the single event installation strategy, the marginal LCOE for each solar field size is minimized by performing the solar project installation some period of time after the initial start of power plant operations. While delaying the installation of the solar project eliminates the possibility of additional power generation from solar heat input during the initial years of power plant operation, the progressive decline in geothermal resource temperature that occurs during this time results in greater solar efficiency upon initial hybrid plant operations. Delaying the solar project installation also decreases the present value of the solar project capital costs. The solar field installation year that minimizes LCOE for the single event installation strategy is presented in Figure 23.

An "on-demand" strategy (in which more collectors are added as the production fluid temperature decreases) may be useful in a scenario where installation of solar collectors is only economically favorable for generating sufficient power to avoid PPA penalties. In this case, the solar collectors could be added in response to production fluid temperature decline to provide thermal energy for generating the required quantity of electrical power. This strategy was not evaluated in this analysis.

The hybrid geo-solar power plants provided increased ability to generate power during the months in which ambient temperature is greatest. Geothermal power plants with declining production fluid temperature and PPA terms that require a fixed level of monthly power generation could utilize solar thermal retrofit technology to meet PPA power generation requirements and avoid or offset PPA penalties. Plants with PPAs that are seasonally adjusted to account for the decrease in air-cooled binary plant performance at higher ambient temperatures may not benefit as much from a solar augmentation. However, the hybrid plant configuration provides additional power generation capacity that can assist with meeting PPA contract obligations on annual, monthly, or even daily reporting periods.

In cases where resource productivity decline is not an issue, an ideal PPA contract for a geo-solar hybrid plant may be one that involves separate contracts for the power generation associated with the separate geothermal and solar heat sources. The geothermal heat source is likely to be best suited to sale of power through a fixed rate base load power contract, while the solar heat source would be best suited for power sales using a time-of-delivery pricing contract. The existence of dual contracts that apply to the power generated from a single power block would most certainly involve a rigorous and likely complicated contract; the details of such a contract are not addressed here other than to note that the contract structure would require the relatively simple requirement that the power plant instrumentation accurately measure and record the quantity of heat utilized from each of the heat sources.

3.3 Greenfield: ORC Working Fluid Heating

3.3.1 Hybrid Plant Configuration

The ORC working fluid heating hybrid plant configuration was introduced in Section 3 as having potential performance and economic benefits in greenfield applications. In the working fluid heating hybrid plant configuration, heat from the solar field is input directly to the ORC working fluid as illustrated in Figure 13. This configuration increases the ability of the solar heat to be utilized at higher temperatures for increased power block efficiency. Addition of the solar heat to the ORC working fluid also minimizes hybrid plant thermodynamic losses since the solar heat is transferred through only one heat exchanger rather than two as required in the brine preheating configuration. As with the brine preheating configuration, the ORC working fluid heating configuration can use solar heat to offset declines in geothermal resource productivity. However, the ORC working fluid heating configuration does increase the power block capital costs as well as modify power block operating conditions.

Two power block plant configurations were evaluated in the greenfield ORC working fluid heating hybrid plant analysis. A basic ORC cycle was used in cases without a brine exit temperature limit and a recuperated ORC cycle was used in cases with a temperature limit. Geothermal resources with design temperatures of 175°C (347°F) and 200°C (392°F) were investigated. The rates of resource temperature decline assumed for each of these geothermal resources are specified in Table 7. Isobutane was used as the working fluid in all of the greenfield ORC working fluid heating hybrid plants evaluated.

Analysis of the greenfield ORC working fluid heating hybrid plant design revealed that planning for solar input at the power plant design point resulted in a plant design with lower cumulative net power generation over a typical operating year. The cumulative net power generation for a greenfield hybrid plant in which no solar heat input was included at the power plant design point was greater. Because solar heat is not available for large periods of time and ambient temperature is generally lower during these time periods, it is more effective to design the plant for maximum efficiency in the absence of solar energy. Said differently, power plants with solar heat input included at the design point perform with lower efficiency when the solar heat is unavailable.

Although the greenfield hybrid plant designs utilized in this evaluation did not include solar thermal heat input at the design point, the pressure drop associated with the solar thermal HTF/working-fluid heat exchanger was included at the design point since this heat exchanger would be installed during plant construction along with all other power cycle components. The solar thermal HTF/working-fluid heat exchanger increases the pressure drop in the working fluid flow loop at all operating points regardless of whether solar heat duty is being added.

Use of variable frequency drive (VFD) pumps provides a significant increase in off-design plant operation performance relative to using a constant speed pump and throttling the pump output with a control valve. The range of pump outlet flow rate and pressures attainable through use of variable frequency drives results in decreased parasitic losses throughout the range of potential off-design operating conditions. Efficient plant operation throughout the range of operating conditions is an important consideration in the greenfield hybrid plant configuration where heat input to the plant can vary

widely over the course of a typical day. The greenfield hybrid plant configurations evaluated in this analysis therefore all utilize VFD drive pumps as the increases in off-design efficiency are significant relative to the use of constant-speed pumps with a control valve. Each greenfield plant configuration was assumed to use a working fluid pump configuration with three identical VFD pumps installed in parallel. The pumps were sized such that plant operation at the design point corresponded to operation of two of the pumps; the third pump is utilized during operating periods when solar heat input is available and increased working fluid flow and/or pressure are required.

The solar field was limited to a size that prevented large increases in turbine-generator capacity in order to minimize power block capital cost increases and to prevent the turbine from operating at conditions far from design during geothermal-only operations. The gross power generation of each plant configuration evaluated was determined at conditions with low ambient temperature (0°F) and no solar heat input. The quantity of solar heat input that resulted in similar levels of gross power generation at an ambient temperature of 70°F (the lower end of the ambient temperature range where maximum solar field thermal output is achieved at the selected geographic location) was then determined; it was assumed that hybrid plants with this quantity of solar heat input would not need a turbine-generator with increased capacity. Of the plants evaluated, those with a brine exit temperature limit could be coupled with a solar field sized to provide heat output of approximately 25% of the design geothermal heat input without increased turbine-generator capacity requirements, while plants without a brine temperature limit could be coupled with a solar field providing approximately 35% of the design geothermal heat input without increasing turbine-generator capacity.

This analysis evaluated hybrid plants with solar field sizes providing up to as much as 50% of the design geothermal heat input to determine if this increased level of solar heat input would be beneficial despite the requirement for increased turbine-generator capacity. For solar fields of this size, the turbine-generator capacity was increased by an amount corresponding to the increase in hybrid plant gross power generation relative to low ambient temperature geothermal heat only operations. Hybrid plants with solar heat input equal to 50% of the design geothermal heat input required turbine-generator capacity increases of approximately 10% and 20% for scenarios without and with a brine exit temperature limit constraint, respectively. Stand-alone and hybrid plant design net power generation is presented in Table 10, where stand-alone plant performance is reported at an ambient temperature of 50°F, while hybrid plant performance is reported at an ambient temperature of 70°F with solar field design thermal output. Capital costs for the hybrid plants with increased turbine-generator capacity were adjusted accordingly (see Section 3.3.3).

Table 10. Stand-alone and hybrid plant design net power generation (MW)

plant configuration	stand-alone geothermal plant	hybrid geo-solar w/o increased turbine-generator capacity*	hybrid geo-solar with increased turbine-generator capacity
basic cycle, 175°C, w/o T limit	24.2	30.7	34.5
recup cycle, 175°C, w/T limit	23.4	27.0	33.2
basic cycle, 200°C, w/o T limit	33.3	42.5	47.3
recup cycle, 200°C, w/T limit	31.5	35.7	43.0

*max solar heat input equal to 25% or 35% of design geothermal heat input for plants with and without brine exit temperature limit, respectively

The primary differences between the brine preheating and ORC working fluid heating hybrid plant configurations are summarized in Table 11.

Table 11. Brine preheating vs. ORC working fluid heating power plant configuration

Retrofit Brine Preheating Configuration	Greenfield ORC Working Fluid Heating Configuration
solar heat added to geothermal production fluid upstream of power block	solar heat added to ORC working fluid upstream of turbine inlet
variable frequency drive (VFD) pump capacity determined from design point pump inlet/outlet conditions	VFD pump capacity determined based on identification of maximum pump capacity requirements during off-design operation
generator output limit imposed	hybrid plant generator capacity determined by comparing gross power output during geo-solar operations with that of low ambient temperature geothermal only operations and scaling design capacity accordingly
additional production fluid pumping may be required to prevent vaporization if solar collectors raise fluid temperature above design point	ORC working fluid heating does not impose any additional production fluid pumping requirements

3.3.2 Hybrid Plant Performance

As with the brine preheating hybrid plant configuration, solar heat addition via working fluid heating can offset the non-linear decrease in power plant performance associated with geothermal resource temperature decline. Figure 24 and Figure 25 indicate that a constant quantity of solar heat addition in the ORC working fluid heating hybrid plant configuration generally results in increasing solar efficiency as the production fluid temperature decreases.

However, relative to the brine preheating configuration, the working fluid heating configuration is able to achieve greater solar efficiency when the geothermal resource conditions are closer to design. The increased performance of the ORC working fluid heating configuration is possible as a result of the additional working fluid pump and turbine-generator capacity. Increased power generation is achieved primarily through simultaneous increases in the working fluid flow rate and turbine inlet pressure, with the amount of superheat remaining largely unchanged from the brine preheating plant configuration (with similar quantities of solar heat input). This operating strategy results in average annual solar efficiencies that are greater than the brine preheating configuration when geothermal resource productivity is close to design conditions, while maintaining the ability to operate with increasing levels of solar efficiency as the geothermal resource productivity declines.

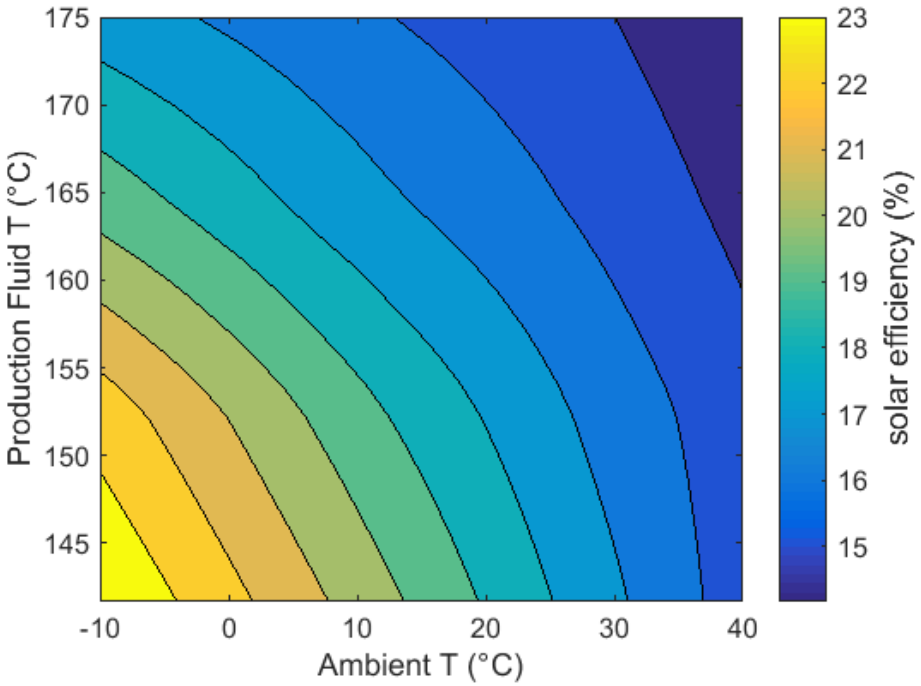

Figure 24. Thermal efficiency of power conversion from solar heat addition equal to 25% of base plant design point heat input plotted as function of production fluid temperature and ambient temperature (basic cycle with 175°C production fluid design temperature)

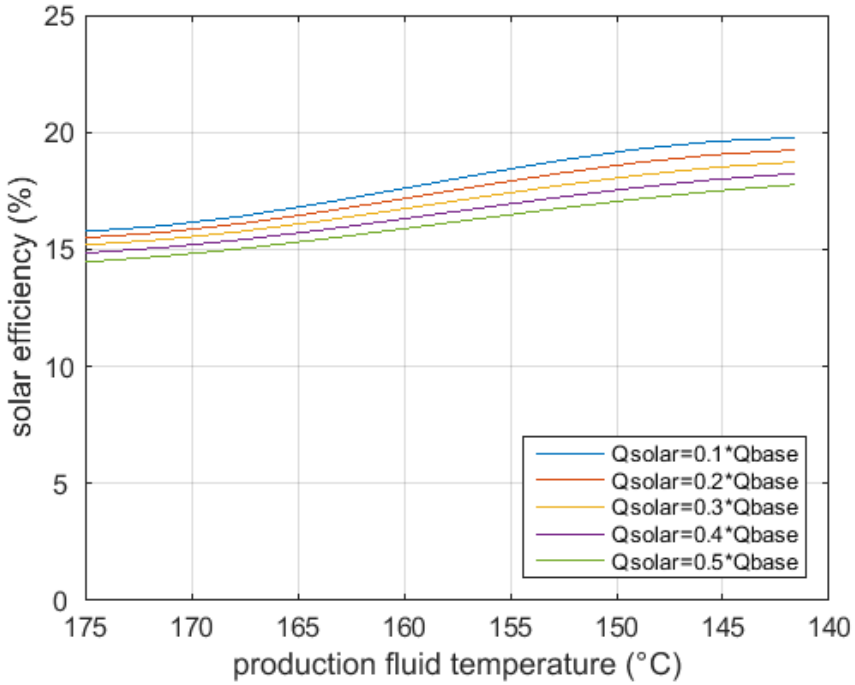

Figure 25. Average annual solar efficiency as a function of production fluid temperature decline (basic cycle with 175°C production fluid design temperature).

Additional power generation resulting from various levels of solar heat input (with the assumed rate of geothermal resource temperature decline) is presented in Figure 26 and Figure 27. As with similar plots previously presented, solar heat input is presented as a percentage of the corresponding stand-alone geothermal plant design point heat addition. Figure 26 presents the ratio of hybrid to stand-alone geothermal plant annual power generation based on design geothermal resource conditions, while Figure 27 presents the same ratio based on the stand-alone geothermal plant performance at the degraded resource condition. The increase in the solar efficiency (from a constant quantity of solar heat addition) with decreasing geothermal resource temperature is apparent in Figure 27. It is important to note that solar efficiency decreases, while overall plant generation increases, with increasing amounts of added solar energy. The performance of the ORC working fluid heating configuration in geothermal resource flow rate decline scenarios is illustrated in plots included in Appendix E.

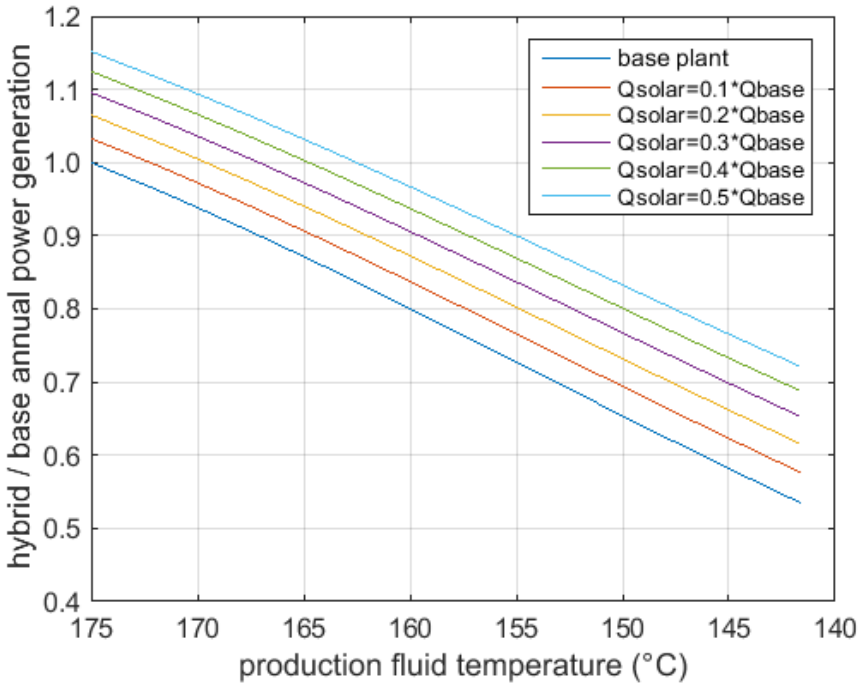

Figure 26. Base and greenfield hybrid plant annual power generation (reported as fraction of base geothermal plant design annual power generation) plotted as function of production fluid temperature decline (basic cycle with 175°C production fluid design temperature).

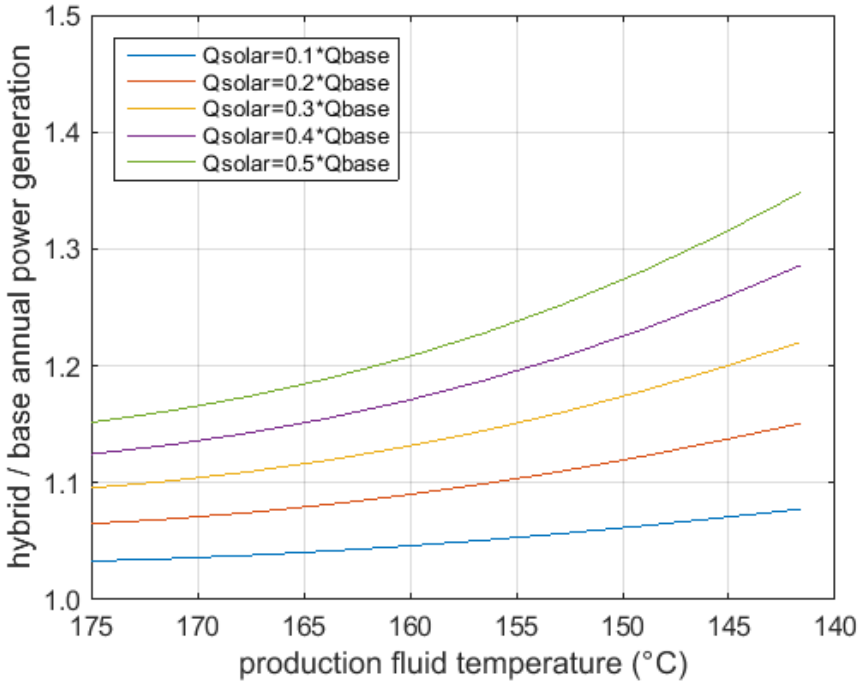

Figure 27. Greenfield hybrid plant annual power generation (reported as fraction of base geothermal plant degraded resource annual power generation) plotted as function of production fluid temperature decline (basic cycle with 175°C production fluid design temperature).

3.3.3 Economic Analysis – Hybrid Plant LCOE

An economic analysis was performed to compare the LCOE of stand-alone geothermal and hybrid power plant configurations. The LCOE for each plant configuration was determined using a discounted cash flow analysis. The discounted cash flow analysis used power plant simulation results and relevant economic parameters to determine project revenues and expenses. The LCOE of the electrical power sales was manipulated to balance the project revenues with expenses such that the net present value was equal to zero.

Stand-alone and hybrid plant configurations with geothermal resource design temperatures of 175°C and 200°C were evaluated in the economic analysis. The specifications and costs for each of these geothermal resources are summarized in Table 12.

Table 12. Summary of assumed geothermal well field specifications and costs

	175°C geothermal resource	200°C geothermal resource	Reference or Comment
brine flow rate (kg/s)	378	378	total brine flow
temperature gradient (°C/m)	0.075	0.075	
well depth (m)	2200	2533	assuming 10°C surface temperature
productivity decline rate (°C/yr)	1.1	1.5	from Table 7
production wells	4	4	assuming ~1500 gpm per production well
injection wells	3	3	
drilling cost per well	$4.54M	$5.48M	2010$, based on well cost to depth correlation developed using 1-6 km depth large diameter production well cost data obtained from Sandia National Laboratory
Exploration/Confirmation			
number confirmation wells drilled	5	5	
confirmation drilling success rate	60%	60%	3 wells used by project (60% of 5 wells drilled)
exploration/confirmation costs			
exploration drilling cost	$5.0M	$5.0M	assumed value
exploration non-drilling cost	$1.5M	$1.5M	assumed value
confirmation drilling costs	$27.2M	$32.9M	20% additional drilling cost per confirmation well
other confirmation costs	$1.4M	$1.6M	5% of confirmation drilling costs
total exploration and confirmation costs	$35.1M	$41.0M	
Wellfield Completion			
number of wellfield completion wells drilled	5	5	
wellfield completion drilling success rate	80%	80%	4 wells used by project (80% of 5 wells drilled)
wellfield completion costs			
wellfield completion drilling costs	$22.7M	$27.4M	
permitting, contingency costs	$1.0M	$1.0M	assumed value
total wellfield completion costs	$23.7M	$28.4M	

Power plant costs were determined using cost correlations for major process equipment components. Producer Price Indices were used to reference these equipment costs to 2010 USD. Multipliers were then used to compute total material costs for piping, concrete, steel, electrical/instrumentation, and other equipment costs. The total material cost was used as the basis for estimating direct construction costs including labor, home office/management, fringe & burden, miscellaneous construction, freight, and taxes and permitting costs. The total plant cost was determined by including direct construction cost multipliers for engineering, other project costs, and contingency.

Total plant costs for both stand-alone geothermal configurations and the corresponding hybrid geo-solar hybrid configurations are summarized in Table 13. As discussed in Section 3.3.1, hybrid plant configurations require additional working fluid pumping capacity to efficiently utilize the solar heat input. Depending on the size of the solar field, additional turbine-generator capacity may also be required. Plants with a brine exit temperature limit require additional turbine-generator capacity if the solar heat input is greater than approximately 25% of design geothermal heat input, while plants without a brine exit temperature limit require additional turbine-generator capacity if the solar heat input is greater than approximately 35% of design geothermal heat input. Table 13 includes capital costs for hybrid plants without increased turbine-generator capacity, as well as capital costs for hybrid plants with turbine-generator capacity sufficient to utilize solar heat input equal to 50% of design geothermal heat input.

Table 13. Summary of total plant costs

plant configuration	stand-alone geothermal plant	hybrid geo-solar w/o increased turbine-generator capacity	hybrid geo-solar with increased turbine-generator capacity
basic cycle, 175°C, w/o T limit	$82.8M	$87.8M	$91.3M
recup cycle, 175°C, w/T limit	$82.5M	$87.7M	$97.7M
basic cycle, 200°C, w/o T limit	$115.0M	$124.1M	$132.9M
recup cycle, 200°C, w/T limit	$103.9M	$111.1M	$123.2M

The solar field costs in the greenfield hybrid plant economic analysis were treated as a parametric variable with the range of costs selected to correspond to current and future target values. Solar field capital costs are the primary component in the total hybridization costs, which also include site preparation, the HTF system, and the solar field HTF-to-WF heat exchanger. Solar field cost components and other economic parameters used in the discounted cash flow analysis are included in Table 14. Solar field sizing was also considered in the economic analysis, with the impact of the solar field size on power block capital costs accounted for as described in Section 3.3.1.

In addition to the parameters listed in Table 14, the discounted cash flow analysis also requires a schedule for exploration, confirmation, wellfield completion, and power plant construction activities occurring prior to power plant startup in order to determine the present value of each of these activities. Exploration and confirmation activities were assumed to start 5 years prior to plant operation and last for 3 years (exploration and confirmation costs distribution of 10%, 30%, and 60% in first, second, and third years, respectively) with a discount rate of 30%. Well field completion activities were assumed to start 2 years prior to plant operation and last for 2 years (costs evenly distributed for duration of well field completion activities) with a discount rate of 15%. Power plant construction was assumed to start 2 years prior to plant operation and last for two years (costs evenly distributed for duration of power plant construction activities) with a discount rate of 7%. The economic analysis assumes hybrid plant geothermal and solar operations commence simultaneously in year 1 of the project.

The discounted cash flow analysis accounts for decreased electrical power sales resulting from power plant and well field parasitic loads. Brine pumping requirements were calculated based on the methods discussed in [35]. The discounted cash flow analysis also includes the impact of geothermal resource temperature decline on power plant output over the project life, which results in greater electricity costs than if the analysis were to assume design point power generation was maintained for the life of the project. Although the decrease in power generation due to geothermal resource temperature decline was included, site/project specific parameters such as PPA penalties, subsidies, and/or incentives were excluded from the LCOE calculation.

Table 14. Discounted cash flow analysis parameters

Cost Components	**Value**	**Reference or Comment**
Installed solar field cost ($/m2)	Parametric variable ranging from 50-350	Includes parabolic trough collector and vacuum-insulated receiver
Site preparation ($/m^2)	10	[21], assuming an existing plant site
HTF system ($/m^2)	40	[26], based on water-HTF solar field as in SAM's linear Fresnel model
HTF-to-WF heat exchanger	calculated based on solar field size	Installed cost from [27]; adjusted to 2013$
Economic Analysis Parameter	**Value**	**Reference or Comment**
Project Life (years)	30	Period of operation
Power Plant Availability Factor	0.95	The amount of time that the plant is able to produce electricity over a certain period, divided by the amount of the time in the period.
Discount rate exploration and confirmation well field completion plant construction and startup	 30% 15% 7%	These are the rates at which future costs and revenues are discounted in the determination of the LCOE
Depreciation year 1 year 2 year 3 year 4 year 5 year 6	 20% 32% 19.2% 11.52% 11.52% 5.76%	5 year MACRS cost recovery schedule
Effective Tax Rate	35%	tax rate on profits
Property Tax & Insurance	0.75%	Taxes and Insurance (% of Project Capital Costs)
Royalties through year 10 after year 10	 1.75% 3.5%	Royalties paid to BLM as percentage of geothermal power sales revenue
Contingency	5%	This contingency is applied to all capital costs
Geothermal O&M cost ($/kWhr)	0.025	based on power plant design point net power generation (brine pumping power excluded)
Solar field O&M cost ($/m^2-year)	4.0	solar field O&M costs per unit area derived from SAM cost model [21]

The LCOE calculated for each of the stand-alone geothermal configurations are presented in Figure 28. The calculated LCOE is lower for the 200°C production fluid temperature scenarios than for the 175°C scenarios. Since available energy and plant efficiency are directly proportional to the production fluid temperature, these benefits more than offset the higher capital costs of the 200°C plants. Electricity prices are also lower for power plants without an exit temperature limit. The exit temperature limit reduces the amount of energy that can be extracted from the production fluid and therefore decreases the quantity of power that can be generated relative to a case without the temperature limit. Additionally,

cases with the exit temperature limit were based on a recuperated cycle plant configuration; addition of the recuperator not only increases pressure losses throughout the cycle but also increases power plant capital costs per unit of electrical power generation ($/kW).

Figure 28 also includes calculated minimum electricity sales pricing for both level (each kWh is valued equally regardless of time/date) and time-of-delivery (TOD) pricing schedules. SAM's generic TOD pricing schedule [36] was used in this evaluation. Use of the TOD pricing schedule results in greater electricity base rate pricing than the level pricing schedule for the stand-alone geothermal plants evaluated. This is due to the fact that TOD schedules in the southwest United States favor summer afternoon periods when higher temperatures lead to higher power demands. The performance of a stand-alone air-cooled geothermal power plant is out of phase with typical TOD schedules (stand-alone geothermal plants generate peak power levels at night when ambient temperatures are lowest), which requires the base electricity sales price to be greater when a TOD pricing schedule is used.

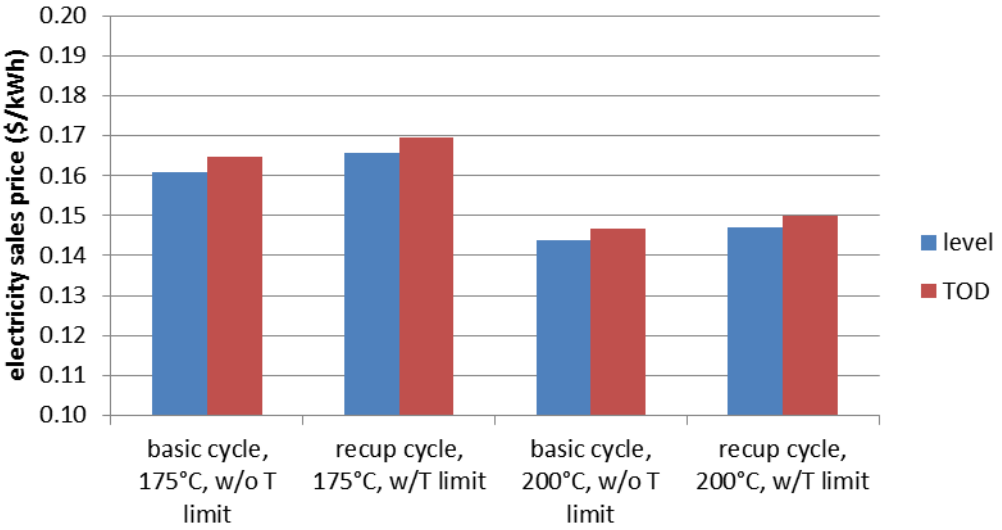

Figure 28. Minimum electricity sales price with level and time-of-delivery pricing schemes for stand-alone geothermal plants at two different resource temperatures

Figure 29 (level pricing schedule) and Figure 30 (TOD pricing schedule) are plots of the hybrid plant LCOE as a function of solar field capital cost with the solar field size included as a parameter. The right side y-axes in Figure 29 and Figure 30 present the hybrid plant electricity sales price as a ratio of the stand-alone geothermal plant electricity sales price.

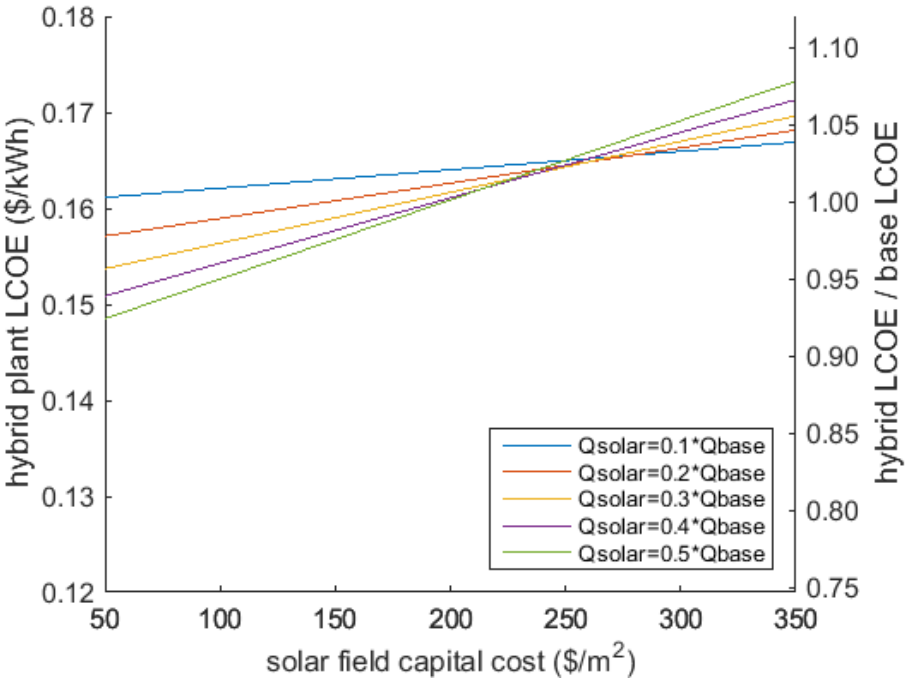

Figure 29. Greenfield hybrid plant minimum electricity sales price (left y-axis) and ratio of hybrid-to-base LCOE (right y-axis) plotted as function of solar field capital costs for level pricing scheme (basic cycle with 175°C production fluid design temperature).

Solar field costs where the hybrid LCOE to base LCOE ratio is lower than 1.0 correspond to conditions where a working fluid heating hybrid could reduce the LCOE relative to a stand-alone geothermal power plant. Solar field costs where the hybrid LCOE to base LCOE ratio is lower than 0.95 correspond to conditions at which hybrid technology could reduce LCOE by 5%.

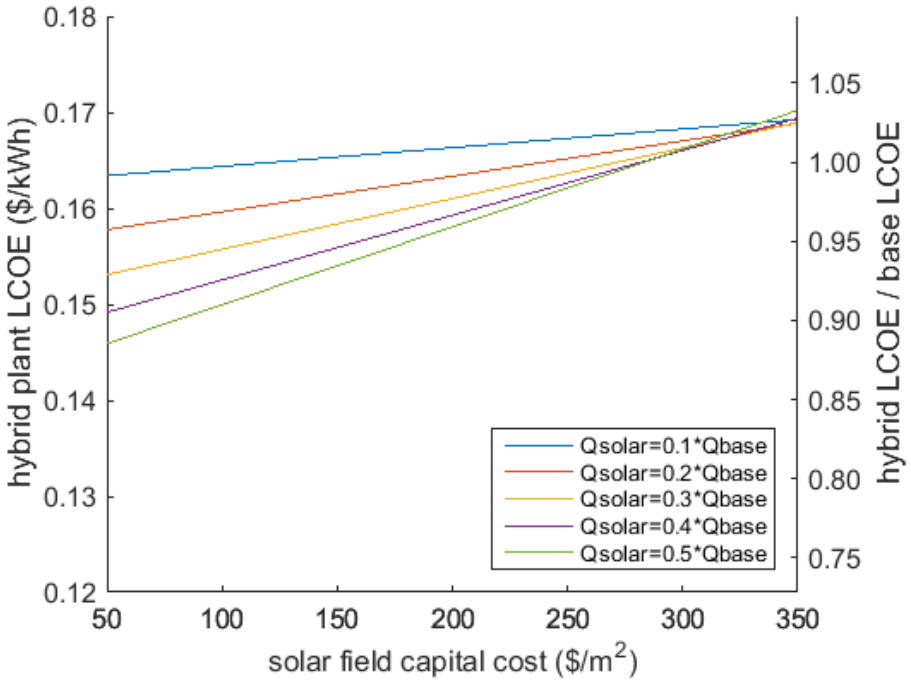

Figure 30. Greenfield hybrid plant minimum electricity sales price (left y-axis) and ratio of hybrid-to-base LCOE (right y-axis) plotted as function of solar field capital costs for time-of-delivery pricing scheme (basic cycle with 175°C production fluid design temperature).

Table 15 summarizes the maximum allowable solar field costs for each hybrid plant configuration to achieve a 5% LCOE reduction relative to the corresponding stand-alone geothermal plant. The power plants with higher geothermal resource design temperatures and level electricity pricing schedules require lower solar field capital costs to achieve 5% LCOE reductions. These results are largely dependent on the magnitude of the stand-alone geothermal plant configuration LCOE values, which provide the reference against which hybrid plant cost reductions are measured.

Table 15. Installed solar field costs ($/m^2) required for 5% LCOE reduction relative to stand-alone geothermal plant.

plant configuration	level pricing schedule*	TOD pricing schedule*
basic cycle, 175°C, w/o T limit	100	182
recup cycle, 175°C, w/T limit	54	138
basic cycle, 200°C, w/o T limit	32	107
recup cycle, 200°C, w/T limit	11	91

*total solar project costs also include site preparation, the HTF system, and the HTF-to-WF heat exchanger

The LCOE values for the 200°C stand-alone geothermal plants are lower than the values for the 175°C stand-alone geothermal plants due mainly to the higher efficiency of the 200°C power plants. Although the solar heat input is converted to power at a higher efficiency by the 200°C plant than the 175°C plant, the higher efficiency does not outweigh the reduced selling price for the electrical power generated by the 200°C hybrid plant. The 200°C hybrid plants therefore require relatively less expensive solar heat than the 175°C hybrid plants to achieve 5% LCOE reductions. Since the cost of solar heat is primarily a function of solar field capital costs, plants with 200°C geothermal resource design temperatures required lower solar field capital costs.

The LCOE values for stand-alone geothermal plants with level electricity pricing schedules are lower than those with TOD pricing schedules. Consistent with the preceding discussion, plants with lower revenue for each unit of electrical power sold require lower solar field costs to achieve 5% LCOE reductions. Furthermore, in the TOD pricing schedule scenarios, higher prices are generally obtained from electrical power sales during periods when solar heat is available, which enables the hybrid plants with TOD pricing schedules to achieve 5% LCOE reductions with higher solar field capital costs than those with level pricing schedules.

Although with variations both in geothermal resource temperature and electricity pricing schedule the recuperated stand-alone geothermal plant LCOE is greater than for the equivalent basic cycle plant, reducing this LCOE requires offsetting the additional capital costs associated with increased recuperated hybrid plant turbine-generator capacity. As previously noted, recuperated plant configurations were used in scenarios with a brine exit temperature constraint. Since the brine temperature constraint limits the stand-alone geothermal plant output, the additional turbine-generator capacity required by a hybrid plant operating off such a geothermal resource results in more extensive increases in hybrid plant power block capital costs.

The maximum allowable solar field costs for TOD pricing scenarios specified in Table 15 are near the installed collector field cost goal of \$100 to \$150/m^2 discussed in Section 2.4, while the maximum allowable solar field costs for level pricing scenarios fall below this cost goal. This indicates that greenfield hybrid plant configurations using the ORC working fluid heating configuration could potentially reduce LCOE by 5% in TOD pricing scenarios, but it is unlikely that use of this hybrid technology would result in 5% LCOE reductions for level pricing scenarios. It is worth reiterating that the LCOE calculation upon which these conclusions are based includes power sales revenue adjusted for declining geothermal resource productivity; additional costs associated with enhanced hybrid plant power block pump and turbine-generator capacity; and solar project costs comprised of the installed solar field costs and other project costs (site preparation, HTF system, HTF-to-WF heat exchanger).

3.3.4 Economic Analysis – Unplanned Resource Decline with PPA Penalties

A follow-up greenfield hybrid plant analysis was performed in which the impact of geothermal resource productivity decline was not included in the determination of the project LCOE. This analysis was performed for a level pricing scenario typical of geothermal power generation projects. All other economic parameters utilized in determining the stand-alone geothermal plant LCOE were unchanged from those specified in Table 12, Table 13, and Table 14. Results of the analysis are summarized in Table 16. As expected, the LCOE calculated without accounting for projected resource temperature decline was lower than the LCOE calculated when projected resource temperature decline was included. The solar field capital costs were identified that resulted in no change to the stand-alone geothermal plant LCOE (maintaining the assumption of no resource temperature decline over the project life). In this analysis the solar field was sized such that additional turbine-generator capacity was not required (solar heat equal to 25% of geothermal heat input for plants with a brine exit temperature limit and 35% of geothermal heat input for plants without a brine exit temperature limit). A solar field installed at the unit cost identified in Table 16 would allow the project to be installed as a greenfield hybrid plant instead of a stand-alone geothermal plant without altering the LCOE at which the power would be sold, while providing the operational advantages of the hybrid plant configuration including increased correlation with utility load curves and reduced risk to geothermal resource productivity decline.

Table 16. Economic analysis of scenario with unanticipated geothermal resource temperature decline

plant configuration	stand-alone geo plant LCOE* ($/kWh)	solar field capital cost required*† ($/m^2)	hybrid NPV minus stand-alone NPV		decrease in project NPV due to PPA penalties	
			w/o PPA penalties	with PPA penalties	stand-alone	hybrid
basic cycle, 175°C, w/o T limit	0.1324	127	$2.2M	$15.5M	53%	11%
recup cycle, 175°C, w/T limit	0.1364	115	$1.5M	$12.4M	56%	21%
basic cycle, 200°C, w/o T limit	0.1192	88	$2.6M	$20.6M	61%	17%
recup cycle, 200°C, w/T limit	0.1208	100	$0.9M	$13.3M	63%	32%

*assuming no geothermal resource productivity decline
†solar field capital costs required to obtain hybrid LCOE equal to stand-alone geo plant LCOE

In order to quantify the potential level of risk reduction provided by the hybrid plant, the impact of a steady geothermal resource temperature decline was then evaluated. In this evaluation, the geothermal resource temperature was assumed to decline at the rate specified in Table 7. Since electrical power from the stand-alone and hybrid plants considered would continue to be sold at the specified LCOE values (which did not include degradation in power output associated with geothermal resource productivity decline), in all cases the project operations would result in a negative net present value as a result of insufficient power sales revenue as shown in Figure 31. Although both the stand-alone geothermal plant and hybrid plant NPV were negative for each of the power plant configurations upon the occurrence of unplanned geothermal resource temperature decline, the hybrid plant NPV was less negative than the stand-alone plant NPV, indicating that use of hybrid technology would mitigate some of the financial risk associated with the geothermal resource.

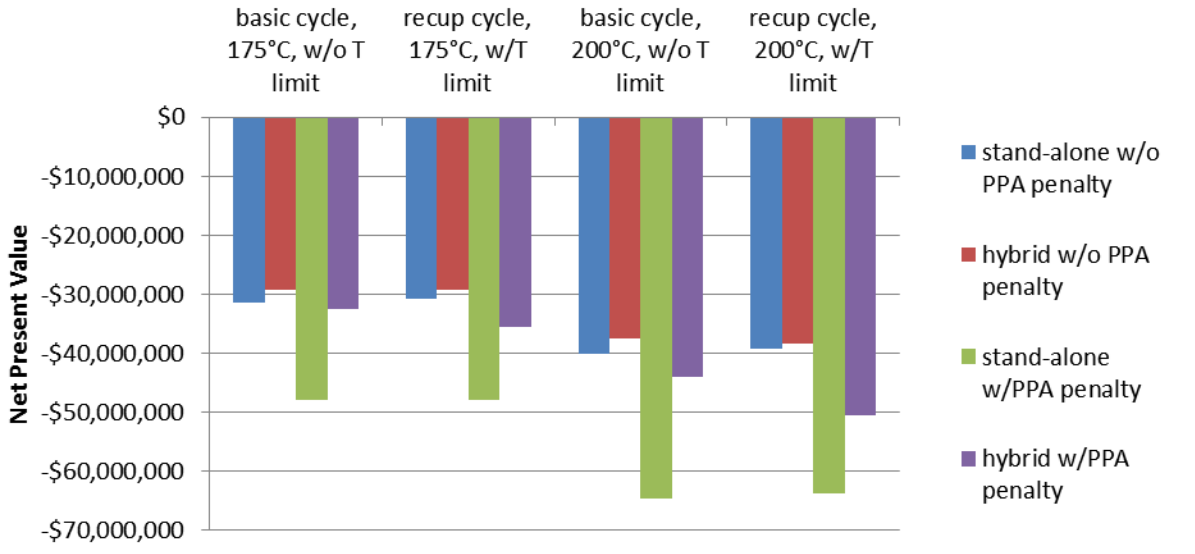

Figure 31. Net Present Value of scenarios with unplanned geothermal resource temperature decline

As previously discussed, the power purchase agreement under which electrical power is sold to the utility may stipulate required levels of power generation. If the electrical power generation of a project

falls below this default level, financial penalties may be assessed to the power plant operator. While PPA default levels and the associated penalties are project specific, the impact of resource temperature decline with an assumed set of PPA contract terms was evaluated to illustrate the potential financial impacts. The assumed PPA contract terms require monthly net power generation greater than or equal to that of the month of lowest power generation with design geothermal resource productivity (the PPA default level is based on power production from the geothermal heat source only), with a penalty equal to 100% of the value of the power sales deficit being assessed on a monthly basis. The monthly net power generation PPA default threshold is assumed to remain constant for the duration of the plant operating life.

For the assumed set of PPA contract terms with the specified rates of unmitigated geothermal resource productivity decline, the impact of the PPA penalties on the stand-alone geothermal plants considered was substantial, with the magnitude of the penalties approaching the value of the power sales revenue lost due to deficient power sales. However, the impact of geothermal resource temperature decline on the hybrid plant NPV was significantly lower. While the assessment of PPA penalties resulted in the stand-alone geothermal plant NPV becoming approximately 53-63% more negative in relation to the NPV associated with reduced power sales revenue only, the hybrid plant NPV only decreased by an additional 11-32%. This is a result of the hybrid plant power output remaining at or above the PPA default level for significantly longer than the stand-alone geothermal plant subjected to unmitigated geothermal resource temperature decline. The use of hybrid technology therefore has additional merit in the application of reducing the financial risks associated with PPA penalties for underperforming geothermal resources.

4. Retrofit Hybrid Options for Flash-Steam Geothermal Plants

A singular challenge of geothermal/solar-thermal hybrids is being able to convert solar-thermal energy to electricity in a cost effective manner. While the solar energy system saves capital expense by not needing to provide a power conversion unit, the typically low thermal-to-electric conversion efficiency of geothermal plants is an impediment to cost-effective solar energy use. Greenhut et al. [3] compared different hybrid configurations assuming the use of a 150°C geothermal resource and concluded the low thermal efficiency of a binary cycle running at 150°C was a significant limitation to hybrid plant efficiency. For this reason, Greenhut proposed using solar energy to heat and flash the brine to produce 200°C, 15.5 bar steam. These conditions allowed operation of a steam turbine at 200°C and use of the flash tank liquids to boost the organic working fluid to 180°C. When solar energy was not available the plant operated the ORC cycle alone at the lower brine temperature. Such a design was able to increase thermal efficiency from approximately 11% with the low-temp ORC power block to about 17.5% with the combined steam/ORC power system [3]. Developing geothermal/solar-thermal hybrids for flash-steam geothermal plants improves economics by allowing the solar energy to be converted in a more efficient steam-Rankine power cycle.

This section explores different methods of integrating solar thermal energy with a flash steam plant. In many aspects the designs are similar to integration with binary ORC plants; however, the possibility of integrating solar steam directly into the power cycle offers advantages. Three primary approaches are outlined in Table 17 and following figures. Each of these scenarios could incorporate thermal energy storage (TES) in the solar system by using hot- and cold-fluid storage tanks.

Table 17. Possible solar integration scenarios for flash steam plants.

Solar Brine Heating	**Condensate Reheating and Injection into Brine**	**Condensate Reboiling and Steam Injection**
Figure 32	Figure 33	Figure 34 and Figure 35
Advantages: • No change in mass flow rate to the flash tank • Higher specific enthalpy in water to flash tank; higher steam fraction in flash and steam flow to turbine	**Advantages:** • Higher specific enthalpy in water to flash tank; greater steam flow to turbine • Condensate heating has less scaling issues; simple water/HTF heat exchanger • Large ΔT across solar unit	**Advantages:** • No change in flash tank • Condensate heating has less scaling issues • All solar input sent to power cycle as steam • Option for direct steam generation in solar field
Limitations: • Potential scaling in brine /HTF heat exchanger • Limited ΔT across solar unit due to brine conditions	**Limitations:** • Higher mass flow rate to the flash tank • Most energy from solar not sent to power block, i.e., only the percent flashing in the flash tank.	**Limitations:** • Water pretreatment may be required for boiler

The scenarios listed in Table 17 are depicted in the following figures and were modeled in Engineering Equation Solver (EES) to estimate the mass and energy balances for a nominal 40 MW_{th} solar addition into a 25 MW_e steam turbine. The solar brine heating option (Figure 32) is the least intrusive to the geothermal hardware because solar energy is simply added to the incoming brine. This design is conceptually the same as the Stillwater hybrid, except the brine is flashed rather than used to heat an organic working fluid. No change is made to the brine mass flow rate. Adding energy to the brine

flow will produce a greater steam fraction in the flash tank. However, the amount of energy that can be added is limited by the temperature of the incoming brine and the operating temperature of the flash tank and steam turbine. Assuming a relatively small temperature differential across the solar-to-brine heat exchanger implies a small temperature differential across the solar field and a very high flow rate through the solar field. In addition, adding solar energy at this point may create a scaling problem in the solar-to-brine heat exchanger.

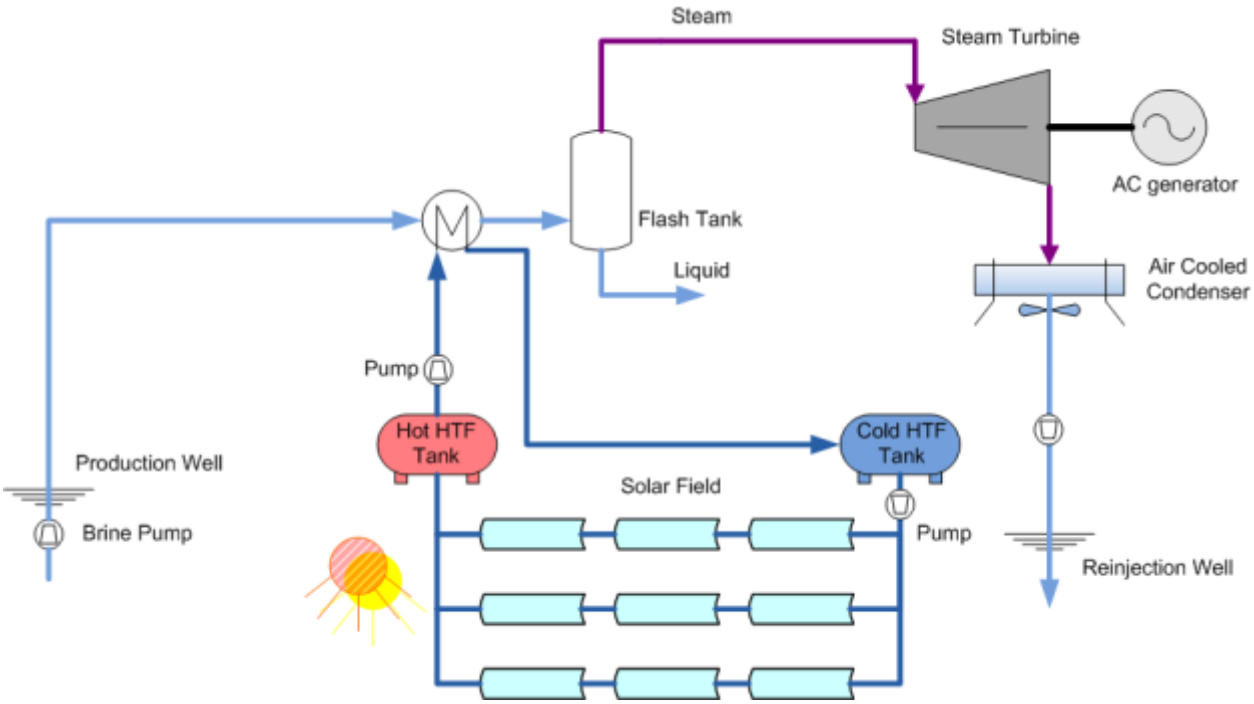

Figure 32. Solar brine heating in a flash steam plant.

The "condensate reheating" option (Figure 33) shares features with, but avoids the major limitations of, the solar brine heating option. The condensate reheating design draws relatively clean condensate from the condenser and reheats this water to the approximate conditions of the flash-tank inlet. The design allows for a relatively large ΔT across the solar field and integration of TES if desired. Scaling in the HTF-to-condensate heat exchanger should be minimal due to the relatively high quality of the condensate liquids; however, some pretreatment of the condensate water may be required.

Figure 34 and Figure 35 show two variations of a "condensate reboiling" option, which both boil condensate to produce solar-generated steam. The first uses a separate steam generation train with an option for hot-HTF storage, whereas the second assumes direct steam generation (DSG) in the solar field. The summary comparison of the different scenarios is given in Table 18.

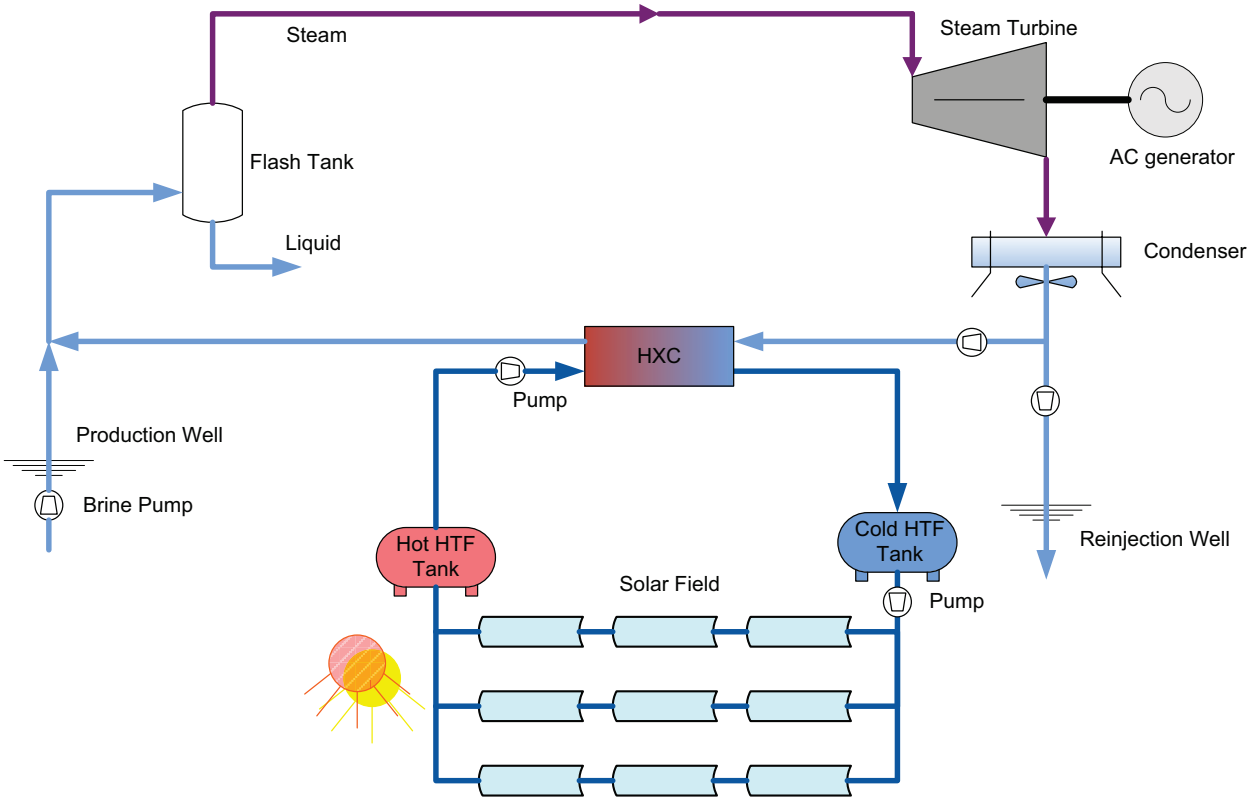

Figure 33. Condensate reheating and injection into the brine flow.

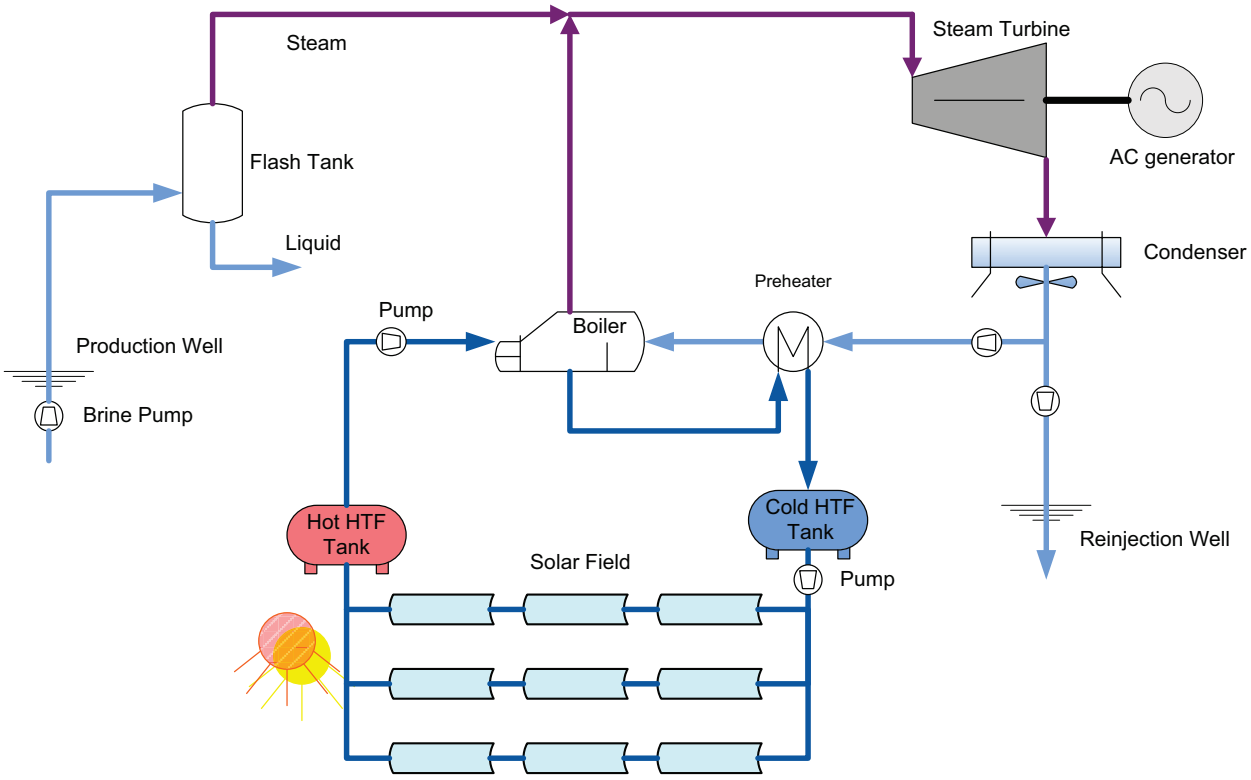

Figure 34. Condensate reboiling and steam injection.

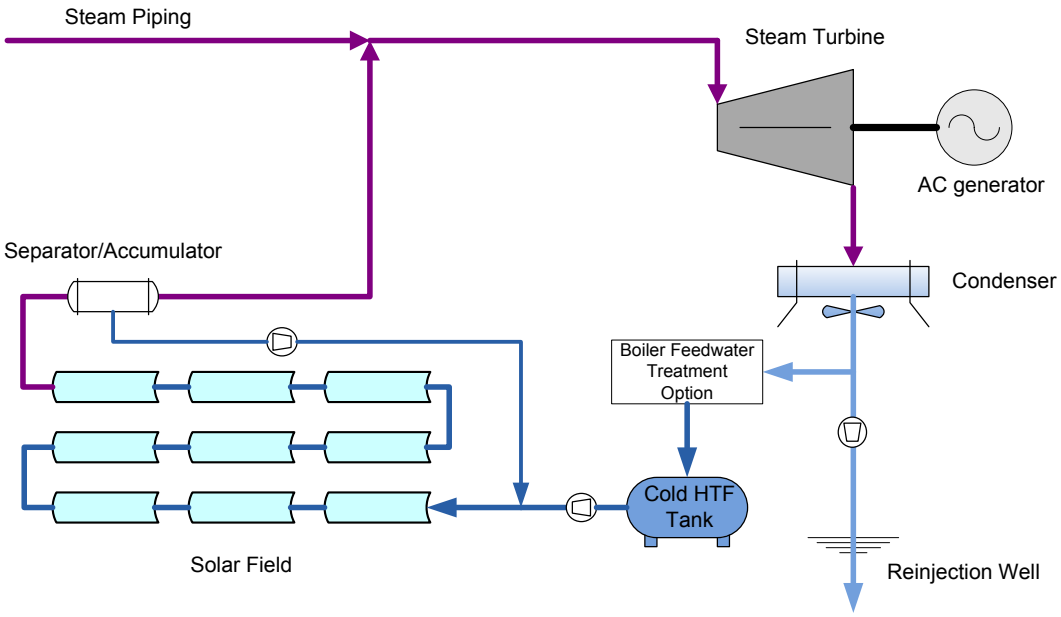

Figure 35. Condensate reboiling using solar DSG and partial recirculation from a steam separator.

Table 18. Summary of flash-steam hybrid integration options.

Parameter	Condensate Reheating and Injection	Condensate Reboiling and Steam Injection	Condensate Reboiling with Solar DSG
Solar capacity (MW_{th})	40	40	40
Solar HTF	water or oil[a]	water or oil[a]	water/steam
Solar-field HTF temp in/out (°C)	60 / 220	178[b] / 220	50 / 182
Solar-field HTF pressure (bar)	28	28	14
Solar-field HTF mass flowrate (kg/s)	58	213	15.6
Steam to turbine at design point (kg/s) [10.5 bar, 182°C]	46.2	46.2	46.2
Steam to turbine from solar (kg/s)	2.5	15.6	15.6
Approximate power from turbine from solar steam (MW_e)	1.4[c]	8.4	8.4
HTF storage efficiency potential (kWh/kg)	0.166	0.24	n/a
Required non-solar equipment	condensate-to-HTF heat exchanger	steam generator, feedwater treatment	feedwater treatment

[a] Either pressurized water or oil could be used as the HTF. Pressurized water is assumed in the calculations.
[b] The energy balance in the boiler forces a high solar field HTF flowrate that translates into a high temperature in the HTF exiting from the preheater
[c] Most of the solar energy is retained in the flash tank liquid fraction

The greatest benefit to a flash steam plant is gained by generating steam and integrating that steam into the steam line feeding the turbine inlet. Furthermore, if one does not have a need for extended TES, the DSG approach requires less hardware and less rigorous conditions (flow, temperature, pressure)

within the solar collector system. Thus, condensate reboiling with DSG is recognized as a preferred approach. As will be shown, this approach is conducive to the use of a steam accumulator to provide a level of thermal energy storage.

4.1 Solar DSG Systems for Hybrids

Analysis and practical experience with DSG systems indicates that operating a DSG system at pressures less than about 20 bar leads to excessive pressure drops in the system and difficult control [37, 38]. Commercially, solar DSG plants are run in recirculating mode (Figure 35) and once-through mode, with the former design being more common. The fact that most flash-steam plants operate with saturated steam further supports the use of the recirculating design.

Figure 36 shows the response of two recirculating DSG systems, one run at 10 bar (top) and the second run at 20 bar (bottom). The figures are plotted as a function of DNI. In the 10-bar (1 MPa) case, the pressure drop in the solar field and outlet steam temperature vary strongly with DNI, which makes for difficult control. In the 20-bar (2 MPa) case, the pressure drop across the solar field is small compared to absolute pressure, and delivered steam pressure and temperature remain relatively constant because the steam fraction increases with increasing DNI. This is the desired mode of operation.

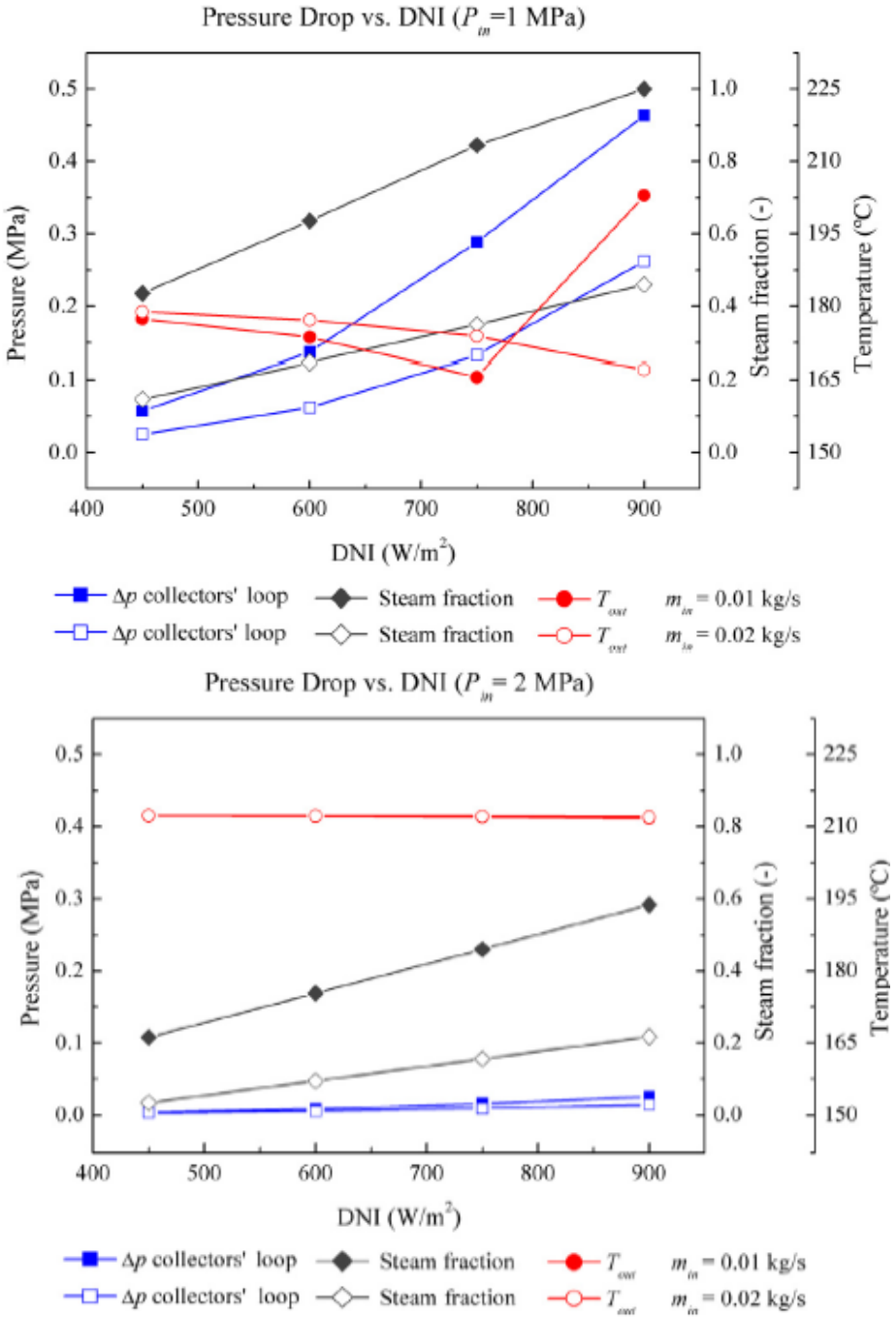

Figure 36. Influence of solar-field inlet pressure on system control. At 1 MPa (10 bar, top), the control of the solar field is complicated by large changes in pressure drop, steam fraction, and temperature. At 2 MPa (20 bar, bottom), the outlet temperature and pressure remain constant and the steam fraction increases with insolation [38].

Operating the solar field at a higher pressure than the geothermal plant brings the added benefit of incorporating some thermal capacitance in the system. As seen in Figure 35, the preferred recirculating configuration requires inclusion of a steam drum or accumulator. A pressure-reducing valve on this accumulator drops the steam pressure to the desired pressure for injection into the steam turbine.

Assuming an adiabatic expansion, the decrease in pressure results in a slight amount of superheat in the steam.

The two largest commercial solar DSG facilities operate at pressures above 20 bar. Hirsch et al. [37] reports that SolarLite's 5-MWe plant in Thailand operates at 30 bar. Novatec Solar's DSG linear Fresnel system in Calasparra, Spain, operates at 55 bar. Both of these facilities generate steam at temperatures that are typically much higher than needed at geothermal power plants. An advantage in operating at higher pressure is the inherent ability to include TES in a steam accumulator. It is worth noting that the Novatec Solar plant produces saturated steam and includes about one full-load hour of steam storage within steam accumulators [39].

In summary, solar DSG facilities produce steam of constant pressure but varying mass flow rate as insolation varies. The fraction of steam at the solar-field outlet varies with insolation and saturated liquid is recirculated to the solar-field inlet. Solar-field inlet pressure must be maintained above about 20 bar to ensure stable control. Product steam pressure is controlled by pressure reduction, and the steam drum can be sized to provide thermal energy storage as a steam accumulator.

4.1.1 Steam Accumulators

Steam accumulators have been used in conventional steam systems for decades and in solar thermal steam systems for several years. The technology provides a simple way to incorporate a small amount of thermal storage into a system and reduce fluctuations in steam delivery or boiler operation due to changes in supply or demand.

Steam accumulators "store" steam as high-pressure saturated water (see Figure 37). The steam accumulator is required to hold the saturated water at a pressure that is greater than the desired steam pressure. When steam is needed, the accumulator can generate steam through a pressure-reducing valve to flash steam at a lower pressure.

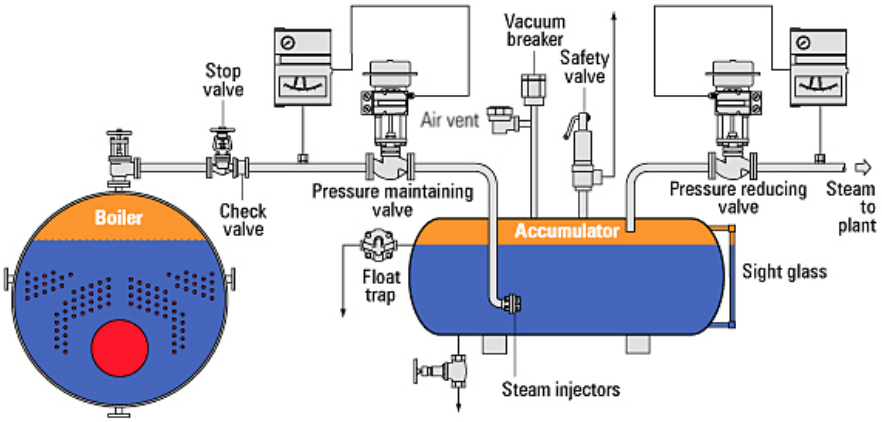

Figure 37. An example steam accumulator for a boiler system [www.spiraxsarco.com].

The maximum release rate of discharging steam from a steam accumulator is proportional to the water surface area in the storage vessel and the saturated water pressure. It can be estimated by the following formula:

$$maximum\ release\ rate\ \left(\frac{kg}{m^2 \cdot h}\right) = 220 \cdot P \tag{1}$$

Here, P is the pressure in bar. In general, maximum release rate can be configured to satisfy most applications. During the discharging process, the pressure in the steam accumulator "slides" from the feed-steam pressure to the exit-steam pressure.

As shown above, steam output in a solar DSG system fluctuates as insolation varies during the day. A steam accumulator can serve as a buffer to regulate the ramping rate of steam supply. The most severe scenario for a DSG plant is the sudden loss of solar power—for example, due to passing clouds. This creates a scenario where the incoming steam from the solar field falls rapidly and the accumulator is asked to maintain discharge steam to the user. The left-hand plot of Figure 38 shows discharging power from a steam accumulator that is 100% full and one that is 25% full as a function of design-point accumulator pressure. While various discharge profiles can be used, from a mathematical point of view, a linear discharge profile yields the minimum ramping rate, given by the slope of the line.

If the nominal steam output is fixed, the ramping rate—the slope in the line in the left-hand plot of Figure 38—will increase when the storage capacity decreases. For comparison, the right-hand plot of Figure 38 gives the steam ramping rate as a function of storage capacity from 5 minutes to 30 minutes. As seen in the figure, the ramping rate (MW/min) increases as storage capacity decreases. If a maximum allowable ramping rate for the solar steam flow to the geothermal plant is known, a minimum required accumulator capacity can be determined. It is important to note that the solar collector field itself will provide some thermal capacitance. In this analysis, it is assumed that the solar field provides the equivalent of five minutes of thermal storage.

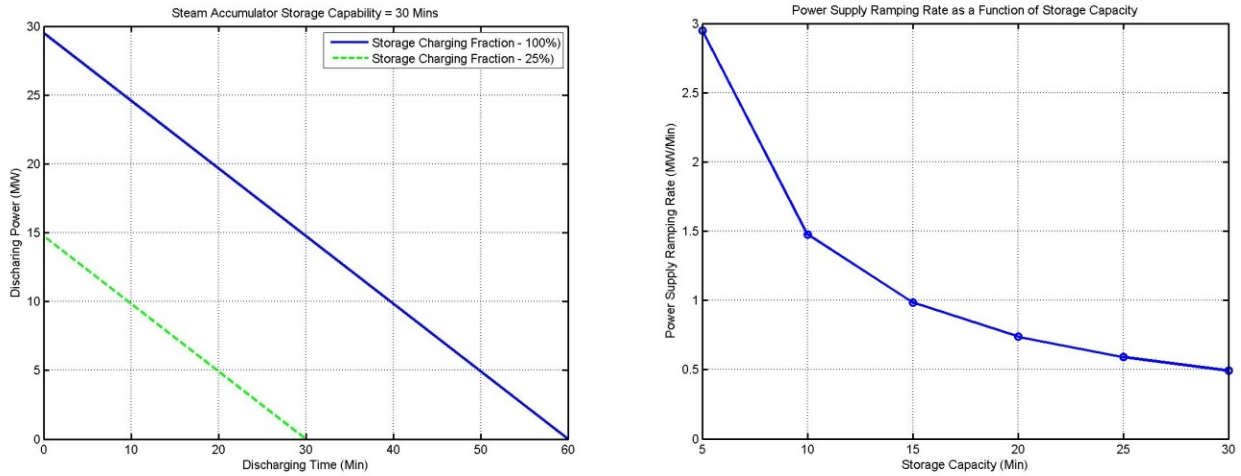

Figure 38. Steam accumulator discharging power for 30-min storage (left) and the ramping rate of the discharging power as a function of storage capacity (right).

A 30-minute steam accumulator is next incorporated into a solar-field model to illustrate its impact on steam supply to a power cycle. A few charging and discharging principles are implemented in the operation strategy of the accumulator:

- In the early morning, the steam accumulator is charged to 50% of its storage capacity before any discharging.
- The discharging power ramping rate does not exceed the ramping rate criteria determined in Figure 38.
- When the steam accumulator is 100% charged, the steam supply will be determined in such a way that dumping will be minimized while meeting the ramping rate constraint.
- The discharging steam is at a constant pressure.
- The steam accumulator will be totally depleted at the end of each day.

Based on the operational principles above, the advantage of the steam accumulator can be illustrated in an example using solar irradiation data from Boulder City, NV. These data were selected to highlight

how the accumulator will respond to intermittent sunshine. The solar irradiation data have a one-minute time resolution, which enables modeling the minute-by -minute behavior of a short-term storage option such as a steam accumulator.

Figure 39 illustrates the advantage of the steam accumulator. The figure shows solar-field collected power, solar-field power output (including 5-minute thermal inertia provided by the solar field), and power output with 30-minute steam accumulator storage. When clouds appear, the steam accumulator buffers the output to prevent rapid changes in steam supply. In Figure 39, the red line representing the 30-minute steam accumulator scenario clearly shows an advantage of providing a smooth power supply though cloudy periods. Even when the red line fluctuates, its ramping rate is constrained by the steam accumulator's response rate. Given the benefit of a smoother steam supply and requirement of a steam drum or accumulator in DSG systems, it is recommended that geothermal/solar hybrids in flash steam plants incorporate steam accumulators.

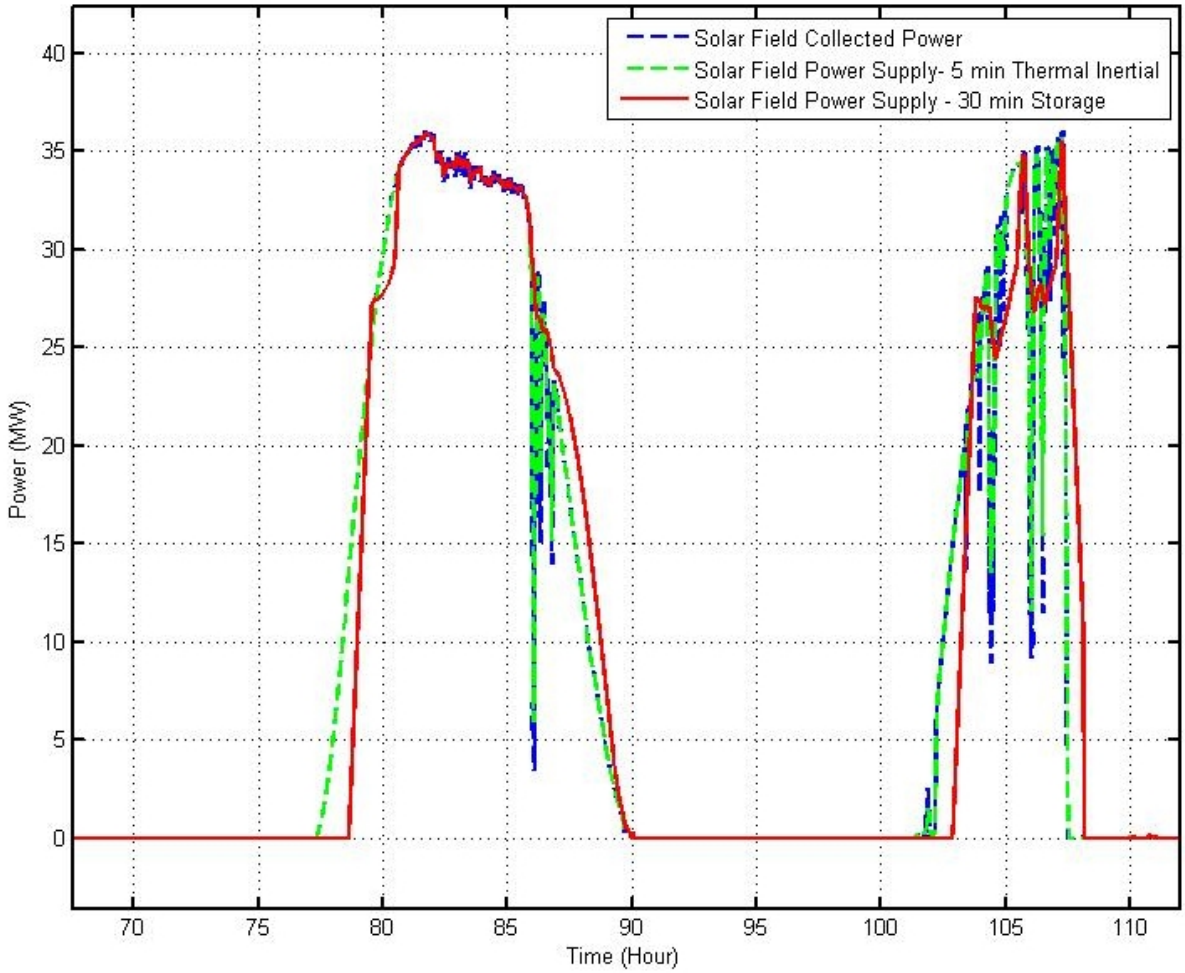

Figure 39. Solar-field thermal power output to power cycle for two days with pronounced solar insolation fluctuation.

5. Applicability

Solar thermal retrofit of a geothermal power plant with declining production fluid temperature can increase net power generation, especially during periods of high ambient temperature when air-cooled binary plant output is typically lowest. The quantity of additional power generation attributed to each unit of solar heat input increases as the production fluid temperature decreases since the solar heat input offsets the progressive degradation in power plant efficiency that occurs as the plant operating point deviates from the original design point. This results in increasing marginal solar efficiency the further the production fluid temperature has decreased from the original design point value.

This report computes the marginal LCOE for additional power generated from solar heat addition in brine preheating hybrid plant configurations as a function of total solar project costs. The marginal solar LCOE only accounts for the revenues and expenses associated with the retrofit of the solar-thermal equipment and does not account for the economics of the base power plant. In general, geo-solar hybrid plant retrofit strategy is increasingly favorable with higher electricity prices and lower solar field costs. Of the scenarios evaluated, the power plants with the higher production fluid design temperatures had higher design point thermal efficiencies, which permitted these plants to generate a greater quantity of power from each unit of solar energy input.

Figure 40 highlights the estimated LCOE of the current brine preheating hybrid design for the generic conditions of the contour plot (DNI = 7.0 kWh/m^2-day and annual solar-to-thermal collection efficiency = 50%). Also highlighted in the figure is the region of interest for "economic" hybrid designs, defined as an LCOE between $0.06 and $0.09/kWh. It is apparent from the figure that reductions in total hybridization cost (via reductions in solar hardware) and improved cycle efficiency are necessary for the hybrid designs to achieve viability across a large range of locations.

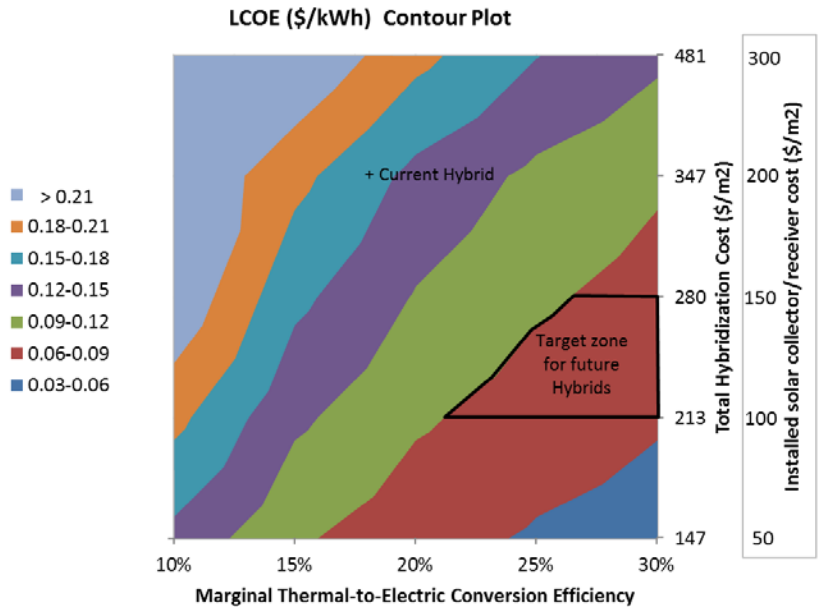

Figure 40. LCOE estimate for current hybrids and target conditions for future designs that can hit a market competitive price in the range of $0.06 to $0.09/kWh. The contour plot assumes DNI = 7.0 kWh/m^2-day, annual solar-to-thermal collection efficiency = 50%, and financial assumptions as provided in Appendix A.

Integrating solar thermal energy into an underutilized binary-cycle ORC raises the overall system efficiency by moving the power cycle back towards its design-point efficiency. Consequently the marginal thermal-to-electric efficiency of the solar energy can be significantly higher than the overall

hybrid or baseline plant efficiency. Nonetheless, with current solar collector costs the ability to cost-effectively integrate solar thermal energy into a geothermal power cycle is severely limited by the low thermal-electric conversion efficiency of the power cycle. In the current analysis, an installed solar array cost of $\$100/m^2$ (total hybridization cost = $\$213/m^2$) would approach an LCOE of \$0.10/kWh with the stated assumptions. Such a solar field is about half the cost reported for current commercial systems, while DOE cost reduction targets call for solar fields (installed collector/receiver system) in this range.

While the brine preheating hybrid design represents only one type of hybridization approach, the parametric results are not design specific and they indicate that, in addition to low-cost solar fields, broadly viable hybrid designs will require a much higher thermal-energy conversion efficiency than is possible with current ORCs operating at 150°C.

The solar heating of ORC working fluid was evaluated for greenfield hybrid applications. In order for the ORC working fluid hybrid plant to reduce stand-alone geothermal plant LCOE values by 5%, solar field costs in the range of $\$11/m^2$ to $\$100/m^2$ were required for level pricing schedules, while solar field costs in the range of $\$91/m^2$ to $\$182/m^2$ were required for TOD pricing schedules. The stand-alone geothermal plant base LCOE values upon which these LCOE reductions are based included the effects of geothermal resource productivity decline, and were calculated to be in the range of \$0.144/kWh to \$0.169/kWh. These values, which do not include any subsidies or incentives, are significantly above the \$0.06/kWh to \$0.09/kWh range of interest for "economic" designs. A 5% reduction in LCOE through use of hybrid technology would not result in LCOE decreases into this range of interest. While hybrid technology could likely be used to reduce the cost of power generation in applications with lower base LCOE values, the solar field costs required to do so would be lower than identified in this evaluation.

A goal for future hybrid plant designs would be application of a flexible power cycle that can operate off the low-temperature geothermal energy alone when necessary, but move to a higher-temperature, more efficient design point when high-temperature solar thermal energy is available. Integration of low-temperature geothermal energy for preheating in a high-temperature solar, biomass, or coal Rankine cycle is one approach than has shown merit in prior studies [5, 40]. These studies also identified that solar-power units would require thermal-energy storage if they were to utilize the geothermal resource at high annual capacity factor. While technically feasible, this would add cost to the hybridization equipment.

More sophisticated hybrid integration schemes offer the potential for higher efficiency operation. These designs require more intimate interaction between the two heat sources and may be most suited to greenfield systems. Effective deployment of these hybrid designs requires either consistent availability of both heat sources or a power system that can adjust between two operating points.

References

[1] M. Astolfi, L. Xodo, M. C. Romano, and E. Macchi, "Technical and economical analysis of a solar–geothermal hybrid plant based on an Organic Rankine Cycle," *Geothermics,* vol. 40, pp. 58-68, 2011.

[2] A. D. Greenhut, "Modeling And Analysis Of Hybrid Geothermal-Solar Thermal Energy Conversion Systems," Master of Science, Department of Mechanical Engineering, Massachussetts Institute of Technology, 2010.

[3] A. D. Greenhut, J. W. Tester, R. DiPippo, R. Field, C. Love, K. Nichols*, et al.*, "Solar-Geothermal Hybrid Cycle Analysis For Low Enthalpy Solar And Geothermal Resources," in *Proceedings World Geothermal Congress*, Bali, Indonesia, 2010.

[4] G. Manente, R. Field, R. DiPippo, J. W. Tester, M. Paci, and N. Rossi, "Hybrid Solar-Geothermal Power Generation To Increase The Energy Production From A Binary Geothermal Plant," in *Proceedings of the ASME 2011 International Mechanical Engineering Congress & Exposition*, Denver, Colorado, 2011.

[5] C. Zhou, E. Doroodchi, and B. Moghtaderi, "An in-depth assessment of hybrid solar–geothermal power generation," *Energy Conversion and Management,* vol. 74, pp. 88-101, 2013.

[6] Y. Alvarenga, S. Handal, and M. Recinos, "Solar Steam Booster in the Ahuachapan Geothermal Field," in *GRC Transactions*, 2008, pp. 395-399.

[7] N. Bezares, C. Augustine, and J. Tester, "Geothermal-Solar Hybrid for Continuous Steam Generation in Cerro Prieto, MX," in *American Institute of Chemical Engineers Annual Meeting*, 2008.

[8] S. Handal, Y. Alvarenga, and M. Recinos, "Geothermal steam production by solar energy," in *GRC Transactions*, 2007, pp. 503-510.

[9] Á. Lentz and R. Almanza, "Parabolic troughs to increase the geothermal wells flow enthalpy," *Solar Energy,* vol. 80, pp. 1290-1295, 2006.

[10] Á. Lentz and R. Almanza, "Solar–geothermal hybrid system," *Applied Thermal Engineering,* vol. 26, pp. 1537-1544, 2006.

[11] S. K. Sanyal, "Sustainability And Renewability Of Geothermal Power Capaciity," in *Proceedings World Geothermal Congress*, 2005.

[12] H. Price, E. Lüpfert, D. Kearney, E. Zarza, G. Cohen, R. Gee*, et al.*, "Advances in Parabolic Trough Solar Power Technology," *Journal of Solar Energy Engineering,* vol. 124, p. 109, 2002.

[13] Abengoa Solar Industrial Systems, "PT-1 Parabolic Trough Technical Description," 2013.

[14] A. Fernández-García, E. Zarza, L. Valenzuela, and M. Pérez, "Parabolic-trough solar collectors and their applications," *Renewable and Sustainable Energy Reviews,* vol. 14, pp. 1695-1721, 2010.

[15] SkyFuel Inc., "SkyTrough brochure," Arvada, Colorado, USA2011.

[16] Inventive Power. *Power Trough 110 brochure*. Available: www.inventivepower.com.mx

[17] K. Riffelmann, T. Richert, P. Nava, and A. Schweitzer, "Ultimate Trough® – A Significant Step towards Cost-competitive CSP," *Energy Procedia,* vol. 49, pp. 1831-1839, 2014.

[18] NEP Solar. (July 14, 2014). *PolyTrough 1200*. Available: http://www.nep-solar.com/products/polytrough-1200/

[19] G. Zhu, T. Wendelin, M. J. Wagner, and C. Kutscher, "History, current state, and future of linear Fresnel concentrating solar collectors," *Solar Energy,* vol. 103, pp. 639-652, 2014.

[20] G. Morin, J. Dersch, W. Platzer, M. Eck, and A. Häberle, "Comparison of Linear Fresnel and Parabolic Trough Collector power plants," *Solar Energy,* vol. 86, pp. 1-12, 2012.

[21] C. Turchi, "Parabolic Trough Reference Plant for Cost Modeling with the Solar Advisor Model (SAM)," National Renewable Energy Laboratory, Golden, Colorado, USA NREL/TP-550-47605, July 2010.

[22] A. Mason and E. Reitze, "Establishing Bankability for High Performance, Cost Reducing SkyTrough Parabolic Trough Solar Collector," *Energy Procedia,* vol. 49, pp. 155-162, 2014.

[23] P. Kurup and C. S. Turchi, "2015 Parabolic Trough Cost Update," National Renewable Energy Laboratory NREL/TP-xxxx-xxxxx, in press.
[24] D. Wendt, G. Mines, C. Turchi, G. Zhu, S. Cohan, L. Angelini, *et al.*, "Stillwater Hybrid Geo-Solar Power Plant Optimization Analysis," in *GRC Transactions*, Reno, NV, 2015, pp. 891-900.
[25] Engineering Page. *Heat Exchangers: Tentative sizing*. Available: http://www.engineeringpage.com/engineering/thermal.html
[26] National Renewable Energy Laboratory. *System Advisor Model (SAM) (2014-01-14 ed.)*. Available: https://sam.nrel.gov/
[27] National Energy Technology Center, "Process Equipment Cost Estimation," National Energy Technology Laboratory, Morgantown, WV DOE/NETL-2002/1169, 2002.
[28] Association for the Advancement of Cost Engineering, "AACE International Recommended Practice No. 16R-90, Conducting Technical and Economic Evaluations as Applied for Process and Utility Industries, TCM Framework: 3.2 Asset Planning, 3.3 Investment Decision Making," April 1991.
[29] National Energy Technology Laboratory, "Cost Estimation Methodology for NETL Assessments of Power Plant Performance," Morgantown, WV DOE/NETL-2011-1455, 2011.
[30] Energy Information Agency. (August 2015). *Natural Gas Summary, historic prices for industrial natural gas*. Available: http://www.eia.gov/dnav/ng/ng_sum_lsum_dcu_nus_a.htm
[31] D. S. Wendt and G. L. Mines, "Simulation of Air-Cooled Organic Rankine Cycle Geothermal Power Plant Performance," Idaho National Laboratory, Idaho Falls, ID INL/EXT-13-30173, 2013.
[32] I. Gunnarsson and S. Arnórsson, "Amorphous silica solubility and the thermodynamic properties of H4SiO°4 in the range of 0° to 350°C at Psat," *Geochimica et Cosmochimica Acta,* vol. 64, pp. 2295-2307, 2000.
[33] W. Short, D. J. Packey, and T. Holt, "A Manual for the Economic Evaluation of Energy Efficiency and Renewable Energy Technologies," National Renewable Energy Laboratory, Golden, ColoradoMarch 1995.
[34] U.S. Department of Energy, "Guide for Technology Roadmapping - DRAFT," Office of Energy Efficiency and Renewable Energy.
[35] X. Xie, K. Bloomfield, G. Mines, and G. Shook, "Design Considerations for Artificial Lifting of Enhanced Geothermal System Fluids," Idaho National Laboratory, Idaho Falls, Idaho INL/EXT-05-00533, July 2005.
[36] NREL. *System Advisor Model 2015.1.30*. Available: https://sam.nrel.gov/
[37] T. Hirsch, J. F. Feldhoff, K. Hennecke, and R. Pitz-Paal, "Advancements in the Field of Direct Steam Generation in Linear Solar Concentrators—A Review," *Heat Transfer Engineering,* vol. 35, pp. 258-271, 2013.
[38] D. H. Lobón and L. Valenzuela, "Impact of pressure losses in small-sized parabolic-trough collectors for direct steam generation," *Energy,* vol. 61, pp. 502-512, 2013.
[39] M. Mertins, E. Link, M. Tscheche, and H. Leuckel, "Experiences of Operation of 30 MW Solar Thermal Power Station Based on Fresnel Collector Technology," in *Proceedings of the SolarPACES 2012 International Conference*, Marrakech, Morocco, 2012.
[40] C. Turchi, G. Zhu, M. Wagner, T. Williams, and D. Wendt, "Geothermal / Solar Hybrid Designs: Use of Geothermal Energy for CSP Feedwater Heating," in *GRC Transactions*, 2014, pp. 817-823.
[41] W. Short, D. J. Packey, and T. Holt, "A Manual for the Economic Evaluation of Energy Efficiency and Renewable Energy Technologies," National Renewable Energy Laboratory, Golden, Colorado NREL/TP-462-5173, 1995.
[42] L. D. Boyko and G. N. Kruzhilin, "Heat Transfer and Hydraulic Resistance During Condensation of Steam in a Horizontal Tube and in a Bundle of Tubes," *Int. J. Heat and Mass Transfer,* vol. 10, pp. 361-373, 1967.

Appendix A

Levelized Cost Calculation

Appendix A
Levelized Cost Calculation

The LCOH and $LCOE_{solar}$ are calculated in a spreadsheet using the formulae for fixed charge rate (FCR) as described in SAM version 2015-06-30, which is based on reference [41]. The explanation below is excerpted from SAM's help menu. An example calculation is shown using the default values for the CSP parabolic trough model in SAM 2015-06-30.

Fixed Charge Rate Calculation for LCOE from SAM 2015-06-30.									
Assumptions									
analysis period	25	years							
inflation	2.5%	per year							
IRR	13%	per year							
Project debt fraction	50%	of CAPEX							
Nominal debt interest rate	7%	per year							
Effective tax rate	40%	per year							
Depreciation	20%	32%	20%	14%	14%	Enter percent of CAPEX for each year up to 5 years			
Annual construction cost sche	100%	0%	0%	Enter percent of CAPEX for each year up to 3 years (must sum to 100%)					
Nominal construction interes	8%	per year		Enter zero for no construction loan					
Calculated Values									
RROE	0.102439024	Real return on investment							
RINT	0.043902439	Real debt interest rate							
WACC	0.059512195	Weighted average cost of capital							
CRF	0.077864494	Capital recovery factor							
PVDEP	0.804964169	present value of depreciation							
PFF	1.130023887	Project financing factor							
CFF	1.023538291	Construction financing factor							
FCR	0.0901	fixed charge rate = CFR*PFF*CFF							
LCOH =	[(CAPEX)*FCR + (annual O&M)] / (Annual thermal generation)								

SAM's LCOE Calculator uses a simple method to calculate a project's levelized cost of energy (LCOE) using only the following inputs:

- Total Capital Cost, $ (TCC)
- Fixed annual Operating Cost, $ (FOC)
- Variable Operating Cost, $/kWh (VOC)
- Fixed Charge Rate (FCR)
- Annual electricity production, kWh (AEP)

The LCOE Calculator uses the following equation to calculate the LCOE:

$$LCOE = \frac{FCR \times TCC + FOC}{AEP} + VOC$$

The fixed charge rate is the revenue per amount of investment required to cover the investment cost. For details, see pp. 22-24 of reference [41]. This method is an alternative to the cash flow method used by SAM's other financial models. It is appropriate for very preliminary stages of project feasibility analysis before you have many details about the project's costs and financial structure. SAM does not contain a geothermal hybrid model, so direct use of SAM's other financial models is not possible.

Capital and Operating Costs

Capital cost

The project's total investment cost.

Fixed operating cost

Annual operating costs that do not vary with the amount of electricity the system generates.

Variable operating cost

Annual operating costs in dollars per kilowatt-hour that vary with the amount of electricity the system generates.

Summary

The Summary values are the inputs to the LCOE equation. These values are calculated from the inputs you specify.

Fixed charge rate

The project fixed charge rate, or revenue per amount of investment required to cover the investment cost. Calculated from the financial details you enter.

Capital cost

The total overnight investment cost in dollars.

Fixed operating cost

The fixed annual operating cost in dollars. It is either the value you enter or a value that SAM calculates based on the value you enter in dollars per kilowatt.

Variable operating cost

The variable annual operating cost in dollars per kilowatt-hour that you enter.

Financial Assumptions

The fixed charge rate represents details of the project's financial structure.

Calculate fixed charge rate

SAM calculates the fixed charge rate from a set of financial assumptions. SAM uses the following equation to calculate the value from the capital recovery factor, project financing factor, and construction financing factor (see below for all equations):

$$\mathrm{FCR} = \mathrm{CRF} \times \mathrm{PFF} \times \mathrm{CFF}$$

Fixed charge rate

The project's fixed charge rate. Note that the value is a factor (between 0 and 1) rather than a percentage.

Analysis period

The number of years that the project will generate electricity and earn revenue.

Inflation rate

The annual inflation rate over the analysis period.

Internal rate of return

The project's annual rate of return requirement.

Project term debt

The size of debt as a percentage of the capital cost.

Nominal debt interest rate

The annual nominal debt interest rate. SAM assumes that the debt period is the same as the analysis period.

Effective tax rate

The total income tax rate. For a project that pays both federal and state income taxes, where the state income tax is deducted from the federal tax, you can calculate the effective tax rate as:

$$TAX = STATE + FED \times (1\text{-}STATE)$$

Depreciation schedule

The annual depreciation schedule. The depreciation basis equals the project's capital cost.

Annual cost during construction

The annual construction cost as a percentage of the project's capital cost. If the construction period is one year or less, enter a single value. If it is more than one year, enter a schedule of annual percentages.

Nominal construction interest rate

The annual interest rate on construction financing.

Capital recovery factor (CRF)

SAM calculates this value from the inputs you specify as described below.

Project financing factor (PFF)

Factor to account for project financing costs. SAM calculates this value from the effective tax rate and depreciation schedule, as described below.

Construction financing factor (CFF)

Factor to account for construction financing costs. SAM calculates the value from the construction cost schedule, effective tax rate, and construction interest rate, as described below.

Equations for FCR Calculation

When you use the **Calculate fixed charge rate** option, SAM uses the following equations to calculate the financing factors.

Nomenclature

c = Construction year

C = Construction period in years

CON = Construction schedule

DF = Project term debt fraction

i = Inflation rate

n = Analysis year

N = Analysis period

IRR = Nominal return on investment

NINT = Nominal debt interest rate

PVDEP = Present value of depreciation

RINT = Real debt interest rate

RROE = Real return on investment

TAX = Effective tax rate

WACC = Weighted average cost of capital (real)

The capital recovery factor (CRF) is a function of the weighted average cost of capital (WACC) and analysis period (N):

$$CRF = \frac{WACC}{1 - \frac{1}{(1+WACC)^N}}$$

Where:

$$WACC = \frac{1 + \left((1-DF) \times \left((1+RROE) \times (1+i) - 1\right)\right) + DF \times \left((1+RINT) \times (1+i) - 1\right) \times (1-TAX)}{1+i} - 1$$

$$RROE = \frac{1 + IRR}{1 + i} - 1$$

$$RINT = \frac{1 + NINT}{1 + i} - 1$$

The project financing factor (PFF) is a function of the effective tax rate and depreciation schedule:

$$PFF = \frac{1-TAX \times PVDEP}{1-TAX}$$

Where:

$$PVDEP = \sum_{n=0}^{N} \frac{DEP_n}{\left((1+WACC) \times (1+i)\right)^{(n+1)}}$$

The construction financing factor (CFF) is a function of the construction cost schedule, effective tax rate, and nominal construction financing interest rate:

$$CFF = \sum_{c=0}^{C} CON_c \times \left(1 + (1-TAX) \times \left((1+CINT)^{(c+0.5)} - 1\right)\right)$$

Appendix B

Using SAM's Physical Trough Model without a Power Cycle

Geothermal Risk Reduction via Geothermal/Solar Hybrid Power Plants

Q2 FY15 Milestone Report:
Parabolic Trough Solar-Thermal Output Model
Decoupled from SAM Power Block Assumptions

Prepared For:

The Geothermal Technologies Office
U.S. Department of Energy – Office of Energy Efficiency and Renewable Energy

March 31, 2015

Prepared By:
Craig Turchi and Ty Neises

NREL
NATIONAL RENEWABLE ENERGY LABORATORY

INTRODUCTION

Geothermal/Solar-thermal hybrid systems integrate two different renewable energy technologies that share the common feature of converting thermal energy into electric power. However, the two technologies have different time-dependent performance and thermal capabilities. Solar thermal systems collect energy during hours with good direct normal insolation (DNI). These systems may incorporate thermal energy storage, for example, by collecting a hot heat transfer fluid (HTF) in an insulated tank for later use. In contrast, geothermal systems have the ability to operate continuously.

The effective modeling of hybrid geothermal/solar-thermal facilities requires accurate modeling of each of the subsystems as well as their integrated design. As reported in prior work, NREL and Idaho National Laboratory (INL) have performed such analyses using a combination of NREL's System Advisor Model (SAM), Excel spreadsheets, and ASPEN simulation code [Turchi et al., 2014, Wendt & Mines, 2014].

While SAM is a state-of-the-art simulation package for concentrating solar power (CSP) systems, the use of SAM for modeling geothermal/solar-thermal hybrid systems is complicated by the fact that SAM's solar-thermal models are provided within systems that include a steam-Rankine power block. The user must understand the complexities added by the included steam power cycle is order to extract model results that are relevant for the case where the solar field is only providing thermal energy.

The objective of this milestone is to simplify access to SAM's powerful solar thermal collector/receiver models so that results from SAM can be used by a wider audience to simulate the solar thermal contribution to geothermal/solar-thermal hybrid systems.

APPROACH

NREL began analysis of the solar field at Enel Green Power's Stillwater Geothermal Plant in fall 2014 using SAM 2014-01-14. This work is part of the Geothermal Technologies Office task *2.5.4.2 Geothermal Risk Reduction via Geothermal/solar Hybrid Power Plants* and a CRADA between Enel, NREL, and INL. A simple representation of the hybrid integration at Stillwater is provided in Figure 1. The design employs 24,778 m^2 of parabolic troughs arranged in 11 loops. Because of the land area at Stillwater, the loops consist of two 115-m SCAs plus two shorter, 86-m SCAs. The troughs are 6-m aperture SkyTroughs supplied by SkyFuel of Arvada, CO. The specific hardware dimensions and operating conditions were set up in a SAM 2014-01-14 case file.

The release of SAM 2015-01-30, a major update from the 2014 version, required recreation of the Stillwater case. Important revisions to SAM in 2015 include greater customization capabilities and a new interface. The update required recoding SAM into C++ to allow provide faster simulation times and use of multicore, parallel processing. Three different cases were made in the new version of SAM:

1) SAM's default Physical Trough model with solar field, collector, and receiver inputs adjusted to represent the Stillwater field,
2) The inputs as in Case (1) plus modifying SAM's Power Cycle page in an effort to avoid having the power cycle code interfere with simulation of the solar field, and

3) The inputs as in Case (1) exported to TCS Console, an NREL software tool that allows manipulation of the core performance code for the Physical Trough model, so that the solar field components could be modeled in the absence of any power cycle.

These simulations proceed in increasing order of sophistication with respect to the understanding of SAM and represent what might be undertaken by a novice SAM user, a frequent SAM user, and an advanced SAM user, respectively. Our goal is to provide the best simulation from SAM with the least required knowledge on the part of the user in order to make SAM more accessible for geothermal/solar-thermal hybrid analysis.

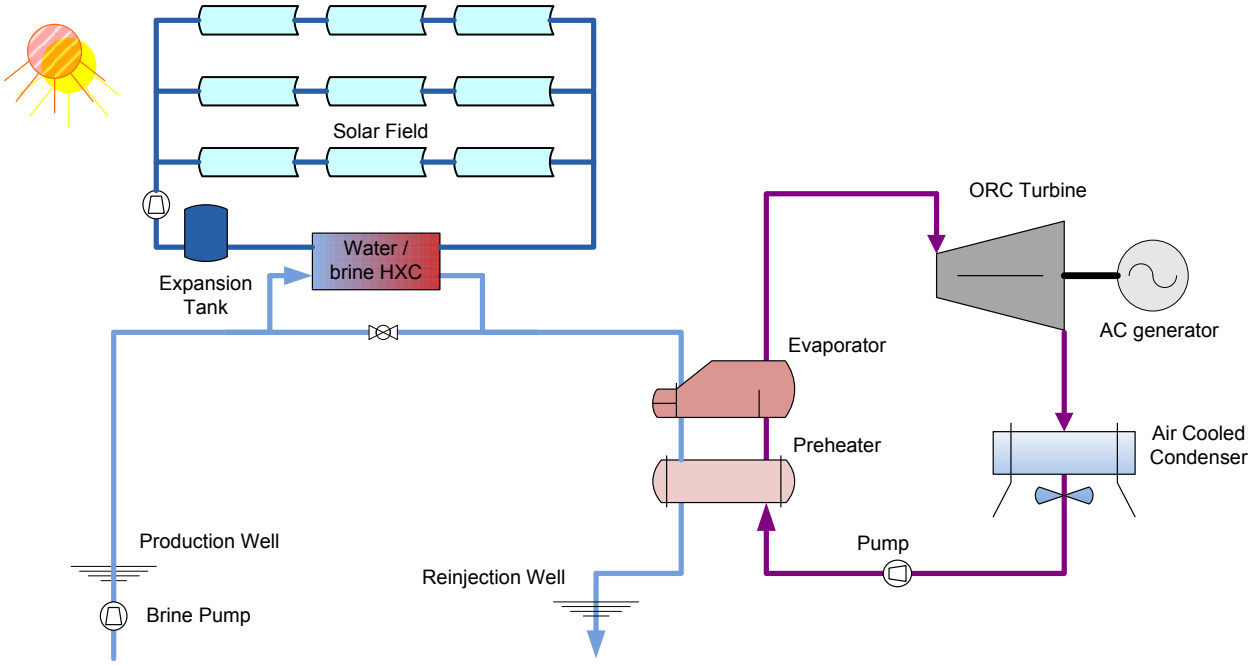

Figure 1. Geothermal/Solar-thermal hybrid configuration similar to that employed at Stillwater.

RESULTS

A comparison of SAM's annual *Field Thermal Power Produced* for the three cases is provided in Table 1. This is one of SAM's output variables for solar field performance and represents the predicted thermal energy from the solar field HTF after accounting for incoming DNI and optical and thermal losses in the solar field. Table 1 also shows the total thermal energy incident on the solar field aperture area, the total thermal energy absorbed by the solar field, and energy dumped due to forced defocusing of the solar field.

Table 1. Relevant annual solar field performance estimates from different cases. Running the solar collector code without any power cycle interference (Case 3) is required to obtain the best estimate of thermal energy potential.

Annual thermal energy estimates (MWh-th)	Case (1) Solar Field with SAM's default power cycle	Case (2) Solar Field with power cycle input changes in SAM	Case (3) Stand-alone trough modeled via TCS Console
Field thermal power incident	76,120	76,120	76,120
Field thermal power dumped	31	518	0
Field thermal power produced	35,506	38,988	41,465
Estimated generation (relative)	85.6%	94.0%	100%

The simplest way to use SAM to simulate the thermal output from a parabolic trough field is to open a default case of the Physical Trough Model and adjust the Location and Resource and solar field settings via the Solar Field, Collectors (SCAs), and Receivers (HCEs) pages to model the size and hardware details of the field in question (see Figure 2). However, as is apparent from Table 1, if the SAM user simply runs the default Physical Trough Model in this fashion without addressing the default Power Cycle inputs, SAM will underestimate energy production. It is also possible the model will not even run due to a mismatch in power cycle and solar field properties. These errant results are due to SAM trying to "force fit" the specified solar field and power cycle parameters.

Case (2) addresses many of these concerns by adjusting Power Cycle inputs to minimize the influence of the power cycle code on the solar field performance. This results in a case with less potential for convergence errors and a better estimate of the potential output from the solar field. The specific recommended changes for this case are outlined in Table 2.

Finally, Case (3) removes the Physical Trough code completely from the SAM interface and runs the code within NREL's TCS Console environment. TCS Console was developed by NREL to allow manipulation of the model systems originally developed the TRNSYS FORTRAN format. For this work, NREL developed a script within TCS Console that separates the power block controller functions from the solar field performance model and allows for recirculation of the solar field HTF as necessary.

Running the Physical Trough model in this fashion avoids any conflict with the power cycle code and provides a clean estimate of parabolic trough performance. However, the process is more complex than simply adjusting inputs within SAM's Graphical User Interface, and requires access to NREL's TCS Console tool. Instructions for extraction and use of the Physical Trough model are provided in the Appendix.

While this report documents a procedure to access accurate predictions from the Physical Trough model in the absence of a steam power cycle, the use of TCS Console is cumbersome and not a long-term solution. TCS Console was an interim fix for NREL programmers and is not intended as a public-use tool. Recognizing the need for access to SAM's collector/receiver models and the limitations of the procedure described here, NREL has proposed to develop a more intuitive SAM-based interface for accessing these tools in FY16. This request has been included in a proposal to the DOE Solar Program.

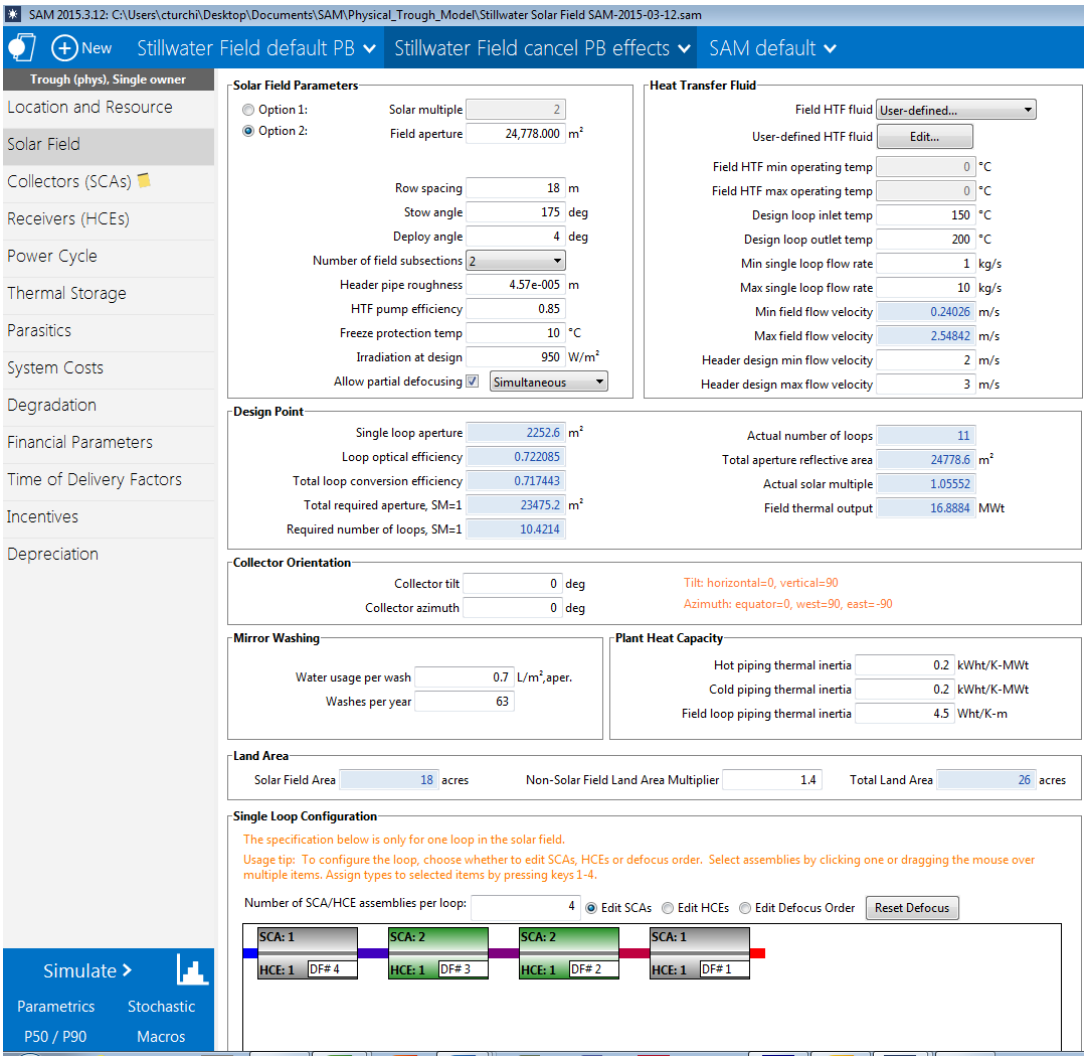

Figure 2. Solar Field inputs page in the Physical Trough Model in SAM 2015-03-12.

Table 2. Changes to SAM's Power Cycle inputs page to minimize power cycle influence over the solar field performance. If thermal storage is used, additional adjustments need to be made on the Thermal Storage page.

Power Cycle page Input	SAM default	Recommended change
Design gross output	111	Set equal to thermal power rating of solar field
Estimated gross to net conversion factor	0.9	no change
Availability and Curtailment inputs	various	no change
Rated cycle conversion efficiency	0.3774	1.0
Boiler operating pressure	100	set equal to saturated steam pressure at solar field outlet temp
Steam cycle blowdown fraction	0.02	no change
Fossil backup boiler LHV efficiency	0.9	no change
Aux heater outlet set temp	391	set equal to solar field outlet temp
Fossil dispatch mode	Min backup level	no change
Low resource standby period	2	no change
Fraction of thermal power needed for startup	0.2	0
Power block startup time	0.5	0
Minimum required startup temp	300	set equal to solar field inlet temp
Max turbine over design operation	1.05	2
Min turbine operation	0.25	0.02
Turbine inlet pressure control	Fixed Pressure	no change
Cooling System inputs	various	no change

CONCLUSIONS AND RECOMMENDATIONS

SAM's normal interface can be used to estimate parabolic trough performance for solar-thermal applications if one takes a number of steps to minimize the influence of the power cycle simulation requirements on the solar field. For the Stillwater solar field, skipping these steps results in solar field thermal-energy generation estimates that are 85% below values estimated without interference from the power cycle component model. Making a series of adjustments to SAM's default power cycle inputs improved the estimate to be within 94% of the estimated stand-alone solar field value.

For initial performance estimates, creating a case with SAM and minimizing the influence of the power cycle by the methods outlined in this report is probably sufficient. For more detailed analysis, stand-alone-trough model estimates can be developed via NREL's TCS Console environment following the process outlined in the Appendix. However, performing this analysis requires requesting access to TCS Console from NREL. TCS Console was not written as a public software tool and lacks usability features and documentation.

Recognition of this limitation has led to a FY16 proposal within the CSP program to modify SAM to allow for easier access to the solar field performance codes within SAM's user-friendly interface. Such a change will promote greater use of SAM of thermal-energy production in geothermal hybrids and for other thermal-energy applications.

Lastly, while this report deals specifically with the Physical Trough model, the same procedures would apply to SAM's linear Fresnel models.

REFERENCES

C. Turchi, G. Zhu, M. Wagner, T. Williams, and D. Wendt, "Geothermal / Solar Hybrid Designs: Use of Geothermal Energy for CSP Feedwater Heating," Geothermal Resources Council 38th Annual Meeting, Portland, Oregon, Sept 28 to Oct 1, 2014.

D.S. Wendt and G.L. Mines, "Use of a Geothermal-Solar Retrofit Hybrid Power Plant to Mitigate Declines in Geothermal Resource Productivity," Geothermal Resources Council 38th Annual Meeting, Portland, Oregon, Sept 28 to Oct 1, 2014.

Download site for System Advisor Model (SAM): https://sam.nrel.gov/

Download site for SAM's software development kit (SDK) tools: https://sam.nrel.gov/content/sam-simulation-core-sdk

APPENDIX

The set of inputs from SAM's Input Browser is provided in the following two tables. The Inputs Browser only shows values that differ from the default inputs in SAM-2015-03-12. The User-defined HTF is pressurized water, but the actual physical properties are not shown here.

Variable	Label	SAM default	Stillwater Field default PB	Stillwater Field cancel PB effects
IAMs_1	Incidence angle modifier coefficients	1;0.0506;-0.1763	1;0.0327;-0.1351;0	1;0.0327;-0.1351;0
P_boil	Boiler operating pressure	100	100	15
Row_Distance	Row spacing	15	18	18
SCA_drives_elec	Tracking power	125	68	68
T_amb_des	Ambient temp at design	20	25	25
T_fp	Freeze protection temp	150	10	10
T_loop_in_des	Design loop inlet temp	293	150	150
T_loop_out	Design loop outlet temp	391	200	200
T_set_aux	Aux heater outlet set temp	391	391	200
T_startup	Minimum required startup temp	300	300	150
T_tank_cold_ini	Initial TES fluid temp	300	100	100
cold_tank_Thtr	Cold tank heater set point	250	25	25
collector_library	Collector library	Solargenix SGX-1	SkyFuel SkyTrough (Manufacturer	SkyFuel SkyTrough (Manufacturer
combo_htf_type	Field HTF fluid	Therminol VP-1	User-defined...	User-defined...
combo_tes_htf_type	Storage HTF fluid	Hitec Solar Salt	User-defined...	User-defined...
const_per_months1	Construction Loan 1 months	24	6	6
csp.dtr.cost.bop_per_kwe	Balance of Plant Cost per kWe	110	0	0
csp.dtr.cost.epc.percent	EPC Costs % direct	11	25	25
csp.dtr.cost.htf_system.cost_per_m2	HTF System Cost Per m2	80	40	40
csp.dtr.cost.plm.per_acre	Land Cost acre	10000	0	0
csp.dtr.cost.power_plant.cost_per_kwe	Power Plant Cost per kWe	830	0	0
csp.dtr.cost.site_improvements.cost_p	Site Improvement Cost per m2	30	10	10
csp.dtr.cost.solar_field.cost_per_m2	Solar Field Cost per m2	270	200	200
csp.dtr.cost.storage.cost_per_kwht	Storage System Cost per kWht	80	0	0
csp_dtr_hce_diam_absorber_inner_1	Absorber tube inner diameter	0.066	0.076	0.076
csp_dtr_hce_diam_absorber_outer_1	Absorber tube outer diameter	0.07	0.08	0.08
csp_dtr_hce_notify_text_1	Receiver name from library	Schott PTR70 2008	Schott PTR80	Schott PTR80
csp_dtr_hce_var1_abs_abs_1	Variation 1 Absorber Absorptance	0.96	0.963	0.963
csp_dtr_hce_var1_bellows_shadowing	Variation 1 Bellows Shadowing	0.96	0.935	0.935
csp_dtr_hce_var1_env_trans_1	Variation 1 Envelope Transmittance	0.963	0.964	0.964
csp_dtr_hce_var1_hce_dirt_1	Variation 1 Dirt on receiver	0.98	0.975	0.975
csp_dtr_hce_var1_rated_heat_loss_1	Variation 1 Rated Heat Loss	150	31	31
csp_dtr_hce_var2_env_trans_1	Variation 2 Envelope Transmittance	0.963	0.964	0.964
csp_dtr_hce_var2_field_fraction_1	Variation 2 Field Fraction	0.01	0.015	0.015
csp_dtr_hce_var2_rated_heat_loss_1	Variation 2 Rated Heat Loss	1100	245	245
csp_dtr_hce_var3_bellows_shadowing	Variation 3 Bellows Shadowing	0.96	0.935	0.935
csp_dtr_hce_var3_field_fraction_1	Variation 3 Field Fraction	0.005	0	0
csp_dtr_sca_aperture_1	Reflective aperture area	470.3	656	656
csp_dtr_sca_ave_focal_len_1	Average surface-to-focus path length	1.8	2.15	2.15
csp_dtr_sca_ave_focal_len_2	Average surface-to-focus path length	1.8	2.15	2.15
csp_dtr_sca_clean_reflectivity_1	Mirror reflectance	0.935	0.93	0.93
csp_dtr_sca_clean_reflectivity_2	Mirror reflectance	0.935	0.93	0.93
csp_dtr_sca_general_error_1	General optical error	0.99	1	1
csp_dtr_sca_general_error_2	General optical error	0.99	1	1
csp_dtr_sca_geometry_effects_1	Geometry effects	0.98	0.952	0.952
csp_dtr_sca_geometry_effects_2	Geometry effects	0.98	0.952	0.952
csp_dtr_sca_length_1	Length of collector assembly	100	115	115
csp_dtr_sca_length_2	Length of collector assembly	100	86	86
csp_dtr_sca_mirror_dirt_1	Dirt on mirror	0.95	0.975	0.975
csp_dtr_sca_mirror_dirt_2	Dirt on mirror	0.95	0.975	0.975
csp_dtr_sca_ncol_per_sca_1	Number of modules per assembly	12	8	8
csp_dtr_sca_ncol_per_sca_2	Number of modules per assembly	12	6	6

Variable	Label	SAM default	Stillwater Field default PB	Stillwater Field cancel PB effects
csp_dtr_sca_notify_text_1	Collector name from library	Solargenix SGX-1	SkyTrough (Manufacturer Specifications)	SkyTrough (Manufacturer Specifications)
csp_dtr_sca_notify_text_2	Collector name from library	Solargenix SGX-1	SkyTrough (Manufacturer Specifications)	SkyTrough (Manufacturer Specifications)
csp_dtr_sca_tracking_error_1	Tracking error	0.994	0.988	0.988
csp_dtr_sca_tracking_error_2	Tracking error	0.994	0.988	0.988
csp_dtr_sca_w_profile_1	Aperture width total structure	5	6	6
csp_dtr_sca_w_profile_2	Aperture width total structure	5	6	6
cycle_cutoff_frac	Min turbine operation	0.25	0.25	0.02
cycle_max_frac	Max turbine over design operation	1.05	1.05	2
dispatch_factor1	Energy Payment Factor 1	2.064	1	1
dispatch_factor2	Energy Payment Factor 2	1.2	1	1
dispatch_factor4	Energy Payment Factor 4	1.1	1	1
dispatch_factor5	Energy Payment Factor 5	0.8	1	1
dispatch_factor6	Energy Payment Factor 6	0.7	1	1
eta_ref	Rated cycle conversion efficiency	0.3774	0.3774	1
field_fl_props	User-defined HTF fluid	[0]	user-defined	user-defined
hot_tank_Thtr	Hot tank heater set point	365	190	190
m_dot_htfmax	Max single loop flow rate	12	10	10
om_capacity	Fixed cost by capacity	65	30	30
pb_rated_cap	Design gross output	111	111	16
q_sby_frac	Fraction of thermal power needed for s	0.2	0.2	0
receiver_library	Receiver Library	Schott PTR70 2008	Schott PTR80	Schott PTR80
specified_total_aperture	Field aperture	877000	24778	24778
startup_frac	Fraction of thermal power needed for s	0.2	0.2	0.01
startup_time	Power block startup time	0.5	0.5	0
store_fl_props	User-defined HTF fluid	[1]	user-defined	user-defined
tank_max_heat	Tank heater capacity	25	1	1
theta_dep	Deploy angle	10	4	4
theta_stow	Stow angle	170	175	175
tod_library		Generic Summer Peak	Uniform Dispatch	Uniform Dispatch
tshours	Full load hours of TES	6	0	0

Instructions to use the stand-alone use of SAM's Physical Trough model.

1) These Instructions assume the work is saved in a folder called *Physical_Trough_Model*
2) Use the 2015-03-12 (or the latest) versions of SAM and SDK. These can be downloaded at https://sam.nrel.gov/
3) Set up SAM simulation
    a. Open SAM and select the Physical Trough model with any financing model.
    b. Configure inputs to define the solar field you want to simulate. Most of the relevant inputs are on the Solar Field, Collector, and Receiver pages.
    c. Select "Shift + F5". This creates a text file titled 'ssc-tcstrough_physical.lk'
    d. Save this file to the *Physical_Trough_Model* folder.
4) Move 'tcsconsole.exe' from the *Physical_Trough_Model* folder to the folder containing SDK\win32. The new location should also contain 'sdktool.exe'.
5) Open 'tcsconsole.exe' from the SDK\win32 folder.
6) In the TCS Console, select the Script Editor tab at the top of the window. Select the 'Open' button and select 'Physical trough stand alone from SSC script.lk'
7) Within 'Physical trough stand alone from SSC script.lk' there are two variables pointing to file paths that need to be defined. (Note that '/' must be used when defining paths rather than '\')
    a. 'data_directory' should point to the full path for *Physical_Trough_Model* folder
    b. 'ssc_lk' should point to the file 'ssc-tcstrough_physical.lk'
    c. 'trough_csv' should point to 'input_data.csv' containing necessary input data. See input data formatting instructions below.
    d. The script is designed to extract Physical Trough inputs from 'ssc-tcstrough_physical.lk' Do not modify this .lk file. If you wish to change SAM variable values, change variables in the SAM UI and repeat the process to create a new .lk file.
    e. Save these changes.
8) Select 'Run'. Output data is available in the 'Data Tables' tab.
    a. The thermal energy produced by the solar field is given by variable *q_avail (MWt)* This is denoted in SAM time series data as *Field thermal power produced (MWt)*

Input Data File Instructions

The input data file (in .csv format) should contain input data for consecutive, evenly spaced timesteps. The following is a list and brief description of each required input. Note that typical weather files give instantaneous temperature, wind speed, and ambient pressure measurements corresponding to the hour of the day, while the irradiance values are averaged over the entire hourly timestep. SAM evaluates at the midpoint of the timestep. Therefore, the irradiance values aren't adjusted, but the other values are averaged with the previous timestep's value. This explains why SAM's temperature, wind speed, and ambient pressure hourly outputs don't exactly match the weather file values.

hr [hr, standard time]: Hour of the year at the *end* of the timestep for which data is provided. For example, if the data represent 10 minutes of measured data from 10:55 to 11:05, then the value should be 11:05 (11.083 on January 1). The simulation code uses this value and the simulation timestep (10 minutes) to calculate the midpoint at which solar position is calculated.

I_b [W/m2]: Beam irradiance.

T_db [C]: Dry bulb temperature.

V_wind [m/s]: Wind speed.

P_amb [mbar]: Ambient air pressure. If this measurement is not available, a constant value can be estimated using an equation found on Engineering Toolbox: http://www.engineeringtoolbox.com/air-altitude-pressure-d_462.html.

T_dp [C]: Dew point temperature. The performance calculations use this value to estimate the Sky Temperature that is used in radiation loss calculations. If this measurement is not available, the input value should be set to -1000 C, and the code estimates the Sky Temperature as T_db – 20 C.

T_cold_in [C]: Inlet temperature to the field.

latitude, longitude, and shift [deg]: Coordinates of the location. Shift is the difference between the site longitude and the longitude corresponding to the time zone of the location.

One can check that these inputs are properly read by displaying the variable in the Data Tables tab of TCSconsole. Select the "output" version of the variable name, which is the variable preceded by an O_ as shown in the figure below:

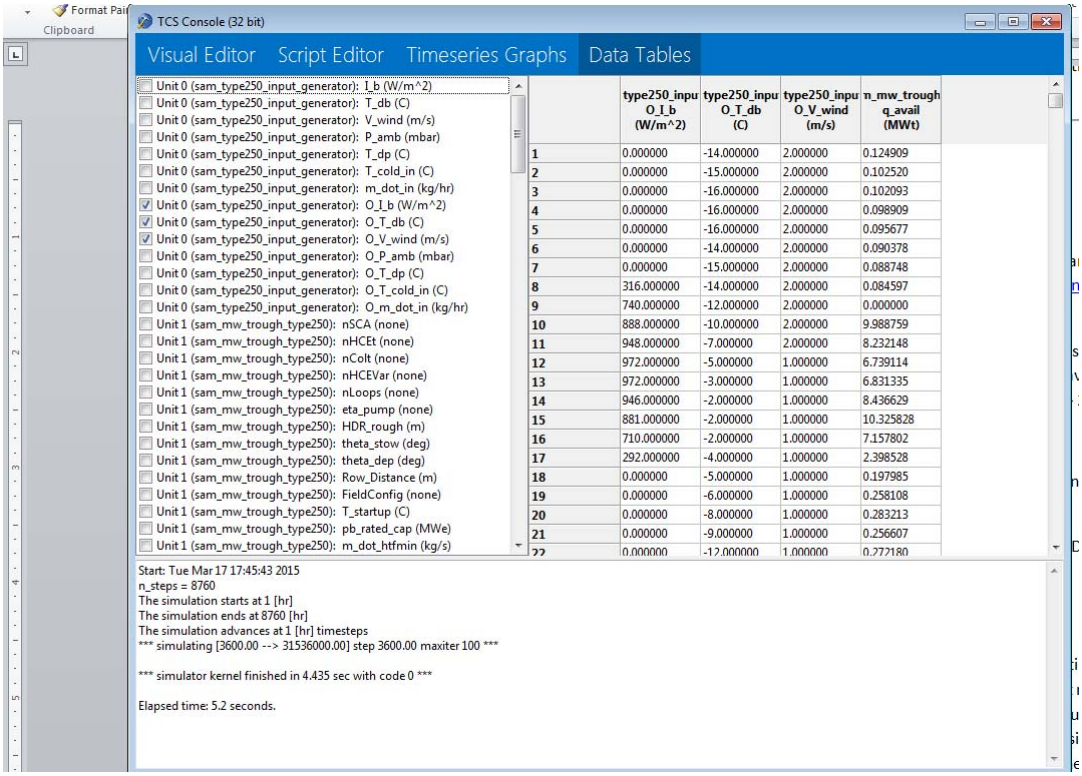

Appendix C

Stillwater Geothermal/Solar-Thermal Solar Field Characterization Analysis

Solar Field Optical Characterization at Stillwater Geothermal / Solar Hybrid Plant

Guangdong Zhu, Craig Turchi

National Renewable Energy Laboratory
15013 Denver West Parkway
Golden, CO 80401
United States
Email: Guangdong.Zhu@nrel.gov

Abstract

Concentrating solar power (CSP) can provide additional thermal energy to boost geothermal plant power generation. For a newly constructed solar field at a geothermal power plant site, it is critical to properly characterize its performance so that the prediction of thermal power generation can be derived to develop an optimum operating strategy for a hybrid system. In the past, laboratory characterization of a solar collector has often extended into the solar field performance model and has been used to predict the actual solar field performance, disregarding realistic impacting factors. This work is the first time that an extensive measurement on mirror slope error and receiver position error has been performed in the field by using the optical characterization tool called Distant Observer (DO). Combining a solar reflectance sampling procedure, a newly developed solar characterization program called FirstOPTIC and public software for annual performance modeling called System Advisor Model (SAM), a most comprehensive solar field optical characterization has been conducted, thus allowing an informed prediction of solar field annual performance. The paper illustrates this detailed solar field optical characterization procedure and demonstrates how the results help to quantify an appropriate tracking-correction strategy to improve solar field performance. In particular, it is found that an appropriate tracking-offset algorithm can improve the solar field performance by about 15%. The work here provides a valuable reference to the growing CSP industry.

Keywords: concentrating solar power, geothermal energy, parabolic trough, optical characterization, optical error, hybrid system

1. Introduction

Concentrating solar power (CSP) uses mirrors to concentrate sunlight and convert solar power into heat, which can then be directed to a thermodynamic cycle to generate electricity [1-4]. As a mature CSP technology, parabolic troughs can produce heat at a temperature of 400 °C or higher [2, 5] and generate electricity through a standalone power plant. In addition, the produced heat can be hybridized naturally with other types of heat sources to produce electricity, such as integrated solar combined-cycle [6, 7] and geothermal/solar hybrid systems [8]. For the latter concept, adding solar heat from CSP to a geothermal power plant can boost power generation during the daytime, when the increasing ambient temperature and/or degrading geothermal resource result in lower power production.

The Stillwater geothermal plant located in Nevada is an example of a geothermal operation where EGP has recently adopted solar hybridization [9, 10]. The solar field is about 17 MWth at the design point and uses SkyTrough parabolic trough collectors [11, 12]. The heat-transfer fluid (HTF) in the trough receiver is pressurized water, and the design HTF inlet and outlet temperatures are about 150 °C and 200 °C, respectively. The heated HTF is used to heat the brine flow with a degraded temperature.

A key task is to properly characterize the performance of the new Stillwater solar field. Optical characterization of a utility-scale solar field is a broad topic. SolarPACES has developed multiple international guidelines on solar mirror reflectance [13, 14] and solar system annual modeling [15-17] that provide guidance to the growing CSP industry. No guidelines exist regarding optical characterization of the solar field. One major reason is that a variety of optical tools exist and each has its limitations regarding measurement results and conditions [18-23]. Most tools are designed to measure one specific type of optical error, such as mirror specular reflectance [13], mirror slope error [18, 19, 22, 23], or receiver temperature [24-26]. Furthermore, very few tools are suitable for use in the field. Past work has predicted solar field performance based on laboratory measurement; such prediction inappropriately disregards the deviation of a solar collector from its design-point performance measured in the laboratory.

To fully characterize the optical performance of a solar field, one needs to obtain precise optical and geometric measurements of solar collectors in the field, including mirror specular reflectance, receiver absorptance and receiver glass-envelope transmittance, mirror slope error, receiver position error, and collector tracking error. Among these, mirror slope error has been considered the dominant error source [27, 28]. Other error sources, such as mirror reflectance, receiver absorptance, and receiver position error, could also significantly impact the collector performance, depending on specific cases [29]. In this work, mirror specular reflectance, mirror slope error, and receiver position error were measured in the field to best predict the actual solar field performance. Mirror reflectance measurements use a newly developed specular reflectance model, and mirror slope error and receiver position error measurements use a newly developed optical tool called Distant Observer (DO) [30, 31]. DO is one of the very few tools suitable for outdoor field environments.

The focus of this paper is to: 1) exhibit a comprehensive and accurate field optical characterization by using state-of-the-art models and tools, which will provide valuable guidance to future field optical characterization work; and 2) employ an optical model and thermal performance model to predict annual thermal energy production as a function of time. The modeling of a geothermal/solar thermal hybrid system is a separate work and can be found elsewhere [9].

In this paper, Section 2 gives the optical test plan. Sections 3 and 4 present and discuss in detail the solar reflectance measurements and collector optical error measurements, respectively. Sections 5 and 6 provide calculations of the overall optical performance and annual energy generation of the solar field, based on the optical measurement results. Finally, discussion and conclusions are given in Section 7 and 8.

2. Optical Test Plan

The optical tools used in this field optical test are summarized in Table **1**. By using these tools, measurements of mirror specular reflectance, mirror slope error, and receiver position error can be

conducted in the field. The solar field at the Stillwater geothermal/solar plant includes eleven SkyTrough collector loops, each of which consists of four solar collector assemblies (SCAs). Each SCA includes eight solar collector elements/modules (SCEs), about 110 meters long and 6 meters in aperture width. The solar field layout is a standard row-to-row formation.

Table 1: Technical specifications of optical test tools used in this study

Instrument	Manufacturer	Measured Parameters	Specifications
410-Solar	Surface Optics Corporation, Inc. [32]	Solar-weighted hemispherical reflectance Solar-weighted total specular reflectance (6° half aperture)	Incidence 20° Wavelengths: seven bands Rechargeable battery (standard NiMH 2 h) Data format: spreadsheet
D&S 15 R	Devices and Services Company [33]	Specular reflectance at 15, 25, and 46 mrad. An optional 7 mrad aperture could replace 46 mrad.	Incidence 15° Wavelength: 660 nm Repeatability: 0.002 reflectance unit Rechargeable battery (Nicad 15 h)
Distant Observer (DO)	NREL under DOE funds	Mirror slope error: transversal direction Receiver position error: two directions in transversal plane	Major components: High-precision camera Photogrammetry-based program

The objective of the optical test is to obtain the average optical performance of the solar field. In reality, it is not possible to measure every single mirror facet or receiver tube. A sampling process needs to be developed to manage measurement time and ensure sufficient accuracy at the same time. For this solar field, Loop 5 is equipped with the most sophisticated instrumentation to measure real-time loop temperature, mass flow rate, and pressure, and it is intended to be used as a test loop for the plant acceptance test to represent the entire solar field. For this reason, a detailed optical test plan is specifically designed for the whole field and Loop 5, as summarized in Table 2.

Table 2: Optical test plan summary

Measurement Metrics of Interest	Instrument	Procedure
Specular reflectance at one acceptance angle	D&S 15R	• Select 44 modules across the whole solar field and select 14 modules at Loop 5 • Clean the mirror patch of interest for measurements for each module • Use D&S 15R to measure specular reflectance at 25 mrad aperture
Specularity and solar-weighted specular	• D&S 15R • 410-Solar	• Select 4 modules at Loop 5 • Clean the mirror patch of interest for measurements for each module Use D&S reflectometer to measure specular reflectance at 7, 25, and 46 mrad

		• Use 410-solar reflectometer to measure solar weighted specular reflectance
Mirror slope error and receiver position error	DO	• Select 10 modules across the whole solar field and select 4 modules at Loop 5 • Implement DO technique for measurements

It is straightforward and efficient (about 30 readings per hour) to use reflectometers (D&S 15R and 410-Solar) to measure mirror reflectance in the field [14, 34, 35]. The DO implementation requires certain preparation steps and may take a half hour to one hour to measure each module [30, 31]. The measurement number for D&S was selected based on previous work [14]; because this is the first time to implement a slope error/receiver position error measurement in the field, a maximum number of sampled measurements are selected during the planned two-day test period.

3. Solar Reflectance Measurement

Solar reflectance correlates mirror reflectance with the solar spectrum [14] and becomes a fairly complex topic in the CSP applications. For a parabolic trough collector, the receiver will only accept the reflected sun rays within about 2° around the specular direction, outside of which the light will not be intercepted/absorbed. It is the specular reflectance of a mirror that determines optical performance of a trough collector (and other types of CSP collectors). Many specular reflectance models have been proposed and often suffer from certain theoretical/realistic limitations [13, 14], such as only being suitable to specific instrumentation or a specific type of reflector. Here, a newly proposed solar reflectance model is adopted [14] that is generic and flexible in accommodating various levels of measurements.

3.1. Solar reflectance model

The mathematical model of solar-weighted specular reflection is defined as follows:

$$\rho_{spec}^{SW}(\varphi) = \rho_{spec,tot}^{SW} \int_0^{\Omega(\varphi)} f^{SW}(\varphi) \cdot d\Omega \,. \tag{1}$$

Here, ρ_{spec}^{SW} is the solar-weighted specular reflectance at the acceptance angle φ, and $\rho_{spec,tot}^{SW}$ is the total solar-weighted specular reflectance. A general description of mirror reflection is provided in Figure 1.

A simple and effective form for mirror specularity profile is a Gaussian distribution:

$$f(\varphi) = \frac{1}{2\pi \cdot \sigma_s^2} \, e^{-\left(\frac{\varphi}{\sqrt{2}\cdot\sigma_s}\right)^2} \tag{2}$$

The coefficient $\frac{1}{2\pi\cdot\sigma_s^2}$ ensures an overall integral equal to 1 when assuming $\sigma_s \ll 1$. Here, σ_s is the root mean square (RMS) of the Gaussian function, expressed in radians.

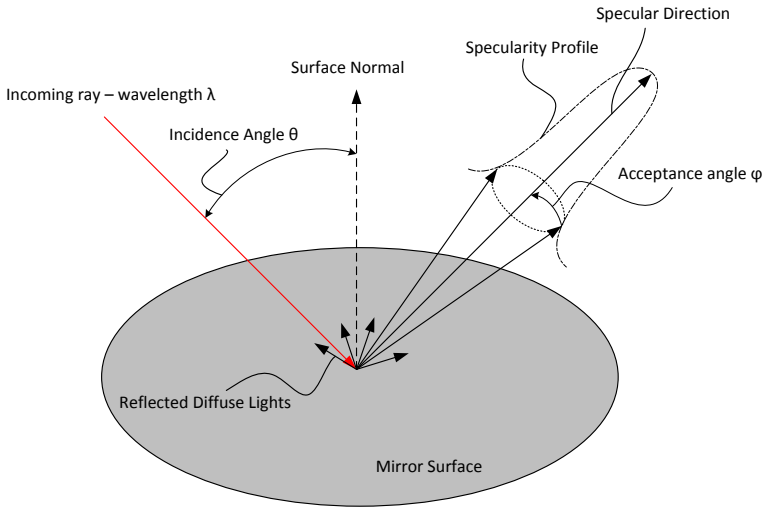

Figure 1: Schematic of mirror reflectance [14].

3.2. Solar reflectance measurements

First, the D&S R15 reflectometer [14, 33] is used to measure the mirror reflectance across the entire solar field. The measurements are plotted for different loops in Figure 2. The mirror reflectance is measured at a full acceptance angle of 25 mrad and at a single wavelength of 660 nm. As seen in the figure, Loops 1, 5, 7, 9, and 10 have a slightly higher reflectance than the average. Some reflectance variance across loops in the figure comes from measurement uncertainties, whereas other variance comes from damage to reflector panels in certain loops (e.g., Loop 8) due to rainwater trapped within some mirror panel storage containers during their long-time outdoor storage prior to solar field construction.

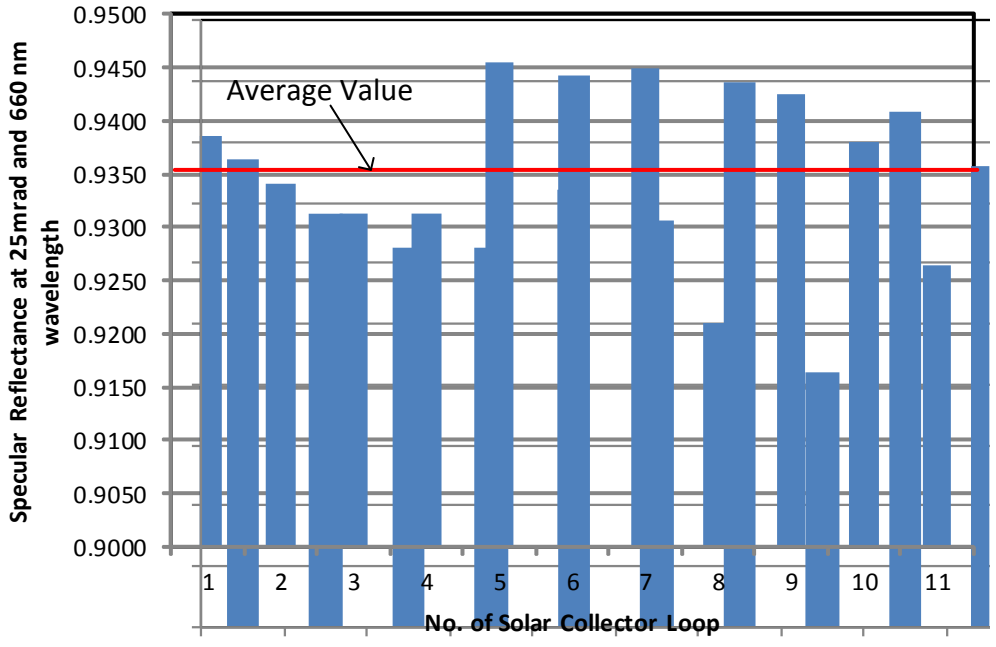

Figure 2: Distribution of solar specular reflectance (at 25 mrad and at a wavelength of 660 nm) among loops. Variability comes from measurement uncertainties and damage to some panels prior to construction.

Next, for selected mirror modules, mirror reflectance at various acceptance angles is also measured using the D&S reflectometer. The results are plotted in Figure 3, and the measurements by the D&S reflectometer are denoted by:

$$\rho_{spc}^{660,m}(\varphi_i), i = 1,2,3. \quad (3)$$

Here, m is the sample number, $m = 1, 2, \ldots, M_{spc}$, and

$$\varphi_1 = 3.5\ mrad; \quad \varphi_2 = 12.5\ mrad; \quad \varphi_3 = 23\ mrad; \quad (4)$$

In the formula, the half acceptance angle is used; the full acceptance angle is twice the half acceptance angle, which is more often referred to in practice.

Specular reflectance increases with acceptance angle. How fast the specular reflectance increases with the increasing acceptance angle defines the mirror specularity. In addition, another reflectometer, the SOC 410-Solar [35], is also used to measure solar-weighted hemispherical and specular reflectance. The two reflectometers complement one another—the D&S measures reflectance at various acceptance angles, but at a single wavelength, whereas the SOC measures solar-weighted reflectance with multiple bands of wavelength representing the solar spectrum, but at a single large acceptance angle.

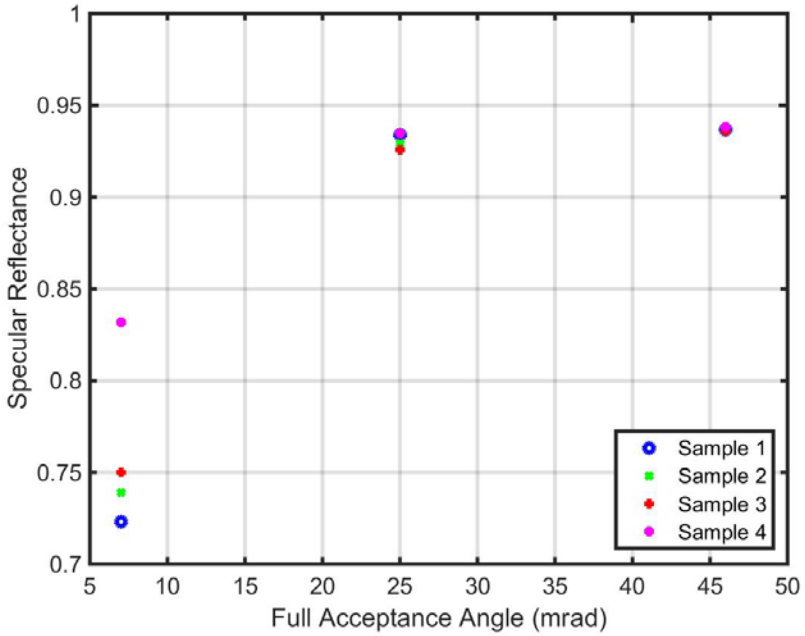

Figure 3: Specular reflectance (at a wavelength of 660 nm) as a function of acceptance aperture size for four mirror panel samples.

3.3. Solar field average reflectance characterization

Based on the data over varying acceptance angles, a single-Gaussian specularity profile can be derived. For three measurements at $\varphi_i, i = 1,2,3$ of each mirror panel m, Equation (2) expands to:

$$\rho_{spec,tot}^{660,m} \cdot \left(1 - e^{-\left(\frac{\varphi_i}{\sqrt{2}\cdot\sigma^{660nm}}\right)^2}\right) = \rho_{spec}^{660,m}(\varphi_i), i = 1,2,3. \quad (5)$$

The unknown parameters $\rho_{spec,tot}^{660,m}$ and σ^{660nm} can be solved from the equations above by using least-squares fitting, based on the measurements at three acceptance angles. The single Gaussian fitting curves are then plotted against the raw data points in Figure 4.

Combined with the average solar field reflectance and the solar-weighted reflectance, the average solar-weighted reflectance is calculated for the whole solar field and Loop 5 in Table 3. The average solar-weighted reflectance is derived using the solar reflectance model in Section 3.1. More specifically:

$$\overline{\rho_{spec,tot}^{SW}} \cdot \left(1 - e^{-\left(\frac{\varphi}{\sqrt{2}\cdot\overline{\sigma^{SW}}}\right)^2}\right) = \overline{\rho_{spec}^{SW}}(\varphi) \quad (6)$$

Here, the calculation of solar-weighted values is simplified with available measurement capabilities by assuming:

$$\overline{\rho_{spec,tot}^{SW}} = \overline{\rho_{spec,tot}^{660}} \cdot \overline{\left(\frac{\rho_{spec,SOC}^{SW}}{\rho_{spec,SOC}^{660}}\right)} \quad (7)$$

$$\overline{\sigma^{SW}} = \sigma^{660nm} \quad (8)$$

Here, $\overline{\rho_{spec,tot}^{SW}}$ is the average solar-weighted specular reflectance derived from the D&S measurements. $\rho_{spec,SOC}^{SW}$ and $\rho_{spec,SOC}^{660nm}$ is the solar-weighted value and the 660-nm-wavelength value measured by the SOC reflectometer; $\overline{\left(\frac{\rho_{spec,SOC}^{SW}}{\rho_{spec,SOC}^{660nm}}\right)}$ is the average of the ratio of two reflectance measurements by the SOC reflectometer. $\overline{\sigma^{SW}}$ is the solar-weighted specularity RMS value.

The measurement uncertainty at a 95% confidence level is also given for the average values and is calculated by using a simple student t method based on the number of measurements.

Table 3: Average solar reflectance measurement for the solar field and Loop 5. The average solar field value is affected by measurement uncertainties and damage to some panels prior to construction. Loop 5 will be used in the future performance acceptance test at the plant.

	Solar Field	**Loop 5**
Average Solar-Weighted Specular Reflectance $\overline{\rho_{spec,tot}^{SW}}$	0.9043 ± 0.0033	0.9124 ± 0.0052
Average Specularity RMS Value $\overline{\sigma^{SW}}$	1.92 ± 0.26	1.92 ± 0.26

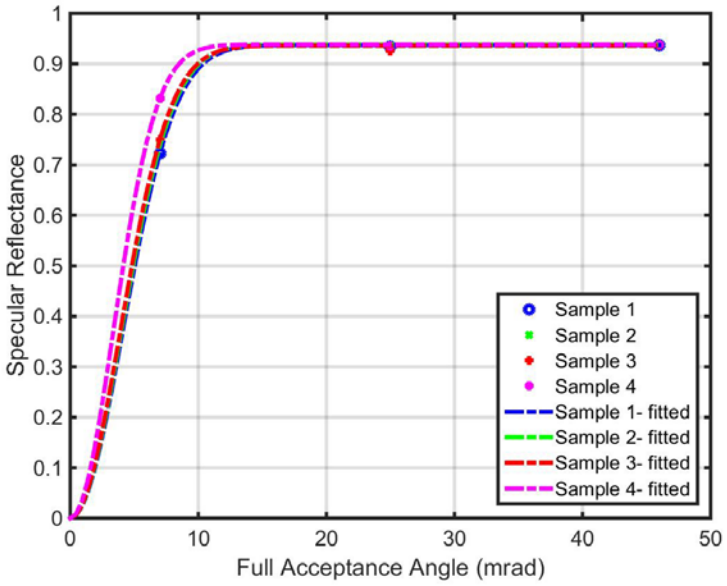

Figure 4: Fitted mirror specularity profile using a single-Gaussian approximation.

4. Measurement of mirror slope error and receiver position error

DO is an optical tool developed by NREL to characterize solar collector optical errors, including mirror slope error and receiver alignment/position error [30, 31]. It uses photogrammetry to capture the collector error through the reflection images of the receiver on the reflector. An example reflection image is given in Figure 5. The distortion of the receiver reflection indicates the inaccurate mirror shape and/or misplaced receiver locations. Four targets (black dot centered on a white background) are attached on the collector module corners and provide the position reference for the photogrammetry analysis, as shown in Figure 6. The original image can then be rescaled to a regular square image (right image in Figure 5). By combining with the camera optical specifications, the mirror slope error can be derived for one horizontal segment of the mirror module by using a sophisticated software package. The characterization of the full collector module requires a series of photos to be taken while the receiver reflection sweeps from one module edge to the other with the collector's rotation. During this measurement, the collector tracking angles stay between 10° and 20° above the horizon.

Figure 5: A snapshot of Distant Observer (DO) optical characterization: raw photo (left) and scaled photo (right).

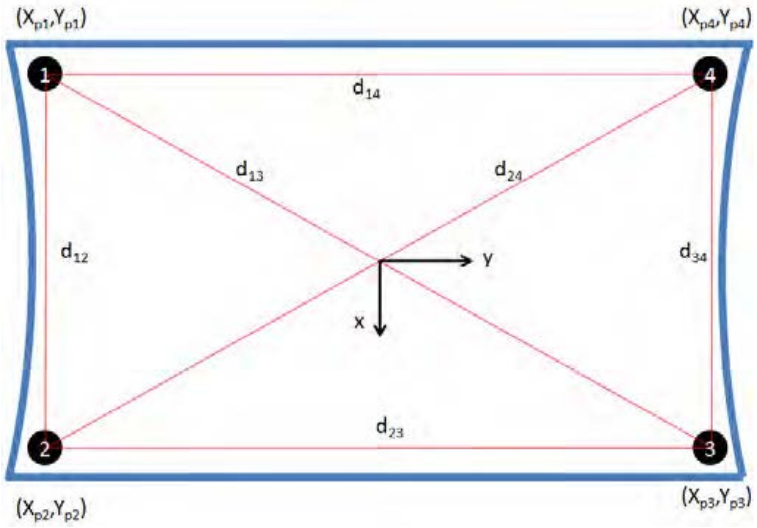

Figure 6: Rescaling of the raw image based on the target locations [30].

The receiver position error along x and z directions are plotted for one 13.9-meter-long module at the Stillwater plant in Figure 7. Note that the receiver position error indicates the receivers' distortion due to gravity. The average position error is about 15.1 mm along x and -8.2 mm along z. The SkyTrough collector is designed with some receivers mounted below focus and some above, so that when they expand at operating temperature, all of the receivers move closer into focus. The receiver offset along z will be reduced under normal operational conditions.

The mirror slope error on the entire sample mirror module is also calculated and plotted in Figure 8. The average and RMS values of the mirror slope error are -3.3 mrad and 2.5 mrad, respectively. Note that the receiver misalignment is included as part of the mirror slope error.

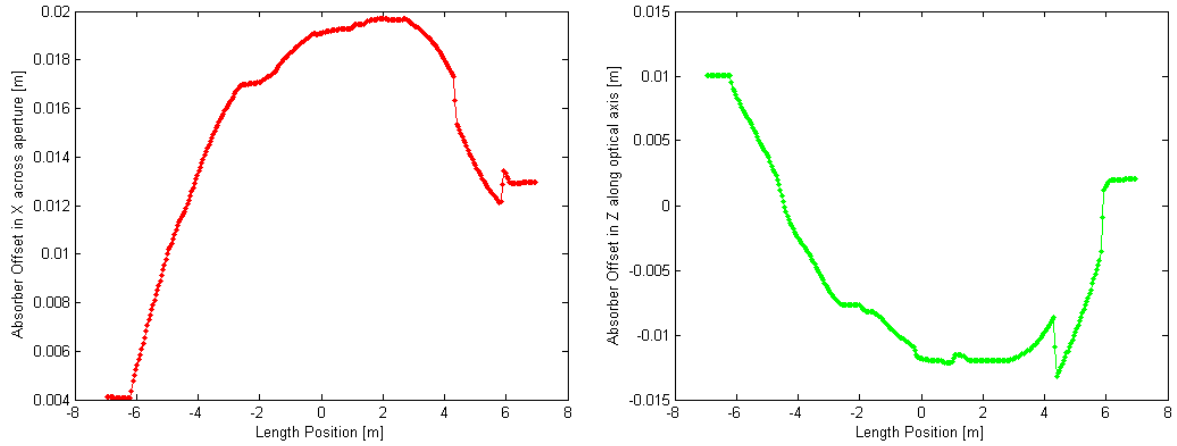

Figure 7: Receiver position error along x and z directions. Because these measurements were taken near the horizon, they represent a worst-case scenario that occurs during operation. Receiver position error during normal operating angles may be substantially less.

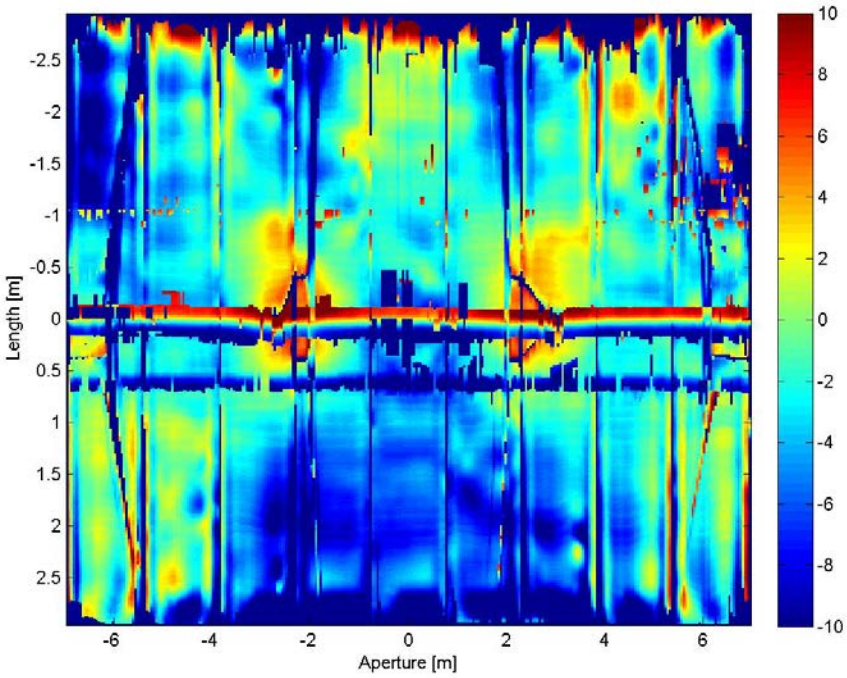

Figure 8: Slope error distribution over one collector module of a SkyTrough collector module (indexed by L5R2M10).

A number of collector modules were measured using DO. A total of 12 data sets were identified to provide valid measurements. The mean value and RMS of the mirror slope error for the valid data sets are plotted in Figure 9. The average mean value is about -4.0 mrad. This non-zero mean value of slope error is due to gravity-induced displacement of the receiver and frame, which is greatest at low tracking angles. The average RMS value is about 3.0 mrad.

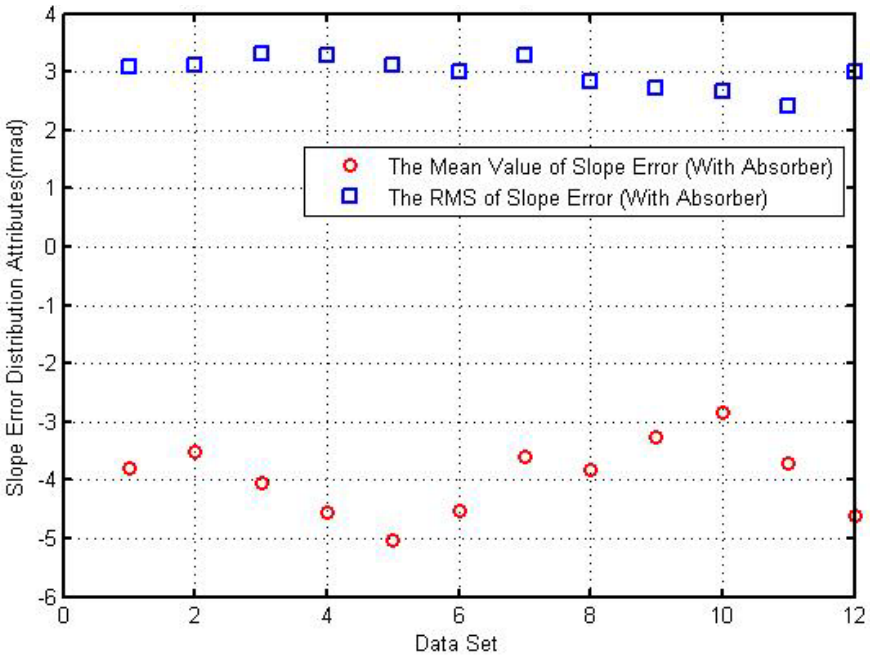

Figure 9: Slope error distribution attributes (mean value and RMS) for all sampled collector modules. Note that the mean value is dominated by the receiver's gravity-induced displacement, which is greatest at the low tracking angle while the DO measurements were conducted. Its impact on the collector performance is compensated by including a tracking-offset algorithm, to be discussed later.

5. Optical characterization of solar collector

5.1. Intercept factor

The optical performance of a solar collector largely depends on two aspects: optical properties and geometric accuracy. Optical properties include mirror reflectance, absorber-tube absorptivity, and receiver-envelope transmissivity; geometric accuracy refers to mirror slope error, receiver position error, and tracking error. The solar collector optical specifications and optical error measurements are summarized for the Stillwater solar field in Table 4.

Table 4: Solar collector optical specifications and optical error measurements

Parameters		Value	Source
Receiver	Absorptance	0.96	Manufacturer
	Glass-envelope transmittance	0.97	Manufacturer
Mirror	Solar-weighted specular reflectance	0.904	Measured
	Specularity – RMS	1.92 mrad	Measured
	Slope error – mean value	-4.0 mrad	Measured, including the receiver position error
	Slope error – mean value with tracking offset	1.0 mrad	
	Slope error – RMS	3.0 mrad	
Collector	Tracking error	1 mrad	Design parameter

Once the collector optical characterization parameters are obtained, an optical performance calculation program called FirstOPTIC can be used to derive the collector optical performance. FirstOPTIC employs the most accurate optical treatment of collector optical error measurements, and it derives analytical mathematical formulae to calculate the intercept factor of a trough collector [28, 29, 36]. It can provide fast, accurate calculation of intercept factor and incidence-angle modifier (IAM) [36]. The intercept factor for each collector module is plotted in Figure 10. The intercept factor varies from 0.65 to 0.95, closely correlated to the slope error measurements in Figure 9 because the collector slope error typically dominates the collector performance.

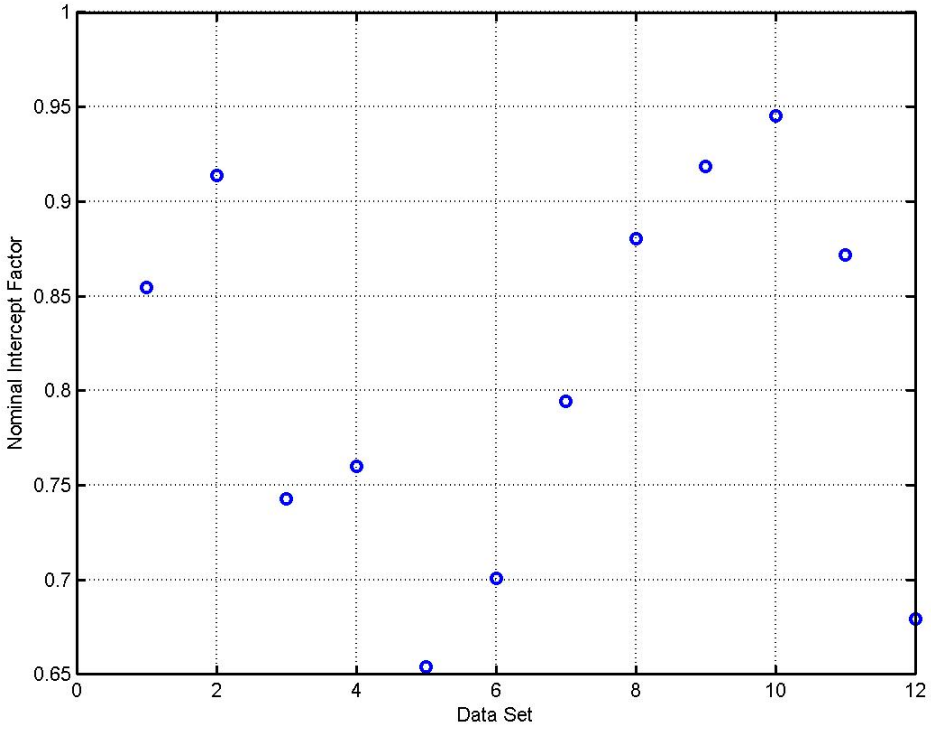

Figure 10: Intercept factor calculation for all sampled collector modules.

5.2. Tracking offset

The predicted intercept factor values above are substantially lower than the anticipated target performance. It can be seen that the slope error magnitude strongly impacts the collector performance. From Figure 9, the mean value of each data set is negative between -2.9 mrad and -5.0 mrad. Theoretically, the slope error with a mean of -1 mrad can be compensated by +2 mrad tracking error, which results in an effective slope error with a mean of 0 mrad. Thus, this tracking-offset strategy can be applied to each collector sample with exactly twice the mean value of the measured slope error. The intercept factor with appropriate tracking offset for each measured collector module is recalculated against the one without the tracking correction in Figure 11. Here, it is assumed that the tracking-offset algorithm is able to reduce the mean value of slope error for any collector to be 1 mrad. As seen in the figure, the collector performance is improved substantially. With the tracking offset, the intercept factor becomes close to the unity for all cases. The average intercept factor increase from 0.827 without tracking offset to 0.991 with tracking offset. According to the vendor, field calibration of the tracking-offset

algorithm is an anticipated step of the field commissioning, and it clearly improve solar field performance to a significant degree.

The large slope error is induced by the effect of gravity on the collector. The gravity-induced deflection is greatest at low tracking angles and is less when the collector is oriented straight up. When the impact of gravity-induced deflection varies with tracking angle, the tracking-offset value is a function of collector position. In reality, a tracking-offset algorithm can be directly incorporated into the tracking control program of the drive so that the collector performance can be improved.

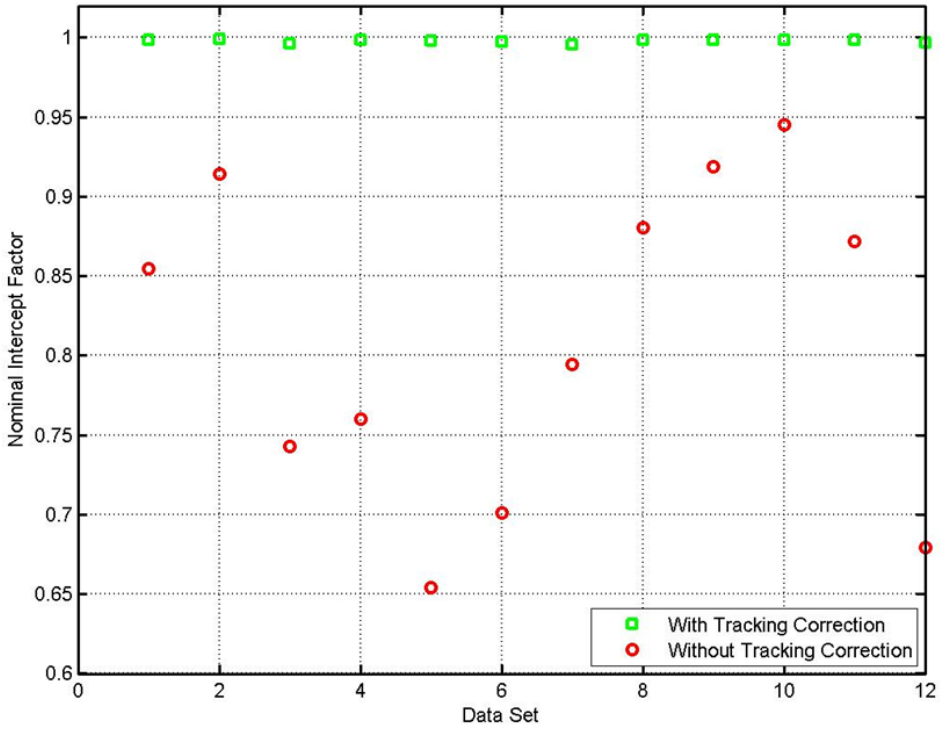

Figure 11: Intercept factor calculation for all sampled collector modules with and without tracking-offset algorithm.

5.3. Incidence-angle modifier (IAM)

An IAM is typically used to describe the solar collector performance under non-zero incidence angles, that is, for different sun positions throughout the year. A common form for the IAM is:

$$IAM(\theta) = k_{\mathrm{IAM},0} + k_{\mathrm{IAM},1} \cdot \frac{\theta}{cos(\theta)} + k_{\mathrm{IAM},2} \cdot \frac{\theta^2}{cos(\theta)} + k_{\mathrm{IAM},3} \cdot \frac{\theta^3}{cos(\theta)} \quad (9)$$

The fitting function is typically of second or third order. In the work described here, it is found that a better fit is provided with the third-order function. In either form, the optical efficiency at a non-zero incidence angle is given by:

$$\eta(\theta) = \eta_o \cdot IAM(\theta) = \rho\tau\alpha\gamma \cdot IAM(\theta). \quad (10)$$

Here, θ is the solar incidence angle in radians, ρ is the parabolic mirror reflectivity, τ is the receiver glass-envelope transmissivity, α is the average receiver coating absorptivity, and γ is the collector

intercept factor. The nominal optical performance and the IAM coefficients are provided in Table 5. The IAM is also plotted as a function of incidence angle in Figure 12.

Table 5: Stillwater solar field optical performance.

	No Tracking Offset	With Tracking Offset
Nominal Optical Efficiency	0. 696	0.840
Nominal Intercept Factor	0. 827	0.991
$k_{IAM,0}$	1	1
$k_{IAM,1}$	0.0138	-0.0140
$k_{IAM,2}$	-0.2234	0.0622
$k_{IAM,3}$	0.1225	-0.0909

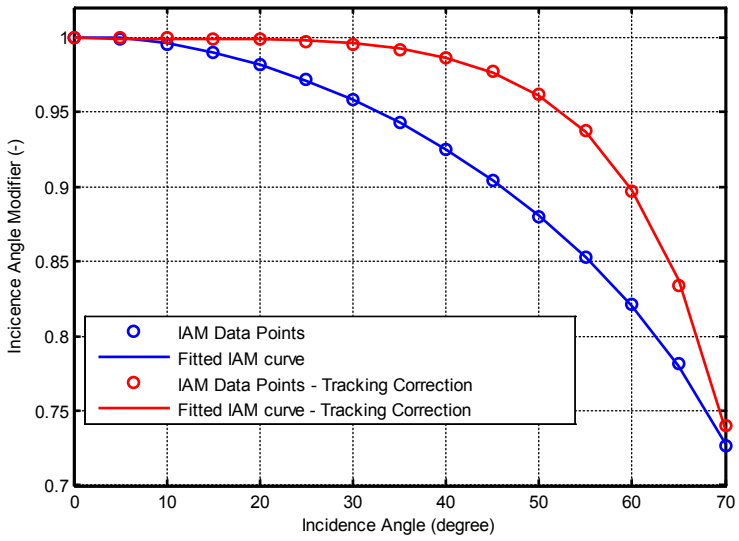

Figure 12: Incidence-angle modifier (IAM) curve: circles mark the predicted data points and the line indicates the fitting function.

6. Annual thermal generation from solar field

After detailed solar field optical characterization, System Advisor Model (SAM) software can be used to calculate annual energy generation performance of a solar field [37]. SAM was developed by NREL to evaluate technical and economic performance of renewable energy systems and is available to the public. SAM allows users to configure a renewable energy system with specific technology and evaluate its performance at certain locations under specific financial conditions. With a temporal weather resource file at a location, SAM can calculate annual performance of a solar field, such as hourly based thermal energy, electricity, and cash flow. Combined with system cost models, SAM can calculate financial matrices of a solar energy system, such as levelized cost of energy (LCOE) and internal rate of return (IRR).

Models for different renewable energy systems are regularly added and updated by NREL researchers. Currently, however, a solar/geothermal performance model is not available in SAM. The strategy to estimate the hybrid plant performance is to combine SMA's solar field performance module and a separate geothermal power-cycle model developed by Idaho National Laboratory (INL). The SAM solar field performance module uses the dimensions of the Stillwater solar field and the collector/receiver parameters from the solar collector manufacturers (SkyFuel [11] and Huiyin [38]). Using a local weather file at the hybrid plant location and optical characterization results from Tables 4 and 5, the SAM solar field module can calculate the thermal power generation as a function of time. The design outlet temperature of the solar field is about 200 °C, but varies during real-world operation because the HTF mass flow cannot be readily controlled at the actual plant.

Thermal energy generation results from SAM can be input to the INL geothermal power-cycle model. The INL model combines these results with the solar heat input and geothermal heat to then calculate real-time power generation. The detailed modeling process and results can be found in [9].

Table 6. Revised input parameters and annual energy output based on measured values at Stillwater

SAM input parameter	**Case 1: Original value from SAM default or vendor literature**	**Case 2: Revised value based on measurement at Stillwater**	**Case 3: Revised value based on measurement at Stillwater**
		Without tracking-offset algorithm, assuming maximum observed error at low tracking angles	**With tracking-offset algorithm**
Absorber absorptance (receiver)	0.963	0.96	0.96
Envelope transmittance (receiver)	0.964	0.97	0.97
Mirror reflectance	0.93	0.904*	0.904*
Geometry effects	0.952	0.883	0.991
Tracking error	0.988	1**	1**
IAM coefficient F0	1	1	1
IAM coefficient F1	0.0327	0.0138	-0.0140
IAM coefficient F2	-0.1351	-0.2234	0.0622
IAM coefficient F3	0	0.1225	-0.0909
SAM annual performance prediction for 11-loop, 24,778-m^2 solar field			
Field thermal power produced (MWh/yr)	38,900	35,500	40,700

* The measurement value accounts for damage to some panels prior to construction

** Included in geometry effects

Three SAM cases are summarized in Table 6, and the hourly output for a typical year in Stillwater, NV, is given in Figure 13. Case 1 provide a reference annual performance for the Stillwater solar field by using the default performance metrics provided by the vendors; Case 2 and Case 3 are the performance modeling based on the field test results given earlier in this paper. Case 2 does not apply the tracking-offset algorithm whereas Case 3 does include the algorithm. The comparison shows that the actual solar field performance will be about 9% lower than that expected from the reference case (Case 1). The vendor

indicated that it was a reasonable value considering the storage history and fabrication details of the Stillwater equipment. The greatest deviations are in the mirror reflectance (-3%) and geometric accuracy of the collector (-7%).

It is also shown that a significant boost in performance can be obtained if an appropriate tracking-offset algorithm is implemented. In the perfect case, this tracking offset could boost the as-measured performance by almost 15%, as shown by Case 3 in Table 6.

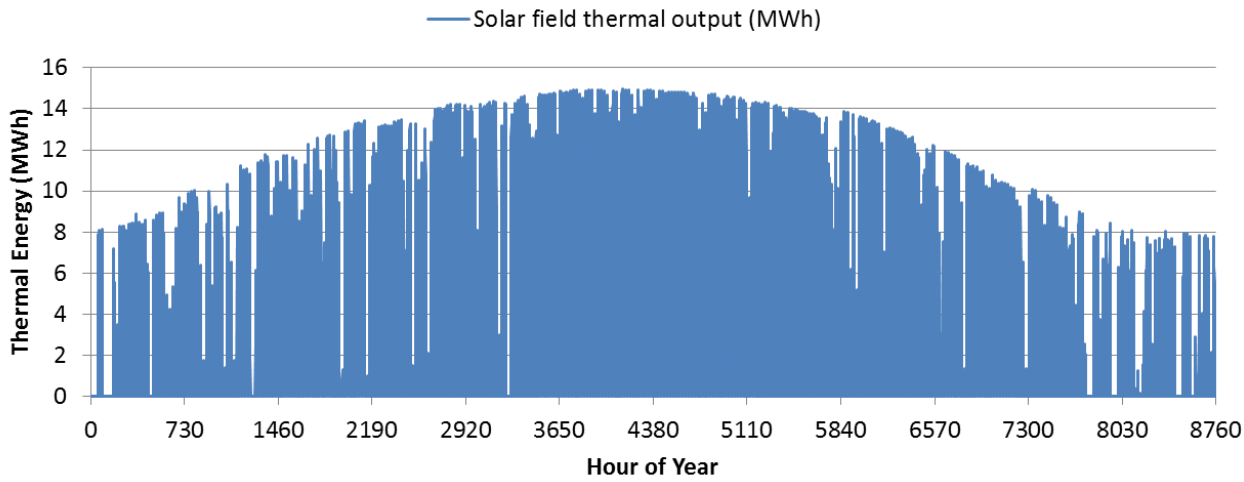

Figure 13. Hourly SAM-predicted solar field thermal energy output for Stillwater based on measured parameters listed in Table 6.

7. Discussion

Optical characterization is always a great challenge in the field, especially at a utility scale. Practically speaking, it is impossible to measure every solar collector module in the field; therefore, a statistical sampling procedure is implemented to ensure a certain level of measurement uncertainties. In reality, numerous factors affect the prediction of solar field performance. So the overall uncertainty of the nominal optical/thermal efficiency may be at a level of 3%~5% [16, 39]. By taking this as a reference, an appropriate number of sampling measurements can be determined. In the real world, the measurement accuracy is often constrained by certain time demands, and the maximum number of measurements is typically taken within the allowable test period. If the measurement uncertainty is not acceptable, additional measurements will be needed.

It is more complex to calculate the uncertainty of the average solar field optical efficiency. As shown in Figure 11, with tracking offset, the collector intercept factor values are all above 0.99 and their variation is not obviously correlated with the slope error variation. This is because the relatively large receiver (80-mm diameter) can tolerate a larger optical error. Thus, the uncertainty of solar field average intercept factor is very small compared with the uncertainty of the solar field average slope error. The dominant source of solar field uncertainty is therefore the uncertainty of the solar-weighted total specular reflectance. According to Equation (10), the uncertainty of solar-weighted total reflectance results in the same amount of uncertainty on the performance prediction, assuming that the uncertainty from other parameters (all manufacturer's values) can be reasonably neglected.

It is also noted that not every optical error source is measured in the field. Measuring certain optical metrics, such as receiver absorptance and receiver-glass transmittance, are not feasible in the field due to unavailability of required instruments. The sun shape is always varying under instantaneous weather conditions. In addition, the work in this paper measured mirror reflectance, mirror specularity, mirror slope error, and receiver position error, and it provides the most comprehensive optical characterization of a large-scale solar field. The metrics missed by the analysis are mirror slope error along longitudinal direction and collector error as a function of tracking position. The former was shown to have a minimal impact on collector optical performance compared with the measured mirror slope error along transversal direction [36, 40]. The impact of the latter is still unknown.

8. Conclusions

To conclude, a comprehensive optical test has been performed at the Stillwater plant solar field. First, the calculation of solar field average solar-weighted reflectance and specularity are allowed by measurements of mirror specular reflectance at various acceptance sizes and solar-weighted reflectance. The mirror slope error and receiver position error are measured by DO, the only tool in the world suitable for both types of collector errors in the field condition. During the optical test, sufficient measurement data were taken to obtain the solar field average values. To the authors' knowledge, this represents the most comprehensive optical characterization in a utility-scale field.

By employing the FirstOPTIC software, the measurement results are readily interpreted to derive the solar field average optical performance under normal incidence and non-normal incidence angle. Then, all measured and derived optical performance metrics are input to SAM for the thermal energy annual performance at an hourly basis by using local satellite weather data. This analysis indicates that annual delivered energy from the solar field would be about 9% lower than the collector manufacturer's prediction if an appropriate tracking-offset algorithm is not implemented. The analysis also shows that further calibration incorporating a SCA tracking-offset algorithm can potentially improve performance by as much as 15%.

The detailed performance predictions from SAM will serve as an input to INL's plant model of the Stillwater power block, thus allowing engineers to model plant performance and explore optimal integration strategies of solar thermal power into a geothermal binary power-cycle. This work can be found at [9].

The work in this paper illustrates a detailed process on how to collect and interpret various types of measurement data by using state-of-the-art optical tools and models, and it will serve as a valuable guideline in the area of solar field optical characterization.

Acknowledgements

The work at NREL was supported by the U.S. Department of Energy under Contract No. DE-AC36-08-GO28308. Funding was supplied by the DOE's Geothermal Technologies Office (GTO). The authors wish to thank Tim Wendelin, Dale Jenne (from NREL), and Daniel Wendt (from INL) for their assistance in taking measurements in the field. Special thanks go to Sander Cohan, Lorenzo Angelini, Alessio De

Marzo, and Fabrizio Bizzarri from EGP for their kind and most considerable support for our test measurements on site.

Nomenclature

ρ	=	Reflectance
λ	=	Light wavelength, *nm*
θ	=	Incidence angle with respect to mirror surface normal, *rad or degree*
Ω	=	Solid angle, *sr*
$\rho_{spec,tot}^{SW}$	=	Solar-weighted total specular reflectance
ρ_{spec}^{SW}	=	Solar-weighted specular reflectance
f	=	Mirror specularity profile distribution function
φ	=	Acceptance (zenith) angle with respect to the specular direction, *mrad*
σ_s	=	Overall RMS value of a specularity profile distribution function, *mrad*
γ	=	Collector intercept factor
τ	=	Transmittance of receiver-glass envelope
α	=	Absorptance of receiver surface
$\rho_{spec,tot}^{660}$	=	Total specular reflectance at 660-nm wavelength
$\overline{\rho_{spec,tot}^{660}}$	=	Solar field average of total specular reflectance at 660-nm wavelength
σ_s^{SW}	=	Solar-weighted mirror specularity RMS of NSO, *mrad*
η	=	Optical efficiency at normal incidence for NSO solar field

Acronyms

CSP	=	concentrating solar power
MW	=	megawatts
RMS	=	root mean square
NREL	=	National Renewable Energy Laboratory
EGP	=	Enel Green Power
IAM	=	incidence-angle modifier
SCA	=	solar collector assembly
SCE	=	solar collector element
SOC	=	Surface Optics Corporation
D&S	=	Devices and Services
SW	=	solar-weighted

References

1. Mills, D., *Adances in Solar Thermal Electricity Technology.* Solar Energy, 2004. **76**: p. 19-31.
2. Price, H., et al., *Advances in Parabolic Trough Solar Power Technology.* Journal of Solar Energy Engineering, 2002. **124**(2): p. 109-125.
3. Zhu, G., et al., *History, Current-State and Future of Linear Fresnel Concentrating Solar Collectors.* Solar Energy, 2014. **103**: p. 639-652.
4. SolarPACES. *Parabolic Dish Systems*. Available from: http://www.solarpaces.org/CSP_Technology/csp_technology.htm.
5. Price, H. and D. Kearney, *Chapter 6: Recent Advances in Parabolic Trough Solar Power Plant Technology.* 2005(NREL Report No. CH-550-36422).

6. Zhu, G., et al., *Thermodynamic Evaluation of Solar Integration into a Natural Gas Combined Cycle Power Plant.* Renewable Energy, 2015. **74**: p. 815-824.
7. Dersch, J., et al., *Trough integration into power plants—a study on the performance and economy of integrated solar combined cycle systems.* Energy, 2004. **29**: p. 947-959.
8. Turchi, C., et al., *Geothermal/Solar Hybrid Designs: Use of Geothermal Energy for CSP Feedwater Heating*, in *Geothermal Resources Council 38th Annual Meeting*. 2014: Portland, Oregon.
9. Wendt, D., et al., *Stillwater Hybrid Geo-Solar Power Plant Optimization Analyses*, in *the Geothermal Resources Council Annual Meeting*. 2015: Reno, NV.
10. DiMarzio, G., et al., *The Stillwater Triple Hybrid Power Plant: Integrating Geothermal, Solar Photovoltaic and Solar Thermal Power Generation*, in *Proceedings World Geothermal Congress 2015*. 2015: Melbourne, Australia.
11. *SkyFuel Inc.*; Available from: http://www.skyfuel.com/.
12. Far, A. and R. Gee, *The SkyTrough Parabolic Trough Solar Collector*, in *Proceedings of the ASME 2009 3rd International Conference of Energy Sustainability, .* 2009: San Francisco, California, USA.
13. Meyen, S., et al., *Parameters and Method to Evaluate the Solar Reflectance Properties of Reflector Materials for Concentraing Solar Power Technology Draft Version 2.4*. 2013: SolarPACES.
14. Zhu, G., D. Kearney, and M. Mehos, *On Characterization and Measurement of Average Solar Field Mirror Reflectance in Utility-Scale Concentrating Solar Power Plants.* Solar Energy, 2014. **99**: p. 185-202.
15. Eck, M., et al., *guiSmo: Guidelines for CSP Performance Modeling - Present Status of the SolarPACES Task-1 Project*, in *17th SolarPACES conference*. 2011: Granada.
16. Kearney, D., *Utility-Scale Parabolic Trough Solar Systems: Performance Acceptance Test Guidelines*. 2011, National Renewable Energy Laboratory.
17. Kearney, D., *Utility-Scale Power Tower Solar Systems: Performance Acceptance Test Guidelines*. 2013, National Renewable Energy Laboratory.
18. Andraka, C., et al., *SOFAST: Sandia Optical Fringe Analysis Slope Tool for Mirror Characterization*, in *SolarPACES 2009, .* 2009: Berlin, Germany.
19. Wendelin, T., K. May, and R. Gee, *Video Scanning Hartmann Optical Testing of State-of-the-Art Parabolic Trough Concentrators*, in *Solar 2006 Conference, .* 2006: Denver, Colorado USA.
20. Pottler, K., et al., *Photogrammetry: A Powerful Tool for Geometric Analysis of Solar Concentrators and Their Components.* Journal of Solar Energy Engineering, 2005. **127**(1): p. 94-101.
21. Roger, M., C. Prahl, and S. Ulmer, *Fast Determination of Heliostat Shape and Orientation by Edge Detection and Photogrammetry*, in *14th CSP SolarPACES Symposium*. 2008: Las Vegas, Nevada.
22. Pottler, K., et al., *Geometric Evaluation of Parabolic Trough Collector Module Ultimate Trough*. 2011, CSP Services GmbH.
23. Ulmer, S., et al., *Slope Error Measurements of Parabolic Troughs Using the Reflected Image of the Absorber Tube.* the ASME Journal of Solar Energy Engineering, 2009. **131**.
24. Burkholder, F. and C. Kutscher, *Heat Loss Testing of Schott's 2008 PTR70 Parabolic Trough Receiver*. 2009, NREL.
25. Kutscher, C., F. Burkholder, and K. Stynes, *Generation of a Parabolic Trough Collector Efficiency Curve from Separate Measurements of Outdoor Optical Efficiency and Indoor Receiver Heat Loss.* Journal of Solar Energy Engineering, 2012. **134**.
26. *Heat Collection Element (HCE) Temperature Survey*. Available from: http://www.nrel.gov/csp/lab_capabilities.html#heatcollection.
27. Gee, R., et al., *An Improved Method for Characterizing Reflector Specularity for Parabolic Concentrators*, in *16th SolarPACES, .* 2010: Perpignan, France.

28. Zhu, G. and A. Lewandowski, *A New Optical Evaluation Approach for Parabolic Trough Collectors: First-principle OPTical Intercept Calculation (FirstOPTIC).* Journal of Solar Energy Engineering, 2012. **134**.
29. Zhu, G., *Study on the Optical Impact of Receiver Position Error on Parabolic Trough Collectors.* Journal of Solar Energy Engineering, 2013. **135**.
30. Stynes, K. and B. Ihas, *Slope Error Measurement Tool for Solar Parabolic Through Collectors*, in *the World Renewable Energy Forum*. 2012: Denver, CO.
31. Stynes, K. and B. Ihas, *Absorber Alignment Measurement Tool for Solar Parabolic Trough Collectors*, in *ASME 2012 6th International Conference on Energy Sustainability*. 2012: San Diego, CA.
32. *Surface Optics Corporation*. Available from: www. surfaceoptics.com.
33. *Devices & Services Co.*; Available from: http://www.devicesandservices.com/.
34. *Portable Specular Reflectometer 15R-USB*. Devices and Services Co.: www.devicesandservices.com.
35. *SOC-100 User's Manual - Hemisperical Directional Reflectometer (HDR)*. 2009, Surface Optics Corporations.
36. Binotti, M., et al., *Geometric Analysis of Three-Dimensional Effects of Parabolic Trough Collectors.* Solar Energy, 2013. **88**.
37. NREL. *System Advisor Model 2015.1.30*. Available from: https://sam.nrel.gov/.
38. *Performance Comparison of Huiyin's Vacuum Receiver Tubes*. 2012, Huiyin-Group.
39. Zhu, G. and T. Neises, *Third-Party Thermal Performance Validation of FLABEG's Ultimate Trough Test Loop Located at the SEGS VIII Plant, Confidential* 2015, National Renewable Energy Lab.
40. Bendt, P., et al., *Optical Analysis and Optimization of Line Focus Solar Collectors*. 1979, SERI: Golden, CO, USA.

Appendix D

Complete Plot Set for ORC Analysis Scenarios

Appendix D
Complete Plot Set for ORC Analysis Scenarios

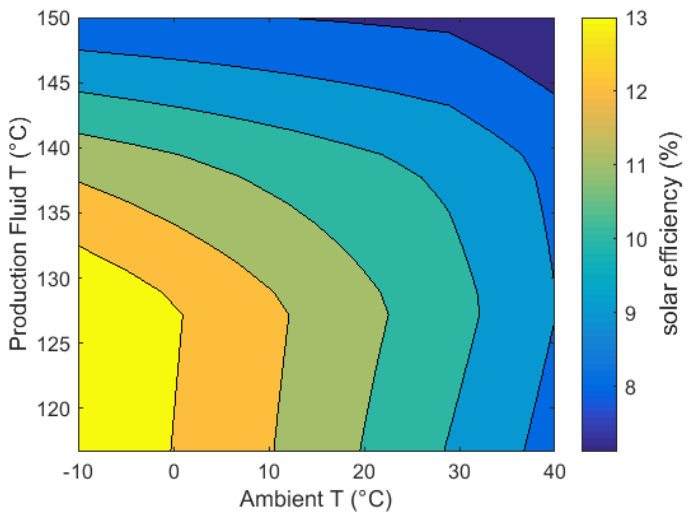

a. 150°C production fluid design temperature

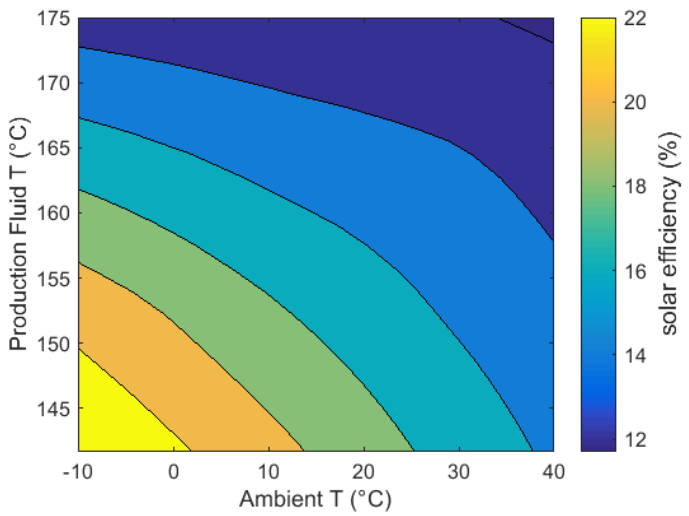

b. 175°C production fluid design temperature

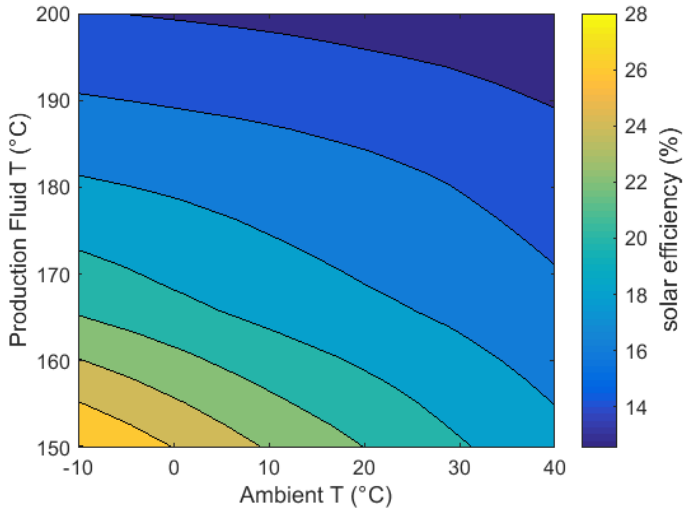

c. 200°C production fluid design temperature

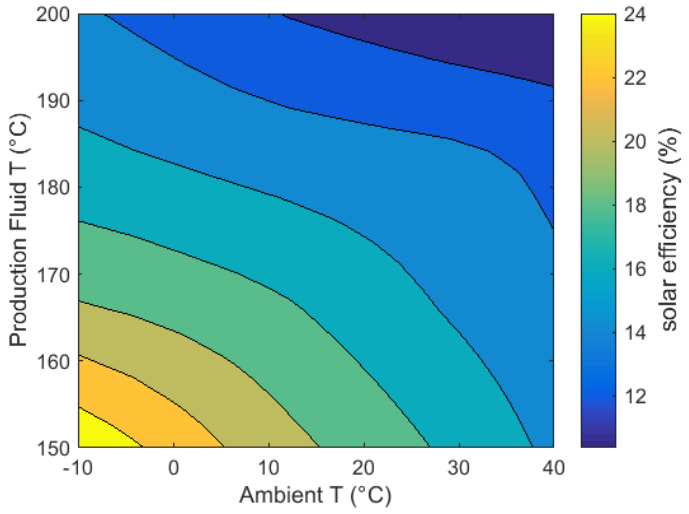

d. 200°C production fluid design temperature (with geofluid exit temperature limit)

Figure D-18. Thermal efficiency of power conversion from solar heat addition equal to 25% of base plant design point heat input plotted as function of production fluid temperature and ambient temperature

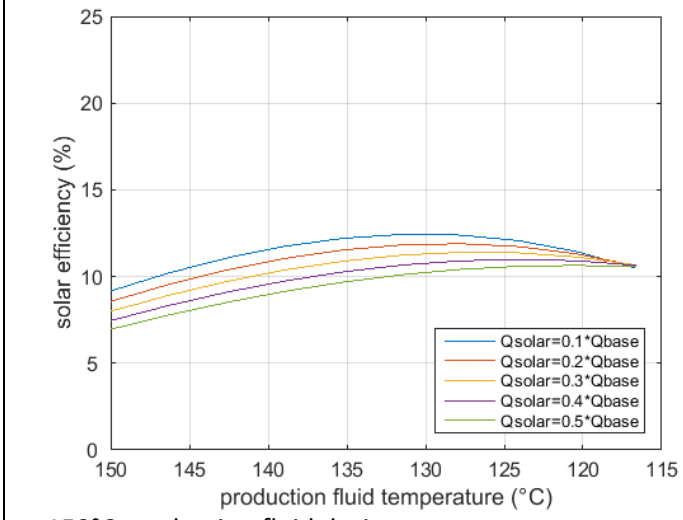

a. 150°C production fluid design temperature

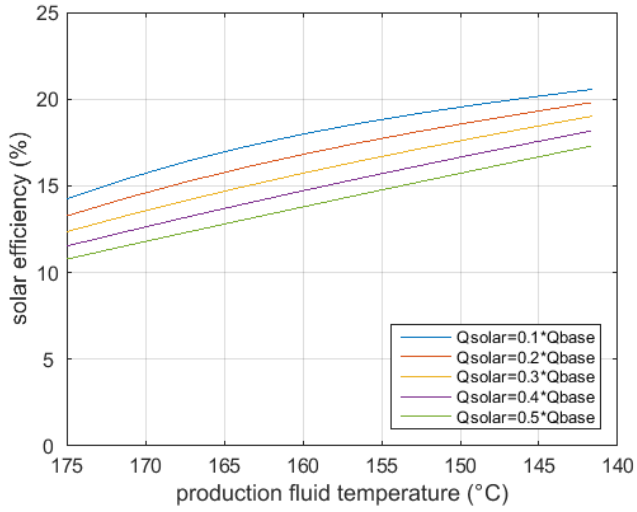

b. 175°C production fluid design temperature

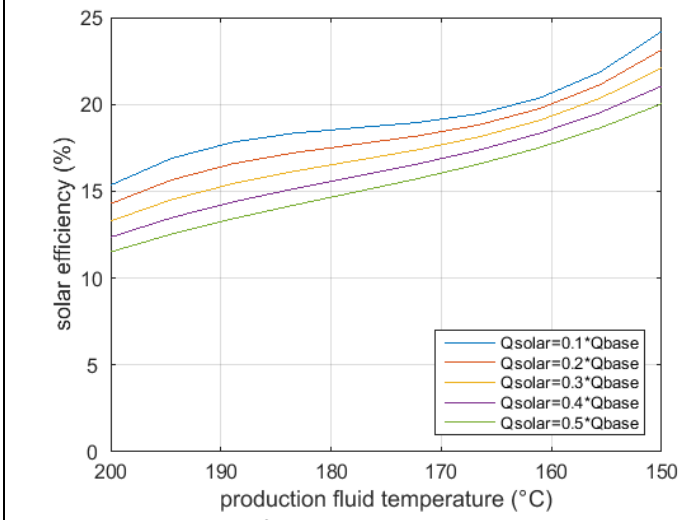

c. 200°C production fluid design temperature

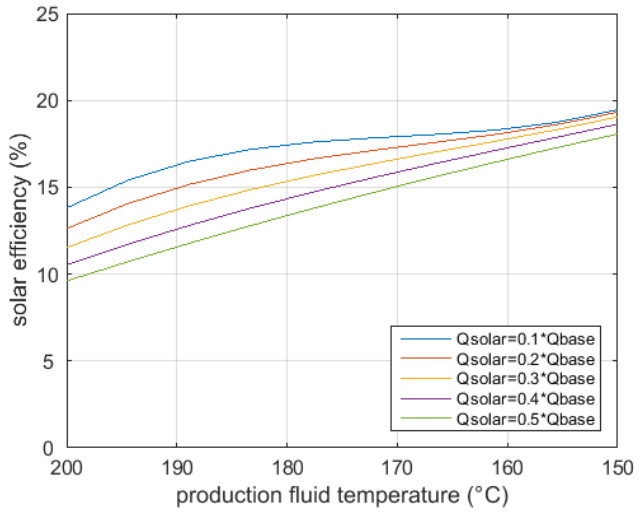

d. 200°C production fluid design temperature (with geofluid exit temperature limit)

Figure D-19. Average annual solar efficiency as a function of production fluid temperature decline.

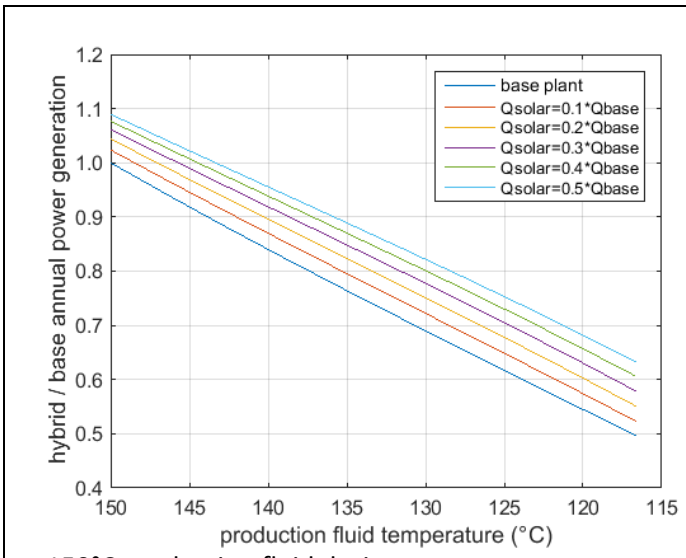

a. 150°C production fluid design temperature

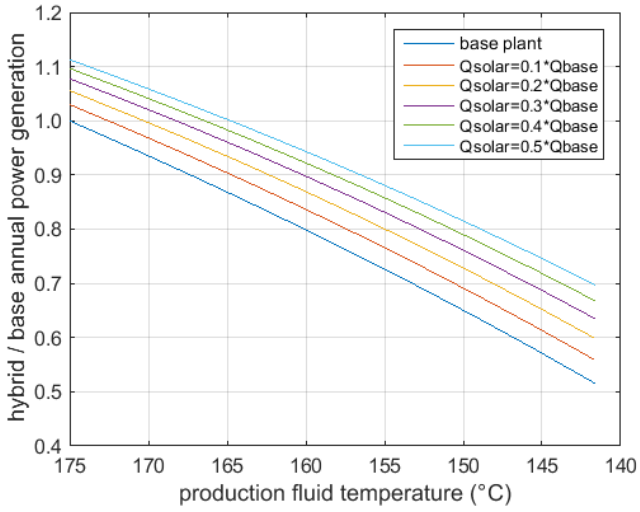

b. 175°C production fluid design temperature

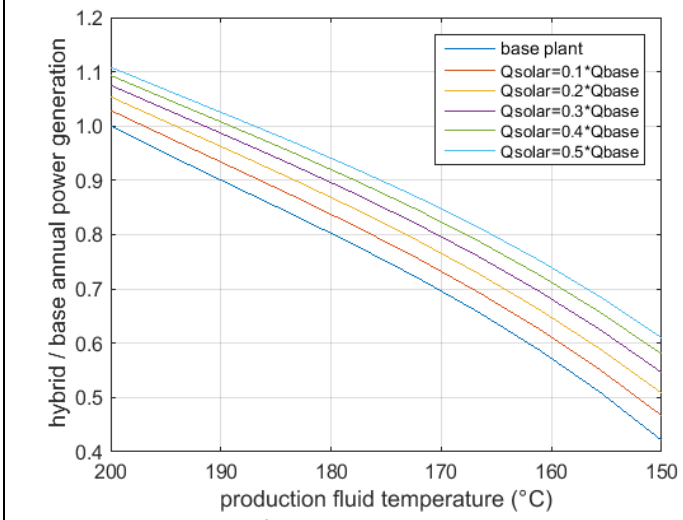

c. 200°C production fluid design temperature

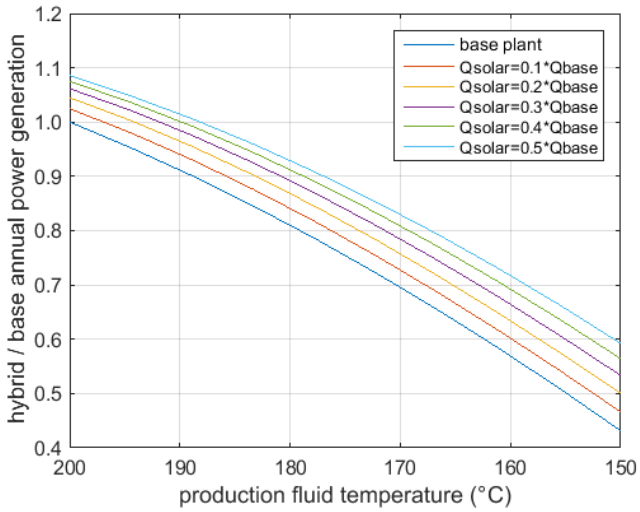

d. 200°C production fluid design temperature (with geofluid exit temperature limit)

Figure D-20. Base and retrofit hybrid plant annual power generation (reported as fraction of base geothermal plant design annual power generation) plotted as function of production fluid temperature decline.

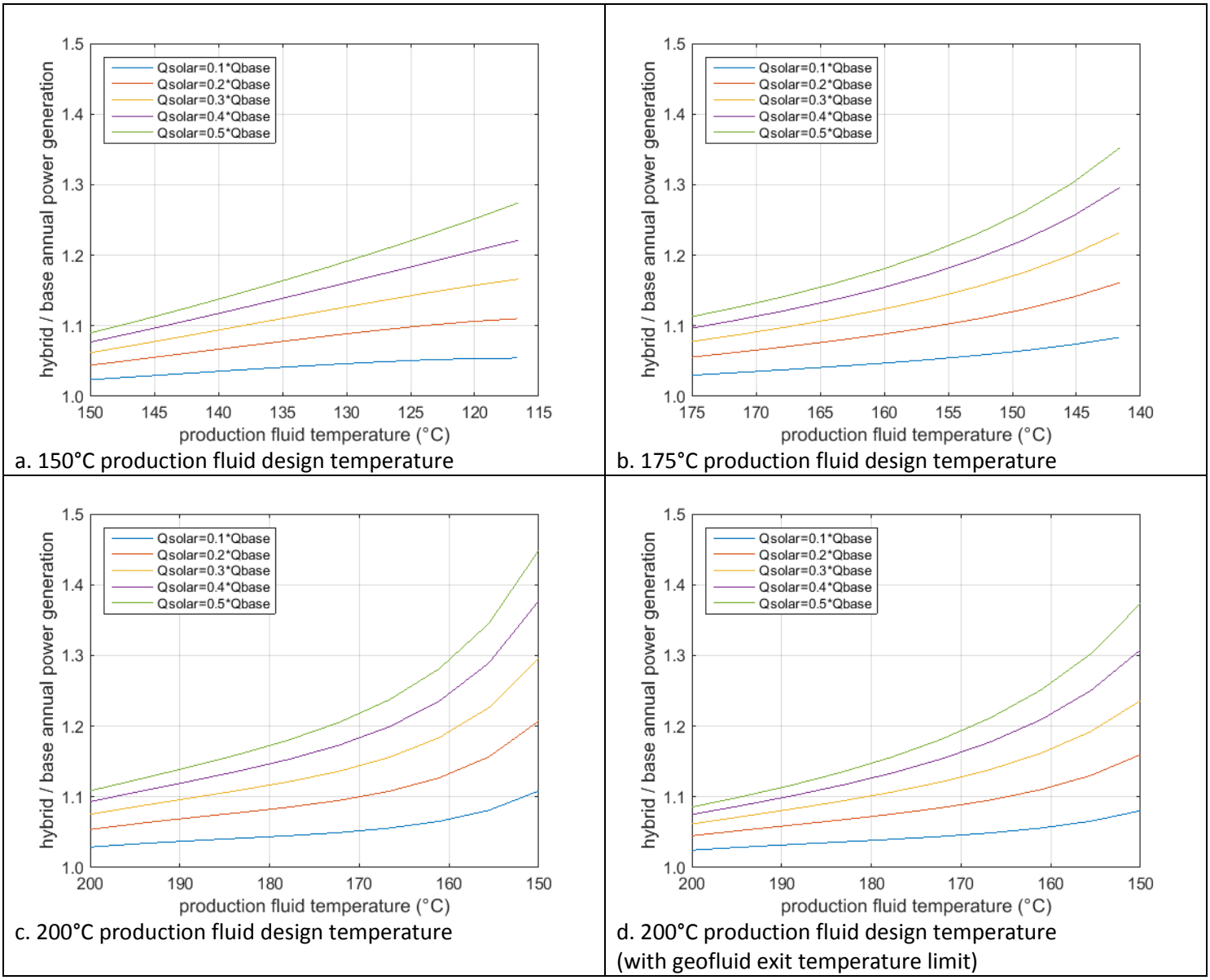

a. 150°C production fluid design temperature

b. 175°C production fluid design temperature

c. 200°C production fluid design temperature

d. 200°C production fluid design temperature (with geofluid exit temperature limit)

Figure D-21. Retrofit hybrid plant annual power generation (reported as fraction of base geothermal plant degraded resource annual power generation) plotted as function of production fluid temperature decline.

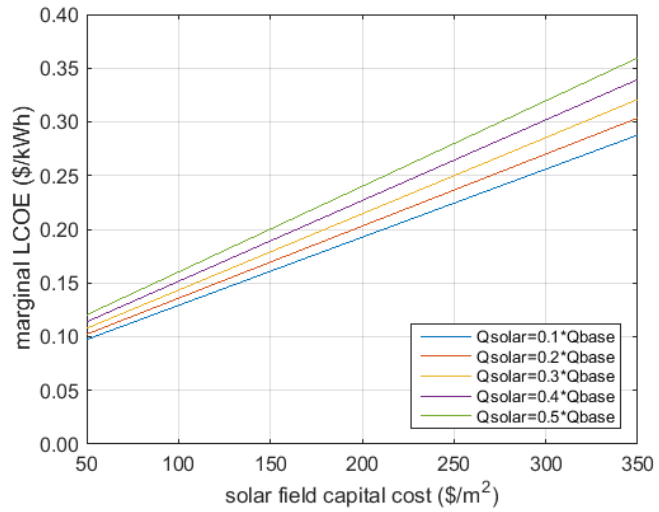

a. 150°C production fluid design temperature

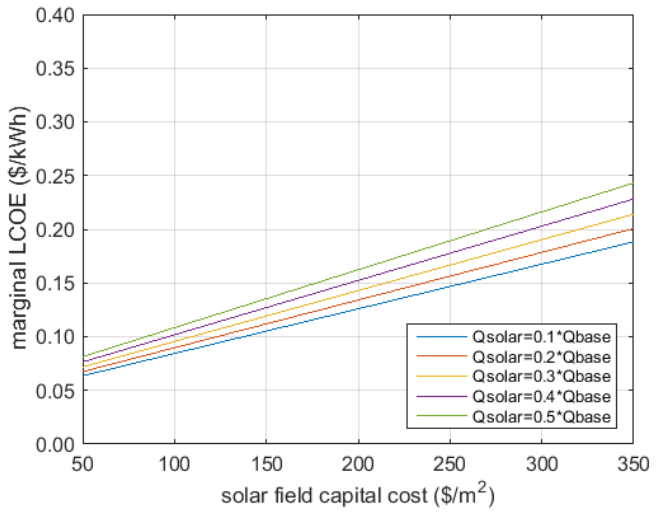

b. 175°C production fluid design temperature

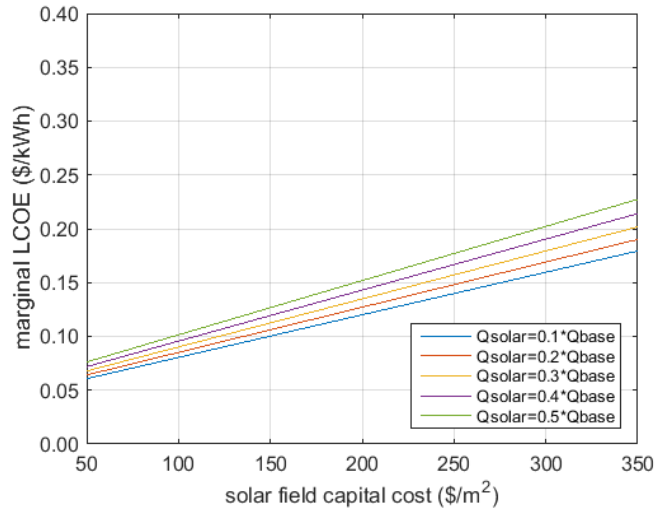

c. 200°C production fluid design temperature

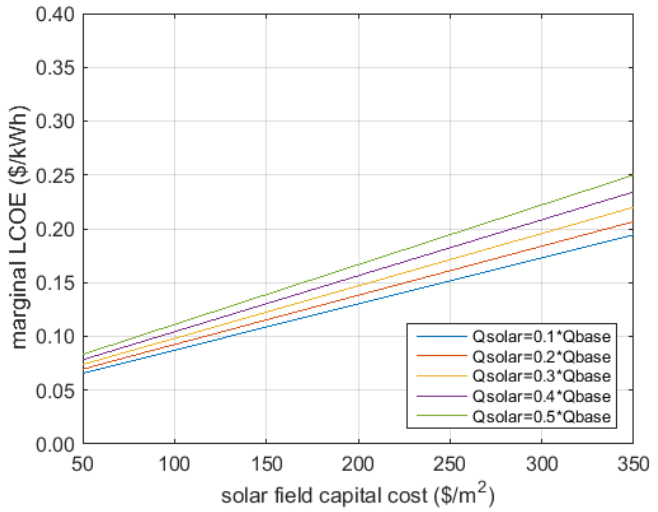

d. 200°C production fluid design temperature (with geofluid exit temperature limit)

Figure D-22. Marginal LCOE of solar retrofit of geothermal power plant plotted as function of solar field capital costs with solar field size as parameter.

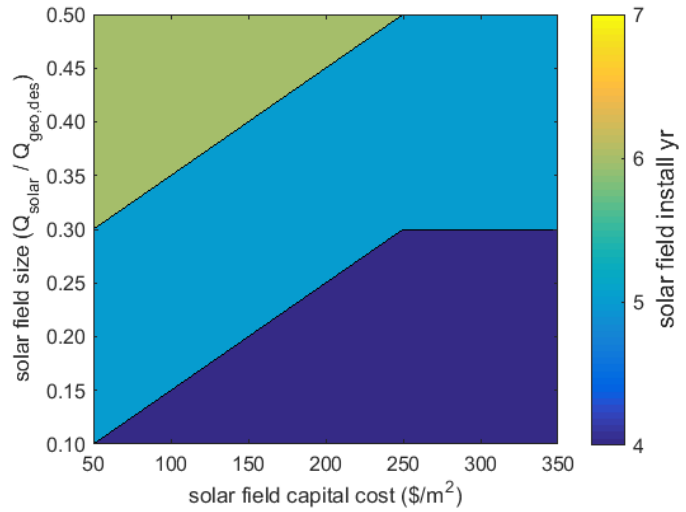

a. 150°C production fluid design temperature

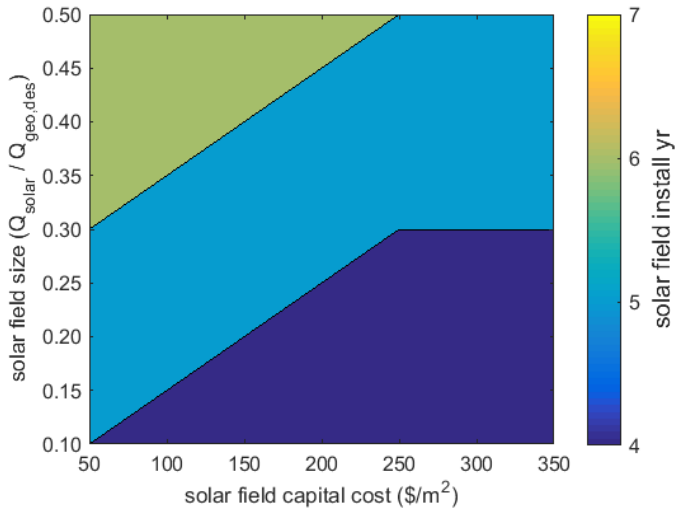

b. 175°C production fluid design temperature

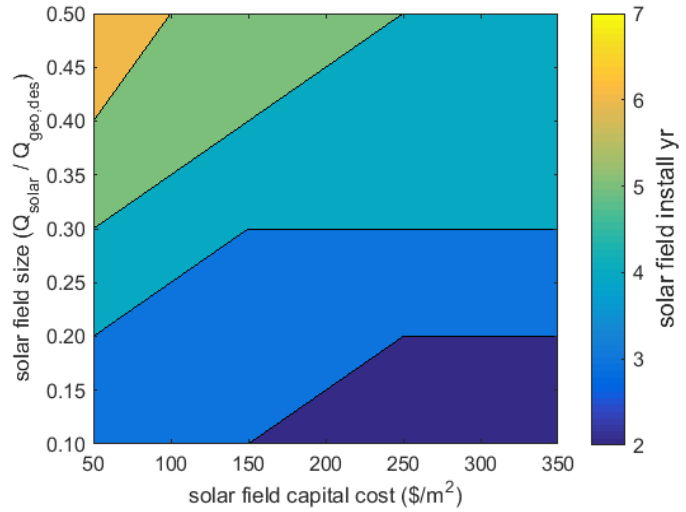

c. 200°C production fluid design temperature

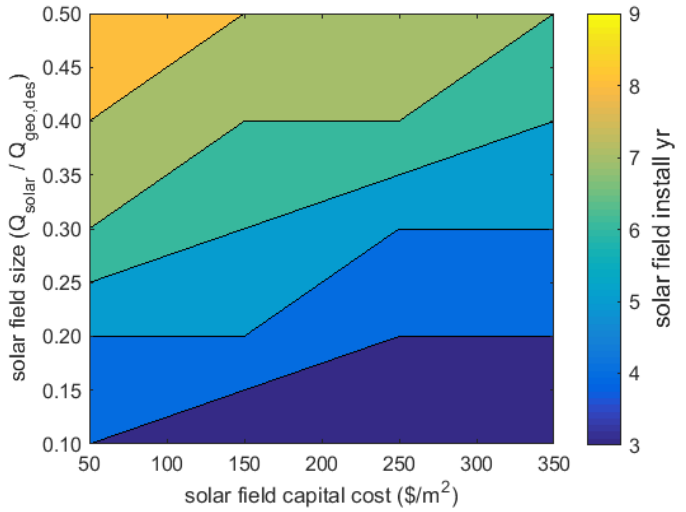

d. 200°C production fluid design temperature (with geofluid exit temperature limit)

Figure D-23. Optimized solar field installation year

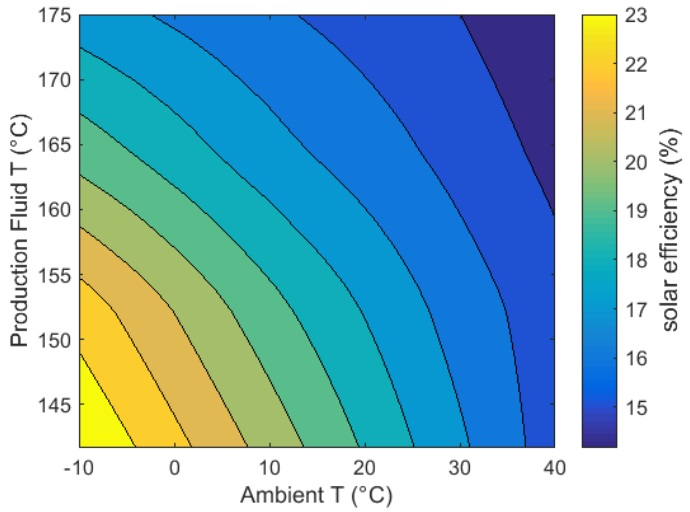

a. 175°C production fluid design temperature (basic cycle without brine exit temperature limit)

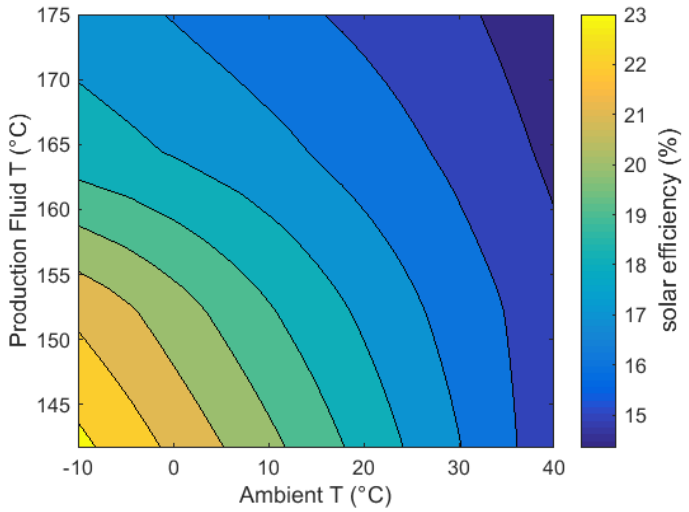

b. 175°C production fluid design temperature (recuperated cycle with brine exit temperature limit)

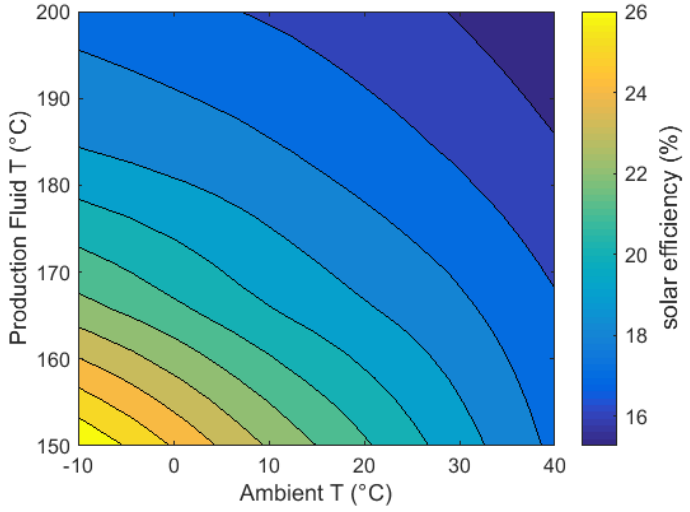

c. 200°C production fluid design temperature (basic cycle without brine exit temperature limit)

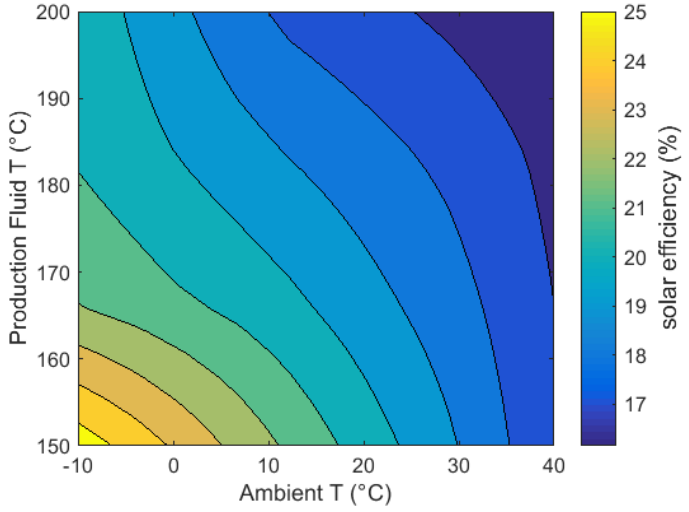

d. 200°C production fluid design temperature (recuperated cycle with brine exit temperature limit)

Figure D-24. Thermal efficiency of power conversion from solar heat addition equal to 25% of base plant design point heat input plotted as function of production fluid temperature and ambient temperature

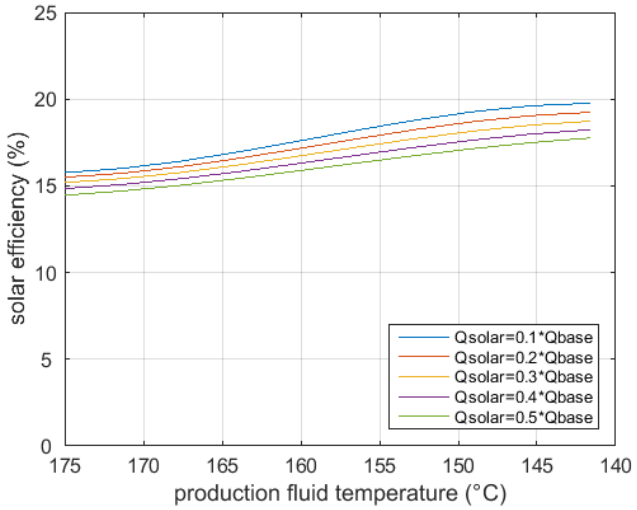

a. 175°C production fluid design temperature (basic cycle without brine exit temperature limit)

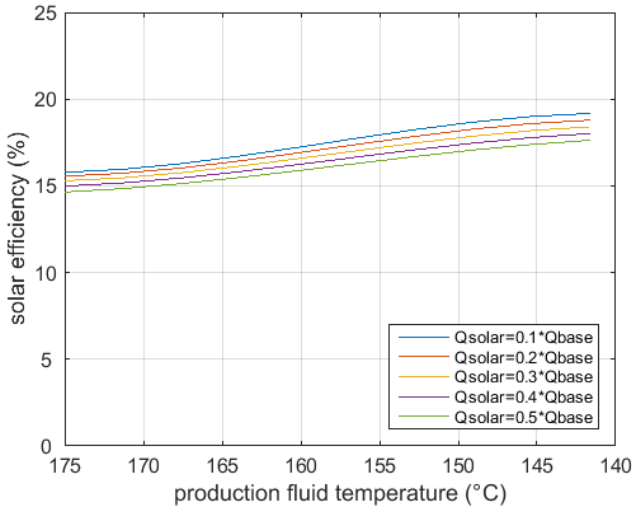

b. 175°C production fluid design temperature (recuperated cycle with brine exit temperature limit)

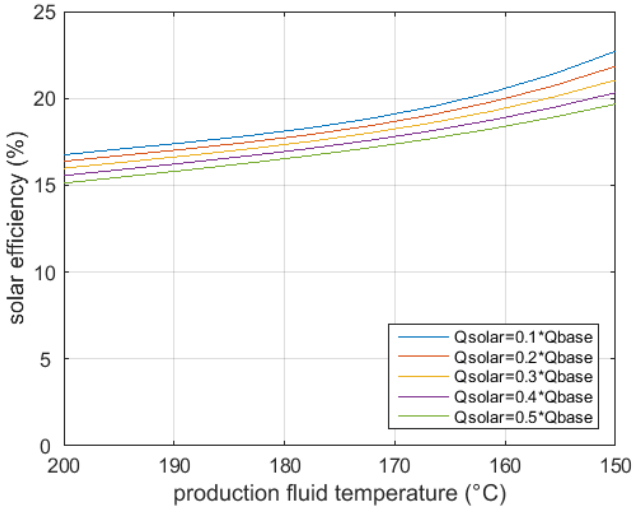

c. 200°C production fluid design temperature (basic cycle without brine exit temperature limit)

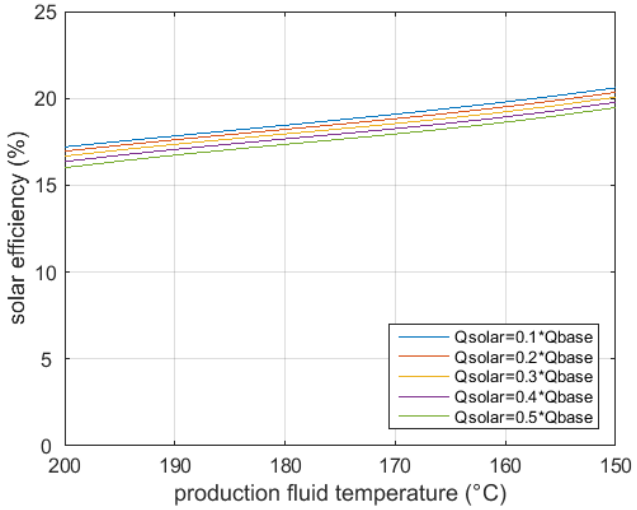

d. 200°C production fluid design temperature (recuperated cycle with brine exit temperature limit)

Figure D-25. Average annual solar efficiency as a function of production fluid temperature decline.

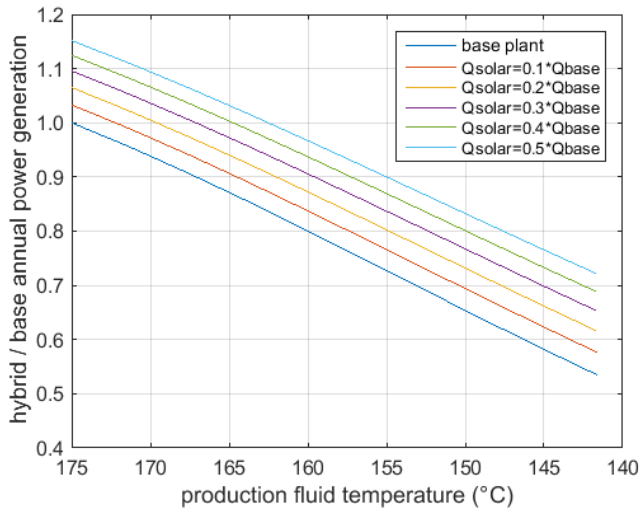

a. 175°C production fluid design temperature (basic cycle without brine exit temperature limit)

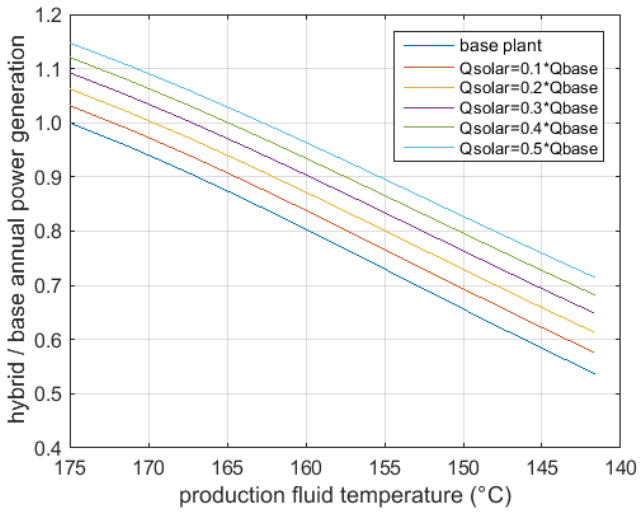

b. 175°C production fluid design temperature (recuperated cycle with brine exit temperature limit)

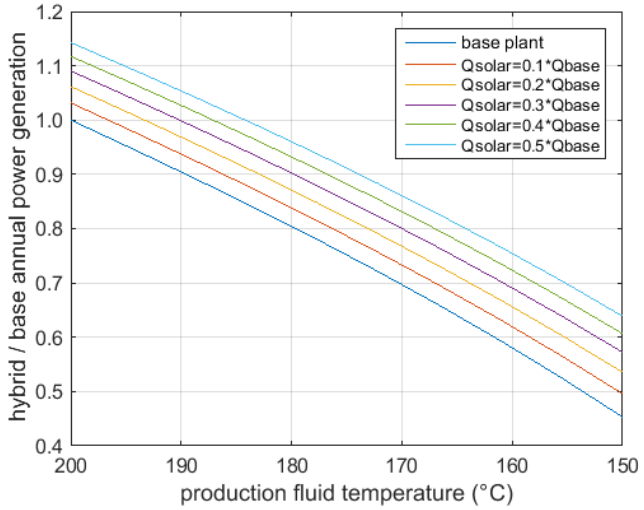

c. 200°C production fluid design temperature (basic cycle without brine exit temperature limit)

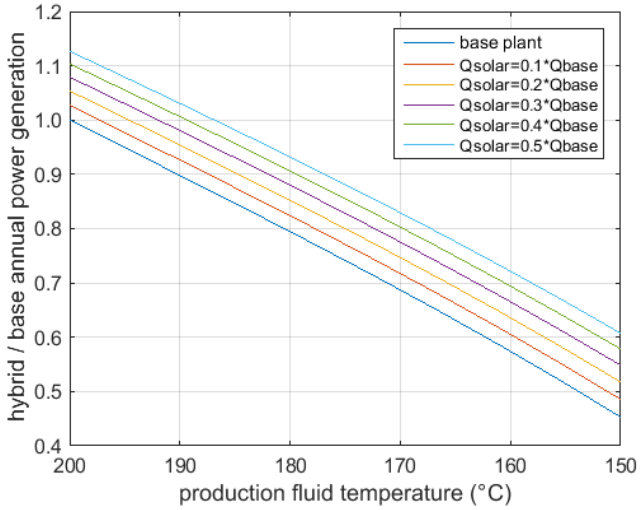

d. 200°C production fluid design temperature (recuperated cycle with brine exit temperature limit)

Figure D-26. Base and greenfield hybrid plant annual power generation (reported as fraction of base geothermal plant design annual power generation) plotted as function of production fluid temperature decline.

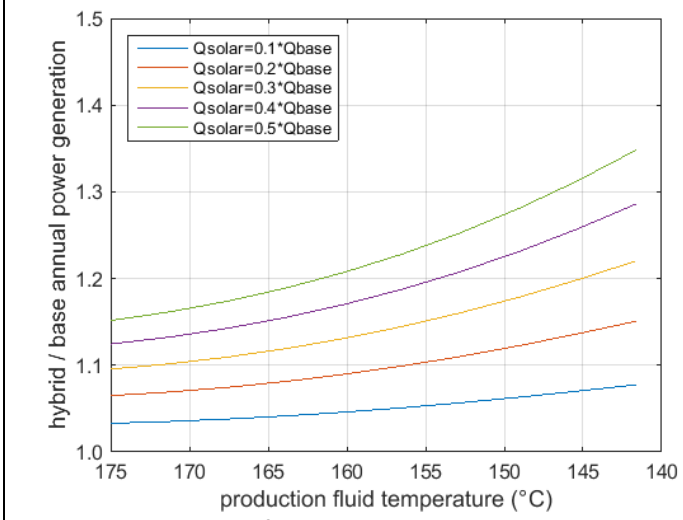

a. 175°C production fluid design temperature (basic cycle without brine exit temperature limit)

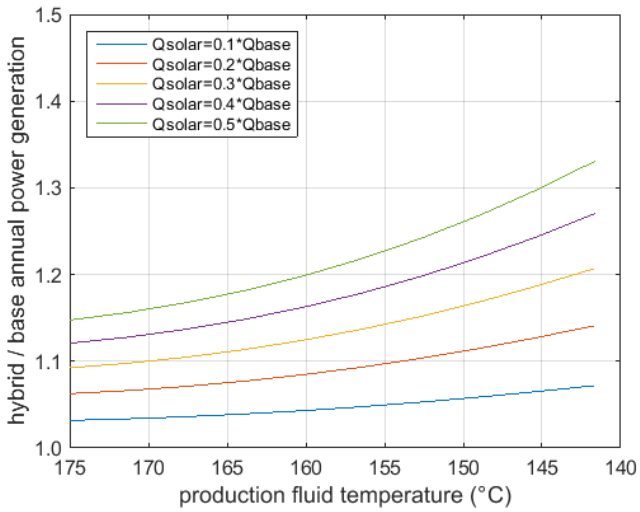

b. 175°C production fluid design temperature (recuperated cycle with brine exit temperature limit)

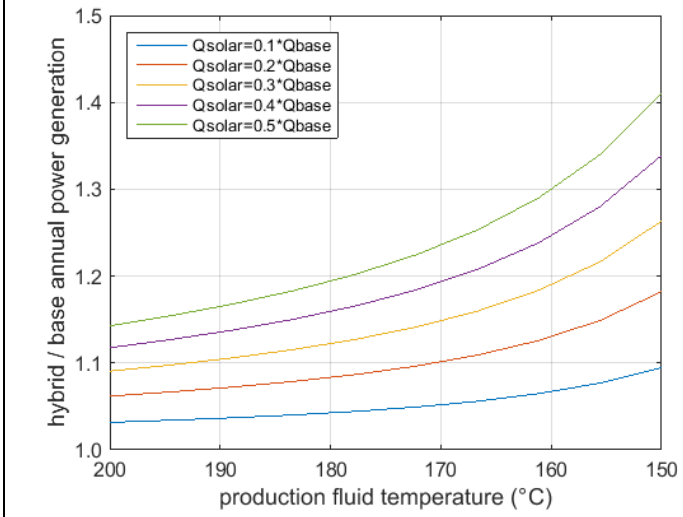

c. 200°C production fluid design temperature (basic cycle without brine exit temperature limit)

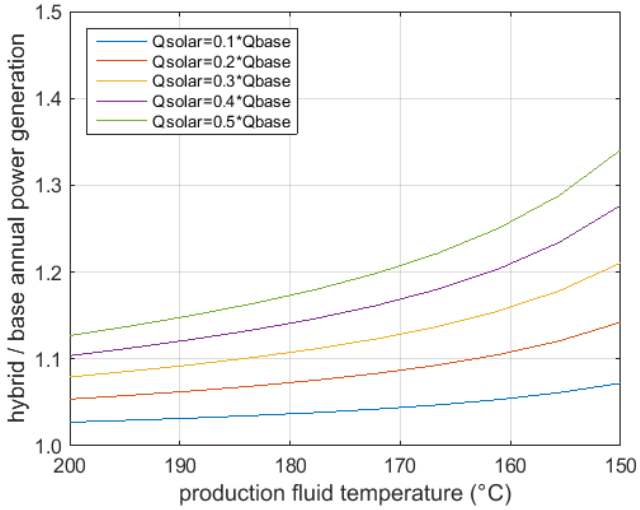

d. 200°C production fluid design temperature (recuperated cycle with brine exit temperature limit)

Figure D-27. Greenfield hybrid plant annual power generation (reported as fraction of base geothermal plant degraded resource annual power generation) plotted as function of production fluid temperature decline.

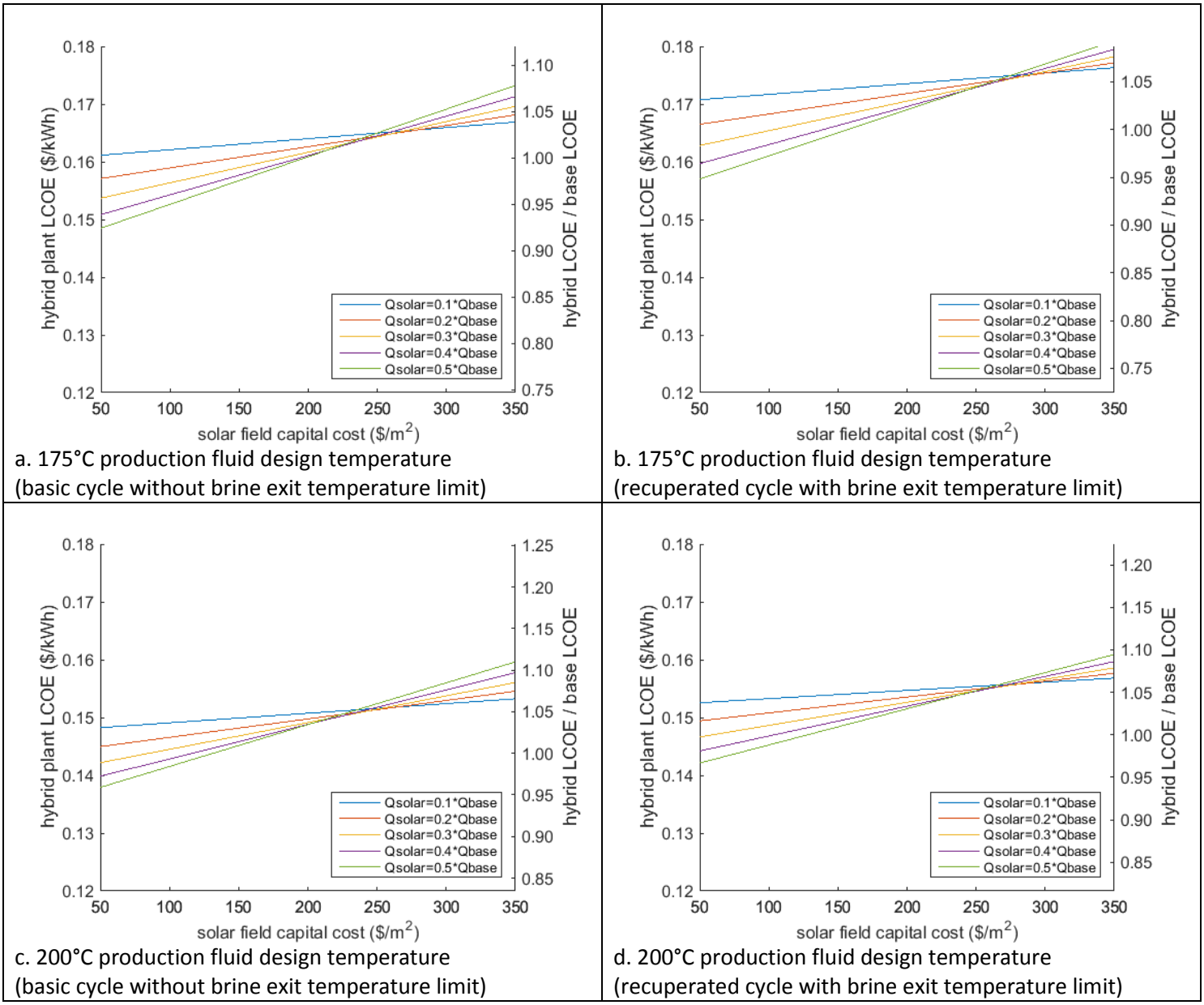

a. 175°C production fluid design temperature (basic cycle without brine exit temperature limit)

b. 175°C production fluid design temperature (recuperated cycle with brine exit temperature limit)

c. 200°C production fluid design temperature (basic cycle without brine exit temperature limit)

d. 200°C production fluid design temperature (recuperated cycle with brine exit temperature limit)

Figure D-29. Greenfield hybrid plant minimum electricity sales price (left y-axis) and ratio of hybrid-to-base LCOE (right y-axis) plotted as function of solar field capital costs for level pricing scheme.

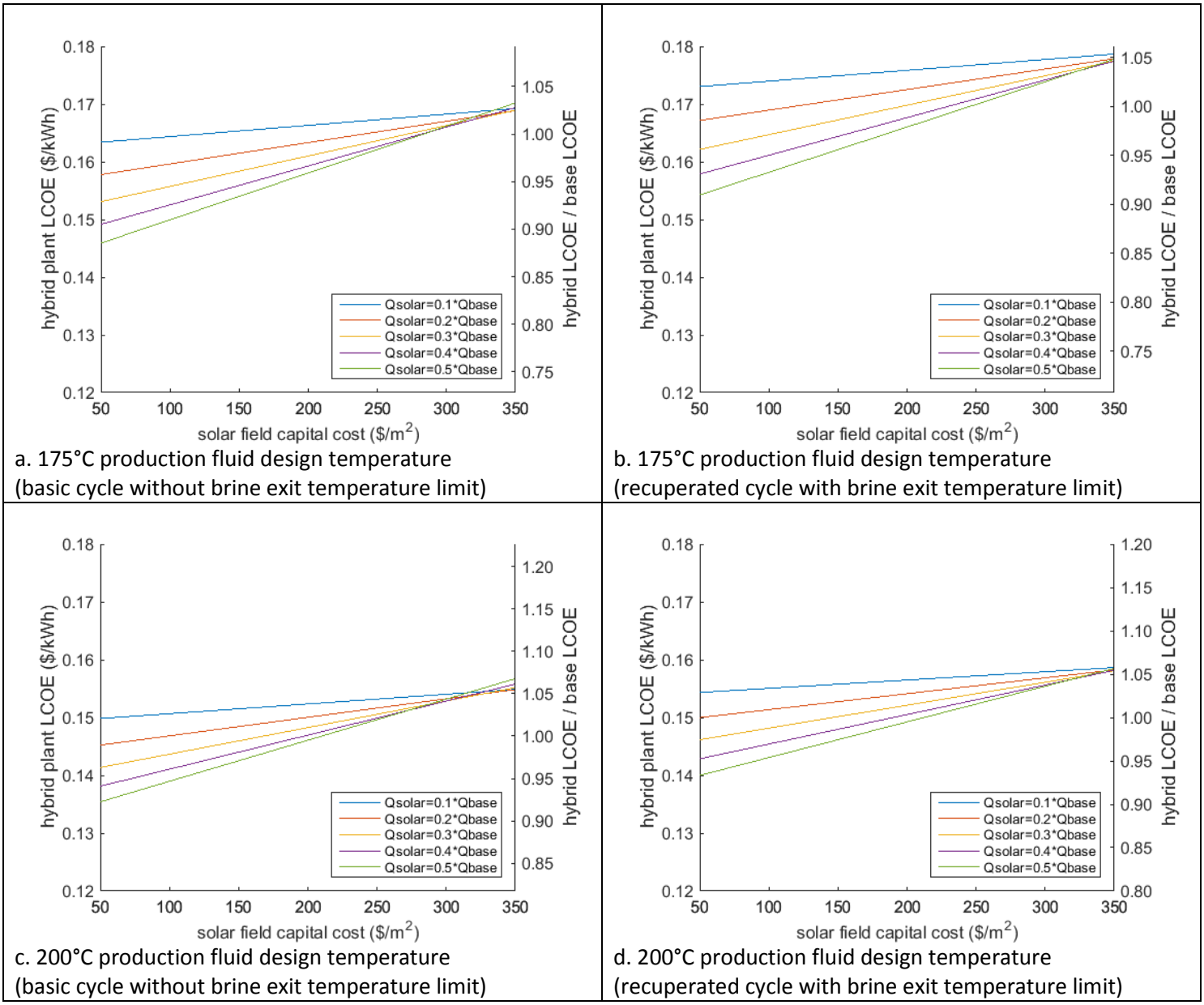

a. 175°C production fluid design temperature (basic cycle without brine exit temperature limit)

b. 175°C production fluid design temperature (recuperated cycle with brine exit temperature limit)

c. 200°C production fluid design temperature (basic cycle without brine exit temperature limit)

d. 200°C production fluid design temperature (recuperated cycle with brine exit temperature limit)

Figure D-30. Greenfield hybrid plant minimum electricity sales price (left y-axis) and ratio of hybrid-to-base LCOE (right y-axis) plotted as function of solar field capital costs for time-of-delivery pricing scheme.

Appendix E

Hybrid Plant Performance as Function of Geothermal Resource Flow Rate Decline

Appendix E
Hybrid Plant Performance as Function of Geothermal Resource Flow Rate Decline

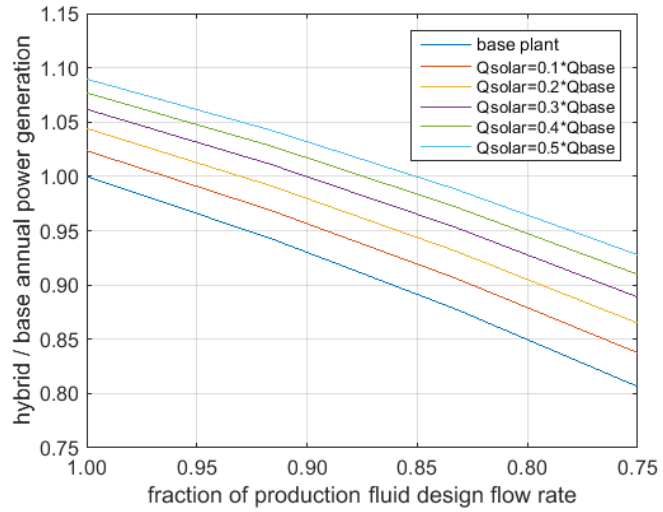

a. 150°C production fluid design temperature

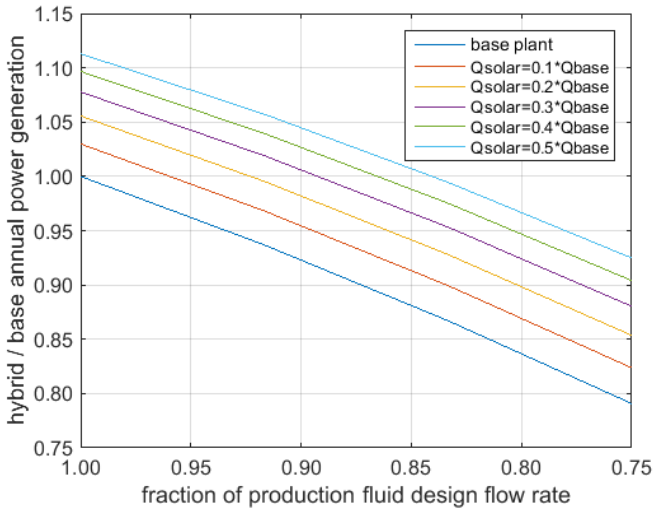

b. 175°C production fluid design temperature

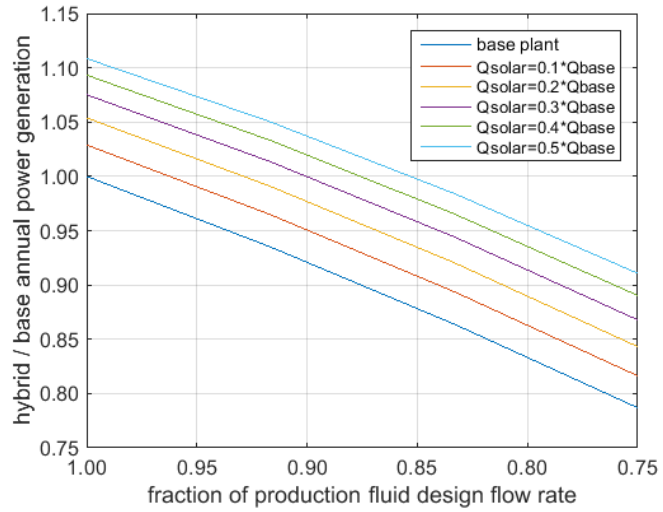

c. 200°C production fluid design temperature

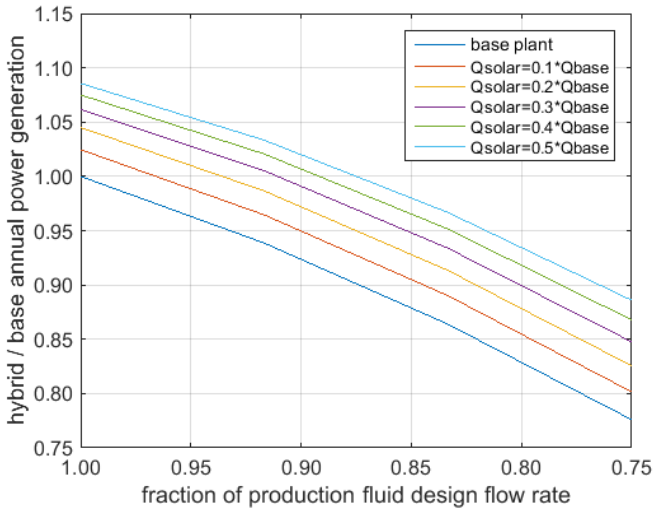

d. 200°C production fluid design temperature (with geofluid exit temperature limit)

Figure E-1. Base and retrofit brine preheating hybrid plant annual power generation (reported as fraction of base geothermal plant design annual power generation) plotted as function of production fluid flow rate decline.

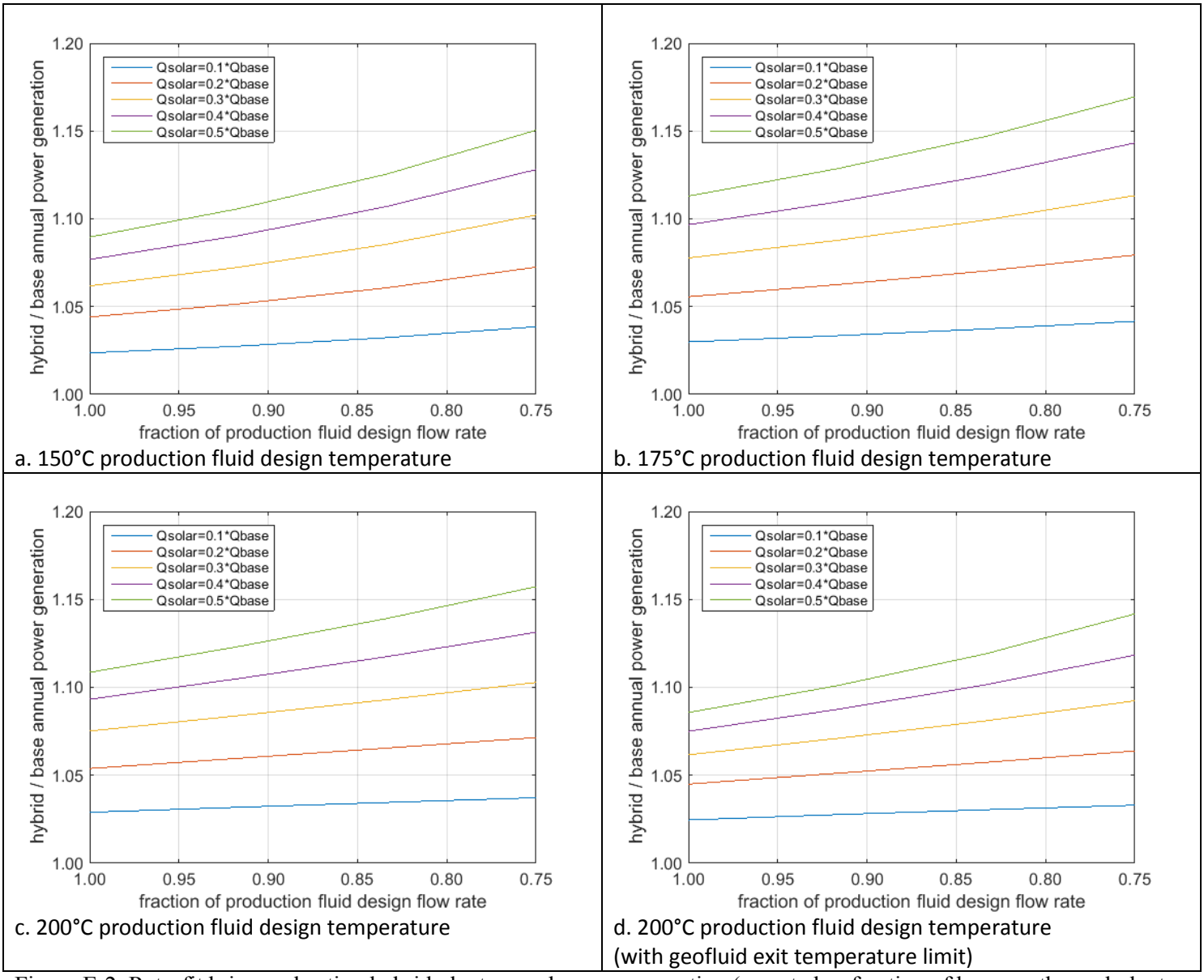

a. 150°C production fluid design temperature

b. 175°C production fluid design temperature

c. 200°C production fluid design temperature

d. 200°C production fluid design temperature (with geofluid exit temperature limit)

Figure E-2. Retrofit brine preheating hybrid plant annual power generation (reported as fraction of base geothermal plant degraded resource annual power generation) plotted as function of production fluid flow rate decline.

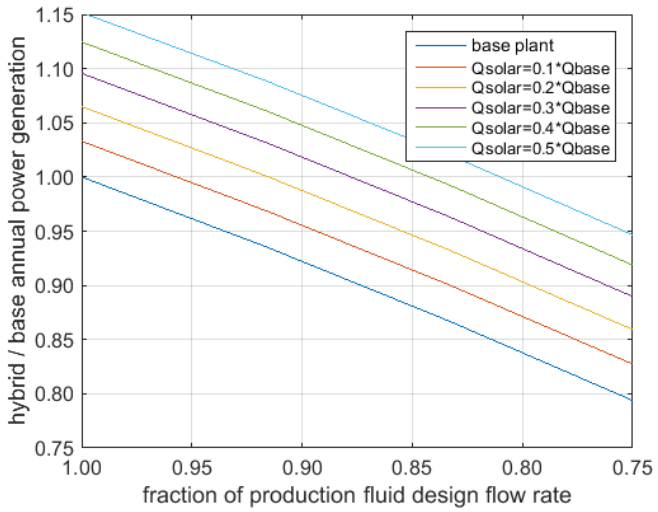

a. 175°C production fluid design temperature (basic cycle without brine exit temperature limit)

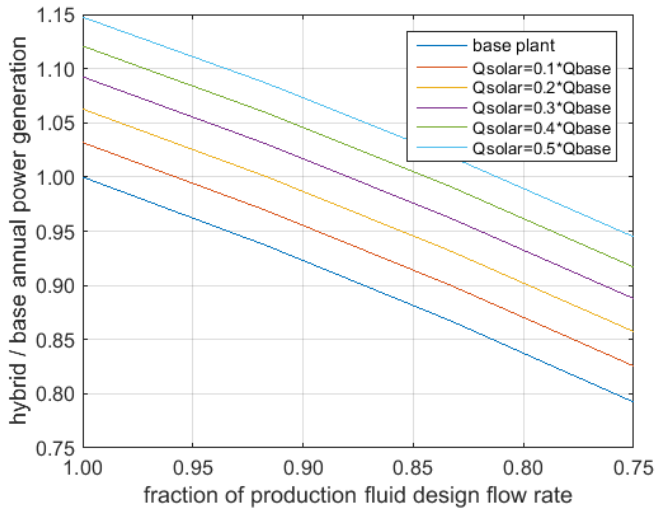

b. 175°C production fluid design temperature (recuperated cycle with brine exit temperature limit)

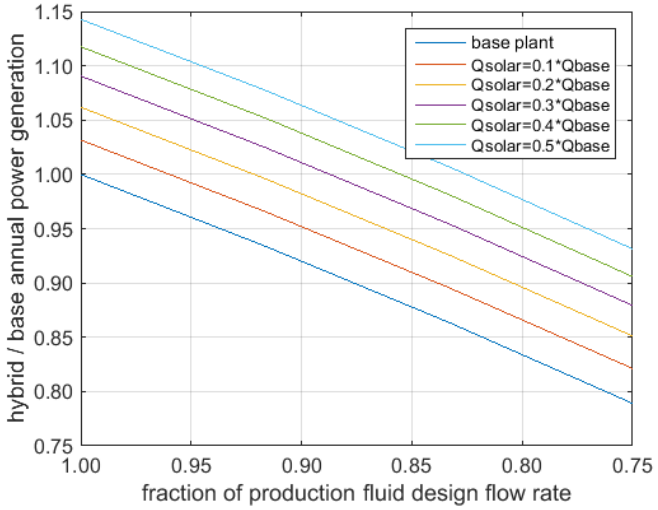

c. 200°C production fluid design temperature (basic cycle without brine exit temperature limit)

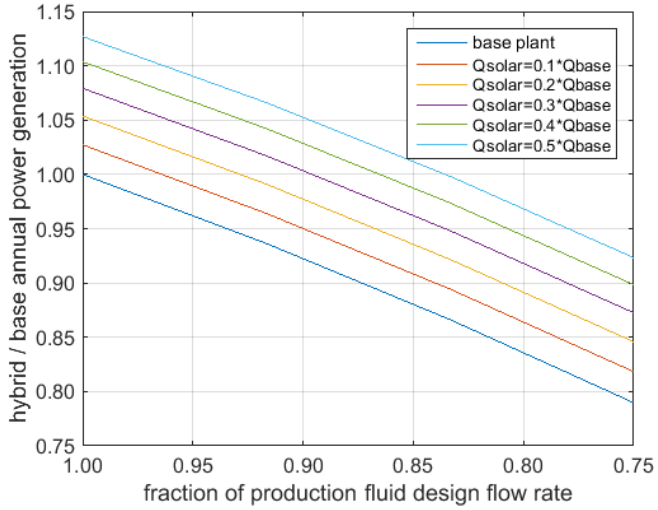

d. 200°C production fluid design temperature (recuperated cycle with brine exit temperature limit)

Figure E-3. Base and greenfield ORC working fluid heating hybrid plant annual power generation (reported as fraction of base geothermal plant design annual power generation) plotted as function of production fluid flow rate decline.

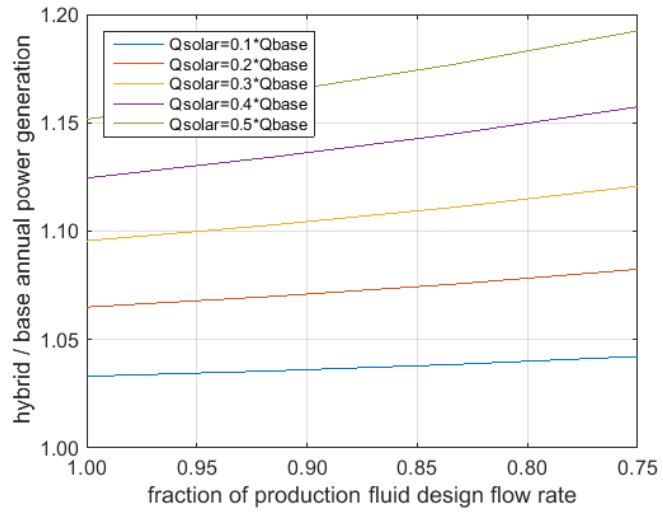

a. 175°C production fluid design temperature (basic cycle without brine exit temperature limit)

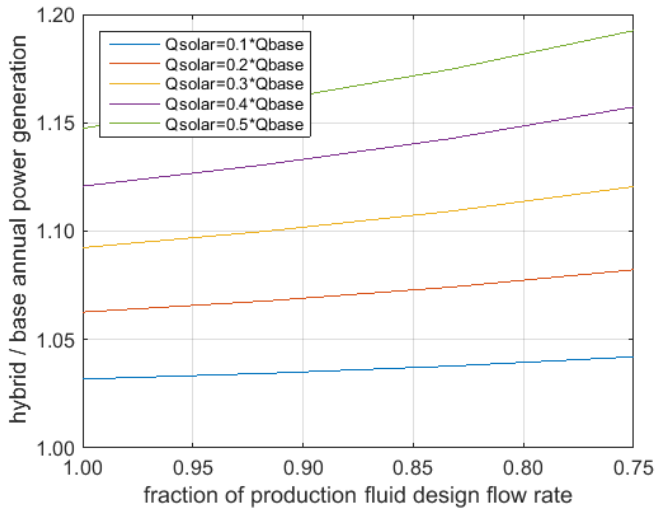

b. 175°C production fluid design temperature (recuperated cycle with brine exit temperature limit)

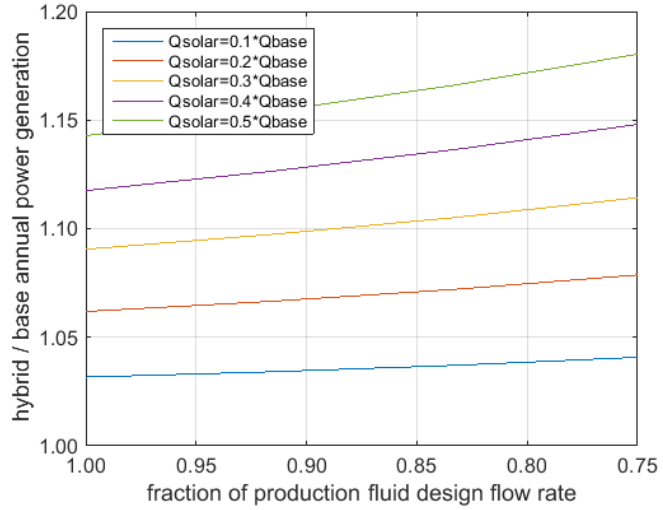

c. 200°C production fluid design temperature (basic cycle without brine exit temperature limit)

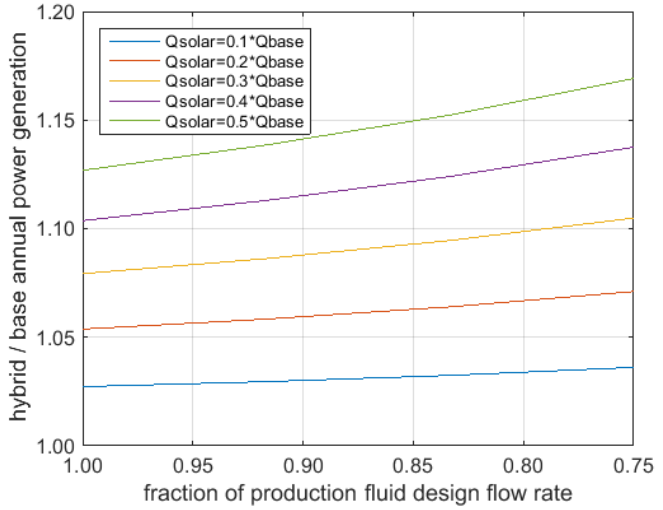

d. 200°C production fluid design temperature (recuperated cycle with brine exit temperature limit)

Figure E-4. Greenfield ORC working fluid heating hybrid plant annual power generation (reported as fraction of base geothermal plant degraded resource annual power generation) plotted as function of production fluid flow rate decline.

Appendix F

Stillwater Hybrid Geo-Solar Power Block Model Description

Appendix F
Stillwater Hybrid Geo-Solar Power Block Model Description

The Stillwater power plant performance was simulated using Aspen Plus V7.3 models developed at the Idaho National Laboratory. Stillwater concentrating solar array performance was simulated using the NREL System Advisor Model (SAM). Equipment specifications for the major process components were provided by Enel Green Power. The solar array thermal output was used to compute the heat input to the brine en route to the power plant. This approach allowed the hybrid plant performance to be 'mapped' as a function of brine flow rate, brine temperature (at solar field heat exchanger inlet), solar field thermal output, and ambient temperature. Power plant performance was simulated at 576 distinct operating points (unique combinations of four m_{gf}, three T_{gf}, four Q_{sol}, and twelve T_{air} input variable values) and a multidimensional interpolation MATLAB function was utilized to predict performance at intermediate combinations of input variables.

The Stillwater power plant includes constant speed as well as variable frequency drive working fluid pumps. The power plant model was configured with the appropriate number of working fluid pumps operating in parallel. Pump curves representative of the Stillwater pumps were input to the unit operation blocks. The constant speed pump model utilized one pump curve to compute pump discharge conditions. The VFD pump model utilized five pump curves [generated using affinity law relationships] to compute the performance of the VFD pump over the range of operating speeds possible. The working fluid flow rate to each of the pumps was manipulated such that the discharge pressure from each of the pumps was equal.

The Stillwater power plant model includes a valve block to simulate the performance of the Stillwater plant control valve. The valve pressure differential can be manipulated by the model to maximize net power generation or meet the power plant operating constraints imposed on the optimization routine.

The Stillwater power plant utilizes a preheater and vaporizer to transfer heat from the brine to the working fluid. The heat transfer performance of the preheater and vaporizer were calculated using inside and outside film coefficient regression correlations based on output from Aspen Shell & Tube Exchanger simulations performed over a range of operating conditions (vaporizer h_i, preheater h_i, and preheater h_o computed as function of working fluid flow rate; vaporizer h_o computed as function of vaporizer inlet pressure). The inside and outside film coefficients, estimated exchanger fouling, and heat exchanger wall construction specifications were used to calculate an overall heat transfer coefficient, U, which was multiplied by the specified heat exchanger area to compute heat exchanger UA. The UA was multiplied by the heat exchanger mean temperature difference to compute heat exchanger duty. The preheater and vaporizer heat exchangers were modeled using Aspen Plus MheatX heat exchanger blocks with countercurrent flow conditions specified. The MheatX log mean temperature difference was multiplied by a lumped correction factor to account for departure from countercurrent flow conditions as well as deviation between computed and actual performance data (determined by comparing predicted performance with plant operating data). The model manipulates the exchanger heat duty until the exchanger UA matches the target value calculated from the heat transfer correlations and exchanger surface area. Iterative solution is necessary since changing the heat duty specification results in changes to the exchanger mean temperature difference:

$$Q = F_T U A \Delta T \quad (2)$$

where Q is the exchanger duty, F_T is the cross flow correction factor, U is the overall heat transfer coefficient, A is the exchanger area, and ΔT is the log mean temperature difference.

Each unit of the Stillwater plant includes two turbines operating in parallel. Each of these turbines is equipped with variable geometry turbine nozzle vanes. The turbine performance was modeled using Aspen Plus Compr blocks. A performance calculator supplied by the turbine manufacturer was adapted for use in computing the efficiency of the turbines in the Aspen Plus model. The working fluid flow rate was restricted to values that could be achieved with the nozzle vanes positioned between the fully opened and fully closed positions with the assumption that choked flow conditions are maintained at the nozzle throat. Depending on ambient conditions, operation of one of the turbines in each unit may be curtailed. Two versions of the power plant model were developed; one model predicted plant performance during single turbine operation while the other model predicted plant performance during dual turbine operation.

The Stillwater plant utilizes an air-cooled working fluid condenser. Air flow across each of the condenser bundles is induced by three fans. Two of these three fans have VFD drives for varying the fan speed while the remaining fan utilizes a constant speed motor and operates at a constant speed. As ambient temperature decreases, the speed of the fans with VFD drives can be decreased to shed parasitic load.

The Stillwater power plant condenser heat transfer performance was calculated using a method similar to that implemented for the preheater and vaporizer. The outside heat transfer film coefficient, h_o, was calculated using a power-law regression correlation based on output from Aspen Air-Cooled Exchanger simulations performed over a range of air mass flow rates. The inside heat transfer film coefficient, h_i, was calculated the Boyko and Kruzhilin [42] correlation for average in-tube condensation heat transfer coefficient with inlet vapor quality of 1 and outlet vapor quality of 0:

$$h_i = 0.024 \frac{k_l}{d_i} Re_{i,l}^{0.8} Pr_{i,l}^{0.43} \left[\frac{1 + \sqrt{\rho_l / \rho_v}}{2} \right] \tag{3}$$

where h_i is the inside heat transfer film coefficient, k_l is the fluid thermal conductivity, d_i is the condenser tube inside diameter, $Re_{i,l}$ is the Reynolds number computed as if the entire condensing flow were liquid, $Pr_{i,l}$ is the Prandtl number for the liquid, and ρ_l and ρ_v are the liquid and vapor phase densities, respectively.

The Stillwater condenser fans were modeled using Aspen Plus Compr blocks. The constant speed fan model utilized one fan curve to compute fan discharge conditions. The VFD fan model utilized four fan curves generated using affinity laws to compute the performance of the VFD fans at decreased operating speeds. Pressure drop through the condenser bundle was estimated by correcting the design point pressure drop for changes in air density and volumetric air flow rate using the Darcy-Weisbach pressure loss equation:

$$\Delta p = f_D \cdot \frac{L}{D} \cdot \frac{\rho v^2}{2} \tag{4}$$

where Δp is the pressure loss due to friction, f_D is the dimensionless Darcy Friction Factor, L/D is the ratio of the length to the diameter of the flow path, ρ is the density of the fluid, and v is the mean fluid flow velocity. An Aspen Plus design spec was used to vary the air flow rate such that the fan discharge pressure was equal to atmospheric pressure.

When the VFD condenser fans are operated at reduced speed the air mass flow rate is not uniform across the bundle length since the operating speed of one of the three fans on each bundle is constant and cannot be changed. The condenser UA is calculated by computing the UA for the regions with constant fan speed and the regions with variable fan speed and then summing these values. As each bundle has 1 constant

speed fan and 2 variable speed fans, the heat transfer area is divided into thirds and the U for each of these areas is correlated to the air mass flow rate induced by the corresponding fan:

$$F_T UA = F_T \left(\frac{1}{3} U_{const\_speed} A_{o,bare} + \frac{2}{3} U_{var\_speed} A_{o,bare} \right) \quad (5)$$

where $F_T UA$ is the product of the cross flow correction factor, overall heat transfer coefficient, and condenser area; F_T is the cross flow correction factor; U_{const_speed} and U_{var_speed} are the overall heat transfer coefficients referenced to the condenser [outside bare tube] areas with constant and variable speed fan motors, respectively, and $A_{o,bare}$ is condenser outside bare tube area.

All condenser fans with VFD drives are generally operated at the same speed such that once the heat transfer performance for one condenser bundle has been determined, it can be assumed to be equivalent for all other condenser bundles. The condenser total UA can therefore be obtained by summing the UA contributions from each of the condenser bundles. The model manipulates the turbine outlet pressure until the condenser UA matches the target value calculated using the method described above.

Aspen pipe blocks were used to calculate the pressure losses through the various power plant pipe segments. Working fluid pressure losses in the preheater, vaporizer, and condenser were calculated using a method analogous to the Aspen Plus pressure drop correlation parameter calculation:

$$\Delta p = kW^2 \frac{(1/\rho_{in} + 1/\rho_{out})}{2} \quad (6)$$

where Δp is the pressure loss due to friction, k is the pressure-drop correlation parameter, W is the mass flow rate, and ρ_{in} and ρ_{out} are the inlet and outlet density, respectively.

Various Aspen Plus design specifications were utilized to emulate the Stillwater power plant control strategy. An optimization block was used to find the plant operating point with maximal net power output at each combination of the input variables (m_{gf}, T_{gf}, Q_{sol}, T_{air}). The optimization block varied the working fluid pump speed, the control valve position, the working fluid flow rate (which is equivalent to varying the turbine nozzle vane position), and the condenser fan speed to maximize net power generation. The optimization was constrained to operating points with specified values for turbine inlet superheat, turbine nozzle vane position, and brine outlet temperature.

Appendix G

Stillwater Hybrid Geo-Solar Power Plant Optimization Analysis

Stillwater Hybrid Geo-Solar Power Plant Optimization Analyses

Daniel S. Wendt[1], Gregory L. Mines[1], Craig S. Turchi[2], Guangdong Zhu[2], Sander Cohan[3], Lorenzo Angelini[3], Fabrizio Bizzarri[4], Daniele Consoli[4], and Alessio De Marzo[4]

[1]Idaho National Laboratory, Idaho Falls ID
[2]National Renewable Energy Laboratory, Golden CO
[3]Enel Green Power North America, Andover MA
[4]Enel Green Power — Innovation Div., Rome IT

Keywords

Hybrid geothermal solar thermal power plant, air-cooled binary cycle, organic Rankine cycle, ORC, concentrating solar power, simulation, optimization

ABSTRACT

The Stillwater Power Plant is the first hybrid plant in the world able to bring together a medium-enthalpy geothermal unit with solar thermal and solar photovoltaic systems. Solar field and power plant models have been developed to predict the performance of the Stillwater geothermal / solar-thermal hybrid power plant. The models have been validated using operational data from the Stillwater plant.

A preliminary effort to optimize performance of the Stillwater hybrid plant using optical characterization of the solar field has been completed. The Stillwater solar field optical characterization involved measurement of mirror reflectance, mirror slope error, and receiver position error. The measurements indicate that the solar field may generate 9% less energy than the design value if an appropriate tracking offset is not employed. A perfect tracking offset algorithm may be able to boost the solar field performance by about 15%.

The validated Stillwater hybrid plant models were used to evaluate hybrid plant operating strategies including turbine IGV position optimization, ACC fan speed and turbine IGV position optimization, turbine inlet entropy control using optimization of multiple process variables, and mixed working fluid substitution. The hybrid plant models predict that each of these operating strategies could increase net power generation relative to the baseline Stillwater hybrid plant operations.

Introduction

Geothermal energy is a reliable source for clean, renewable, base-load power. However, air-cooled geothermal power plants operate at reduced output levels during periods of elevated ambient temperature. Unfortunately, electrical power demand also tends to be greatest during periods at which ambient temperature is elevated, which results in power generation from air-cooled geothermal plants being out of sync with typical electrical load profiles.

Solar energy is also used for renewable power generation. Solar energy can be either directly converted to electrical power via photovoltaic devices or captured via concentrating solar thermal collectors such that the thermal energy output can be utilized by a thermoelectric power plant. In contrast to power generated from air-cooled geothermal plants, solar power is most plentiful during the time periods in which the electrical load is greatest. However, in the absence of thermal storage, solar power is unavailable at night or when the sun is obscured.

The aforementioned characteristics of geothermal and solar power generation create opportunities for synergistic use of these heat sources in a geothermal / solar-thermal hybrid power plant [1-12]. Geothermal / solar-thermal hybrid power plants have the ability to operate at higher output levels than comparably-equipped stand-alone air-cooled geothermal plants during periods when solar energy is available. Geo-solar hybrid plants don't require the heat storage infrastructure that would be required for a stand-alone solar plant to operate during periods when solar energy is unavailable. Additionally, a

single power block can be utilized to convert the geothermal and solar-thermal energy to electrical power rather than the two power blocks that would be required for two stand-alone geothermal and concentrated solar power plants.

Figure 1. EGP Stillwater Geothermal/PV/CSP Plant Rendering.

The primary disadvantages associated with geo-solar hybrid plant technology are attributed to the relatively high capital costs for concentrating solar thermal collectors, and the inability of many power cycle configurations to effectively utilize heat supplied at different temperatures for efficient power generation. These challenges are currently being investigated via a Cooperative Research and Development Agreement (CRADA) partnership involving Enel Green Power (EGP), the National Renewable Energy Laboratory (NREL), and the Idaho National Laboratory (INL) with oversight from the U.S. Department of Energy Geothermal Technologies Office (GTO).

EGP, NREL, INL and the GTO are working together to study the integration of geothermal and concentrated solar thermal heat sources for electrical power generation, with the goal of opening doors for the development of future hybrid renewable energy facilities. This paper describes CRADA tasks completed to date, including modeling the combination of geothermal and concentrating solar thermal systems, validating simulated results with real-world data from EGP's Stillwater hybrid facility, and using the validated models to quantify the potential benefits of different operating strategies.

The Enel Green Power Stillwater Hybrid Geothermal/Concentrating Solar Power (CSP) Project

Enel Green Power's Stillwater Geothermal/CSP project is the first hybrid plant in the world able to bring together at the same site the continuous generating capacity of binary-cycle, medium-enthalpy geothermal power with solar photovoltaic and solar thermal power.

Commencing operations during March 2015, the concentrating solar field adds an estimated 2MW of capacity (17MW thermal) to the existing 33MW Stillwater geothermal power plant. Production from the CSP plant will be integrated directly into the geothermal plant. It is the second solar facility on the site, joining a 26MW photovoltaic plant.

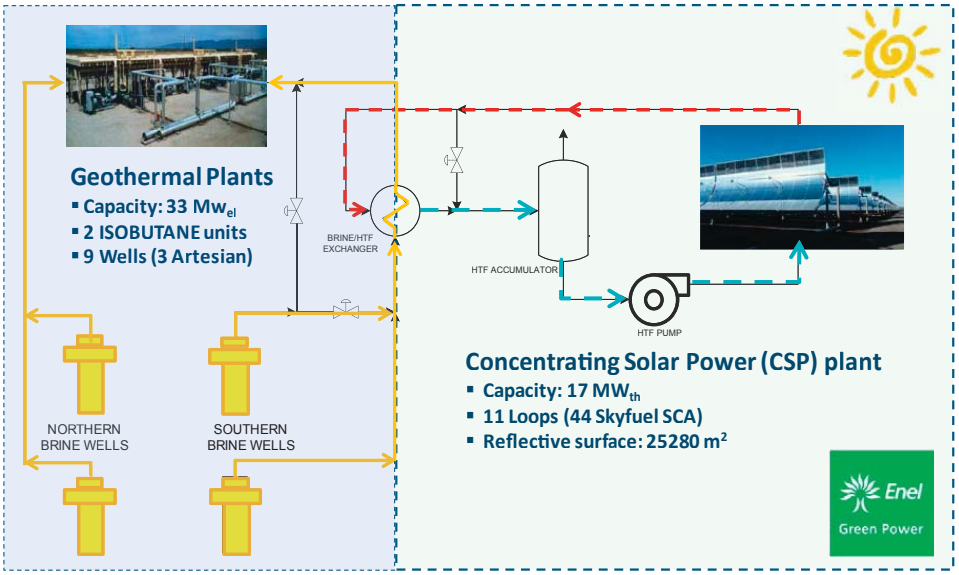

Figure 2. Stillwater CSP/GEO Process Flow Diagram Showing CSP Contribution to Geothermal Brine Temperature.

Figure 2 describes the main process of the project. The parabolic mirrors of the plant are used to direct solar energy to heat vacuum tubes filled with demineralized water. The heat collected by this system is then transferred to and augments the temperature of the geothermal fluid extracted from the facilities production wells, which is then used by the geothermal plant (via an Organic Rankine Cycle) to produce power.

The project consists of:

- 22 rows (11 loops) of parabolic solar concentrating mirrors; each row is 700 feet, each mirror is approximately 20 feet across, spread across more than 20 acres.

- Total of 2,772 mirror panels.
- Linear parabolic mirror totaling 24,778 m^2 (approx. 270,000 sq. ft.), capable of concentrating the solar radiation some 75 times, onto receiver tubes filled with demineralized water under pressure.

Enel Green Power embarked on this project as part of its ongoing Innovation efforts, specifically engaging in efforts to use hybrid applications to increase availability and mitigate intermittency seen in renewable energy projects.

As with the PV project before it the application of CSP is aimed at achieving these goals. The CSP plant is designed to improve the performance of the geothermal plant as a whole by providing an option of augmenting the input temperature of the geothermal plant with the heat of the sun, whose resource is more predictable and easily measurable. Specific anticipated benefits include:

- Increased production when the thermal efficiency of the geothermal unit is at its lowest.
- More delivery of power during peak hours, enabling a more load-following production profile.
- Less environmental footprint per unit of renewable energy produced and delivered.

In addition to near-term benefits of co-locating geothermal and CSP, the addition of CSP will allow for more effective management of the geothermal heat resource, which will potentially lead to lower long-term O&M costs.

Solar Field Characterization

Optical characterization of the solar field is critical to conduct the accurate prediction of solar field power output, which is essential for predicting how a combined geothermal/solar-thermal system will behave. A comprehensive optical test of the Stillwater plant's solar-thermal collector field was performed in December 2014. The optical testing measured the average solar field reflectance and the average solar collector optical error.

The solar field reflectance is obtained by using two portable reflectometer devices: Devices & Services R15 (D&S) [13] and Surface Optics Corporation Solar 410 (SOC) [14]. The former measures specular reflectance at varying acceptance aperture angles at a single wavelength of 660 nm and the latter measures solar-weighted specular reflectance at a large aperture angle. By combining measurements from two devices, solar weighted average reflectance including total specular reflectance and specularity can be derived.

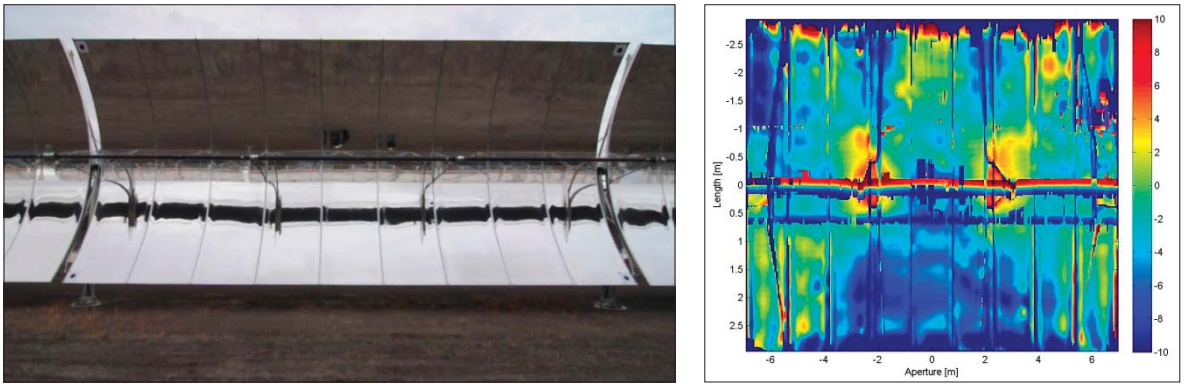

Figure 3. A snapshot of Distant Observer (DO) optical characterization: raw photo (left) and slope error map (right).

The collector optical error was characterized using NREL's Distant Observer (DO) methodology [15, 16]. DO is the first optical characterization tool in the world that can efficiently measure both the reflector slope error and the receiver position error at the same time in the field. DO simply requires a camera on a tripod to collect the reflection image. An example of a reflection image is shown in the left part of Figure 3. Then, an image-processing program is employed to analyze the images to derive mirror slope error. The right plot of Figure 3 shows an example of a mirror-slope error map, which accounts for both mirror slope error and receiver position error in this case.

The solar field at the Stillwater hybrid plant includes 11 loops of SkyTrough collectors, which con-

Table 1. Solar Collector Optical Specifications and Optical Error Measurements.

Parameter		Value	Source
Receiver	Absorptivity	0.96	Manufacturer
	Glass envelope transmissivity	0.97	Manufacturer
Mirror	Solar-weighted specular reflectance	0.904*	Measured
	Specularity RMS	1.915 mrad	Measured
	Slope error – mean value	-3.94 mrad	Measured, including the receiver position error.
	Slope error – mean value with tracking correction	1.00 mrad	
	Slope error – RMS	2.99 mrad	
Collector	Tracking error - RMS	1 mrad	Assumption

* measured average reflectance impacted by degradation to some panels that resulted from accidental water damage during storage

sists of a total 308 solar collector modules. Among all the modules, 44 modules were selected for reflectance measurements and 14 modules for DO measurements. After post-processing of the measurement data, the average optical measurement results were obtained, which are summarized in Table 1. The detailed results are reported elsewhere [17].

The overall solar field performance can be predicted from the optical test results using NREL's FirstOPTIC software [18] and System Advisor Model (SAM) [19]. An incident angle modifier (IAM) is typically used to describe the solar collector performance under non-zero incidence angle, that is, for different sun positions throughout the year. A common form for the IAM is:

$$IAM(\theta) = k_{IAM,0} + k_{\mathrm{IAM},1} \cdot \frac{\theta}{cos(\theta)} + k_{\mathrm{IAM},2} \cdot \frac{\theta^2}{cos(\theta)} + k_{\mathrm{IAM},3} \cdot \frac{\theta^3}{cos(\theta)} \quad (1)$$

The fitting function could be second-order or third-order. In general, the latter may provide less fitting error. SAM currently adopts the second-order IAM fitting function; however, an equation of this form was found to yield a poor fit to the Stillwater data. Accordingly, a third-order fit was applied and is shown in Figure 4.

The optical efficiency at a non-zero incidence angle is then:

$$\eta(\theta) = \eta_o \cdot IAM(\theta) = \rho\tau\alpha\gamma \cdot IAM(\theta) \quad (2)$$

Here, θ is the solar incidence angle in radians, ρ is the parabolic mirror reflectivity, τ the receiver glass envelope transmissivity, α the average receiver coating absorptivity, and γ the collector intercept factor. As measured, the predicted intercept factor is about 0.827 if no correction mechanism is used in the solar field. At the same time, it is observed that the total slope error has a mean value with a substantial magnitude, ranging from -2.9 mrad to -5.0 mrad. This indicates gravity-induce deflection of the receiver, which is most pronounced when the collectors are pointed at the horizon as they were for these measurements. In practice, this is compensated for by modification of the tracking algorithm. The slope error with a mean of -1 mrad can be compensated by +2 mrad tracking bias, which results into an effective slope error with a mean of 0 mrad. Thus, a similar strategy with tracking correction is applied to each collector samples with exactly twice the mean value of the measured slope error. It is assumed that the tracking correction method is able to reduce the mean value of slope error for any collector to be less than 1 mrad. When such a tracking correction mechanism is applied, the average intercept factor can be improved to 0.991. Tracking correction strategy also makes a great improvement on the IAM curve, as shown in Figure 4.

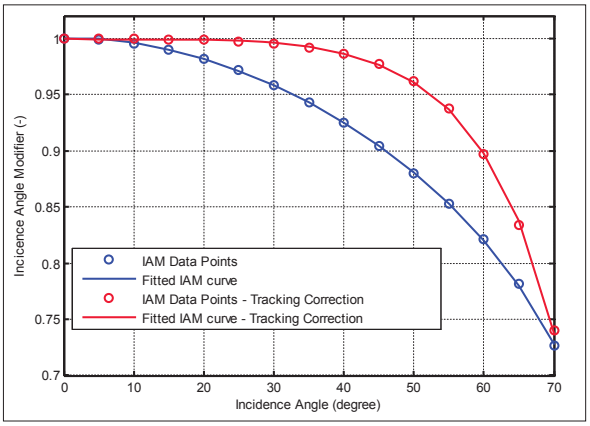

Figure 4. Incidence angle modifier curve: circles mark the predicted data points and the line indicates the fitting function.

Solar Field Model Description

The annual performance of the solar field array at Stillwater was simulated with the Physical Trough model within SAM. The 24,778 m^2 array consists of 11 loops, each loop having two 8-module solar collector assemblies (SCAs) and two 6-module SCAs. The shorter, 6-module SCAs were necessary to allow the trough loops to fit within the available land area. An initial SAM case was created based on the known dimensions of the solar array plus parameters from SkyFuel (collector) and Huiyin (receiver) vendor literature where available. SkyTrough parameters are provided within the SAM Solar Collector library. Default SAM values were used where vendor values were not available. The simulation used pressurized water as the solar-field heat transfer fluid (HTF) for the system. The initial analysis was performed with satellite-

Table 2. Revised input parameters and annual energy output based on measured values at Stillwater.

SAM input parameter	Original case based on SAM default or vendor literature values	Worst case based on measurements at Stillwater in the absence of a tracking offset	Best case based on measurement at Stillwater with Tracking Offset Algorithm
Absorber absorptance (receiver)	0.963	0.96	0.96
Envelope transmittance (receiver)	0.964	0.97	0.97
Mirror reflectance	0.93	0.904	0.904
Geometry effects	0.952	0.883	0.991
Tracking error	0.988	1*	1*
IAM coef. $k_{IAM,0}$	1	1	1
IAM coef. $k_{IAM,1}$	0.0327	0.0138	-0.0140
IAM coef. $k_{IAM,2}$	-0.1351	-0.2234	0.0622
IAM coef. $k_{IAM,3}$	-	0.1225	-0.0909
SAM annual performance prediction for 11-loop, 24,778 m^2 solar field			
Field thermal power produced (MWh/yr)	38,900	35,500	40,700

* tracking error corrections are included in geometry effects

generated solar resource data for Stillwater, NV, for 2013. The site now maintains a pyroheliometer for measurement of direct normal insolation (DNI) that will provide resource data measurements for subsequent simulations.

Following the collector field optical measurements, two cases were created that bound the anticipated field performance based on the effectiveness of the vendor's tracking offset algorithm. Actual performance will be evaluated by on-sun thermal tests. An estimate of solar field thermal energy over the course of a year is given in Figure 5.

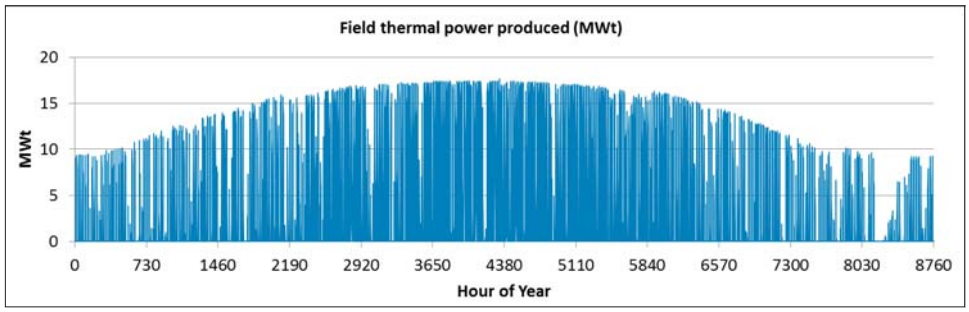

Figure 5. Hourly SAM-predicted solar field thermal energy output for Stillwater based on measured parameters listed in Table 2 and Stillwater, NV, solar resource for 2013.

As noted above, this work found that a third-order IAM equation was required to accurately represent the measured results. This necessitated a revision within SAM, and an internal-NREL version, designated SAM-2015-03-12, was utilized to allow a third-order IAM equation for the analysis. This feature will be available in the next public release of SAM.

The comparison outlined in Table 2 estimates the actual solar field performance will be about 9% lower than the published vendor estimates in the absence of any tracking correction. The greatest deviations are in the mirror reflectance (-3%) and the geometric accuracy of the collector (-7%). It is estimated that a significant boost in performance can be obtained through the tracking correction listed in the previous section. In the correction were 100% effective, this tracking correction could boost the annual field thermal power produced from the un-adjusted level by almost 15%, from 35,500 MWh to 40,700 MWh as shown in Table 2.

Hybrid Plant Model Description

The Stillwater power plant performance was simulated using Aspen Plus V7.3 models developed at the Idaho National Laboratory. Equipment specifications for the major process components were provided by Enel Green Power. The Stillwater power plant utilizes turbines with variable position inlet guide vanes (IGV), variable speed working fluid pumps, and variable speed air-cooled condenser fans. Each of these equipment components is present as multiple items operated in parallel. Certain operating conditions favor curtailing operations from one or more of the parallel equipment components, i.e. during periods of very low ambient temperature one of the cooling fans on each ACC bundle may be operated at a reduced speed or completely powered off.

As described in the previous section, the Stillwater concentrating solar array performance was simulated using the NREL System Advisor Model (SAM). The SAM solar array thermal output was used to compute the heat input to the brine en route to the power plant. This approach allowed the hybrid plant performance to be 'mapped' as a function of brine flow rate (m_{gf}), brine temperature (T_{gf}), solar field thermal output (Q_{solar}), and ambient temperature (T_{air}). Power plant performance was simulated at 576 distinct operating points (unique combinations of four m_{gf}, three T_{gf}, four Q_{solar}, and twelve T_{air} input variable values) and a multidimensional interpolation MATLAB function was utilized to predict performance at intermediate combinations of input variables.

The hybrid plant model was validated using operating data from the Stillwater plant. Net power generation is the primary value of interest for evaluation of hybrid plant performance. Therefore, the model validation evaluated the accuracy of predicted net power generation relative to actual net power generation.

Model validation was performed for both the base and hybrid plant configurations. Several years of base plant operating data was made available by Enel Green Power for validation of the base plant model. Base plant hourly operating data from 2013 was used for model validation purposes. The 2013 Stillwater operating data was parsed to identify week-long (168 hr) periods where the plant operated with a constant number of turbines and without any large disruptions in brine flow rate or temperature due to changes in well field operations. Twelve 168 hr periods meeting these criteria were identified. Ambient temperature values included in these periods ranged from 16°F to 106°F.

The base power plant performance predictions were compared with the plant operating data from each of the twelve 168 hour periods. A coefficient of determination, or R^2, was calculated to evaluate how well the model predictions fit the operational data. The R^2 values for the twelve 168 hr periods evaluated ranged from 0.953 to 0.987, implying very good correlation between predicted and actual values. Additionally, the cumulative power generation predicted by the model was compared with that from the actual plant operations for each of the 168 hr periods. The percentage error was then

calculated to indicate how much the predicted power generation differed from the values obtained from plant operating data. The predicted cumulative power generation for each of the 168 hr periods was within ±2% of the values obtained from plant operating data. This metric provides a useful measure of the model accuracy, since the evaluation of various hybrid plant operating strategies and configurations will require comparison of cumulative power generation over specified time periods. A graphical comparison of the predicted and actual base plant net power generation is provided in Figure 6. Net power generation y-axis values are not provided due to the proprietary nature of the plant operating data.

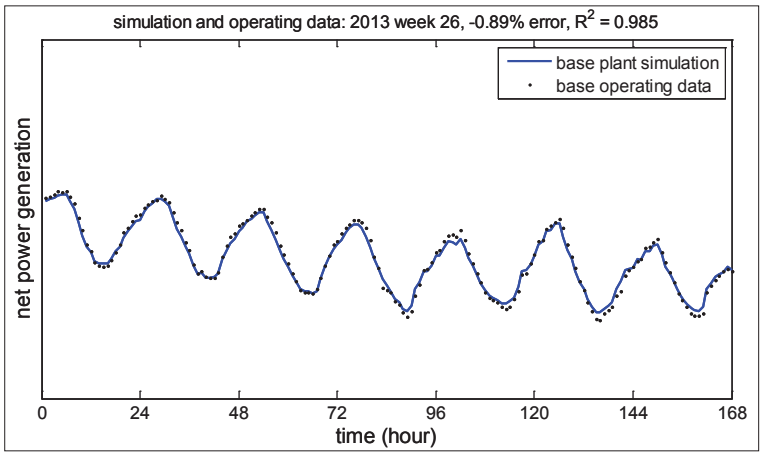

Figure 6. Comparison of simulated and reported base plant net power generation.

A less extensive operating data set was available for validating the hybrid plant model, due to the fact that the Stillwater hybrid plant operations had only recently commenced at the time the model validation was performed. The predicted hybrid plant cumulative power generation was within ±2% of the reported Stillwater hybrid plant power generation with an R^2 value greater than 0.95. Figure 7 is a graphical comparison of the predicted and reported hybrid plant net power generation. The predicted base plant net power generation is included for comparison purposes.

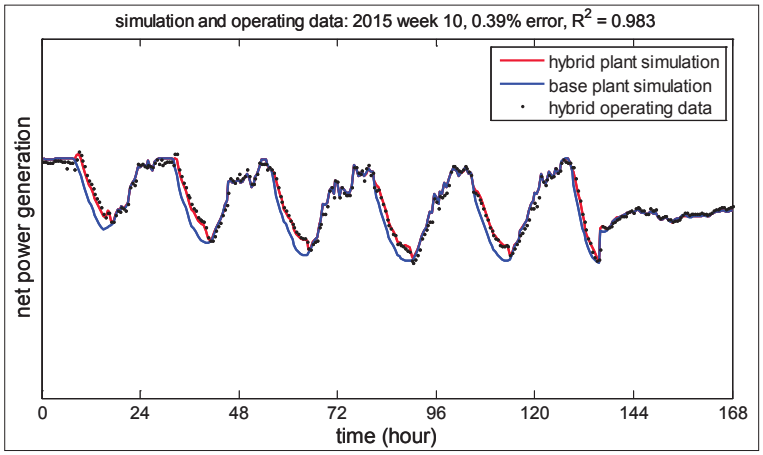

Figure 7. Comparison of simulated and reported hybrid plant net power generation.

Hybrid Plant Optimization

Several Stillwater hybrid plant operating strategies were investigated to identify methods that could be used to optimize hybrid plant performance. This analysis focused on performance optimization of the Stillwater hybrid plant as configured, i.e. the optimization considered modifications to the power plant operations and control strategies but configurations other than the brine preheating were not evaluated. The operating strategies considered include baseline Stillwater hybrid plant operations, IGV position optimization, ACC fan speed optimization, multivariable optimization with control of minimum turbine inlet entropy, and use of mixed working fluids.

The selected power plant operating strategies were evaluated using the validated Aspen Plus Stillwater hybrid plant model with the Aspen Plus Optimization Model Analysis Tool. The operating strategy optimizations sought to maximize net power generation while simultaneously satisfying all plant operating constraints. Operating constraints include specific limits on the working fluid minimum turbine inlet superheat (to prevent expansion within the two-phase region) and geothermal brine minimum exit temperature (to minimize preheater fouling from precipitation of minerals in the geothermal brine). The optimization was constrained to operating points attainable with the existing process operating equipment, i.e. combinations of turbine vane position, control valve position, working fluid pump speed, and ACC fan speed that can be achieved with the existing process equipment.

Plant performance comparisons were made for two operating periods: (1) a one month period representative of March 2015 and (2) a one year period with ambient conditions representative of a typical meteorological year and brine conditions representative of March 2015. The one month period analysis utilized brine temperature, brine flow rate, ambient temperature, and solar DNI data recorded during March 2015 at the Stillwater plant site. The one year period analysis utilized TMY ambient temperature and DNI data, while the average brine flow rate and brine temperature from March 2015 plant operations were used. The baseline hybrid plant turbine IGV position was input using either plant operating data (one month analysis) or a generalized correlation for turbine IGV position based on plant operating data (one year analysis). The number of turbines in service was based on plant operating data for the one month baseline hybrid plant evaluation, while all other evaluations used the configuration that maximized plant performance for each five day interval within the overall analysis period.

Turbine IGV Position Optimization

The Stillwater power block turbines are equipped with adjustable inlet guide vanes (IGVs). The IGV position can be utilized to adjust the turbine inlet pressure and working fluid flow rate. Active IGV control could be utilized to increase plant net power generation and/or respond to short term variances in the hybrid heat sources such as rapid increase or decrease in solar thermal energy input as a result of passing cloud cover.

The Stillwater plant IGVs are manually adjusted by the plant operators to accommodate changes to plant operations (i.e. changes in number of turbines operating or changes in production fluid conditions). The Stillwater IGVs are not typically adjusted in response to changes in ambient temperature.

The baseline hybrid plant simulation was performed using the IGV position reported in the operating data. The effect of optimizing the IGV position, and therefore the working fluid flow rate and turbine inlet pressure, was investigated by allowing the IGV position to be varied in the hybrid plant optimization simulations. It was determined that decreasing the IGV flow area at higher ambient temperatures resulted in decreased working fluid flow rate and increased turbine inlet pressure and temperature, which resulted in greater net power generation. The operating conditions associated with reduced IGV flow area were also utilized at low ambient temperatures to assist in preventing the geothermal brine minimum exit temperature limit from being exceeded. Relative to the baseline Stillwater hybrid plant operation, the hybrid plant model predicts that turbine IGV position optimization would increase net power generation by 1.2% for the March 2015 operating period and 2.0% for the TMY operating period. The optimized IGV position is plotted in Figure 8 as a function of ambient temperature, plant configuration (single and dual turbine operations), and solar heat input for brine conditions representative of March 2015.

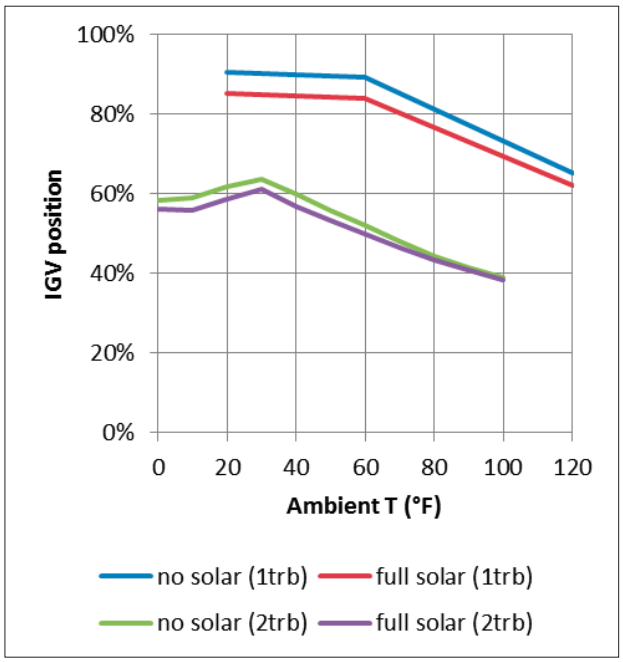

Figure 8. Simulation IGV position as function of ambient temperature, plant operating configuration, and solar heat input (March 2015 brine conditions).

ACC Fan Speed and Turbine IGV Position Optimization

The Stillwater hybrid plant VFD air-cooled condenser fans are slowed during periods of low ambient temperature to reduce power cycle parasitic loads. Reducing the ACC fan speed also assists in preventing working fluid condensation at pressures (and consequently temperatures) that result in the cooling of the geothermal brine to temperatures below the designated temperature limit for prevention of preheater fouling.

The baseline plant simulation used a control strategy that reduced the fan speed at low ambient temperature to prevent the working fluid condensing pressure and the geothermal brine exit temperature from dropping below the designated minimum values. The optimized fan speed simulations eliminated the working fluid condensing pressure constraint and allowed the fan speed to be varied as needed to reduce parasitic loads and maximize net power. When combined with turbine IGV position optimization, the fan speed can be reduced over a wider range of ambient temperature conditions to decrease parasitic loads and increase net power generation. The Stillwater hybrid plant model predicts that combined optimization of ACC fan speed and turbine IGV position would increase net power generation by 1.7% for the March 2015 operating period and 2.9% for the TMY operating period, relative to the baseline hybrid plant

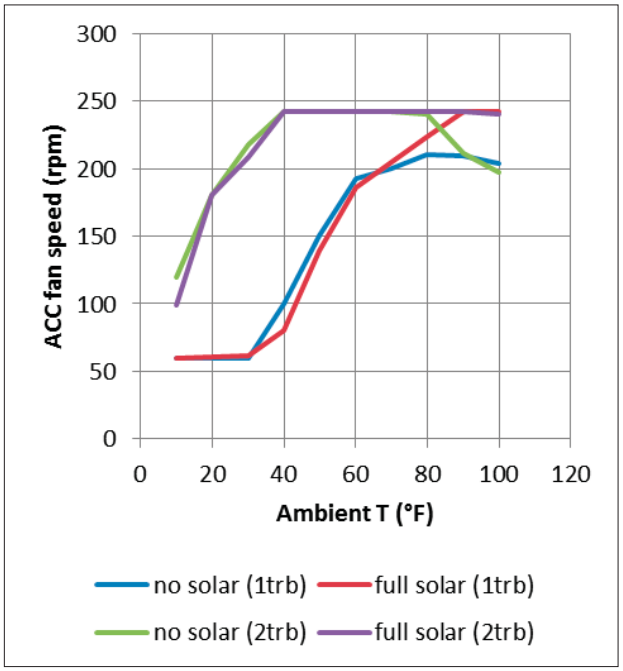

Figure 9. Optimized ACC fan speed as function of ambient temperature, plant operating configuration, and solar heat input (March 2015 brine conditions).

operation. The optimal ACC fan speed is plotted in Figure 9 for various ambient temperatures, plant operating configurations, and solar heat input levels. The geothermal brine minimum exit temperature constraint continued to be satisfied through manipulation of all available process operating variables (ACC fan speed, turbine vane position, control valve position, working fluid pump speed).

Multivariable Optimization Control Strategy

A control strategy that manipulated multiple process variables to control the minimum turbine inlet entropy and maximize net power generation was investigated. The process variables manipulated by this control strategy include the turbine IGV position, ACC fan speed, and working fluid pump speed. The control valve is left in the fully open position with minimal differential pressure drop unless throttling is necessary to satisfy the process operating constraints. In actual operations it is more common for a single process control variable to be associated with a single process operating target; this control strategy may therefore be more complex to implement in an operations environment.

The minimum turbine inlet entropy is a function of temperature and pressure as illustrated in Figure 10. The maximum working fluid dew point entropy is identified as point 'Smax' on the temperature-entropy diagram. At pressures above the maximum dew point entropy pressure, the control strategy adjusts the turbine inlet entropy to the value that corresponds to 1 degree of superheating of the conditions where the maximum dew point entropy occurs. At pressures below the maximum dew point entropy pressure, the control strategy adjusts the turbine inlet entropy to a value that corresponds to 1 degree of superheating. This control strategy prevents turbine inlet conditions that could result in expansion within the two-phase region while minimizing working fluid superheating to increase gross turbine power generation.

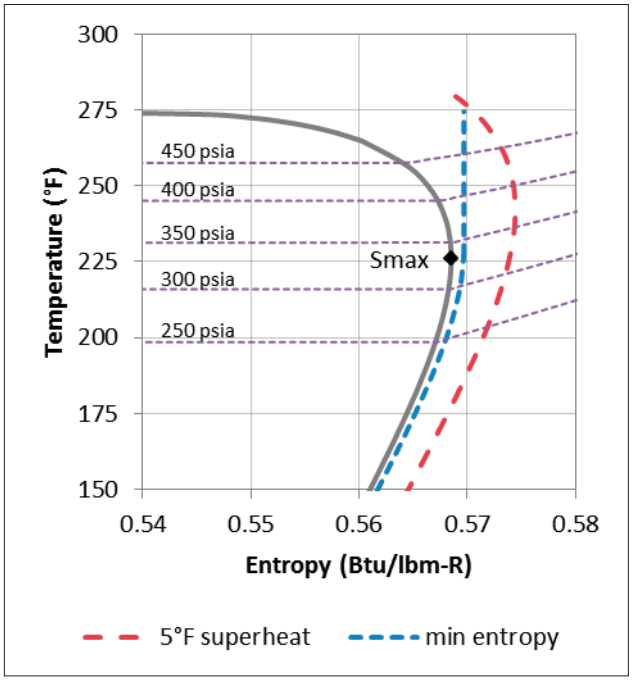

Figure 10. T-S diagram with comparison of minimum entropy vs. constant superheat turbine inlet conditions.

The Stillwater hybrid plant model predicts that the multivariable optimization control strategy would increase net power generation by 2.5% for the March 2015 operating period and 3.8% for the TMY operating period, relative to the baseline hybrid plant operation.

Mixed Working Fluid Retrofit

Mixed working fluids have non-isothermal vaporization and condensation behavior that cause them to perform differently than pure working fluids in organic Rankine cycle operation. The non-isothermal phase change properties of mixed working fluids can eliminate heat exchanger pinch points and decrease the mean temperature difference between the hot and cold fluids so as to reduce power cycle thermodynamic losses. These performance gains typically come at the expense of increased heat exchanger area due to decreased heat transfer performance and heat exchanger mean temperature differences. The potential performance gains associated with mixed working fluids may therefore be negated by the additional capital costs necessary to achieve optimal mixed working fluid power cycle performance.

In the event an organic Rankine cycle is operating at conditions different from the original design conditions, use of mixed working fluids could increase plant performance. The primary power plant equipment requirements include heat exchangers with sufficient heat transfer surface area, multi-pass air-cooled condensers to approximate counter-current condensation, and counter-flow shell and tube style (rather than kettle-type) vaporizers.

The performance of the Stillwater hybrid plant with the multivariable optimization control strategy was evaluated with a 30 wt% propane 70 wt% isobutane mixed working fluid composition. The Stillwater hybrid plant model predicts that the mixed working fluid substitution would increase net power generation by 10.0% for the March 2015 operating period and 7.6% for the TMY operating period, relative to the baseline hybrid plant operation. The evaluation did not consider the detrimental effects of the mixed working fluid on the convective heat transfer coefficients or the possibility of differential condensation (vapor and liquid phases are separated in condenser with a subsequent departure from phase equilibrium conditions) as the current model configuration does not include these capabilities, nor has it been validated for

use with mixed working fluids. The mixed working fluid performance results therefore represent the best case scenario, and further investigation is needed to refine the mixed working fluid results.

Table 3 summarizes the net power generation change of the hybrid plant operating strategies evaluated relative to the baseline Stillwater hybrid plant operation.

Table 3. Predicted net power generation changes for selected hybrid plant optimization strategies relative to baseline Stillwater hybrid plant operation.

	March 2015 power generation	**TMY annual power generation**
input data	**March 2015 Stillwater hybrid plant operating data (ambient T, solar DNI, brine flow, brine T)**	**TMY ambient T and solar DNI; March 2015 Stillwater hybrid plant average brine conditions**
turbine IGV position optimization	+1.2%	+2.0%
ACC fan speed + turbine IGV position optimization	+1.7%	+2.9%
multivariable optimization control strategy	+2.5%	+3.8%
mixed working fluid (30% C_3 + 70% iC_4)*	+10.0%	+7.6%

*effect of mixed working fluid composition on heat transfer coefficients and possibility of differential condensation not considered

Conclusion

CRADA activities have resulted in the optical characterization of the Stillwater hybrid plant solar field and the development and validation of a hybrid plant model. The solar field optical characterization analysis indicated that solar field tracking correction to counteract the effects of reflector slope error and receiver position error could improve the solar field thermal performance by up to 15% relative to uncorrected solar field operation. The hybrid plant model was used to evaluate operating strategies that included turbine IGV position optimization, ACC fan speed and turbine IGV position optimization, turbine inlet entropy control using optimization of multiple process variables, and mixed working fluid substitution. For a one month period with brine and ambient conditions corresponding to March 2015, the hybrid plant model predicted that these operating strategies could result in net power generation increases of up to 10%. For a one year period with brine conditions corresponding to March 2015 and ambient conditions corresponding to a typical meteorological year, the hybrid plant model predicted that these operating strategies could result in net power generation increases of up to 7.6%.

Acronyms

ACC	air-cooled condenser
CRADA	cooperative research and development agreement
CSP/CST	concentrating solar power/thermal
DNI	direct normal insolation
DO	distant observer
EGP	Enel Green Power
GTO	Geothermal Technologies Office
HTF	heat transfer fluid
IAM	incident angle modifier
IGV	inlet guide vanes
INL	Idaho National Laboratory
NREL	National Renewable Energy Laboratory
ORC	organic Rankine cycle
PV	photovoltaic
SAM	System Advisor Model
SCA	solar collector assembly
TMY	typical meteorological year
VFD	variable frequency drive

Acknowledgement

This work was supported by the United States Department of Energy under contract numbers DE-AC07-05ID14517 with the Idaho National Laboratory and DE-AC36-08-GO28308 with the National Renewable Energy Laboratory.

References

1. Astolfi, M., et al., *Technical and economical analysis of a solar–geothermal hybrid plant based on an Organic Rankine Cycle.* Geothermics, 2011. 40(1): p. 58-68.
2. Greenhut, A.D., *Modeling And Analysis Of Hybrid Geothermal-Solar Thermal Energy Conversion Systems*, in *Department of Mechanical Engineering*. 2010, Massachussetts Institute of Technology.
3. Greenhut, A.D., et al. *Solar-Geothermal Hybrid Cycle Analysis For Low Enthalpy Solar And Geothermal Resources*. in *Proceedings World Geothermal Congress*. 2010. Bali, Indonesia.
4. Handal, S., Y. Alvarenga, and M. Recinos. *Geothermal steam production by solar energy*. in *GRC Transactions*. 2007.
5. Lentz, Á. and R. Almanza, *Parabolic troughs to increase the geothermal wells flow enthalpy.* Solar Energy, 2006. 80(10): p. 1290-1295.
6. Lentz, Á. and R. Almanza, *Solar–geothermal hybrid system.* Applied Thermal Engineering, 2006. 26(14-15): p. 1537-1544.
7. Manente, G., *Analysis and Development of Innovative Binary Cycle Power Plants for Geothermal and Combined Geo-Solar Thermal Resources*. 2011, Università degli Studi di Padova.
8. Manente, G., et al. *Hybrid Solar-Geothermal Power Generation To Increase The Energy Production From A Binary Geothermal Plant*. in *Proceedings of the ASME 2011 International Mechanical Engineering Congress & Exposition*. 2011. Denver, Colorado.
9. Paci, M., I. Fastelli, and N. Rossi, *Advanced Systems For Power Production From Geothermal Low Temperature Resources*. 2009.
10. Todorovic, M.S., *Parametric Analysis And Thermodynamic Limits Of Solar Assisted Geothermal Co- And Tri-Generation Systems.* ASHRAE Transactions, 2011.
11. Zhou, C., *Figure of merit analysis of a hybrid solar-geothermal power plant.* Engineering, 2013. 05(01): p. 26-31.
12. Zhou, C., E. Doroodchi, and B. Moghtaderi, *An in-depth assessment of hybrid solar–geothermal power generation.* Energy Conversion and Management, 2013. 74: p. 88-101.
13. Devices & Services Co.; Available from: http://www.devicesandservices.com.
14. Surface Optics Corporation. Available from: http://www.surfaceoptics.com.
15. Stynes, K. and B. Ihas, *Slope Error Measurement Tool for Solar Parabolic Through Collectors*, in *the World Renewable Energy Forum*. 2012: Denver, CO.
16. Stynes, K. and B. Ihas, *Absorber Alignment Measurement Tool for Solar Parabolic Trough Collectors*, in *ASME 2012 6th International Conference on Energy Sustainability*. 2012: San Diego, CA.
17. Zhu, G., et al., *Solar Field Optical Characterization at Stillwater Geothermal/Solar Hybrid Plant.* In preparation, 2015.
18. Zhu, G. and A. Lewandowski, *A New Optical Evaluation Approach for Parabolic Trough Collectors: First-principle OPTical Intercept Calculation (FirstOPTIC).* Journal of Solar Energy Engineering, 2012. 134.
19. NREL. *System Advisor Model 2015.1.30*. Available from: https://sam.nrel.gov/.

Appendix H

Use of Geothermal Energy for CSP Feedwater Heating

Geothermal / Solar Hybrid Designs: Use of Geothermal Energy for CSP Feedwater Heating

Craig Turchi[1], Guangdong Zhu[1], Michael Wagner[1], Tom Williams[1], and Daniel Wendt[2]

[1]National Renewable Energy Laboratory, Golden, Colorado, USA
[2]Idaho National Laboratory, Idaho Falls ID, USA

Keywords

Geothermal, solar, CSP, hybrid, feedwater heating

ABSTRACT

This paper examines a hybrid geothermal / solar-thermal plant design that uses geothermal energy to provide feedwater heating in a conventional steam-Rankine power cycle deployed by a concentrating solar power (CSP) plant. The geothermal energy represents approximately 11% of the annual thermal input to the hybrid plant. The geothermal energy allows power output from the hybrid plant to increase by about 8% relative to a stand-alone CSP plant with the same solar-thermal input. Geothermal energy is converted to electricity at an efficiency of 1.7 to 2.5 times greater than would occur in a stand-alone, binary-cycle geothermal plant using the same geothermal resource.

While the design exhibits a clear advantage during hybrid plant operation, the annual advantage of the hybrid versus two stand-alone power plants depends on the annual operating hours of the different plants. Annual net power from the hybrid plant matches the combined output from a stand-alone CSP plant and stand-alone geothermal plant when the assumed stand-alone geothermal plant availability is 74% or less. The cost implications are not covered in this study, but the hybrid plant avoids the need for an ORC power block and produces more power during hot afternoons that generally correspond to peak demand periods.

Introduction

Solar thermal power, also known as concentrating solar power (CSP) differs from solar photovoltaic power in that thermal energy is collected and converted into electricity via a thermo-electric power cycle. Thus, CSP shares similarities with other thermo-electric generation methods that use nuclear, fossil, or geothermal heat sources. This commonality has led to frequent and various investigations of ways to combine CSP with other thermal sources. While a multitude of possible integrations are possible, the challenge is to combine two heat sources in a synergistic fashion, that is, one in which benefits are realized by both technologies.

This paper describes a geothermal / solar thermal hybrid design that utilizes low-temperature geothermal heat to provide feedwater heating in a CSP plant that operates at a much higher temperature. The CSP plant drives an air-cooled, steam-Rankine power cycle with superheated-steam inlet conditions of 371°C and 91 bar, and a gross thermal-to-electric conversion efficiency of approximately 35% [1]. This hybrid design allows for integration of the two heat sources at temperatures that best align with their resources and collection technologies.

Background

In 2013 Zhou et al. summarized a number of studies that proposed or examined geothermal / solar thermal hybrids [2]. The reports listed in Zhou's paper included various schemes for use of

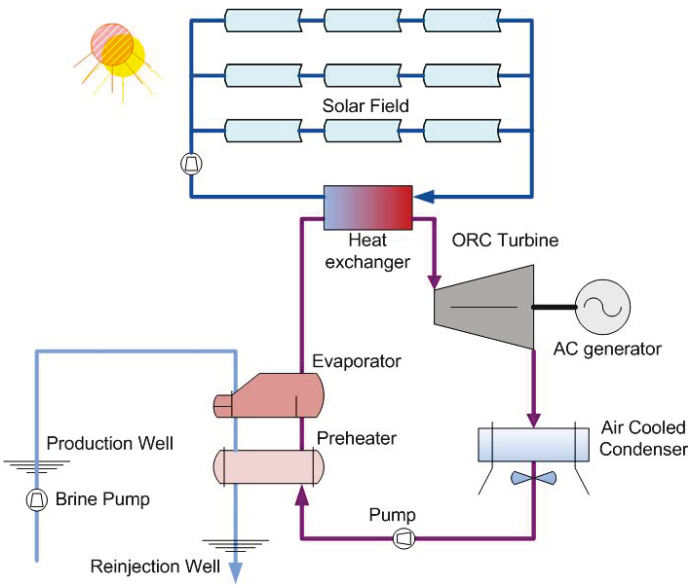

Figure 1. Hybrid geothermal / solar thermal system with solar heating of the ORC working fluid [2].

the solar energy, including (i) preheating binary cycle brine, (ii) preheating flash cycle brine to increase vapor fraction in the flash tank, (iii) superheating the organic Rankine cycle (ORC) working fluid, and (iv) reheating brine or condensate and recycling the fluid to the power cycle.

Zhou assumed an ORC binary-cycle plant and studied a design that provided solar heat into the power cycle working fluid (Figure 1). An important feature of Zhou's work is the conclusion that either of two control strategies designed to maintain the working fluid near its saturation point (i) fixing mass flow and varying temperature and pressure, or (ii) fixing temperature and pressure and varying mass flow rate, resulted in comparable thermodynamic performance. These control strategies were nearly as effective as assuming the system was optimized by allowing mass flo , temperature, and pressure to simultaneously vary, which was assumed to be too complex for plant control. Zhou also proposed a more complex integration that included a dedicated turbine for the solar-heated working fluid combined with a low-temperature turbine that can operate on geothermal energy alone.

Greenhut et al. [5] compared different hybrid configurations assuming the use of a low-temperature geothermal resource (150°C). The low thermal efficiency of a binary cycle running at ca. 150°C was a significant limitation to hybrid plant efficienc . For this reason, the authors proposed using solar energy to heat and flash the brine to produce 200°C, 15.5 bar steam. These conditions allowed operation of a steam turbine at ca. 200°C and use of the flash tank liquids to boost the organic working fluid to 180°C. When solar energy was not available the plant operated the ORC cycle alone at the lower brine temperature. Such a design was able to increase thermal efficiency from approx. 11% with the low-temp ORC power block to about 17.5% with the combined steam / ORC power system. However, moving to a flash-plant design with steam and ORC turbines brings additional complexity as well as scaling and emission concerns.

A general challenge for any hybrid design is how to efficiently accommodate two different operating points, typically corresponding to operation with and without solar energy input. Binary geothermal power plants generally have low operating temperatures (~150°C) and correspondingly low thermal-to-electric effi iency. In contrast, modern solar thermal collectors can readily achieve temperatures of 390°C, but are available on an intermittent basis. Designing a single power block to handle these different conditions is challenging, yet using two different power units increases cost and complexity, and negates advantages of having an integrated system. Of course, solar energy can be collected at lower temperature or down-graded for use in a lower temperature ORC power cycle. There are some advantages to using low-temperature solar collectors, for example, heat losses will be lower and lesser optical and material requirements can lower the cost of the solar collectors. Yet the experience of the CSP industry indicates that high-temperature and high-efficiency systems are required for favorable economics.

In 1979, the Aerospace Corporation completed a study of geothermal / solar thermal hybrids for the U.S. Department of Energy [3]. The report concluded that two issues challenge the economics of hybrid designs. The first issue is the low conversion efficiency of typical binary-cycle geothermal power cycles. This makes their use for conversion of (relatively expensive) solar-thermal energy into electricity unappealing. Flash-cycle plants offer higher efficienc , but suffer emission issues from non-condensable gases. The potentially attractive ability to heat the brine directly in solar collectors prior to flashing is countered by fouling issues. The report concluded that the best integration was to use the geothermal fluid to provide the low-temperature feedwater heating needs for a higher-temperature, higher-efficiency steam-Rankine power cycle that is driven by a CSP system.

Approach

This study simulates the use of a geothermal resource to provide feedwater heating in a CSP system running a superheated-steam-Rankine power cycle. The steam power cycle was modeled in IPSEpro process simulation software (enginomix.net), where IPSEpro was used to examine the thermodynamic performance of the power cycle with and without geothermal energy integration. IPSEpro calculated the performance of the cycle at its normal design point and at off-design conditions representing partload operation and varying ambient temperature. These results were used to map performance as a function of ambient and operating conditions that was then used in the calculation of annual system performance.

A representative steam-Rankine power cycle for a parabolic trough CSP plant was created in IPSEpro and is shown schematically in Figure 2. This power cycle has five feedwater heaters (FWH), an HTF-to-steam boiler and superheater train, and single-stage reheat. Our modeling assumes that all scenarios – solar,

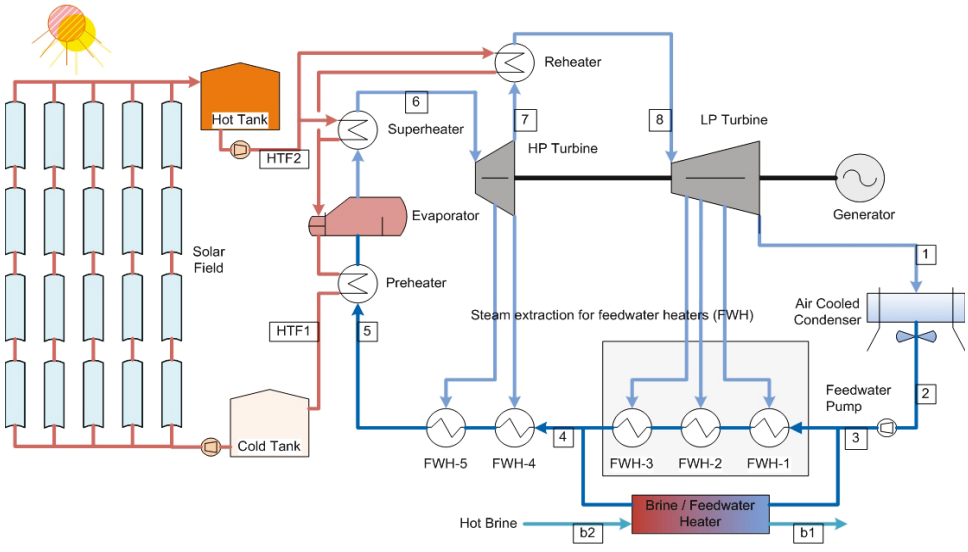

Figure 2. Schematic of a representative CSP plant showing energy from geothermal brine replacing the three low-temperature feedwater heaters (FWH-1, FWH-2, and FWH-3), thereby eliminating steam extractions from the low-pressure turbine. Open, hot (direct contact) FWHs are shown for simplicity, although the model uses closed FWHs.

geothermal, and hybrid – use air-cooled condensers to minimize water consumption. In the stand-alone solar plant, condensate from the air-cooled condenser runs through a series of FWHs that preheat the water with steam extracted from various stages of the power turbine. The first three FWHs raise the feedwater from the condenser outlet temperature (which depends on ambient conditions) to approximately 140°C. The hybrid-plant scenario looks at the effect of replacing those steam extractions with a brine-to-feedwater heat exchanger operating over the same temperature conditions (see Figure 2).

The solar resource was estimated using the typical meteorological year (TMY) weatherfile for Imperial, CA. The region around Imperial possesses good solar thermal and geothermal resources, e.g., Salton Sea and Cerro Prieto geothermal sites. TMY data sets are hourly values of solar radiation and meteorological elements for a 1-year period [4]. Their intended use is for computer simulations of solar energy conversion systems and building systems to facilitate performance comparisons of different system types, configurations, and locations. The TMY file covering 1998-2009 for Imperial, CA was downloaded from the National Renewable Energy Laboratory's (NREL) Solar Power Prospector at http://maps.nrel.gov/prospector.

The annual performance of the stand-alone solar and hybrid systems was modelled using the System Advisor Model (SAM, https://sam.nrel.gov/). SAM is a free performance and financial model designed to facilitate decision making for people involved in the renewable energy industry. First, SAM's Physical Trough model was used to simulate the hourly performance of a conventional, utility-scale parabolic trough plant. The default values present in SAM-2014-01-14 for performance and financial inputs were used, with the exception of the location as described above and assumption of dry cooling. Following the SAM default case, the CSP and hybrid plants were assumed to include 6 hours of thermal energy storage. Second, the power block routine within the SAM Physical Trough model was modified to incorporate geothermal energy integration as modeled by IPSEpro. Results from the two scenarios provided a comparison of the annual performance of the hybrid plant and the conventional CSP parabolic trough plant.

The stand-alone CSP cycle efficiency provided in Table 1 was estimated by WorleyParsons Group and is documented in reference [1]. This value is higher than that estimated by our IPSEpro model (approx. 31.9%). The IPSEpro model is used to explore the relative behavior of the hybrid cycle. For absolute cycle efficiency we rely on the more detailed WorleyParsons optimization. SAM takes as an input the design-point gross power-cycle effic ency as reported in Table 1. SAM estimates gross power and parasitic loads on an hourly basis and calculates the corresponding net power output.

The assumed stand-alone CSP plant produces 100 MWe, net at design-point conditions and the energy from the LP turbine steam extractions totals 43 MW_{th} (see Table 1). The assumed geothermal plant is sized to supply this energy, which corresponds to a brine flow rate of approximately 122 kg/s, assuming a 150°C resource and 70°C re-injection temperature.

Lastly, a model for ORC geothermal plants developed at Idaho National Laboratory (INL) was used to simulate the performance of a stand-alone, binary-cycle geothermal plant at the same site [6]. The stand-alone geothermal plant was assumed to run an isobutane ORC with variable-frequency drive isobutane pumps, variable-geometry turbine nozzle vanes, and an air-cooled condenser. The median annual ambient temperature of Imperial, CA is approximately 25°C; this value was selected as the ambient design-point temperature. Other design parameters including heat exchanger minimum temperature approach values, turbomachinery flu d and mechanical efficiencies, and frictional pressure losses at the design point were set equal to the values specified in Section 3.3 and adjusted for off-design operation as described in Section 4 of Reference [6]. No constraints on the generator output or the geofluid temperature exiting the plant were imposed. The models allowed comparisons between the hybrid design and separate CSP and geothermal plants.

Table 1. Plant characteristics. Input values used the default settings for SAM's CSP Physical Trough model except where noted. Geothermal conditions and efficiencies calculated using [6].

Parameter	Value
Stand-alone CSP plant net capacity	100 MWe
Solar field outlet temperature	391°C
Solar field area (held constant for stand-alone CSP and hybrid cases)	910,000 m^2
Stand-alone CSP design-point, gross thermal efficiency (dry cooled, T_{amb} = 42°C, 16K ITD)	35.4%
Location	Imperial, CA
Geothermal resource temperature	150°C
Brine flow rate (assuming 70°C injection temperature)	128 kg/s
Geothermal capacity	43 MW_{th}
Stand-alone geothermal design-point, net thermal efficiency, $\eta_{g0,design\text{-}point}$ (dry cooled, T_{amb} = 25°C, 15K ITD)	8.5%
Stand-alone geothermal design-point net exergy efficiency (dry cooled, T_{amb} = 25°C, 15K ITD)	28.9%

Results

Hybrid Benefit to Solar Technology

Figure 3 shows IPSEpro's estimated net thermal efficiency of the stand-alone CSP power cycle and the proposed hybrid plant as a function of power block output (recall that design-point output of the stand-alone CSP plant is 100 MWe). The data in Figure 3 are normalized by the design-point efficiency of the stand-alone CSP plant (see Table 1). First-law, thermal-to-electric efficiency is defined by the work produced divided by the thermal energy input (see Nomenclature section for variable definitions)

$$\eta_{s0} = W_{s0} / Q_{s0} \tag{1}$$

$$\eta_{hyb} = \frac{W_{hyb}}{\left(Q_s + Q_g\right)} \tag{2}$$

$$\overline{\eta}_{s0} = \frac{\eta_{s0}}{\eta_{s0,\ design-point}} \tag{3}$$

$$\overline{\eta}_{hyb} = \frac{\eta_{hyb}}{\eta_{s0,\ design-point}} \tag{4}$$

The SAM user defines the design-point case by specifying the ambient temperature, air-cooled condenser initial temperature difference (ITD), rated gross cycle capacity, and gross cycle efficienc . During annual simulations, SAM calculates gross cycle efficiency as a function of ambient temperature and cycle load on an hourly basis by using the performance map and site weather data. SAM also tracks plant parasitic loads such as cooling fans, HTF pumps, and solar collector tracking, and uses these values to calculate hourly net power.

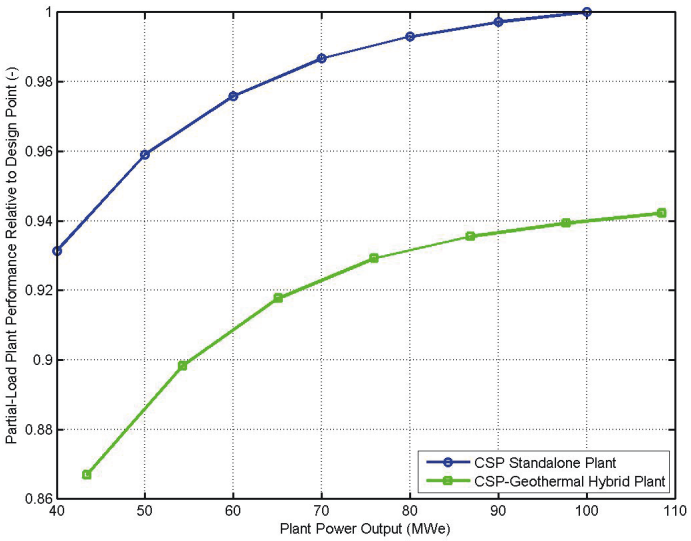

Figure 3. Stand-alone CSP plant ($\overline{\eta}_{s0}$) and hybrid plant net thermal efficiency ($\overline{\eta}_{hyb}$) vs. plant load. The efficiencies are normalized by the design-point, stand-alone CSP efficiency (see Table 1).

Three results are apparent from Figure 3. First, cycle effi iency falls off as the plant drops to lower output (as expected). Second, the hybrid power cycle has a lower overall cycle efficiency than the stand-alone solar case. This drop in efficiency results from the inclusion of low-temperature geothermal energy, which decreases the average temperature of energy addition to the power cycle and, following Carnot's theorem, decreases thermal conversion efficienc .

In contrast to the thermal efficienc , the exergy efficienc of the hybrid plant (Eqn 5) exceeds that of the stand-alone CSP plant (see Figure 4), indicating more effective utilization of the available heat sources.

$$\eta_u = \frac{W_{hyb}}{E_s^{'} + E_g} \tag{5}$$

Where exergy from solar is given by:

$$E_s^{'} = \dot{m}_{HTF}\left[\begin{matrix}\left(h_{HTF2} - h_{HTF1}\right) - \\ T_{amb}\left(s_{HTF2} - s_{HTF1}\right)\end{matrix}\right] \tag{6}$$

and exergy from geothermal from geothermal is:

$$E_g = \dot{m}_b\left[\begin{matrix}\left(h_{b2} - h_{amb}\right) - \\ T_{amb}\left(s_{b2} - s_{amb}\right)\end{matrix}\right] \tag{7}$$

The solar exergy definition (Eqn 6) follows the suggestion of Greenhut et al. [5], and defines exergy to account for the fact that

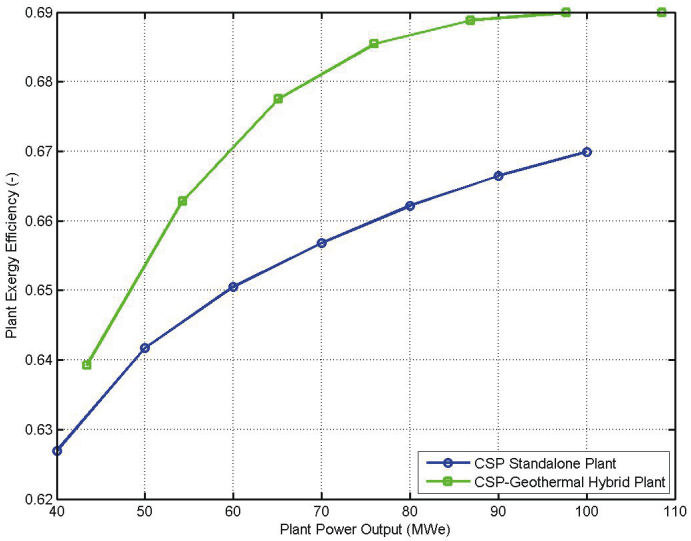

Figure 4. Stand-alone CSP plant and hybrid plant net exergy efficiency as a function of Plant power output.

exergy remaining in the HTF is not lost, but recycled to the solar fi ld. The subscripts correspond to stream labels shown in Figure 2.

The third result from Figure 3 is the greater power output from the hybrid plant. While the hybrid cycle thermal efficiency is lower than the stand-alone CSP case, the overall power output from the hybrid plant is greater, due to inclusion of the geothermal energy. This is indicated in Figure 3 by the shift in the hybrid plant data points (which correspond to the same solar-thermal input) to higher plant power output. For example, the power output at design point has risen from 100 MWe to 108.5 MWe.

If one views the geothermal energy as "free" to the solar plant, this greater power output represents a performance boost of 8.5% (at design point) above that of the stand-alone solar case. From the solar plant perspective, the benefit of the hybrid design is higher exergy efficiency resulting in greater total power output for the same solar-thermal input.

Hybrid Benefit to Geothermal Technology

The benefi of the hybrid design from the geothermal perspective is manifested in a higher thermal and exergy efficiency compared to a stand-alone geothermal plant.

Mathur [3] used the simple ratio of hybrid efficiency to stand-alone geothermal efficienc , η_{hyb} / η_{g0}, to illustrate the benefit of the hybrid design. We prefer to define a geothermal efficiency ratio (*GER*) estimated by comparing the efficiency at which geothermal energy is converted in the hybrid plant, η_g, with stand-alone geothermal efficienc , η_{g0}:

$$GER = \frac{\eta_g}{\eta_{g0}} = \frac{\left(W_{hyb} - Q_s\eta_{s0}\right)/Q_g}{\eta_{g0}} \tag{8}$$

In *GER*, power contribution from solar energy is estimated as the solar thermal energy, Q_s, multiplied by its conversion effi iency in the stand-alone CSP plant, η_{s0}. This product is subtracted from the total hybrid plant power generation, W_{hyb}, to yield a conservative estimate (lower bound) of the power contribution from geothermal energy. The result is conservative, because the energy efficiency of the hybrid plant is actually slightly lower than in the stand-alone solar plant. This defi ition accounts for the lower

thermal efficiency imposed on the solar plant by inclusion of the low-temperature geothermal energy.

Figure 5 and Figure 6 compare geothermal energy conversion efficiency for a stand-alone geothermal plant and the hybrid. The values indicate a *GER* that is 1.7 to 2.5, indicating more efficient use of the geothermal energy in the hybrid than in a stand-alone geothermal plant. Note that this represents conversion of geothermal energy only; the overall hybrid plant efficiency is on the order of 3.6 times greater than η_{g0}.

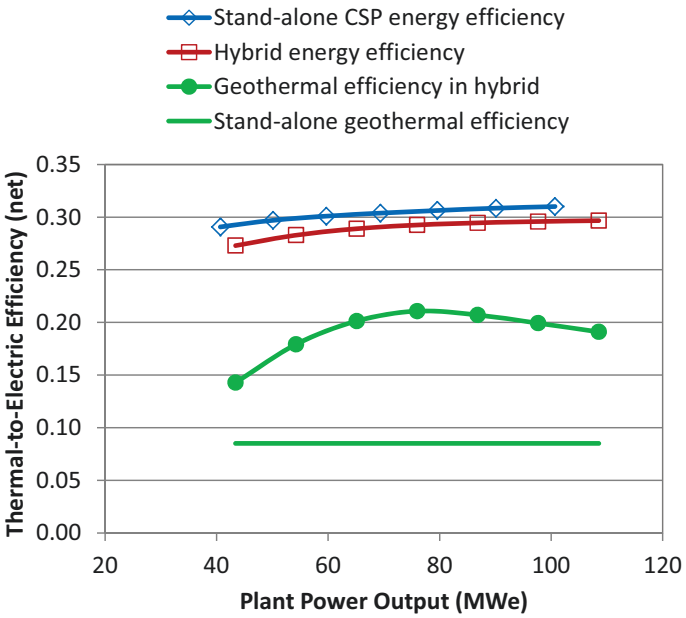

Figure 5. Comparison of system efficiencies: geothermal energy conversion efficiency in the hybrid plant (η_g), exceeds the stand-alone geothermal plant efficiency (η_{g0}) by a factor of 2 or more.

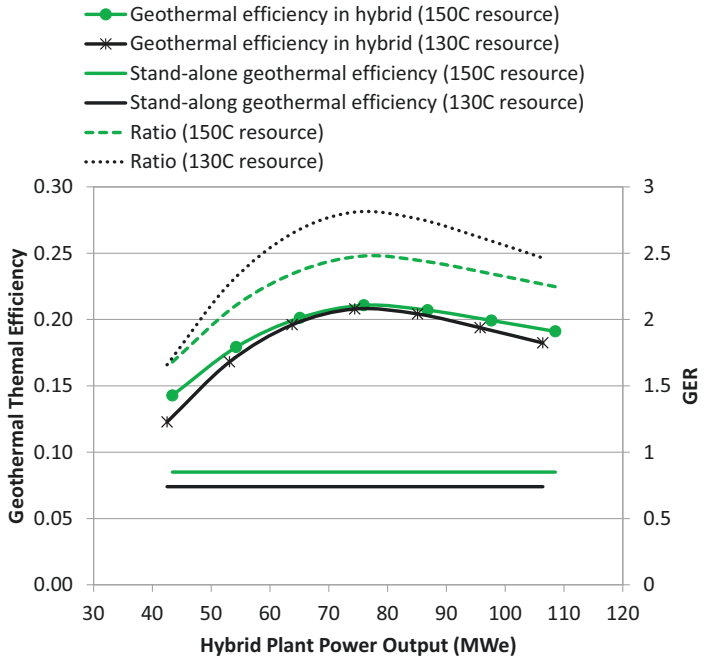

Figure 6. Impact of geothermal resource temperature on the geothermal efficiency in a hybrid plant and in a stand-alone geothermal plant.

An issue that often plagues geothermal power plants is degradation of the resource over time. The geothermal resource temperature or flow rate may fall with time, leading to a serious drop in power output from the geothermal plant. This behavior may trigger drilling of additional production well(s), at significan expense and risk. In the hybrid plant, the impact of decreasing geothermal energy can be offset by instigating or increasing steam extraction from the LP turbine, with a relatively minor penalty to plant output. Figure 6 shows how geothermal efficiency in the hybrid plant, η_g, and in a stand-alone geothermal plant, η_{g0}, change if the resource temperature falls from 150°C to 130°C. As indicated by the efficienc ratios, the relative advantage of the hybrid plant increases when the resource temperature drops.

In summary, the benefit of the hybrid from the geothermal perspective is the higher geothermal energy conversion efficienc obtained in the hybrid plant and less sensitivity to ambient conditions and resource degradation.

Annual Performance

The preceding analysis suggests advantages for the hybrid system relative to both the solar and geothermal stand-alone plants. The next step is to determine how this potential manifests itself over the course of a typical year, where solar conditions and ambient temperature are constantly changing. The comparison is made by modeling a stand-alone CSP plant in SAM, using INL's ORC model for a stand-alone binary-cycle geothermal plant, and finally modeling the proposed hybrid design in SAM with the use of the modified power block algorithm.

The overall comparison between the hybrid vs. two stand-alone plants can be measured by the figure of merit (*FM*) suggested by Zhou [2]:

$$FM = \frac{W_{hyb}}{W_{s0} + W_{g0}} \tag{9}$$

$$FM_{annual} = \frac{W_{hyb,annual}}{W_{s0,annual} + W_{g0,\,annual}} \tag{10}$$

A favored hybrid design is indicated by $FM_{annual} > 1$, which means the hybrid produces more energy than two stand-alone power plants using the same capacity solar and geothermal resources. *FM* can be calculated instantaneously (Eqn 9) or annually (Eqn 10).

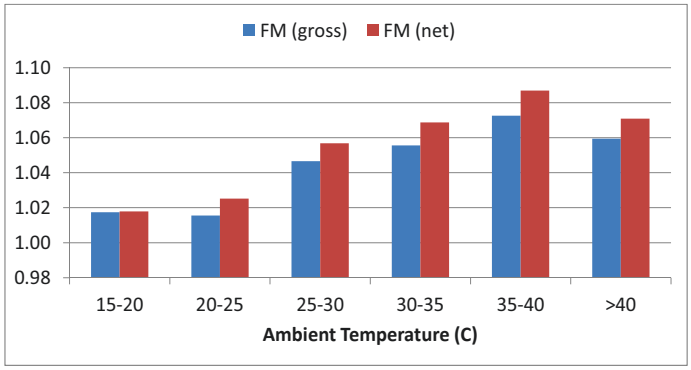

Figure 7. Figure of Merit (Eqn 9) for the hybrid plant when operating. Annual average values are 1.048 for gross generation and 1.059 for net generation.

Figure 7 shows the results for net- and gross-power hourly *FM* during the year when the hybrid plant is operating. The bars depict average hourly *FM* for different ambient temperature ranges. The average *FM* exceeds 1 in all cases, indicating the hybrid plant is producing more power than two, stand-alone CSP and geothermal plants of equivalent thermal capacities to that used in the hybrid. A greater benefit is realized at higher ambient temperatures because the hybrid plant is less affected by ambient temperature than the performance of a stand-alone geothermal plant.

The latter point is also illustrated by plotting the hourly *GER* (see Eqn 8) as a function of ambient temperature. Average *GER* is highest during periods of high ambient temperature, showing that use of the geothermal energy for feedwater heating in the CSP plant is much more effective than use in a stand-alone geothermal plant during these periods, due to the ORC's sensitivity to condenser pressure.

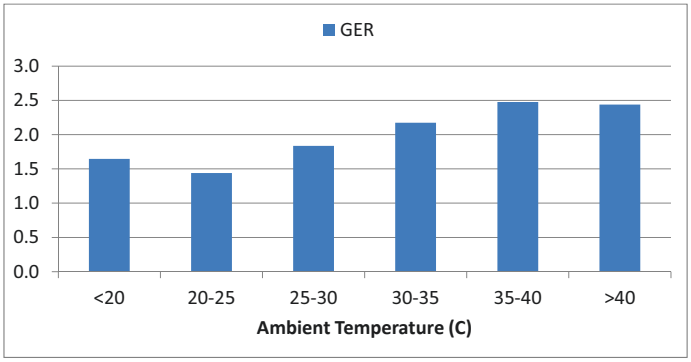

Figure 8. Average Geothermal Efficiency Ratio (*GER*) for different ambient temperatures when the hybrid plant is operating. Values greater than 1 indicate superior geothermal-to-electric conversion efficiency in the hybrid.

An interesting finding from the annual analysis was a small decrease in hybrid plant efficiency at low condenser pressures (i.e., low ambient temperature). The result was counter-intuitive as cycle efficiency normally increases as ambient temperature falls. This behavior was attributed to use of more geothermal energy to preheat the lower-temperature condensate to the target feedwater temperature at point 4 in Figure 2 – a temperature that was assumed to be a fixed value in the model. As previously described, a greater contribution for geothermal energy results in a lower overall cycle efficienc . The results suggest that more sophisticated integration schemes, for example, varying steam extraction rates, could yield additional benefits in cycle performance.

Impact of Annual Operating Hours

The *FM* and *GER* values strongly favor the hybrid design *when the hybrid plant is operating*. However, the solar plant has an annual capacity factor of about 42%, meaning the geothermal energy can heat feedwater for only about 42% of the year. Consequently, the value of FM_{annual} depends on the annual capacity factor of the different plants.

Figure 9 shows how annual *FM* varies with the capacity factor of the stand-alone geothermal plant. The breakeven point ($FM_{annual} = 1$) in this study falls at a capacity factor of about 0.74. If the solar and hybrid plants are designed with more thermal energy storage to achieve capacity factors of 0.56, the FM_{annual} value would never fall below 1 (dotted line). Also shown in Figure 9 are the results if one employs an ORC power block for use when the CSP plant is offline (dashed line). In this scenario, FM_{annual} is never lower than 1.02. The ORC power block is estimated to run with an annual-average net efficiency of 9.2%, which is higher than the value of 8.6% estimated for the stand-alone geothermal. The higher efficiency results from use of the ORC only when the CSP plant is offline, which typically corresponds to cooler ambient conditions. Of course, adding another power block eliminates that cost-saving advantage of the hybrid integration.

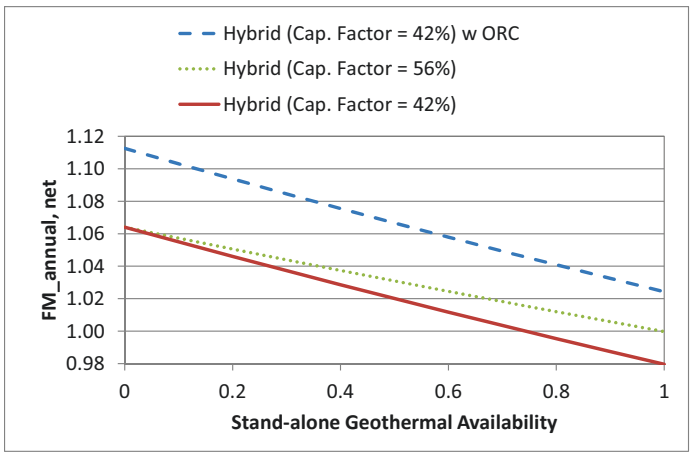

Figure 9. Annual figure of merit, FM_{annual}, for the hybrid design. A value greater than 1 indicates the hybrid produces more energy than the combined output of a stand-alone geothermal and stand-alone CSP plant.

Conclusions

This paper examined a hybrid geothermal / solar-thermal plant design that uses the geothermal energy to provide feedwater heating in a conventional steam-Rankine power cycle such as used by parabolic-trough CSP plants. The geothermal energy represented 11.4% of the annual thermal input to the hybrid plant. The geothermal energy allowed power output from the hybrid plant to increase by about 8.5% relative to a stand-alone CSP plant with the same solar-thermal input. Geothermal energy was converted to electricity at an efficiency of 1.7 to 2.5 times greater than would occur in a stand-alone, binary-cycle geothermal plant at the same site. These benefits led to the hybrid plant generating approximately 6% more power at design-point compared with two stand-alone plants.

While the design exhibited a clear advantage during operation, the annual generation advantage of the hybrid versus two stand-alone power plants depended on the total annual operating hours of the plants. Annual generation from the hybrid design exceeds that of two stand-alone plants only if the stand-alone geothermal plant operates at an annual capacity factor of 74% or less. (Note that in this study the hybrid plant had a capacity factor of 42%.)

The cost and revenue implications of the hybrid design have not been assessed in the present analysis, but are expected to favor the hybrid design due to the elimination of the geothermal power block and the good correlation of solar resource with electricity demand in the US southwest that leads to higher pricing per kWh during plant operation. Revenue and cost advantages will be explored in future work. Other potential benefits for future examination include:

- Utilizing geothermal energy to maintain the steam turbine in a hot-standby mode overnight, thereby improving plant start-up time in the morning and avoiding that energy parasitic on the solar plant,
- Examining the benefits with alternative CSP plant designs, for example, molten-salt power towers running at higher efficiency and greater capacity factor than the trough plant assumed here, and
- Assessing if lowering the brine flow rate overnight will extend geothermal resource life, and
- Testing if addition of an ORC to operate on the available geothermal energy when the CSP plant is offl ne (e.g., overnight) provides a net cost benefit.

Nomenclature

Acronyms:

CSP	= concentrating solar power
GER	= geothermal efficienc ratio
HP	= high pressure
HTF	= heat transfer flui
INL	= Idaho National Laboratory
ITD	= initial temperature difference
LP	= low pressure
NREL	= National Renewable Energy Laboratory
ORC	= organic Rankine cycle
SAM	= System Advisor Model

Variables:

Q	= *thermal energy*
E	= *exergy*
W	= *work (i.e., electrical energy)*
h	= *specific enthalp*
s	= *specific ent opy*
$\dot{m}$	= *mass flow rat*
T	= *temperature*
η	= *thermal (1st law) efficie cy*
η_u	= *utilization (2nd law) effi iency*

Subscripts:

amb	= *evaluated at ambient conditions*
b	= *geothermal brine*
g	= *geothermal contribution within hybrid*
g0	= *stand-alone geothermal*
hyb	= *hybrid*
HTF	= *solar heat transfer flui*
s	= *solar contribution within hybrid*
s0	= *stand-alone solar*

Acknowledgments

This work was supported by the U.S. Department of Energy under Contract No. DE-AC36-08-GO28308 with the National Renewable Energy Laboratory.

References

[1] Turchi, C., 2010. "Parabolic Trough Reference Plant for Cost Modeling with the Solar Advisor Model (SAM)," NREL/TP-550-47605.

[2] Zhou, C., E. Doroodchi, and B. Moghtaderi, 2013. "An in-depth assessment of hybrid solar–geothermal power generation," *Energy Conversion and Management*, **74,** 88-101.

[3] Mathur, P.N., 1979. "An Assessment of Solar-Geothermal Hybrid System Concepts," Report ATR-79(7773-01)-2, under contract EY-76-C-03-1101, Aerospace Corporation, El Segundo, CA.

[4] Stoffel, T., D. Renné, D. Myers, S. Wilcox, M. Sengupta, R. George, and C. Turchi, 2010. "Concentrating Solar Power, Best Practices Handbook for the Collection and Use of Solar Resource Data," NREL/TP-550-47465.

[5] Greenhut, A.D., J.W. Tester, R. DiPippo, R. Field, C. Love, K. Nichols, C. Augustine, F. Batini, B. Price, G. Gigliucci, I. Fastelli, 2010. "Solar-Geothermal Hybrid Cycle Analysis for Low Enthalpy Solar and Geothermal Resources," Proceedings World Geothermal Congress 2010, Bali, Indonesia, 25-29.

[6] Wendt, D.S., and G.L. Mines, 2013. "Simulation of Air-Cooled Organic Rankine Cycle Geothermal Power Plant Performance," Idaho National Laboratory, INL/EXT-13-30173.